

NANOARCHITECTURE-PROPERTY RELATIONSHIPS IN TiSe_2 BASED
NANOLAMINATES FOR DEVELOPMENT OF NOVEL
DESIGN STRATEGIES IN COMPOSITE
THERMOELECTRIC MATERIALS

by

SAGE R. BAUERS

A DISSERTATION

Presented to the Department of Chemistry and Biochemistry
and the Graduate School of the University of Oregon
in partial fulfillment of the requirements
for the degree of
Doctor of Philosophy

December 2016

DISSERTATION APPROVAL PAGE

Student: Sage R. Bauers

Title: Nanoarchitecture-Property Relationships in TiSe_2 Based Nanolaminates for Development of Novel Design Strategies in Composite Thermoelectric Materials

This dissertation has been accepted and approved in partial fulfillment of the requirements for the Doctor of Philosophy degree in the Department of Chemistry and Biochemistry by:

Shannon W. Boettcher	Chairperson
David C. Johnson	Advisor
George Nazin	Core Member
Ben McMorran	Institutional Representative

and

Scott L. Pratt	Dean of the Graduate School
----------------	-----------------------------

Original approval signatures are on file with the University of Oregon Graduate School.

Degree awarded December 2016

© 2016 Sage R. Bauers

DISSERTATION ABSTRACT

Sage R. Bauers

Doctor of Philosophy

Department of Chemistry and Biochemistry

December 2016

Title: Nanoarchitecture-Property Relationships in TiSe_2 Based Nanolaminates for Development of Novel Design Strategies in Composite Thermoelectric Materials

This dissertation is centered on investigation of metastable thermoelectric thin film materials and is split into 3 primary sections. Section 1 focuses on formation mechanisms of FeSb_x compounds from layered precursors. It was found that a compositionally favorable and homogeneous nucleation environment allowed for the nucleation of a metastable phase, which surprisingly resembles the local coordination environment of the precursors, even in cases where they are compositionally unfavorable. Over the course of this work, the technique of normal-incidence thin film pair distribution function analysis is introduced, which allows for rapid acquisition and analysis of local structure data from intact thin films.

Section 2 investigates changes in the stacking sequences of $([\text{PbSe}]_{1+\delta})_m(\text{TiSe}_2)_n$ nanolaminate materials, which consist of interleaved layers of each compound in the chemical formula, and how these changes effect the thermoelectric power factor. Homologous series of systematically varying m and n values are investigated and measured properties are correlated back to the designed nanoarchitecture of the laminate materials. It is found that the compounds are stabilized by electron exchange between constituents at the interfaces, and that ‘doping’ of the laminate structure by changing the relative

amounts of each constituent is an effective means of optimizing their transport properties. It is also shown that interface density between constituents can be utilized to optimize performance.

Section 3 moves from the case of PbSe layers, which maintain their structure, to SnSe layers that significantly distort as the layer size is changed. The distortions in SnSe are observed to occur from templating off TiSe_2 layers. As the size of the SnSe layers increases, relatively fewer templated interfacial atoms exist and stabilization of interior atoms must also be considered. The coarse behaviors developed in $([\text{PbSe}]_{1+\delta})_m(\text{TiSe}_2)_n$ hold, but the structural distortions in SnSe likely change the band structure of this constituent and hence the composite material, complicating the analysis. In some cases, these changes allow for radically different behavior, best exemplified with high TiSe_2 ratios in $([\text{SnSe}]_{1+\delta})_l(\text{TiSe}_2)_n$ displaying significant enhancement of the Seebeck coefficient at cryogenic temperatures over the low- n and PbSe-containing analogues.

This dissertation includes previously published and unpublished coauthored material.

CURRICULUM VITAE

NAME OF AUTHOR: Sage R. Bauers

GRADUATE AND UNDERGRADUATE SCHOOLS ATTENDED:

University of Oregon, Eugene, OR
California State University, Sacramento, CA
Sacramento City College, Sacramento, CA

DEGREES AWARDED:

Doctor of Philosophy, Chemistry, 2016, University of Oregon
Master of Science, Applied Physics, 2013, University of Oregon
Bachelor of Science, Physics, 2012, California State University

PROFESSIONAL EXPERIENCE:

Co-op Process Control Monitor Engineer
IBM Corporation, 2013

GRANTS, AWARDS, AND HONORS:

Graduate Student Award, International Thermoelectric Society, 2016

Dean's Award, California State University, Sacramento, 2012

PUBLICATIONS:

Bauers, S. R. and Johnson, D. C. Designing thermoelectric materials using 2D layers. In *Handbook of Solid State Chemistry*; Stein, A., Ed.; Wiley-VCH. *Accepted - In Press*.

Bauers, S. R.; Ditto, J.; Moore, D. B.; Johnson, D.C. Structure–property Relationships in Non-Epitaxial Chalcogenide Heterostructures: The Role of Interface Density on Charge Exchange. *Nanoscale* **2016**, 8 (30), 14665–14672.

Bauers, S. R.; Wood, S. R.; Jensen, K. M. O.; Blichfeld, A. B.; Iversen, B. B.; Billinge, S. J. L.; Johnson, D. C. Structural Evolution of Iron Antimonides from Amorphous Precursors to Crystalline Products Studied by Total Scattering Techniques. *J. Am. Chem. Soc.* **2015**.

Bauers, S. R.; Merrill, D. R.; Moore, D. B.; Johnson, D. C. Carrier Dilution in TiSe₂ Based Intergrowth Compounds for Enhanced Thermoelectric Performance. *J. Mater. Chem. C* **2015**, 3 (40), 10451–10458.

Bauers, S. R.; Moore, D. B.; Ditto, J.; Johnson, D. C. Phase Width of Kinetically Stable ([PbSe]_{1+δ})₁(TiSe₂)₁ Ferecrystals and the Effect of Precursor Composition on Electrical Properties. *J. Alloys Compd.* **2015**, 645, 118–124.

Merrill, D.; Moore, D.; Bauers, S.; Falmbigl, M.; Johnson, D. Misfit Layer Compounds and Ferecrystals: Model Systems for Thermoelectric Nanocomposites. *Materials (Basel)*. **2015**, 8 (4), 2000–2029.

Jensen, K. O.; Blichfeld, A. B.; Bauers, S. R.; Wood, S. R.; Johnson, D. C.; Iversen, B. B.; Billinge, S. J. L. Demonstration of Thin Film Pair Distribution Function analysis (tfPDF) for the study of the local structure of amorphous and crystalline thin films. *IUCrJ*. **2015**.

Merrill, D. R.; Sutherland, D. R.; Ditto, J.; Bauers, S. R.; Falmbigl, M.; Medlin, D. L.; Johnson, D. C. Kinetically Controlled Site-Specific Substitutions in Higher-Order Heterostructures. *Chem. Mater.* **2015**, 27 (11), 4066–4072.

Falmbigl, M.; Putzky, D.; Ditto, J.; Esters, M.; Bauers, S. R.; Ronning, F.; Johnson, D. C. Influence of Defects on the Charge Density Wave of ([SnSe]_{1+δ})₁(VSe₂)₁ Ferecrystals. *ACS Nano* **2015**, 9 (8), 8440–8448.

Alemayehu, M. B.; Falmbigl, M.; Ta, K.; Grosse, C.; Westover, R. D.; Bauers, S. R.; Fischer, S. F.; Johnson, D. C. Structural and Electrical Properties of ([SnSe]_{1+δ})₁M(NbSe₂)₁ Compounds: Single NbSe₂ Layers Separated by Increasing Thickness of SnSe. *Chem. Mater.* **2015**, 27 (3), 867–875.

Carnes, M.E.; Knutson, C.C.; Nadarajah, A.; Jackson, M.N.; Oliveri, A.F.; Norelli, K.M.; Crockett, B.M.; Bauers, S.R.; Moreno-Luna, H.A.; Taber, B.N.; Pacheco, D.J.; Electrochemical synthesis of flat-[Ga_{13-x}In_x(μ₃-OH)₆(μ₃-OH)₁₈(H₂O)₂₄(NO₃)₁₅] clusters as aqueous precursors for solution-processed semiconductors. *J. Mater. Chem. C* **2014**, 2 (40), 8492–8496.

ACKNOWLEDGMENTS

During this work I have had the good fortune to engage with several researchers locally, nationally, and globally. I would like to recognize all of these individuals whose time, encouragement, and guidance helped me find success.

First I would like to thank my advisor, Professor David C. Johnson. He allowed me to join his group sight-unseen from 3000 miles away and yet somehow our abilities, interests, and approach meshed such that in three years we've achieved more than I'd ever have expected. Thank you - I couldn't have found a better mentor. I would also like to thank my colleagues in the Johnson lab. Dr. Devin Merrill, Dr. Jeff Ditto, Suzannah Wood, and especially Dr. Dan Moore have all directly had a hand in my work and have been my coauthors. Danielle Hamann deserves special thanks and encouragement – the torch has been passed and I hope it burns brightly. Marco Esters, Gavin Mitchson, Erik Hadland, Dr. Richard Westover, Kyle Hite, Dr. Noel Gunning, and Dr. Matti Alemayehu were always available for helpful conversation and a second opinion. Our former post-doctoral researcher, Dr. Matthias Falmbigl was always present to share his wealth of knowledge. I would like to thank all of our lab undergraduates. Duncan Sutherland deserves special recognition for always demanding a better explanation, which in turn helped to deepen my own understanding. Several colleagues from other labs at UO have also helped along the way, and I thank you all as well.

I would also like to acknowledge the several collaborators I have had the pleasure to work with. This includes, Dr. Kirsten Jensen, Dr. Bo Iversen, Dr. Simon Billinge, Dr. Sabrina Disch, Dr. Austin Minnich, and Dr. Stephen Cronin. You and your students, especially Anders Blichfeld and Maria

Hentschel have been critical to moving my research forward. Thank you all for the guidance and good times, whether in Eugene, Manhattan, Chicago, Grenoble, Aarhus, or elsewhere.

Most importantly, I need to thank my wonderful partner, Katherine Dudney, whose love, support, and help made this whole process both easier and much more worthwhile than if I'd been on my own. Thank you for being my best friend and sharing the adventure.

Other facilities, individuals, and support staff deserve recognition. This includes Jenia Karapetrova at the Advanced Photon Source, Dr. Roberto Felici at the European Synchrotron Radiation Facility, Dr. Milinda Abeykoon at the National Synchrotron Radiation Facility, and both Julie Chouinard and Josh Razink at CAMCOR. The support and technical expertise of Kris Johnson, Cliff Dax, and Steve Wiemholt deserves special thanks for keeping the ship afloat!

Lastly, I would like to acknowledge funding from the National Science Foundation under grant DMR-1266217 and also under the Center for Chemical Innovation (CCI) grant CHE-1102637. Use of the Advanced Photon Source, an Office of Science User Facility operated for the U.S. Department of Energy (DOE) Office of Science by Argonne National Laboratory, was supported by the U.S.DOE under contract no. DE-AC02-06CH11357. Use of the National Synchrotron Light Source, Brookhaven National Laboratory, was supported by the DOE-BES, under Contract No. DE-AC02-98CH10886. Use of the Pacific Northwest National Laboratory electron microscopy facility was supported by the DOE under contract no. DE-AC05-76RL01830.

To my parents whose encouragement, not pressure, allowed me to find my way.

TABLE OF CONTENTS

Chapter	Page
I. INTRODUCTION: DESIGNING THERMOELECTRIC MATERIALS USING 2D LAYERS	1
1.1. Introduction	1
1.2. Physical Picture	2
1.3. Optimizing Thermoelectric Materials: Minimizing Lattice Conductivity	6
1.3.1. The Electron Crystal Phonon Glass Approach	6
1.3.2 Other Methods to Reduce Thermal Conductivity	8
1.4. Optimizing Thermoelectric Materials: Maximizing Power Factor	10
1.5. Bridge to Nanolaminate Structures	14
1.6. Transition Metal Dichalcogenide Compounds.....	16
1.7. Misfit Layer Compounds	16
1.8. Thin-Film Superlattice Materials.....	19
1.9. Van der Waals Heterostructures	20
1.10. Kinetically Trapped Nanolaminates	22
1.11. $([\text{MSe}]_{1+\delta})_1(\text{TiSe}_2)_1$ Ferecrystals	25
1.12. Outlook	31
1.13. Overview of Dissertation	31
II. SYNTHESIS AND CHARACTERIZATION METHODS	34
III. SYNTHETIC CONSIDERATIONS FOR METASTABLE THIN-FILM THERMOELECTRIC MATERIALS FROM AMORPHOUS PRECURSORS	41
3.1. Structural Evolution of Iron Antimonides from Amorphous Precursors to Crystalline Products Studied by Total Scattering Techniques	41

Chapter	Page
3.1.1. Introduction	41
3.1.2. Structures in FeSb _x Chemical System	43
3.1.3. Experimental Methods	44
3.1.4. Results and Discussion	46
3.1.5. Conclusions	55
3.2. Demonstration of Thin Film Pair Distribution Function Analysis (tfPDF) for the Study of the Local Structure of Amorphous and Crystalline Thin Films	56
3.2.1. Introduction	56
3.2.2. Experimental Details	59
3.2.2.1. Preparation of FeSb _x	59
3.2.2.2. tfPDF measurements	60
3.2.2.1. Data analysis.....	62
3.2.3. Results and Discussion	62
3.2.3.1. Obtaining the tfPDF: Amorphous and crystalline FeSb ₃ films	62
3.2.3.2. Structures in the FeSb _x system: Sample 1	66
3.2.3.3. Structures in the FeSb _x system: Sample 2	70
3.2.4. Conclusion	73
3.3. Bridge.....	74
IV. PHASE WIDTH OF KINETICALLY STABLE ([PbSe] _{1+δ}) ₁ (TiSe ₂) ₁ FERECRYSTALS AND THE EFFECT OF PRECURSOR COMPOSITION ON ELECTRICAL PROPERTIES.....	75
4.1. Introduction	75
4.2. Materials and Methods	77
4.3. Results and Discussion	79

Chapter	Page
4.3.1. Structural Characterization	79
4.3.2. Electrical Characterization	82
4.3.3. Defect Characterization	87
4.4. Conclusions	89
4.5. Bridge	90
V. STRUCTURE-PROPERTY RELATIONSHIPS IN NON-EPITAXIAL CHALCOGENIDE HETEROSTRUCTURES: THE ROLE OF INTERFACE DENSITY ON CHARGE EXCHANGE	91
5.1. Introduction	91
5.2. Materials and Methods	92
5.3. Results	94
5.3.1. Structure	94
5.3.2. Transport	98
5.4. Discussion	103
5.5. Conclusions	106
5.6. Bridge	107
VI. BURIED INTERFACES IN THE UNI CELL OF $[(\text{PbSe})_{1+\delta}]_4(\text{TiSe}_2)_4$ NANOLAMINATE THIN FILMS AND THEIR EFFECT ON THE THERMOELECTRIC TRANSPORT PROPERTIES	108
6.1. Introduction	108
6.2. Experimental Methods	110
6.3. Results	110
6.3.1. Synthesis/Structure	111
6.3.2. Transport Properties	114
6.4. Conclusions	120
6.5. Bridge	121

Chapter	Page
VII. CARRIER DILUTION IN TiSe_2 BASED INTERGROWTH COMPOUNDS FOR ENHANCED THERMOELECTRIC PERFORMANCE.....	122
7.1. Introduction	122
7.2. Experimental	125
7.3. Results and Discussion	126
7.3.1. Structural.....	126
7.3.2. Electrical	129
7.4. Conclusions.....	138
7.5. Bridge.....	138
VIII. HIGH THERMOELECTRIC POWER FACTOR AT CRYOGENIC TEMPERATURES IN $([\text{SnSe}]_{1+\delta})_l(\text{TiSe}_2)_n$ HETEROSTRUCTURE NANOLAMINATES.....	139
8.1. Introduction	139
8.2. Experimental Methods	141
8.3. Results and Discussion	142
8.3.1. Structural Characterization	142
8.3.2. Electrical Characterization.....	144
8.4. Conclusions.....	149
8.5. Bridge.....	150
IX. DIVERSE AND BIPOLAR TRANSPORT BEHAVIOR IN $([\text{SnSe}]_{1+\delta})_m(\text{TiSe}_2)_n$ NANOLAMINATES UNDERGOING STRUCTURAL DISTORTIONS	151
9.1. Introduction	151
9.2. Materials and Methods	153
9.3. Results and Discussion	154
9.3.1. Synthesis.....	154

Chapter	Page
9.3.2. Structure.....	154
9.3.3. Transport	160
9.4. Conclusions.....	163
X. CONCLUSIONS, SUMMARY, AND OUTLOOK FOR FUTURE WORK	165
REFERENCES CITED	168

LIST OF FIGURES

Figure		Page
1.1.	Speculative band structure from a compound with (left) a single heavy carrier pockets and a compound with (middle) several lighter carrier pockets. However, both compounds might integrate to similar profiles (right) in $g(E)$ and have similar effective masses as perceived by the density of states. When doped n-doped (p-doped), the chemical potential in each moves toward μ' (μ''), populating the respective pockets with carriers. The light degenerate bands maintain their high mobility, despite the high perceived mass.....	05
1.2.	Polyhedral and ball-and-stick schematics of a filled skutterudite structure. The rattling atoms are typically low-valance heavy atoms to maximize their displacement parameters and thus their effectiveness at phonon-scattering. The host lattice consists of metal centers octahedrally coordinated by a pnictide and should be highly covalent and conductive.....	08
1.3.	(left) Adapted from reference ²⁵ . Schematic $g(E)$ for PbTe with and without resonant levels. (right) Adapted from reference ²⁶ . Sharp features in $g(E)$ from resonant states created by Tl doping increase the Seebeck coefficient relative to PbTe that is Na-doped to a similar carrier concentration but without resonant coupling. However, recent density function theory (DFT) calculations of PbTe have predicted a values similar to PbTe:Tl without enhancement from band resonances. ^{26,27}	12
1.4.	Density of states for YbAl ₃ modeled after calculated data in reference. ⁴¹ The delta-function like features in $g(E)$ near the chemical potential result in high Seebeck coefficients for the compound, despite a metal-like carrier density. This results in unparalleled room-temperature power factors for the material.....	14
1.5.	Schematic of the structures found in a chalcogenide misfit compound. The basal planes of the rock-salt (MX) and octahedrally coordinated transition metal dichalcogenide (TX ₂) have a commensurate a-axis, but distinct b-axes (given by b_1 and b_2 , respectively), and the structures are interleaved along the c-axis.....	17
1.6.	Structures of ([PbSe] _{1+δ}) ₄ (TiSe ₂) ₄ isomers. (left) The six structural isomers that can be made in the $m=n=4$ layering scheme. (right) Confirmation of consistent c-lattice parameters from samples with these structures, but different peak intensities due to the unique electron density profiles within the superlattice.....	24

1.7.	Schematic density of states based on electronegativity and coordination environments for $([\text{PbSe}]_{1+\delta})_m(\text{TiSe}_2)_n$ compounds. The composite band structure is considered to be a superposition of the individual constituents' band structures and conduction is assumed to occur through a single band – in this case by electrons populating the Ti-3d band. In this model, the extent of charge transfer between PbSe and TiSe_2 constituents will determine the carrier density.....	26
1.8.	Carrier densities as a function of temperature in $([\text{MSe}]_{1+\delta})_1(\text{TiSe}_2)_1$ for $\text{M} = \text{Sn}^{97}, \text{Pb}^{95}, \text{Bi}^{104}$. The compounds containing isovalent Sn and Pb atoms show very similar carrier concentrations. As expected from the conduction mechanism shown and discussed in Figure 1.7., the compound containing trivalent Bi atoms have an increased carrier concentration of approximately 1 electron per Bi atom.....	27
1.9.	Atomic plane positions along the stacking direction of the superlattice in $([\text{MSe}]_{1+\delta})_1(\text{TiSe}_2)_1$ where $\text{M} = \text{Sn}, \text{Pb}$ as determined from Rietveld refinement. Two unit cells are shown for each superlattice, with the origin at the central Ti plane. Line positions are to scale.....	28
1.10.	In-plane diffraction patterns ($\lambda = \text{Cu-K}\alpha$) of $([\text{MSe}]_{1+\delta})_1(\text{TiSe}_2)_1$ for $\text{M} = \text{Sn}, \text{Pb}$, and Bi adapted from reference ⁹¹ . The MSe layer indices are shown in bold and match the curve colors, with the SnSe and BiSe indices also being italicized. TiSe_2 peaks are indexed in black and in normal type. The in-plane MSe layers are square for PbSe, slightly tetragonally distorted for SnSe, and highly distorted for BiSe. Also shown is a schematic of the approximate lattice match of SnSe in TiSe_2 in the distorted SnSe layers with lattice parameters taken from reference. ⁹¹	29
1.11.	Seebeck coefficients and power factors of $([\text{MSe}]_{1+\delta})_1(\text{TiSe}_2)_n$ for $\text{M} = \text{Sn}, \text{Pb}$, and Bi. A systematic increase in the magnitude of the Seebeck coefficient is observed for increasing n in all material systems. This also translates to increased power factor, though variation in sample quality, and hence mobility ¹⁰⁶ , results in slightly more scatter in the data.....	30
2.1.	Schematic of physical vapor deposition chamber used for the synthesis of thin-film layered precursors. The simplified schematic (right) highlights the vacuum pump system and uses the acronyms CT for cryogenic entrapment pump, G1 and G2 for gate valves, AV for angle valve, and TM for turbo-molecular pump.....	35

2.2.	Schematic of the homogeneous nucleation environment that can be created in thin layers deposited from the vapor phase and the interfacial nucleation environment found in thicker layers or bulk reactions. While the local composition of the homogeneous precursor can be controlled with the layers, the chemical gradient present in the thick layers necessarily provides regions of compositional favorability for the formation of thermodynamic products.....	35
2.3.	Calibration of the deposition tooling factors for a laminate system consisting of thin Fe and Sb layers. One elemental layer thickness is varied as the other is held constant. Slopes correspond to the tooling factor of the varied constituent while intercepts correspond to the constant constituent.....	36
2.4.	Composition ratios (Fe/Sb) of layered precursors plotted against the layer thickness ratios measured at the QCM during deposition. The Fe layers have much higher atomic packing density relative to Sb layers.....	37
2.5.	Schematic of a ternary layered precursor that is calibrated such that when gently heated the layers self-assemble into multicomponent layered heterostructures.....	38
2.6.	Examples of several layered structures that may be formed from the self-assembly of designed layered precursors. Well-calibrated precursor parameters can be scaled as necessary to form any of the above structures.....	39
3.1.	Crystalline phases of (top) FeSb ₃ and (bottom) FeSb ₂ in both ball-and-stick and polyhedral representations, generated from available crystallographic data. The FeSb ₂ polyhedral representation shows 2 unit-cells along each lattice vector (8 unit cells total). The FeSb ₃ polyhedral representation has an offset origin relative the ball-and-stick model.....	45
3.2.	Diffraction patterns taken from iron antimonide samples. In the triantimonide phase, the above markers correspond to the marked phase and the lower markers correspond to antimony. The markers in the diantimode pane refer to the marked phase.....	47
3.3.	PDFs of FeSb ₂ and FeSb ₃ compounds with models, as well as theoretical PDFs of constituent phases. The difference between data and fit is shown below in black. Fits were performed with an <i>r</i> range of 5-60 Å. For the full fit- range of the PDFs see the supporting information.....	49

3.4.	Pair distribution functions of as-deposited (AD), interdiffused (ID), and annealed samples generated from total scattering data. The difference curves between the as-deposited and interdiffused samples (AD-ID) show little structural change during the diffusion process, as seen by the small deviations from the lines showing zero change.....	52
3.5.	PDFs of precursors overlaid with annealed samples for (a) FeSb_2 and (b) FeSb_3 . (c) Overlaid FeSb_2 and FeSb_3 precursors show similar peak positions but varying relative intensities. Peak positions corresponding to pairs in the FeSb_3 PDF are shown by colored triangles. (d) Similar pair distances from a disordered arrangement of corner sharing octahedra are shown in corresponding colors.....	54
3.6.	Crystal structure of A) FeSb_3 and B) FeSb_2 (4 unit cells). The red polyhedra show FeSb_6 octahedra, with Sb marked as blue spheres in the corners.....	59
3.7.	Setup used for tfPDF measurements. The x-ray beam hit the substrate before the film.....	61
3.8.	A) Normalized data collected for sample 1C (black) and a clean substrate (red). The difference curve is shown in green and is plotted on an ex- panded scale in B. C) Normalized data collected for sample 1A (black) and the clean substrate (red), and difference between the two (green), also shown on an expanded scale in D.....	63
3.9.	A) Reduced total scattering function $F(Q)$ for sample 1A (black) and 1C (red). B) Reduced pair distribution function $G(r)$ for 1A (black) and 1C (red). C) $G(r)$ obtained for clean substrate. D) Comparison between the tfPDF for sam- ple 1A and similar sample, where the data were obtained for a sample meas- ured in a standard capillary.....	65
3.10.	Fits (red) to the experimental PDF from sample 1C (black). The green line shows the difference curve. A) Only FeSb_3 included in the model. B) FeSb_3 and crystalline Sb included in the model.....	67
3.11.	Comparison between the PDF obtained from sample 1A (red) and sample 1C (black). Pairs contributing to the low r region are indicated with errors, and color coded with the bond illustrated in B) showing a cut-out from the FeSb_3 unit cell, with corner-sharing FeSb_6 octahedra. Iron is shown in red and antimony in blue.....	69
3.12.	Comparison between the PDFs from sample 1A (red) and 2A (black)...	71
3.13.	A) Fit of FeSb_3 and Sb to the PDF from sample 2C. B) Fit of FeSb_3 and FeSb_2 to the PDF from sample 2C. The experimental PDF is shown in black, the fit in red and the difference in green.....	73

4.1.	Low-angle diffraction patterns collected from samples. Data from the previously reported 1:1 compound (labelled Moore 1:1) is shown as the bottom curve in each pane. (a) Set A. The first loss of intensity near the critical angle is a substrate artifact. The critical angle is taken from the second loss. (b) Set B. The apparent amplitude difference is due to the stacking. The range of normalized data is comparable for all samples.....	80
4.2.	High angle specular diffraction patterns collected from samples in (a) set A and (b) set B. Data from the previously reported 1:1 compound (labelled Moore 1:1) is shown for comparison as the bottom curve in each pane. The apparent difference in scales is due to a reduced range in the pane with fewer curves.....	82
4.3.	Sample resistivities and carrier concentrations. Values cluster in two regions for the two sample sets and loosely trend with the overall Pb/Se ratio measured by EPMA, which is at best only proportional to the composition of the ferecrystal. The lines are provided as a guide to the eye.....	83
4.4.	Variable temperature resistivity data for select ferecrystal samples from set A. Solid lines are from Bloch-Gruneisen fits of samples a1 and a3 and show the samples follow a metallic behavior.....	84
4.5.	Carrier concentration as a function of temperature for a subset of samples.....	85
4.6.	Effective masses determined from the Pisarenko relationship plotted against cation ratios for all samples and the previously reported 1:1 compound (labelled Moore 1:1). A general trend of decreasing effective with cation concentrations is apparent. The inset shows the magnitude of the Seebeck coefficients as a function of carrier concentration. Symbol allocation is consistent between the main figure and inset.....	87
4.7.	HAADF-STEM images of sample a5 and b2. In both cases, excess PbSe can be seen on the surface. Regular, uninterrupted layering is visible in a5, whereas the highly lead-rich b2 sample shows excess lead incorporates itself as PbSe inclusions rather than dispersed Pb, however the global layering scheme is hardly interrupted.....	89
5.1.	Schematic of $([\text{PbSe}]_{1+\delta})_m(\text{TiSe}_2)_m$ heterostructure nanolaminates for $1 \leq m \leq 4$. Each structure has the same composition and only one interface per repeating unit, but decreasing interface density with increasing m	95

- 5.2. Out-of-plane diffraction patterns for $([\text{PbSe}]_{1+\delta})_m(\text{TiSe}_2)_m$ nanolaminates for $1 \leq m \leq 4$. The outlined peaks correspond to the adjacent indices of the same color. The inset shows the c -lattice parameter, which also corresponds to the PbSe-TiSe₂ interface density in the out-of-plane direction, as a function of m 95
- 5.3. In-plane diffraction patterns for $([\text{PbSe}]_{1+\delta})_m(\text{TiSe}_2)_m$ nanolaminates for $1 \leq m \leq 4$. Peaks correspond to PbSe (Fm-3m) and TiSe₂ (P-3m1) $hk0$ planes, showing the nanolaminates crystallize as 2D powders of these phases. Inset is the full-width at half-maximum (FWHM) of the PbSe (220) and TiSe₂ (110) peaks. The systematic decrease is indicative of increasing crystallite size. The $m=2$ sample shows traces of an impurity phase alongside the majority compound. Calculations from the measured lattice parameters indicate a formula-unit mismatch $(1+\delta)$ of 1.17 between PbSe to TiSe₂ for all m 97
- 5.4. HAADF-STEM images of $([\text{PbSe}]_{1+\delta})_m(\text{TiSe}_2)_m$ nanolaminates for $m=3, 4$. The leftmost image shows 10 $([\text{PbSe}]_{1+\delta})_4(\text{TiSe}_2)_4$ structures, which indicates a loss of one $([\text{PbSe}]_{1+\delta})_4(\text{TiSe}_2)_4$ repeat unit from the precursor with 11 repeats and is believed to occur on annealing. The high-magnification right images show changing lattice faces between constituents highlighting the rotational misregistration in the layers..... 98
- 5.5. In-plane temperature-dependent resistivity for $([\text{PbSe}]_{1+\delta})_m(\text{TiSe}_2)_m$ nanolaminates with $1 \leq m \leq 4$. Each curve is normalized to the room temperature value (see Table 5.2.). The size of the data points is a conservative estimate of the error in the measurement. Between 100K and room temperature, resistivity generally increase with temperature, as expected for metallic behavior. In this range the relative change in resistivity with temperature increases with m due to increasing phonon scattering..... 99
- 5.6. In-plane temperature-dependent carrier concentration for $([\text{PbSe}]_{1+\delta})_m(\text{TiSe}_2)_m$ nanolaminates with $1 \leq m \leq 4$. The size of the data points is a conservative estimate of the error in the measurement. The carrier concentration consistently decreases with increasing m . The decrease appears to accelerate at lower temperatures. This behavior is qualitatively indicated by the dashed lines and black arrows, which are both added to serve as a guide to the eye..... 101
- 5.7. Seebeck coefficients (left axis, red diamond symbols) and carrier concentrations (right axis, blue triangle symbols) of $([\text{PbSe}]_{1+\delta})_m(\text{TiSe}_2)_m$ nanolaminates for $1 \leq m \leq 4$. The size of the data points is a conservative estimate of the error in the measurement. The Seebeck coefficient systematically decreases and appears to be saturating with increasing m . The decreasing carrier concentration with m is not expected from the rigid-band model..... 103

5.8.	Schematic of proposed band-bending that occurs in the heterostructures. The low interface density of the high m samples leads to the valence (conduction) band of PbSe (TiSe ₂) crossing back over the chemical potential as the bulk band positions are reestablished, which does not occur in the low m samples with high interface density.....	104
5.9.	Calculated coulomb potential per interface (closed markers, solid lines) and per total volume (open markers, dashed lines) across PbSe-TiSe ₂ interfaces. Data is presented both using the measured carrier densities from the $1 \leq m \leq 4$ nanolaminates (red diamond markers) and also assuming charge is separated in rigid-bands and normalized to the $m=1$ value from the data-derived calculation (blue triangle markers).....	106
6.1.	(top-left) Schematic representation of the modulation profile of PbSe and TiSe ₂ within λ_k for each nanolaminate. (right) X-ray reflectivity patterns (in color) shown against idealized models of the targeted nanolaminate (in black). (bottom-left) Grazing incidence in-plane diffraction pattern showing $hk0$ lattice planes.....	113
6.2.	HAADF-STEM images of each nanolaminate highlighting the formation of the targeted nanoarchitecture, sharp interfaces between constituents, and rotational misregistration between layers. The colored traces show the relative intensity of characteristic X-ray signals from Pb and Ti when moving down the $k=2\mathbf{321}$ structure.....	114
6.3.	Temperature dependent resistivity of 6 [(PbSe) _{1+δ}] ₄ (TiSe ₂) ₄ nanolaminates. Both (left) measured values and (right) normalized values are shown.....	116
6.4.	Temperature dependent carrier concentration of 6 [(PbSe) _{1+δ}] ₄ (TiSe ₂) ₄ nanolaminates. Values are calculated from Hall coefficients assuming a single n-type band. Both (bottom) measured values and (top) normalized values are shown.....	117
6.5.	Temperature dependent mobility of 6 [(PbSe) _{1+δ}] ₄ (TiSe ₂) ₄ nanolaminates calculated from resistivity and carrier concentration data.....	118
6.6.	Room-temperature Seebeck coefficient of [(PbSe) _{1+δ}] ₄ (TiSe ₂) ₄ nanolaminates. Colors correspond to nanoarchitecture and symbols correspond to precursor parameters.....	119
6.7.	Room-temperature power factor of [(PbSe) _{1+δ}] ₄ (TiSe ₂) ₄ nanolaminates. Colors correspond to nanoarchitecture and symbols correspond to precursor parameters.....	119

Figure	Page
7.1. Data corresponding to the 00 <i>l</i> reflections of the (PbSe) _{1+δ} (TiSe ₂) _{<i>n</i>} ferecrystals. (a) Diffraction patterns plotted on a log scale and (b) <i>c</i> -lattice parameters as a function of <i>n</i> . Different sets correspond to samples prepared in different deposition cycles.....	127
7.2. Log-scale in-plane diffraction patterns corresponding to <i>hk</i> 0 reflections.....	128
7.3. HAADF-STEM image of the (PbSe) _{1+δ} (TiSe ₂) ₁₂ sample showing the 1-T polymorph for the block of 12 TiSe ₂ layers.....	129
7.4. Density of state schematic for (PbSe) _{1+δ} (TiSe ₂) _{<i>n</i>} intergrowths for both low (red) and high (blue) values of <i>n</i> . As seen in the central portion, the charge donated from the PbSe layers increases with <i>n</i> but the number of populated bands in TiSe ₂ decreases, effectively reducing the carrier density relative to a low <i>n</i> compound. From top to bottom, the horizontal black lines illustrate the filled levels for low, high, and infinite <i>n</i>	130
7.5. (a) Room temperature carrier concentrations for the (PbSe) _{1+δ} (TiSe ₂) _{<i>n</i>} samples determined from van der Paaw Hall measurements assuming a single band model. The black line shows a fit of the expected functional form. (b) Temperature dependence of the normalized carrier concentration for the (PbSe) _{1+δ} (TiSe ₂) _{<i>n</i>} samples showing the change as a function of increasing thickness of the TiSe ₂ layer. The arrow indicates the general trend.....	132
7.6. (a) Room temperature Seebeck coefficients for the (PbSe) _{1+δ} (TiSe ₂) _{<i>n</i>} samples. (b) Seebeck coefficient versus carrier concentration shown as a Pisarenko plot with <i>m</i> [*] =6.39 <i>m</i> _{<i>e</i>}	133
7.7. (a) Temperature dependent resistivity for the (PbSe) _{1+δ} (TiSe ₂) _{<i>n</i>} samples. (b) Room temperature resistivity versus <i>n</i> , with the variation between sample sets highlighted.....	134
7.8. (a) Room temperature mobility values as a function of carrier concentration for the (PbSe) _{1+δ} (TiSe ₂) _{<i>n</i>} samples. (b) Room temperature mobility values plotted versus the thickness of the TiSe ₂ layer in the unit cell.....	136
7.9. (a) Room temperature power factor as a function of the thickness of the TiSe ₂ layer in the unit cell for the (PbSe) _{1+δ} (TiSe ₂) _{<i>n</i>} samples. (b) Room temperature power factor plotted versus room temperature mobility values. The adjacent numbers indicate <i>n</i>	138
8.1. Out-of-plane diffraction patterns of samples. All reflections can be indexed to (00 <i>l</i>) reflections from the superlattice. The asterisk marks a Si reflection.....	143

Figure	Page
8.2. In-plane diffraction patterns of select samples. All reflections can be indexed to $(hk0)$ planes of either TiSe_2 or distorted SnSe , with the relative intensity of TiSe_2 reflections increasing with n , as expected.....	144
8.3. Room-temperature Seebeck coefficients of $([\text{SnSe}]_{1+\delta})_l(\text{TiSe}_2)_n$ nanolaminates. The values for $n=1$ are from previous work of Merrill et al. Error bars correspond to the precision of the measurement.....	145
8.4. Temperature-dependent resistivity of $([\text{SnSe}]_{1+\delta})_l(\text{TiSe}_2)_n$ nanolaminates. Inset are values normalized to room-temperature.....	146
8.5. Temperature-dependent carrier concentrations of $([\text{SnSe}]_{1+\delta})_l(\text{TiSe}_2)_n$ nanolaminates calculated from Hall coefficients assuming a single n-type band.....	147
8.6. (left) Temperature-dependent Seebeck coefficient measurements on $([\text{SnSe}]_{1+\delta})_l(\text{TiSe}_2)_n$ ($n=3, 15$) nanolaminates. (right) Schematic showing side and top view of measurement stage with Cu cold finger, stainless steel standoffs, silica substrate and nanolaminate film. Hall and resistivity measurements are made using C_1 - C_4 and Seebeck coefficients using the top and bottom thermocouples ($\text{TC}_{\text{top/bottom}}$). Thermocouple wires run along Cu blocks to reduce hot/cold finger effects.....	149
9.1. Coupled θ - 2θ out-of-plane diffraction patterns of $([\text{SnSe}]_{1+\delta})_m(\text{TiSe}_2)_n$ ($1 \leq m=n \leq 8$). A systematic increase in the c -lattice parameter of 11.89 \AA , corresponding to a single TiSe_2 unit cell and half SnSe unit cell, is seen as m and n are increased.....	156
9.2. (left) In-plane diffraction patterns of $([\text{SnSe}]_{1+\delta})_m(\text{TiSe}_2)_n$ nanolaminates. The SnSe must be indexed differently as the layers thicken. The asterisk marks the location expected from SnSe_2 . (top-right) Lattice parameters of SnSe for $m=n \geq 2$ and ratio of a/b . (bottom-right) Schematic of face-to-body centering symmetry shift of SnSe	157
9.3. HAADF-STEM images of $([\text{SnSe}]_{1+\delta})_m(\text{TiSe}_2)_n$ nanolaminates showing templated interfaces for $m=n=1$ and several stabilized structures for $m=n=2$	158
9.4. Temperature-dependent resistivity of $([\text{SnSe}]_{1+\delta})_m(\text{TiSe}_2)_n$ nanolaminates.....	161
9.5. Temperature dependent Hall coefficients of $([\text{SnSe}]_{1+\delta})_m(\text{TiSe}_2)_n$ nanolaminates.....	163

LIST OF TABLES

Table	Page
3.1. Summary of precursors	47
3.2. Summary of pair distances that correspond to the first peaks in the FeSb ₂ and FeSb ₃ PDFs	50
3.3. Sample list.....	60
3.4. Refined parameters for the crystalline	68
3.5. Refined parameters for modeling of sample 2C	72
4.1. Summary of all samples as well as data from the previously reported 1:1 compound (labelled Moore 1:1). Samples from the first deposition cycle, set A, were deposited in order from a1 to a9. Samples from the second deposition cycle, set B, were deposited in order from b1 to b4.....	81
5.1. Lattice parameters and compositional misfit of PbSe and TiSe ₂ found in the ([PbSe] _{1+δ}) _m (TiSe ₂) _m heterostructures	96
5.2. Room-temperature in-plane transport properties of ([PbSe] _{1+δ}) _m (TiSe ₂) _m heterostructures. Estimates of error are given in parentheses for the last digit reported.....	100
7.1. Summary of room-temperature power factors for published ferecrystal and misfit layered compounds	137
9.1. Lattice parameters of SnSe, TiSe ₂ , and the superlattice period (<i>c</i>) the ([SnSe] _{1+δ}) _m (TiSe ₂) _n nanolaminates from Le Bail fits of the diffraction patterns	155
9.2. Room-temperature transport measurements for ([SnSe] _{1+δ}) _m (TiSe ₂) _n nanolaminates	163

CHAPTER I

INTRODUCTION: DESIGNING THERMOELECTRIC MATERIALS USING 2D LAYERS

The work in this chapter was accepted on 2016-01-27 for publication as a chapter in *Handbook of Solid-State Chemistry* published by Wiley-VCH and is coauthored with my advisor and research group leader, David C. Johnson. I am the primary author.

1.1. Introduction

Thermoelectrics have long been a tantalizing class of devices – solid state junctions with no moving parts and the ability to reversibly convert between thermal and electric field gradients and only fundamentally limited by Carnot efficiency. Since almost all industrial processes produce waste heat, accounting for an estimated 20-50% of the initial energy input, capturing this heat as a usable form of energy could significantly reduce both cost of operation and offset the total environmental cost of said processes. This has never been a more important consideration than now. The 2015 revision of United Nations' world population prospects announced the world population is expected to reach 8.5 billion by 2030 and over 11 billion by 2100. Climate change makes reducing carbon dioxide emissions critically important to maintain the livability of the planet, and producing additional power from waste heat obviously reduces the amount of fossil fuels that need to be consumed. To sustain our growing population, and indeed support the current numbers, every effort must be made to maximize our resources, and thermoelectric power generation may be one viable option. However, the discovery of materials with high enough thermoelectric performance to provide either power or cooling on a cost competitive basis has proved difficult except in niche applications. Even after several concentrated waves of concerted research efforts in the US and around the world, most current commercial devices still rely on decades-old material technologies. The crux of this problem lies in the difficulty of balancing the several interdependent and contradictory material properties.

This discussion is written for an audience familiar with the basic tenants of solid state physics and chemistry, but not necessarily with thermoelectric materials. Discussion is centered around optimization at the material level as opposed to modules. We begin with a colloquial discussion of how the basic transport physics that govern thermoelectric performance can be used to guide materials research. Also presented are the common strategies for finding high performance materials that have been traditionally used over the last two decades. The body of the work outlines the current and recent strategies both for finding new materials and for further optimizing the existing library of high performance materials. Throughout we include examples and discussions of some of the current ‘state of the art’ materials. We especially emphasize the role of low dimensional composite structures and give our perspective on future directions of research in this realm.

1.2. Physical Picture

Understanding the flow of charge and heat has been the focus of both fundamental and applied transport studies in solid state materials for decades. Nontrivial thermoelectric materials display an entanglement of the processes by which these flows proceed – an electronic or heat current may induce a current of the other property. This behavior is captured by the Seebeck coefficient – a spatially independent material property defined as the electric field generated by a thermal gradient across a material, which is obtained experimentally by measuring a voltage as a function of the magnitude of an applied temperature difference.

Conceptually, the Seebeck coefficient is a reasonable material parameter to define when considering any solid material outside of thermal equilibrium. The larger thermal motion from carriers at the hot end of a material will cause diffusion of these carriers towards the cold side of the material. The open-circuit equilibrium between this diffusive separation and the restoring electric field defines the Seebeck coefficient of the material. When separately considering the flow of charge or heat in a particular material, we have a strong intuitive base we can draw upon to roughly determine the properties, but the same is not

immediately obvious for the Seebeck coefficient. However, an expression for the Seebeck coefficient may be derived from Boltzmann transport theory, which describes both heat and charge flow in most solids. The full integral expression reduces to a simple relationship in the degenerate carrier regime, which is a reasonable regime for functional thermoelectric materials. This relationship is called the Mott formula:¹

$$S = \frac{\pi^2}{3} \frac{k^2 T}{e} \left. \frac{d \ln[\sigma(E)]}{dE} \right|_{E=E_F}$$

where S is the Seebeck coefficient, k is Boltzmann's constant, σ is the electrical conductivity, T is the absolute temperature, e is the elementary charge, and E_F is the Fermi energy. Over a small energy range it is reasonable to consider mobility, μ , to be energy independent and conductivity to be monotonic with the density of states (DOS). Thus a convenient metric to find materials with large Seebeck coefficients is to begin the search in materials with large energy derivatives in the density of states function, $g(E)$, near the chemical potential.

However, functional implementation of thermoelectric materials depends on more than the Seebeck coefficient. In addition to the maximization of the Seebeck voltage, it is also important to consider materials such that energy may be effectively transferred to (from) a load (source) (high electronic conductivity) and that a temperature gradient may be maintained (low thermal conductivity). The combination of these parameters leads to a temperature-dependent dimensionless figure of merit defined for thermoelectric materials as:

$$zT = \frac{S^2 \sigma}{\kappa} T$$

Where κ is the total thermal conductivity, which is the sum of contributions from both the lattice (κ_L) and the charge carriers (κ_e). The co-dependence of the terms in the figure of merit makes finding materials with high zT values a

challenging task. The figure of merit for useful thermoelectric materials typically has a value of approximately 1. Given a promising starting material, there are two obvious routes for obtaining a higher zT values: maximizing the numerator, which contains the electronic contributions (called the power factor) while maintaining a low thermal conductivity, or minimizing the thermal conductivity without impacting the power factor. However, the interplay between the various parameters has shown either task to be far from trivial. First, let us look at the power factor.

The higher dimensionality of the Seebeck coefficient in the figure of merit of thermoelectric materials has given an historic precedent to research focused on finding a high Seebeck coefficient. If one considers the approximations of a parabolic band and energy independent scattering, the Mott formula reduces to the Pisarenko relationship:²

$$S = \frac{8\pi^2 k^2}{3eh^2} m^* T \left(\frac{\pi}{3n} \right)^{\frac{3}{2}}$$

Where h is Planck's constant, m^* is the carrier effective mass from the shape of $g(E)$, and n is the carrier density. We see that high Seebeck coefficients result from heavy bands with low carrier concentrations, similar to as expected from a chemical potential at the μ' or μ'' positions in the left pane of Figure 1.1. This is consistent with our previous metric of finding high Seebeck coefficients in regions with rapidly changing DOS, as flat bands (high m^*) will integrate to a high DOS over narrow ΔE , and the edge of these bands, where carrier density is lowest, will give the largest energy derivatives. However, recent works have discussed at length that many of the efforts to find high Seebeck coefficients have been stymied by these heavy bands, which negatively affect mobility, and thus the electrical conductivity.^{3,4} Instead, a balance of a high Seebeck coefficient and carrier mobility can be achieved in a material with several low-mass pockets in the band structure, as shown in the center pane of Figure 1.1., which when integrated result in a high effective mass as perceived in the density of states.⁵ This case of several degenerate band extrema is most-likely to

occur in compounds with high symmetry, further guiding our search towards materials with these structures.⁶

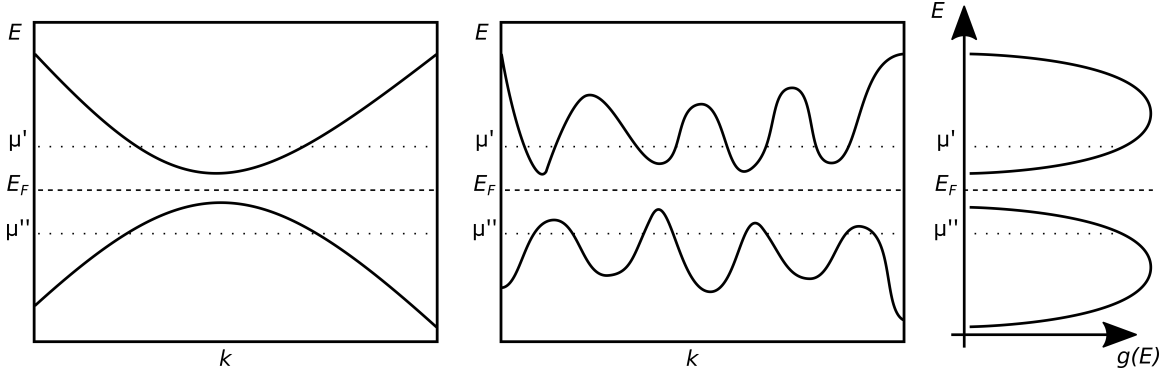


Figure 1.1. Speculative band structure from a compound with (left) a single heavy carrier pockets and a compound with (middle) several lighter carrier pockets. However, both compounds might integrate to similar profiles (right) in $g(E)$ and have similar effective masses as perceived by the density of states. When doped n-doped (p-doped), the chemical potential in each moves toward μ' (μ''), populating the respective pockets with carriers. The light degenerate bands maintain their high mobility, despite the high perceived mass.

A second approach is to focus on the denominator of zT , the thermal conductivity. The total thermal conductivity is the sum of heat moved by the lattice, or phonons, and heat flow associated with the flow of charge ($\kappa = \kappa_L + \kappa_e$). A coupling in the mechanisms by which heat and charge are moved through a material by the electronic component leads to compounds with a high electrical conductivity also having a high thermal conductivity. This is often estimated using the Wiedemann-Franz law, which states that at a certain temperature κ_e is proportionally related to the electronic conductivity of the material by a constant called the Lorenz number, L ($\kappa_e = L\sigma T$). Even when taking this coupling is taken into account, the maximization of the electronic conductivity is still always favorable to achieve a high value of zT due to the figure of merit's functional form. Thus, the total thermal conductivity must be lowered by either minimizing the Lorenz number, L , or the lattice contribution to the thermal conductivity, κ_L .

While there is no explicit necessity for it to be so, there is often an observed coupling of high κ_L in materials with high σ . To be very general, crystalline materials might conduct both well, whereas glasses would not. Still, the general strategy of finding materials with structures conducive to inherently low thermal conductivities at the expense of the electronic component has been fruitful. For example, compounds with octahedrally coordinated metal centers, such as the various IV-VI metal dichalcogenides, generally have a large degree of phonon-phonon interactions and show much better thermoelectric performance than III-V compounds with higher mobilities.⁷ Outside of these few cases, materials with low thermal conductivities have historically been found by searching for complex inorganic structures, typically ternary or quaternary compounds with large and sometimes highly anisotropic unit cells. More recently, several other approaches and extensions to this strategy have been taken to decouple phonon and electronic transport in thermoelectric materials, which will be discussed later.

Armed with the previous discussions, it is valuable to consider limits to a material's thermoelectric performance. Assuming a material that behaves according to the Wiedemann-Franz law, has a zero thermal conductivity of the lattice, and a Lorenz number for a typical metal ($2.45 \times 10^{-8} \text{ V}^2 \text{ K}^{-2}$), we can determine a minimum Seebeck coefficient that will define an upper limit to the figure of merit. The expression for the minimum Seebeck coefficient is simply $S_{\text{Min}} = (L \times zT_{\text{Target}})^{1/2}$. For example, if we want to target a value of zT of 1 in a particular compound, the absolute lowest value of Seebeck coefficient for the compound to hit the target is $157 \text{ } \mu\text{V K}^{-1}$. Similarly, to obtain a zT value of 2, S must be $221 \text{ } \mu\text{V K}^{-1}$ and for a value of 4 this becomes $313 \text{ } \mu\text{V K}^{-1}$. This reinforces the earlier discussion about the importance of the magnitude of the Seebeck coefficient in determining zT . As a material's carrier density decreases and carriers move away from the degenerate limit, L decreases and the S_{Min} slightly decreases. This suggests that the Seebeck coefficient serves as a useful guide for evaluating a material's prospects as a functional thermoelectric with a single measurement, provided a model exists that extrapolates Seebeck coefficients for different carrier concentrations and temperatures. It also

emphasizes the need to minimize lattice thermal conductivity, which will be discussed next.

1.3. Optimizing thermoelectric materials: minimizing lattice conductivity

1.3.1. The electron crystal phonon glass approach

Since its introduction by Slack in the 1990s, much of the research in bulk thermoelectric materials have centered around the pursuit of his electron crystal/phonon glass (PGEC) concept.⁸ Two approaches to lowering thermal conductivity have dominated: the development of new bulk single phase structures, which typically have large and very complex unit cells, and the synthesis of nanocomposites, which consist of nanoscale inclusions within a bulk material, most often with both constituents having more conventional and simple structures. Both of these approaches were inspired in part by Slack's framing of the challenge in finding an improved thermoelectric material. Slack argued that by finding structures with rigid covalent cages that incorporate loosely bound "rattling" atoms with large displacement parameters into the cage voids, one could create a material with a high figure of merit. He reasoned that electrical mobility would remain high by conduction via the cage behaving as an electron crystal, but the material would effectively scatter acoustic phonons via interactions with the "rattling" atom, lowering the phonon mean free path. The material would behave as a phonon glass due to the static and dynamic displacement of the "rattling" atom. In general, to maximize the effects from the structure, the host cage should be designed as a narrow band-gap semiconductor with small differences in electronegativity between atoms whereas the rattling ion should be a small but heavy atom to maximize the thermal displacement and disorder from the rattling. Several classes of materials fit Slack's criteria, and a large body of work exists investigating the thermoelectric properties of clathrates⁹, zintl phases¹⁰, skutterudites¹¹, and other structures. A few specific examples are briefly discussed below.

Skutterudites are typically made up of MX_6 metal-pnictide octahedra and have a cubic structure similar to the ReO_3 motif but with the anions along four parallel edges of the unit cell displaced inward resulting in a structure

consisting of eight corner sharing MX_6 octahedra per unit cell. This anion displacement creates a four-fold ring and an adjacent open cage, within which a rattling atom may be incorporated. The skutterudite structure is shown in Figure 1.2. For thermoelectric applications, antimonide skutterudites are of the most interest. The cation composition of the host skutterudite lattice and both the composition and fill ratio of ions incorporated into the cage are used to tailor and optimize the material's physical properties. Researchers have also focused on tuning the temperature at which an optimal value for zT is achieved via chemical substitutions. To date the highest performing skutterudite, a CoSb_3 host filled with Ba, La, and Yb making an n -type material, exhibits a zT value of 1.7 at 850 K.¹² Skutterudites are among the highest performing materials optimized to date and have been prepared with similar properties by many research groups around the world. Consequently, considerable development has been done to incorporate them into both working modules and segmented couples.

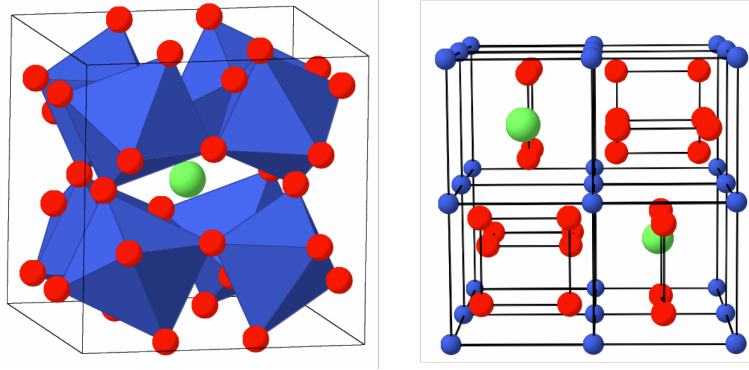


Figure 1.2. Polyhedral and ball-and-stick schematics of a filled skutterudite structure. The rattling atoms are typically low-valence heavy atoms to maximize their displacement parameters and thus their effectiveness at phonon-scattering. The host lattice consists of metal centers octahedrally coordinated by a pnictide and should be highly covalent and conductive.

Zn_4Sb_3 has also been the focus of considerable detective work as researchers focused on initial reports of unusual properties that were greatly dependent on composition and preparation conditions. It was discovered that interstitial Zn atoms in Zn_4Sb_3 greatly reduce the thermal conductivity relative

to the ZnSb compound, which has similar stoichiometry, structural features, and transport properties. Multiple interstitial sites in the Zn_4Sb_3 unit cell were shown to have large displacement parameters, which serve to lower the thermal conductivity below those of the best skutterudites, due to the greater degree of disorder available to the lattice.¹³ This results in a two- to three-fold increase in the figure of merit in between 200-400 °C, demonstrating the power of Slack's original concept.

1.3.2. Other methods to reduce thermal conductivity

Other methods besides the PGEC concept have also been used to discover new materials with low thermal conductivities. Among these strategies are using engineered structures and interfaces to scatter phonons, which can include low dimensional materials, defect incorporation, or controlling crystalline grain size. Another approach altogether has been finding simple lattices with natural tendencies for phonon-phonon scattering interactions to occur.

By introducing nanoscale precipitates with similar structures into the lattice of a host bulk material the thermal conductivity may be substantially lowered without severely impacting the power factor. For example, several enhancements to the zT value of PbTe have been seen in the LAST and SALT compounds, which incorporate of AgSbTe_2 or NaSbTe_2 clusters into the rock-salt structure.^{14,15} These results have lead to further work on optimizing PbTe and the approach of using materials that have been designed with a patterned structure over many length scales to scatter phonons, which has provided us with some of the most promising thermoelectric materials to date. By strategically controlling and introducing point defects, nanoprecipitates, and grain boundary size, lead chalcogenide thermoelectric materials have been synthesized with lattice thermal conductivities at or near the amorphous limit.¹⁶⁻¹⁸ By carefully selecting synergistic band structures in the components of the composite material, favorable electrical transport properties between the host and guest compounds can be tailored, enhancing the power factor as well.¹⁹ This approach has resulted in bulk PbTe with embedded SrTe

nanoprecipitates and engineered grain boundaries having an exceptional 2.2 value for zT . The Bi_2Te_3 family has also benefitted from the nanostructuring approach, resulting in BiSbTe alloys having an enhanced room-temperature zT value of 1.2 and a peak value of 1.4 at ca. 100 °C.²⁰ These results are extremely promising, though questions about the long-term stability of nanostructured composites at elevated temperatures in large thermal gradients remain.

Perhaps the most exciting recent development in thermoelectric materials has come from single-crystal SnSe , which doesn't follow Slack's guidelines. It was found that SnSe displays an exceptionally high (record) value of zT (2.6) along the b -axis at 923 K, due to favorable electronic transport ($S^2\sigma \sim 10 \mu\text{W cm}^{-1} \text{K}^{-2}$) and very low thermal conductivity ($< 0.4 \text{ W m}^{-1} \text{K}^{-1}$) in this direction.²¹ SnSe takes on a distorted rock-salt structure, which forms layers along the a -axis. One would expect this direction to exhibit both the lowest thermal and electrical conductivity and while this is true in SnSe , the increased thermal conductivity along the b - and c -lattice directions is negligible compared to the increased electrical conductivity, leading to the exceptional values of zT along these directions. Unlike typical metals and semiconductors, thermal conductivity in SnSe decreases with T in the range of 300-700 K. A thermal conductivity that is inversely related to temperature is indicative of a material with a high degree of Umklapp scattering. This behavior and the high value of zT in SnSe is highly surprising for both a simple structure and single crystal and highlights a different strategy – finding materials with a large inherent phonon anharmonicity – as an avenue for achieving a high figure of merit.

Another particularly exciting avenue for bulk materials with low thermal conductivity and high values of zT is in materials which undergo structural instabilities such as Peierls distortions or charge density waves (CDW). CDWs are structural distortions arising from strong electron-phonon coupling and are found in layered materials whereby an in-plane pairing of atoms serves to stabilize the structure. This stabilization breaks the symmetry of the 2D 'sheet' as a modulation of atomic density along one direction in the in-plane structure is formed. This affects both electrical and thermal transport properties in the material. A CDW exists in the layered structure of $\text{In}_4\text{Se}_{3-6}$ and it was shown that the distortion lowers the in-plane thermal conductivity below that of the

stacking direction, which is quite surprising as the layers in the material are bonded by weaker van der Waals type forces.²² The lower thermal conductivity, as well as a more favorable power factor along the in-plane direction, lead to value of 1.48 for zT , which is ~300% higher than reported for the cross-plane value in the same material.²²

1.4. Thermoelectric materials: maximizing power factor

Traditionally, maximizing the power factor in a thermoelectric material is done by doping the compound to control carrier concentration. In most cases, the Seebeck coefficient varies inversely with carrier density while the conductivity varies proportionally. Neglecting the thermal component, the ideal carrier density optimizes the power factor with respect to these behaviors. In essence, this puts the chemical potential at the ideal level for mixed electronic/thermoelectric transport for a given shape of $g(E)$. Doping any material in this fashion will continue to be an important step in any future work, but several additional approaches have been either proposed or implemented in achieving power factors much greater than possible with carrier concentration optimization alone.

Deliberate band engineering of bulk materials by the introduction of resonance states near the Fermi level has been a promising direction to increase the power factor.²³ By carefully selecting a dopant level with states overlapping those of the host compound, electronic coupling between the host and dopant can introduce a resonance level in the density of states, which perturbs the electronic structure towards the ideal case of a delta function at the Fermi level, as argued by Mahan and Sofo and seen in Figure 1.3.²⁴ Resonant states in Tl doped PbTe considerably raise the Seebeck coefficient above the value expected by the Pisarenko relationship, resulting in an enhancement of zT at these carrier concentrations.²⁵ This leads to a zT of about 1.5 at 800K without nanostructuring the material. It should be noted that while the net gain in zT is appreciable, the introduction of the resonant states did come at the expense of mobility in the form of higher effective carrier mass. Other dopants, such as Na in PbTe, have been shown to enhance the zT value

nearly as much, but these results are attributed to moving the chemical potential to sharp regions within the PbTe DOS profile as opposed to the introduction of resonant states.²⁶ The increase in Seebeck coefficient is less pronounced than the Tl doped compound, but a higher mobility results in similar overall performance.²⁶ In each of these cases, the favorable electronic interaction between the host and added element (Tl or Na) may be optimized by controlling dopant densities.

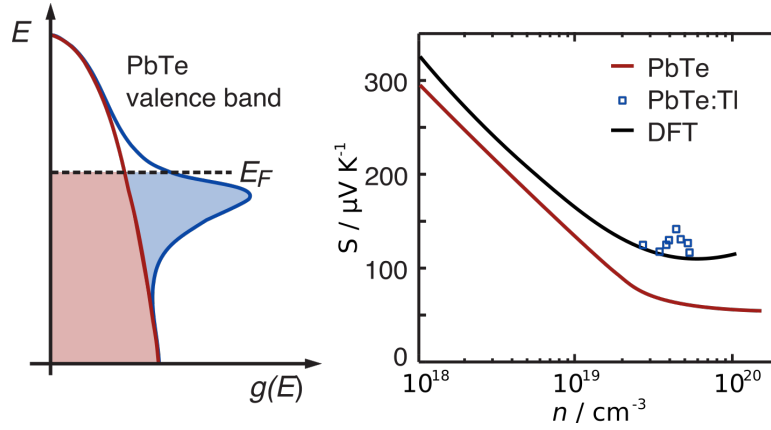


Figure 1.3. (left) Adapted from reference ²⁵. Schematic $g(E)$ for PbTe with and without resonant levels. (right) Adapted from reference ²⁶. Sharp features in $g(E)$ from resonant states created by Tl doping increase the Seebeck coefficient relative to PbTe that is Na-doped to a similar carrier concentration but without resonant coupling. However, recent density function theory (DFT) calculations of PbTe have predicted a values similar to PbTe:TI without enhancement from band resonances.^{26,27}

Another approach to thermoelectric materials discovery based on increasing the power factor is based on the ideas and theory of which were pioneered by Hicks and Dresselhaus in the early nineties. By incorporating promising materials into quantum well or quantum wire nanostructures, Hicks and Dresselhaus noted that an enhancement of zT could be achieved by the introduction of sharp features into the density of states and greatly enhancing the Seebeck coefficient.^{28,29} This is consistent with the theory developed by Mahan and Sofo, showing that the power factor is maximized when the density of states at the chemical potential takes the form of a Dirac delta function.²⁴

The papers published by Hicks and Dresselhaus began a wave of research on low dimensional systems. Shortly after the initial predictions by Hicks and Dresselhaus, an enhancement of the Seebeck coefficient and in some cases zT was observed from low dimensional materials, in both quasi 1D and 2D confined structures of bismuth, antimony, or their chalcogenides.^{30–34} However, these results have not always been repeatable and increases in the value of zT were attributed to a decrease in the lattice conductivity as much as enhancement of the power factor.^{35–37}

High power factors have also been discovered in strongly correlated electron systems. In these materials, interactions between carriers become too strong to be neglected. This typically happens when electrons are localized to f - or d -orbitals and strong Coulombic and spin interactions lead to correlated behavior between carriers. This leads to the creation of hybridized heavy bands. The existence of the heavy correlated bands can amplify the thermopower significantly over an uncorrelated material. Depending on filling in these heavy fermion systems, both correlated metals and correlated semiconductors may be formed. The highest energy derivative in $g(E)$ is expected to occur in rare-earth compounds with mixed valence f -level electrons, implying metals containing these electrons near the chemical potential should be promising grounds for finding anomalously high Seebeck coefficients for their carrier densities.^{38,39} YbAl_3 is an example of such a material, possessing an exceptionally high room-temperature power factor of $180 \mu\text{W K}^{-2}\text{cm}^{-1}$ at 300 K.⁴⁰ The large peaks in $g(E)$ of YbAl_3 near the Fermi energy, shown in Figure 1.4., come from the $4f$ -levels in Yb ⁴¹ and without the background states come very close to approximating the δ -function like profile. Enhancement of the Seebeck coefficient in correlated semiconductors is especially highlighted by FeSb_2 , which has a colossal Seebeck coefficient of $45,000 \mu\text{V K}^{-1}$ and an unparalleled power factor of over $10^3 \mu\text{W K}^{-2}\text{cm}^{-1}$ at low temperatures.⁴² This behavior has been explained by enhancement of the thermopower by strongly correlated $3d$ -electrons in the system. While the high thermal conductivity at these temperatures has limited FeSb_2 use as a functional thermoelectric material, the results illustrate the exceptional power factors that have been found in correlated electron systems.

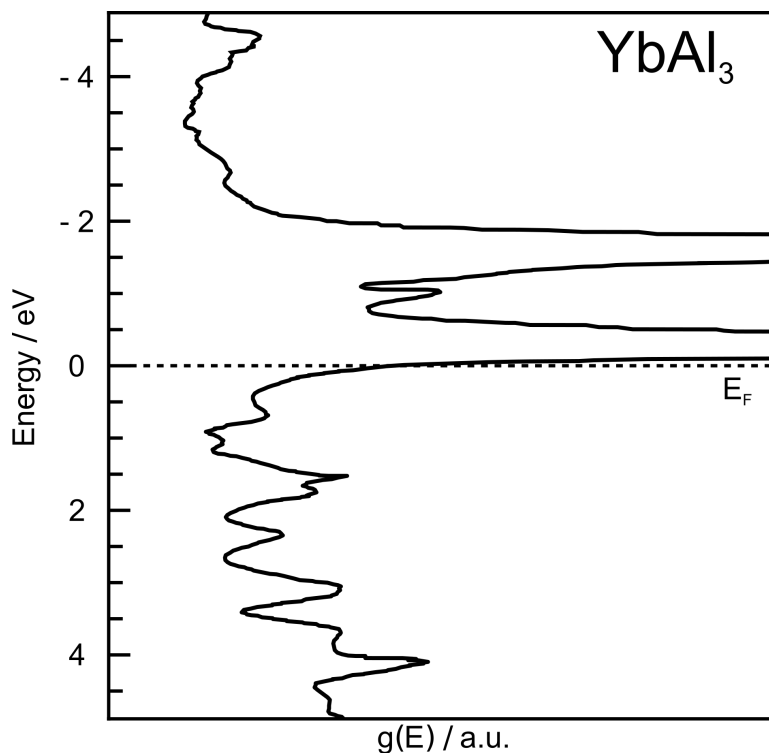


Figure 1.4. Density of states for YbAl_3 modeled after calculated data in reference ⁴¹. The delta-function like features in $g(E)$ near the chemical potential result in high Seebeck coefficients for the compound, despite a metal-like carrier density. This results in unparalleled room-temperature power factors for the material.

Another class of compounds that have also shown great promise as spin-correlated thermoelectric materials are the layered cobalt oxides. The compound $\text{Na}_x\text{Co}_2\text{O}_4$ shows a high Seebeck coefficient for its carrier density, on the order of $100 \mu\text{V K}^{-1}$.⁴³ A large spin entropy present in the family of materials is responsible for the significantly increasing the Seebeck coefficient. This degeneracy can be removed by making measurements at low temperatures and high magnetic fields, which suppresses the thermopower and indicates that the correlated spin behavior is the source. Careful extrapolation of these results to 300K for the $\text{Na}_x\text{Co}_2\text{O}_4$ compound shows that most of the room temperature thermopower results from the correlated spin enhancement.⁴³

1.5. Bridge to nanolaminate structures

Looking at the last few decades of research, a rational methodology and understanding for systematically reducing the thermal conductivity of materials has been well developed. Gains have also been made in the power factors of materials, but most of the highest gains come outside the classic picture of balancing the contribution of the Seebeck coefficient and conductivity by optimizing the carrier concentration. The current forum is too brief and the collective understanding too narrow to give a full account of the how strongly correlated electron behaviors affect thermoelectric properties. However, there is currently a large research effort in understanding this behavior. Further investigating and developing a deeper understanding of structure-property relationships in systems with quantum well structures or materials where electron-electron, electron-spin, or electron-phonon behavior enhance the power factor are a means by which we might expect to see considerable gains in high-performance thermoelectric materials.

On the other hand, nanostructuring and rational doping of promising bulk materials remains a promising to enhance their thermoelectric properties. For the first time, scalable materials technologies that easily surpass bismuth telluride are coming to the fore, which may lead to more widespread implementation of thermoelectric devices both for power generation and temperature control. However, the avenues by which these gains have been made result in materials that are inherently difficult to characterize, especially at the scale of the structural details that lead to the enhanced behavior.

While eventual implementation of thermoelectric materials in everyday devices will likely result from progress made in nanostructured bulk materials, further research on more readily characterizable systems remains a valuable tool to understand the underpinning physical phenomena and as a means to discover promising new material systems for further investigation. This is especially true in the case of finding, understanding, and describing cases that are dominated by correlated electron behavior, where simple physical models are often inadequate to describe the enhancement material parameters. For the remainder of the chapter, we will discuss a brief history, the current state, and

future prospects of thermoelectric materials research in designed layered materials.

1.6. Transition metal dichalcogenide compounds

The simplest form of composite nanolaminate structures investigated as thermoelectric materials are intercalates of transition metal dichalcogenides. While several systems have been investigated, the titanium-based transition metal dichalcogenides TiS_2 and TiSe_2 have been the most promising both as host materials and for the properties found in their intercalation compounds.^{44–48} Several guest atoms (e.g. Mn, Fe, Co, Ni, Cu, Nd, Bi) have been used in TiX_2 intercalates, with the best results coming from Cu intercalated compounds at about a 0.1 Cu to Ti ratio. Unfortunately, there hasn't been much improvement from intercalates beyond finding optimal guest atoms and their doping concentrations, which haven't shown enough enhancement for implementation. The highest value of zT reported for these materials is 0.45 in $\text{Cu}_{0.1}\text{TiS}_2$ at 800K.⁴⁶

1.7. Misfit layer compounds

A class of naturally occurring nanolaminate materials, called misfit layer compounds (MLCs), has been investigated with respect to potential thermoelectric applications. These compounds consist of two structures that are interleaved as 'sheets' such that the constituents layer along the c -axis of the composite crystal. In order to accommodate the different structures in the nanolaminate material, the structures distort relative to bulk constituents. The resulting structures typically have a four dimensional unit cell, with a commensurate (or common) a -axis between the constituents, incommensurate b -axes (one for each constituent), and a c -axis defined by the layering of the superstructure.⁴⁹

There are two main families of these compounds that have been examined as potential thermoelectric materials. The first and the most widely studied are the layered cobalt oxides, which can be considered a subset of the

spin-correlated compounds previously mentioned in this chapter.^{50,51} The second are chalcogenide composites made up of interleaved rock-salt and transition metal dichalcogenide structures. The general formula for these materials is $([MX]_{1+\delta})_m(TX_2)_n$, where M=Sn, Pb, Bi or rare earth, T=Ti, V, Cr, Nb, or Ta, and X=S or Se. The subscripts $1+\delta$, m , and n denote the difference in basal-plane area per cation of the two structures, the number of rock-salt bilayers per repeating unit, and the number of dichalcogenide trilayers per repeating unit, respectively. Typically only the $m=n=1$ compound can be prepared using high temperature synthesis techniques. The structure of a chalcogenide MLC is shown in Figure 1.5.

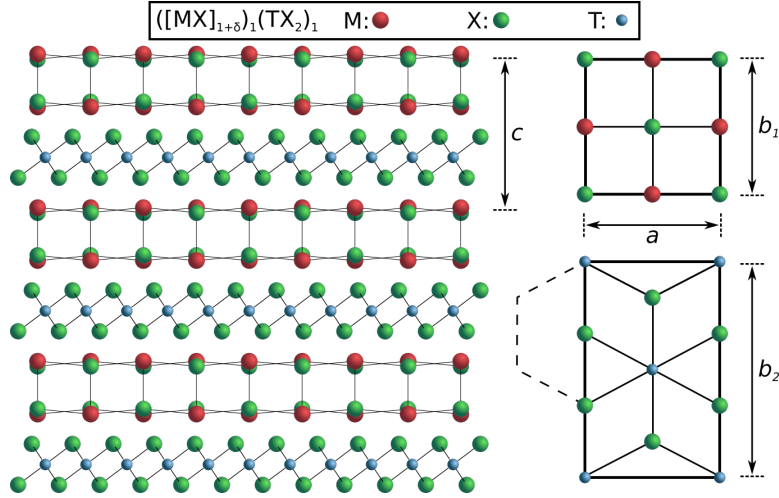


Figure 1.5. Schematic of the structures found in a chalcogenide misfit compound. The basal planes of the rock-salt (MX) and octahedrally coordinated transition metal dichalcogenide (TX₂) have a commensurate a-axis, but distinct b-axes (given by b_1 and b_2 , respectively), and the structures are interleaved along the c-axis.

Some of the most notable and thoroughly studied materials in the chalcogenide family are the intergrowths of TiS₂ with SnS, PbS, or BiS. It was found the Sn-based materials have the best figure of merit, due to both an increased power factor and reduced total thermal conductivity relative the the Pb and Bi containing compounds.⁵² Peak values of zT for pellets pressed from powders of these compounds range from ~0.3-0.4, with peak values measured

at 700K.⁵² These compounds showed a very low lattice thermal conductivity, with the Bi containing compounds falling below the theoretical minimum of $\sim 0.5 \text{ Wm}^{-1}\text{K}^{-1}$ at and above 350 °C. Additionally, hot-pressed pellets of NbS₂ and CrS₂ compounds interleaved with LaS rock-salt layers have shown promising thermoelectric properties with zT values of about 0.15.⁵³ Further optimization by further controlling the microstructure, similar to what has been done in the IV-VI dichalcogenide systems, could improve these values.

The interleaved structure of the MLCs has resulted in the literature discussing them as two constituents with weak interactions between the incommensurate layers. However, the traditional high temperature synthesis approach used to make them from a direct reaction of the constituent elements requires that the MLC is more thermodynamically stable than a bulk mixture of the two constituents. This implies that the interaction between the constituent layers in the MLC's lowers the free energy enough to overcome the truncated structures and incommensurate interface between them. The stabilization interaction has been suggested to be charge transfer between the constituents, which would create a large capacitive energy.^{54,55} The rigid band structure picture where the bands of the constituents can be summed to produce the bands of the MLC is certainly an oversimplification of these complicated materials. Understanding the interaction between the constituents and how the bands change as the structures distort is required to control and optimize the band structures of these compounds and to control doping for optimal thermoelectric performance. Due to the method of their synthesis, however, there is little inherent tunability in either composition or layering sequences. To date, all of the MLCs discovered form with $n=1$ or 2 (with one 3) and $m=1$, with the notable exception of $([\text{EuS}]_{1.15})_{1.5}(\text{NbS}_2)_1$, which forms a trilayer of the rocksalt structure.⁵⁶ This is an especially interesting example as it shows a mixed valence rare earth, indicating f -electrons may be available to introduce resonant levels and correlated behavior. Reports of rationally doping misfit layered materials are few, and mostly limited to the oxide systems.^{57,58} Thus, within the common realms of their synthesis, MLCs do not have the tunability necessary to be functional thermoelectric materials.

1.8. Thin-film superlattice materials

Spurred by the work of Hicks and Dresselhaus, the search for low dimensional confined structures with favorable thermoelectric properties became an active field of research.^{28,29} In short time, researchers realized that the inherent anisotropy of superlattices lends itself to the study of properties in two directions – both in-plane and cross-plane relative to the stacking direction of the material. Possible mechanisms for enhancement of the figure of merit are unique along each direction. Cross-plane enhancement of zT in a superlattice would primarily come about by interfaces scattering phonons by reflection while still transmitting electrons. On the other hand, in-plane thermoelectric enhancement can be imagined to be enhanced both in the power factor by band structure changes associated with quantum confinement (see previous section) and in increased interface scattering of phonons lowering the thermal conductivity.

Almost immediately after the theoretical predictions, reports of promising superlattice compounds were being made. Two reports in particular stood out for their large enhancement of zT . After several reports of systematically optimizing $\text{Bi}_2\text{Te}_3\text{-Sb}_2\text{Te}_3$ superlattices from the Venkatasubramanian group at RTI, they eventually reported an unprecedented room-temperature zT value of ~ 2.4 in the material.⁵⁹ Harman and coworkers also released a series of papers on PbTe based superlattices where zT was systematically increased four-fold from the bulk value of ~ 0.4 to ~ 1.6 .⁶⁰ Unfortunately, neither result has been reproduced despite several efforts.^{61,62} These and other works on superlattice thermoelectric materials are summarized in a short review from Bottner.⁶³

The rapid progress in material properties spurred interest in the field, including a quick succession of readily characterizable, thought-provoking structure-property relationships that were developed because materials structures could be varied to test optimization strategies.^{64–68} However, it is important to note these results were confined to materials where epitaxial synthesis was possible. The decades of refinement in various epitaxial growth systems and well-developed growth mechanisms has naturally led to synthesis and optimization of superlattice thermoelectric materials to be confined to thin films within these systems. Little work has been done outside of what is

accessible by these means. However, the strong theoretical arguments for enhanced performance and their potential use as a thermoelectric based on-chip cooler, provides motivation for further research in this area.

1.9. Van der Waals heterostructures

In the last two decades there has been a surging interest in 2D materials resulting in a Nobel prize in physics for work in graphene⁶⁹ and over 15,000 annual publications as properties emerged in 2D layers that were not found in the bulk. While this interest grew out of exceptional properties discovered in graphene, several other 2D and few-layer materials have been discovered or predicted to have properties not found in the bulk. These include planar hexagonal boron nitride, black phosphorous which forms puckered sheets, Bi and Sb chalcogenides, several oxides, including more complex compounds, and several transition metal dichalcogenides^{35,70–79}. These low-dimensional materials possess a broad array of unique physical properties not found in the bulk compounds, which result from unique electronic environments, quantum confinement, and surface to volume enhancement (by several orders of magnitude). An example of this is MoS₂, where the band structure near the Fermi energy systematically changes as the thickness is reduced down to a single S-Mo-S trilayer.⁷⁸ Both calculation and initial results have also found that the thermoelectric properties of isolated layers can be enhanced.^{35,80–83}

As the major breakthroughs in isolated 2D materials have become less frequent, attention is turning to the development and investigation of vdW heterostructures, where several 2D layers are stacked to form a superstructure. The individual layers exhibit sufficient stability to maintain the distinct layers but the weak van der Waals bonding between them acts to keep the superstructures intact, hence the name. The promise of these heterostructures is that stacks comprised of 2 or more complimentary constituents can be potentially created to yield emergent properties that do not exist in the individual constituents. In this way, researchers are actively pursuing new “designed” materials, which truly are, as the old adage says, greater than the sum of their parts. And while the field is new, if given the appropriate 2D

building blocks and a method to assemble them into a superstructure, no shortage of big ideas have been conjured up.⁸⁴

Heterostructures could be an especially interesting approach to the study of thermoelectric materials, since several designed properties are simultaneously needed for high performance. Building on the ideas from Hicks and Dresselhaus and their suggestions of quantum confinement as an effective means of achieving high power factors, it could be expected that vdW heterostructures would naturally exhibit high zT values by their anisotropic structure alone. However, in addition to possible enhancement by quantum confinement, rationally designed vdW structures may potentially give additional tunability due to the composite properties of the system. For example, if considering designing a heterostructure optimized for in-plane maximization of zT , an unprecedented number of controllable parameters are available. A material or even a composite with a ‘working’ band structure could be chosen which possesses a promising electronic structure (bandgap and shape of $g(E)$) for having a high power factor. A second constituent containing a ‘distribution’ band could then be included. This would be designed to donate or accept carriers as needed for optimized transport in the ‘working’ material, but the structure should maintain high mobility in the working band as no impurities are introduced. An ideal system would not be perturbed by addition of additional constituents, but would instead modulation dope the structure allowing for optimizing materials without perturbing the working band structure. The lack of a strong bonding network along stacking direction should result in inherently low thermal conductivity, which could be further optimized by controlling stacking orders or thicknesses of insulating layers. Alternatively, a third constituent designed to minimize thermal transport could also be added to the heterostructure.

While the potential for van der Waals systems as a platform for composite thermoelectric materials discovery is high, they currently suffer from need to isolate and reassemble several constituent monolayers. This is a considerable synthetic burden, even in a case of pure academic interest. Currently, there is a lack of a high-throughput fabrication method and it will be necessary to test large suites of materials to develop knowledge of how layers in

a composite will interact. These together prevent the use of heterostructures as an efficient research vehicle for thermoelectric materials. Previously investigated laminate structures such as misfit layer compounds or dichalcogenide superlattices, however, provide a useful structure and property relationship platform from which the interplay between composition, structure and properties can be systematically developed.

1.10. Kinetically trapped nanolaminates

Recently, a bottom-up synthetic approach that can be used to create a large class of materials similar to the chalcogenide misfit layered compounds has been introduced.^{85–87} These materials, called ferecrystals, are based on the chalcogenide MLCs, with the bulk of this family of compounds consisting of interleaved metal chalcogenide rock-salt bilayers, MX, and transition metal dichalcogenide trilayers, TX₂. The compounds form over a wide range of material systems, with many of the ternary selenide members such that T=Ti, V, Nb, Mo, Ta, W and M=Sn, Pb, Bi having been reported.⁸⁸ The first telluride misfits in the PbTe-TiTe₂ system were also prepared using this synthetic approach.⁸⁹ Because of the wide range of chemical systems available, a wide range of physical properties have been observed, with transport in materials ranging from superconductivity, *n*- or *p*-type metallic to semimetallic to semiconducting.

Ferecrystals are made as thin-films by sequentially depositing thin elemental layers from the vapor phase onto a substrate to form an amorphous precursor which, when properly calibrated, has similar composition profiles and nanoarchitecture as the desired final crystalline product.^{86,90} With modest heating, this approximate elemental distribution can be kinetically trapped to form a material consisting of crystallographically-aligned 2D layers precisely stacked with structurally abrupt interfaces in a layering sequence determined by the local precursor structure. While crystallites are precisely aligned along the *c*-axis of the composite, they crystallize with an average random in-plane orientation, resembling a systematic layering of 2D powders.^{88,90,91} Little registration in the basal planes has been observed between constituents in the

structure, leading to a global rotational, or turbostratic, disorder through the compound. This severely impacts phonon propagation in the materials and is structurally distinct relative to MLCs, where a coherent arrangement persists between layers in the composite structure. While the MLCs already have very low thermal conductivities due to the high interface volume ratio of the laminated layers, ferecrystals have even lower thermal conductivities. Disordered WSe₂ layered compounds have the lowest thermal conductivity ever measured perpendicular to the layering direction ($\sim 0.05 \text{ Wm}^{-1}\text{K}^{-1}$)⁹² with insulating intergrowths being slightly higher along this direction ($\sim 0.1 \text{ Wm}^{-1}\text{K}^{-1}$)⁹³ but lower along the layers ($\sim 0.4 \text{ Wm}^{-1}\text{K}^{-1}$)⁹⁴. These measurements were made at room temperature and in all cases, the values are lower than state of the art thermoelectric materials.

Since the sequence of layers in ferecrystals is kinetically controlled by the structure of the precursor, designed composite structures can be prepared. The large breadth of synthetic space afforded by this approach allows for unprecedented accessibility to explore properties of solid state materials over a wide range of local structures and compositions. As long as materials are synthesized as a superlattice – with several repeating units along the stacking direction, a unique diffraction pattern allows structure to be determined for the constituent layers that make up the compound. This is highlighted in Figure 1.6. showing the six structural isomers, which have very similar compositions and *c*-lattice parameters, which can be formed from four repeating units of MX and TX₂. The compounds all have similar *c*-lattice parameters, given by the positions of the peaks, due to the identical bulk constituents. However, the unique stacking sequences result in unique diffraction patterns as the different locations of atomic planes within the unit cell will scatter with differing intensities. This approach can be extended further and the number of unique structures, or distinct sequences of layers, is describable by the combinatorics mathematics of a necklace of *n* beads of *m* colors. For example, a two-constituent (*m*=2) composite structure comprised of 20 layers (*n*=20), which would be on the order of 12nm thick, could have about 27 thousand distinct layering motifs. If this is extended to three constituents (*m*=3), the number of unique structures increases to nearly 90 million, and this goes well into the

billions with four constituents ($m=4$). To-date, there is nothing to suggest that the synthetic method of kinetically trapping the local structure of a thin layered precursor into a designed compound could not be applied to each of the cases above in several material systems. Thus, unlike typical hurdles in solid state chemistry, a point has been reached where the number of metastable compounds that are synthetically accessible vastly exceeds the practical experimental throughput. Developing the theory and intuition of the best layering schemes to test the fundamental interactions in these materials will be a necessary step to move forward with maximum efficiency.

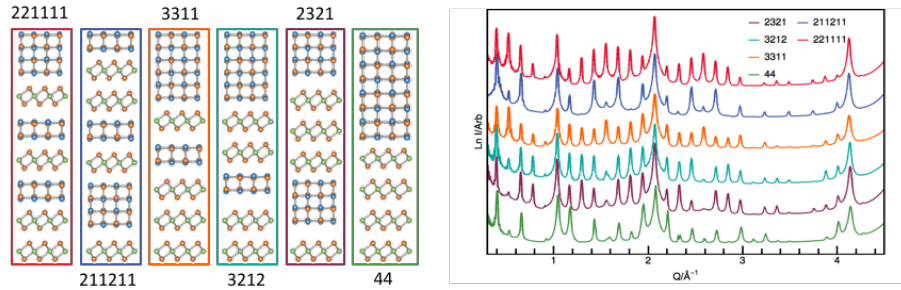


Figure 1.6. Structures of $([\text{PbSe}]_{1+\delta})_4(\text{TiSe}_2)_4$ isomers. (left) The six structural isomers that can be made in the $m=n=4$ layering scheme. (right) Confirmation of consistent c-lattice parameters from samples with these structures, but different peak intensities due to the unique electron density profiles within the superlattice.

The published body of literature on the chalcogenide misfit compounds universally suggests conduction is localized to the dichalcogenide constituent.^{49,54} This behavior is also seen in several experiments in several ferecrystal material systems. Much of the research in these systems also suggests that stabilization of compounds is aided, at least in part, by charge transfer across constituents in the laminate structure. Because of this transfer, layering sequences within a material system may be changed to modulation-dope the layers. Complicated layering structures may be created as necessary for optimization of material properties, for example: structurally isomeric suites of samples comprised of the same composition and c-lattice parameter, but a distinct layering pattern within the unit cell, such as the $([\text{PbSe}]_{1+\delta})_4(\text{TiSe}_2)_4$

structural isomers shown above. As long as we don't exceed the depletion width or change the modulation doping efficiency, this may preserve the electronic interactions governed by the integer number of layers of each constituent. Recent work on $([\text{MSe}]_{1+\delta})_1(\text{TiSe}_2)_n$ ferecrystals⁹⁵⁻⁹⁹ suggests that they provide a promising platform for systematically making changes to a compound to optimize the figure of merit as discussed next.

1.1.1. $([\text{MSe}]_{1+\delta})_1(\text{TiSe}_2)_n$ ferecrystals

Bulk stoichiometric TiSe_2 is a semimetal, but generally the compound forms with a small (2-4%) excess of Ti atoms residing in the van der Waals gaps. The resulting free carrier density is on the order of 10^{21} . The misfit layered compound literature often assumes a rigid band approximation for the interactions of the composite crystal such that the density of states of the laminate structure is simply a superposition of those from each constituent. While the structural distortions and interactions between layers perturb the band structures, this approximation's agreement with data suggests that is a reasonable initial assumption and it has been made in the TiX_2 MLC literature for both the Pb-selenides¹⁰⁰ and the Pb- and Sn-sulfides.^{101,102} In the family of compounds containing TiSe_2 dichalcogenide layers the electrons occupying the Se-4p levels in the rock salt are higher energy than the empty Ti-3d states and charge is donated to the TiSe_2 layers, as shown in Figure 1.7. These populated states in the TiSe_2 are considered to dominate the charge transport in the composite compound. Evidence for conduction within the TiSe_2 layers is given in intergrowths with alloyed rock-salts, where compounds with $\text{Pb}_x\text{Sn}_{1-x}\text{Se}$ layers show unchanged or even higher mobilities relative to the endmembers.¹⁰³ The donated charge increases the carrier concentration above the intrinsic values for bulk TiSe_2 . This simple band filling picture also suggests the Bi containing compounds relative to the isovalent Pb and Sn will have higher carrier concentrations due to more filling of the Ti-3d band. This was observed and discussed in the n-type $([\text{MS}]_{1+\delta})_1(\text{TiS}_2)_2$ suite of misfit layered compounds⁵², and also in the $([\text{MSe}]_{1+\delta})_1(\text{TiSe}_2)_1$ family of ferecrystal compounds (where $\text{M}=\text{Sn}^{97}$, Pb^{95} , Bi^{104}) as shown in Figure 1.8. Normalizing these data to

the basal plane cation density shows that bismuth substitution results in an increase in carrier concentration of approximately 1 electron per bismuth atom, further agreeing with the rigid band picture and showing high modulation doping efficiency for the $m=n=1$ structures. This effect appears stable with temperature, though a slight convergence between the Bi and other datasets is observed at low temperatures suggesting more of the donated charge localizes to the Bi layers at low temperatures. The room-temperature Seebeck coefficient of the three $([\text{MSe}]_{1+\delta})_1(\text{TiSe}_2)_1$ compounds are -75, -66, and -42 $\mu\text{V K}^{-1}$, for Sn, Pb, and Bi, respectively. Calculating the effective carrier mass with the Pisarenko relationship shows the compounds to be similar, with m^* values of 5.8(3) m_e , suggesting the effect in all cases is being dominated at different levels within the same parabolic band in the common TiSe_2 constituent.

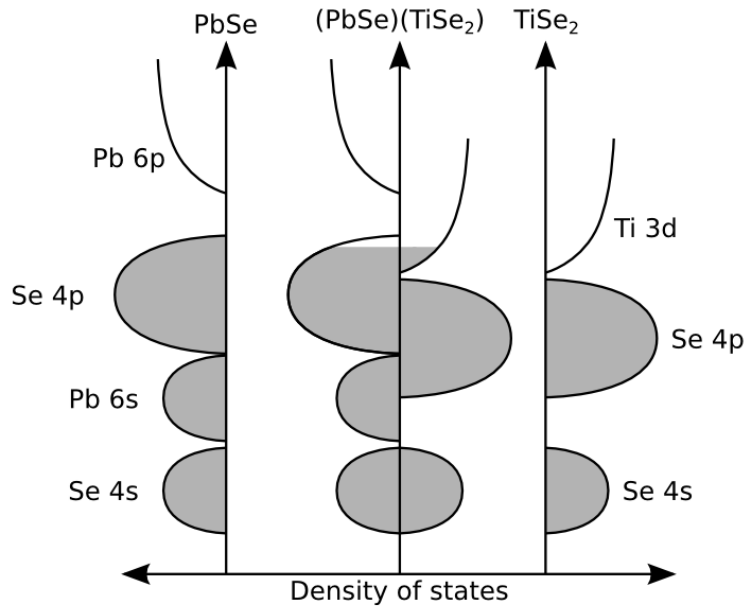


Figure 1.7. Schematic density of states based on electronegativity and coordination environments for $([\text{PbSe}]_{1+\delta})_m(\text{TiSe}_2)_n$ compounds. The composite band structure is considered to be a superposition of the individual constituents' band structures and conduction is assumed to occur through a single band – in this case by electrons populating the Ti-3d band. In this model, the extent of charge transfer between PbSe and TiSe_2 constituents will determine the carrier density.

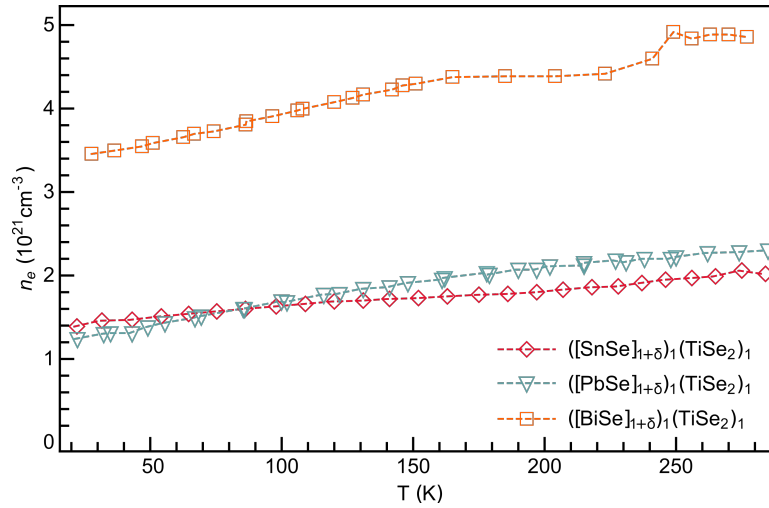


Figure 1.8. Carrier densities as a function of temperature in $([MSe]_{1+\delta})_1(TiSe_2)_1$ for $M = Sn^{97}, Pb^{95}, Bi^{104}$. The compounds containing isovalent Sn and Pb atoms show very similar carrier concentrations. As expected from the conduction mechanism shown and discussed in Figure 1.7., the compound containing trivalent Bi atoms have an increased carrier concentration of approximately 1 electron per Bi atom.

Especially powerful in these samples for tracking structure property relationships is the ability to structurally characterize the nanolaminate systems. Rietveld refinement of the 001 composite structure can be performed to obtain planes of atoms in the out-of-plane direction. Structural refinements of the stacking planes within the $m=n=1$ structures of $TiSe_2$ interleaved with SnSe and PbSe are shown in Figure 1.9.^{95,97} Both compounds exhibit a similar total thickness of the $TiSe_2$ constituent when including the ‘van der Waals’ gap, but the SnSe containing compound shows a slightly larger Ti-Se distance and a slightly smaller gap between the two structures. A puckering distortion of Se atoms moving inward within the rock salt structure is also observed in both cases, however the distortion in the SnSe is of much greater magnitude despite the smaller distance between the terminating metal planes. Structural changes can also be tracked within a material system as the layers are changed, for example in the $([BiSe]_{1+\delta})_1(TiSe_2)_n$ ($n=2-4$) compounds. Here, a systematic increase in the degree of BiSe puckering is observed alongside an offset in Ti planes relative to the Se planes in the $TiSe_2$ trilayers, which trends towards the

bulk structures as n is increased.¹⁰⁵ Current work is underway to relate these structural behaviors to transport measurements both within and across homologous series' of compounds to build libraries of structure property relationships in these materials. Future corroboration of band structure calculations will also aid in a deeper understanding of how to optimize nanolaminate materials.

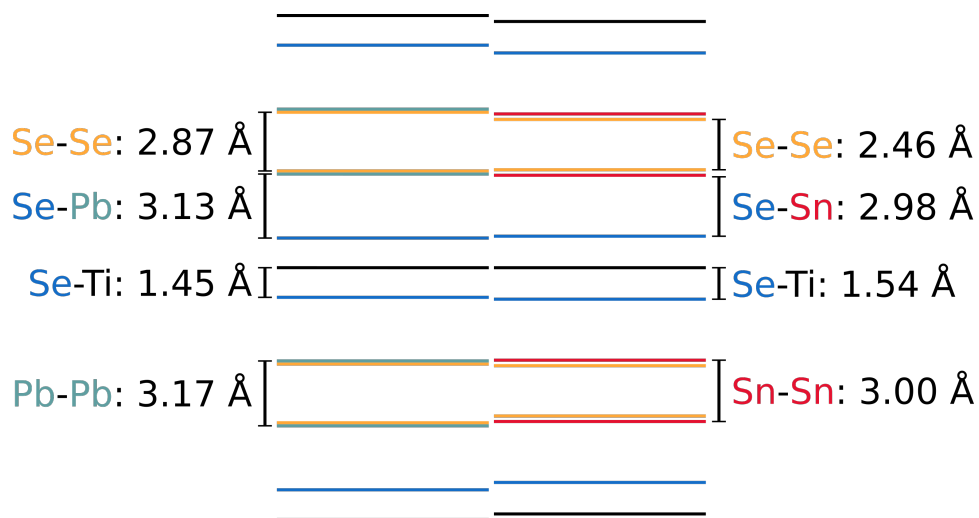


Figure 1.9. Atomic plane positions along the stacking direction of the superlattice in $[(\text{MSe})_{1+6}]_1(\text{TiSe}_2)_1$ where $\text{M}=\text{Sn}, \text{Pb}$ as determined from Rietveld refinement. Two unit cells are shown for each superlattice, with the origin at the central Ti plane. Line positions are to scale.

The greater puckering distortion within the SnSe structure alludes to a greater interaction between layers. Some additional insight as to why is gained from the in-plane lattice parameters of the $[(\text{SnSe})_{1+6}]_1(\text{TiSe}_2)_1$ compound relative to other ferecrystal intergrowths. The SnSe a -lattice parameter is much greater when interleaved with TiSe_2 relative to the same MX layer in other dichalcogenides.⁹¹ On the other hand, the TiSe_2 a -lattice shows less sensitivity as the MX layer is changed and is typically much larger than then the TMD lattice in other intergrowths. Projecting the SnSe lattice onto the TiSe_2 lattice, as seen in the inset of Figure 1.10., shows that because of a small lattice mismatch, a regular repeating structure along one dimension can be accommodated between constituents. Perhaps the structures distort due to an

energetic gain by this repeating structure, similar to the structural distortions found in misfit compounds. The Pb and Bi containing $([\text{MSe}]_{1+\delta})_1(\text{TiSe}_2)_1$ ferecrystals show an entirely different structures, with the PbSe containing compound having square in plane rock-salt layers and the BiSe containing compound showing a far more distorted structure than SnSe.

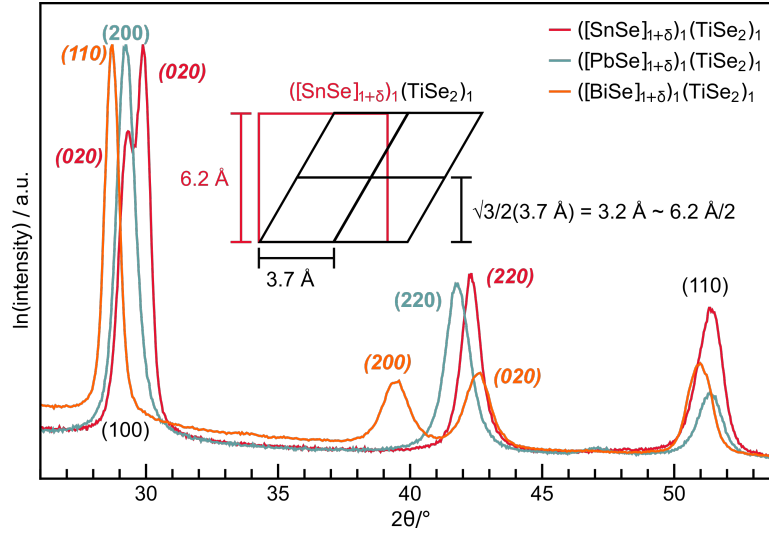


Figure 1.10. In-plane diffraction patterns ($\lambda = \text{Cu-K}\alpha$) of $([\text{MSe}]_{1+\delta})_1(\text{TiSe}_2)_1$ for $\text{M} = \text{Sn, Pb, and Bi}$ adapted from reference ⁹¹. The MSe layer indices are shown in bold and match the curve colors, with the SnSe and BiSe indices also being italicized. TiSe_2 peaks are indexed in black and in normal type. The in-plane MSe layers are square for PbSe, slightly tetragonally distorted for SnSe, and highly distorted for BiSe. Also shown is a schematic of the approximate lattice match of SnSe in TiSe_2 in the distorted SnSe layers with lattice parameters taken from reference ⁹¹.

The first step of optimizing typical thermoelectric materials is optimizing the carrier concentration of the existing material by a means that doesn't severely perturb the band structure. Considering the Pisarenko relationship, which appears valid for these compounds, the synthetic control, and the stability of the TiSe_2 bands as the interleaved layers are changed, modulation doping the structure by changing the relative ratio of the layers is a logical step forward. A general trend across the 3 rock salt systems is that by adding additional TiSe_2 layers, the charge donated into the Ti-3d band can be diluted, lowering the carrier concentration and raising both the Seebeck coefficient and

the power factor as seen in Figure 1.11.^{99,105} While thermal conductivity measurements of the structures are necessary for a full validation of the effectiveness, this example illustrates the power of using interlayer interactions within different nanolaminate material systems for enhancing the thermoelectric power factor. However, if we consider the single band model to be valid, this is still within the classic regime of carrier concentration optimization, albeit by modulation doping. Exploring the more recent strategies of enhancing the power factor in nanolaminate structures by incorporating composite bands, resonant states, or correlated electron behaviors is an available and hopefully fruitful approach for future materials improvement.

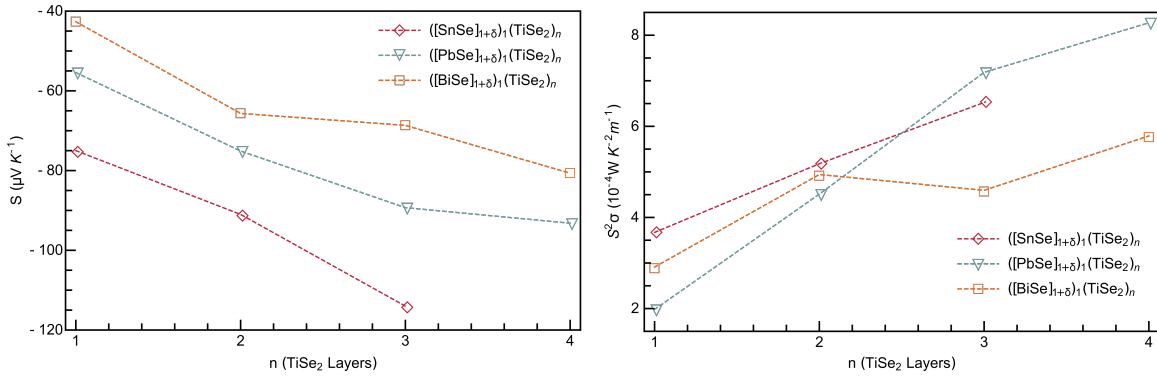


Figure 1.11. Seebeck coefficients and power factors of $([MSe]_{1+\delta})_1(TiSe_2)_n$ for $M=Sn, Pb,$ and Bi . A systematic increase in the magnitude of the Seebeck coefficient is observed for increasing n in all material systems. This also translates to increased power factor, though variation in sample quality, and hence mobility¹⁰⁶, results in slightly more scatter in the data.

Moving forward with these materials, combining the synthesis and characterization of strategic sets of compounds with calculations in a feedback loop that quickly develops functional materials has great appeal. Once a more complete understanding of how the layers interact is developed, which can only be achieved by synthesis and characterization, structure-property relationships may be extended by computational work, which could suggest new promising chemical systems and layering sequences. These may then be tested, the theory refined, and new predictions made. In this way, the vast synthetic space

afforded by assembling 2D structures may be narrowed to only the most promising suites of compounds, maximizing both throughput and results.

1.12. Outlook

The discussions within this chapter have focused on only the first aspects of developing efficient thermoelectric devices: finding materials with high zT values. However, several additional considerations are necessary: For every promising material found, a counter-material of opposite carrier type must also be developed for integration into a working device. Each must also be optimized for contact resistances and other parasitic effects within the module and to maximize the efficiency of the couple rather than just the materials themselves. Similarly, each must also share similar zT values and temperature ranges wherein they operate. Furthermore, as devices operate across some temperature difference and zT values are highly dependent on temperature, the average zT value of the device is more critical than the peak values. Thus, within each n -type or p -type leg, segmenting a device into several materials at different points along the operating temperature gradient is often done to achieve the highest device efficiencies. This creates the need to ensure additional compatibility requirements between materials. Depending on the end-use the total device performance might then be expressed as the maximum temperature difference attainable across a thermoelectric cooler or a generator's efficiency, as given by the thermodynamic cycle (Carnot) that governs it.

While the ambitions for earth-abundant thermoelectrics for large-scale use may still be a long time coming, the recent advances in materials should open up further niche applications for thermoelectric devices, which in turn should hopefully drive further interest in materials and device development. It is rare that one physical phenomenon has potential to be utilized across such a large scope of human needs. For example, thermoelectric devices have the potential to be used as power generators not only as the New Horizons spacecraft captures Pluto in unforeseen detail, but also to recapture considerable energy from waste heat from every industrial cooling tower or

automobile exhaust across the world. Similarly, their use as automobile seat warmers may be extended to large-scale refrigeration, or even cryogenic cooling.

Since nearly all of the current state-of-the art materials have thermal conductivities approaching the amorphous limit, reexamining old methods or finding new strategies to enhance the power factor, and specifically the Seebeck coefficient, will be necessary push zT values further. This task has been a far from trivial as shown by the slow progress over half a century of active research. The considerable materials challenge in discovering new compounds and new strategies beyond optimally-doping bulk semiconductors will be aided by the synthetic, analytical, and predictive tools that recently have become available. The next decade promises considerable progress!

1.13. Overview of Dissertation

The work contained within the chapters of this dissertation has the overarching goal of building an understanding of how structural distortions, transport properties, and stability of metastable nanolayered thermoelectric materials are affected as their layering architecture, defect densities, nanostructures, compositions, or chemical systems are changed on both global and local scales. Generally, each chapter outlines an experiment where one or more of these aspects are investigated, but Chapters II and III preface the bulk of the work. Chapter II outlines the synthetic route to the metastable compounds found in this text, and briefly introduces the characterization tools that are used in this work. Chapter III has two parts, both of which have been published and are in collaboration with Kirsten Jensen, Anders Blichfeld, Suzannah Wood, Bo Iversen, Simon Billinge, And David Johnson. The first portion, of which I am the primary author, investigates the formation mechanism of metastable iron antimonide films from amorphous layers. The second portion, of which Kirsten Jensen is the primary author, reports the first demonstration of thin film pair distribution function analysis (tfPDF) on the same material. Many functional thermoelectric materials require extensive ‘designing’ at the nanoscale to achieve optimum performance. There is outstanding question as to the stability of these features as well as ways to

probe them. The work in Chapter III aims to address this by development of both an understanding of localized nucleation of metastable solids and new ways to probe thin film materials.

Chapters IV-X investigate the structure and properties of $([\text{MSe}]_{1+\delta})_m(\text{TiSe}_2)_n$ compounds as M , m , and n are systematically changed. Chapters IV-VII investigate several homologous series with $M=\text{Pb}$. Chapter IV explores the effects of nonstoichiometry on $([\text{PbSe}]_{1+\delta})_1(\text{TiSe}_2)_1$ compounds and was published with Daniel Moore, Jeffrey Ditto, and David Johnson. Chapter V investigates interface density in $([\text{PbSe}]_{1+\delta})_m(\text{TiSe}_2)_m$, reporting a breakdown of long-held models in nanolaminate systems for thick layers ($m>1$), also providing insight into stabilization of the broader family of misfit compounds. This was published with Jeffrey Ditto, Daniel Moore, and David Johnson. Chapter VI, written with Jeffrey Ditto, Daniel Moore, and David Johnson, is unpublished and reports the effects of buried PbSe-TiSe_2 interfaces within the unit cell of $([\text{PbSe}]_{1+\delta})_4(\text{TiSe}_2)_4$ structural isomers. It is found that an intermediate interface density enhances the thermoelectric power factor relative to other stacking sequences. Chapter VII is published work written in collaboration with Devin Merrill, Daniel Moore, and David Johnson. This work reports a strategy for ‘diluting’ the mobile carriers in $([\text{PbSe}]_{1+\delta})_1(\text{TiSe}_2)_n$ nanolaminates, which serves to significantly increase the thermoelectric power factor to levels higher than previously observed in misfit nanolaminates.

The remaining chapters (Chapters VIII-X) investigate compounds where $M=\text{Sn}$. Chapters VIII and IX repeat experiments from chapters VII and V respectively, but in the new chemical system. Though vestiges of the initial behaviors remain, structural distortions in the SnSe layers also result in behaviors not present in the $M=\text{Pb}$ compounds. Chapter VIII, which is currently unpublished, reports exciting low-temperature thermoelectric behavior and was written in collaboration with Danielle Hamann, Devin Merrill, and David Johnson. Chapter IX, which is unpublished, reports changing structure in SnSe layers with layer thickness, significantly altering the transport behavior. This was written in collaboration with Danielle Hamann and David Johnson. Chapter X discusses next steps, and gives a first look at rare earth intercalated $([\text{SnSe}]_{1+\delta})_1\text{RE}:(\text{TiSe}_2)_2$ compounds.

CHAPTER II

SYNTHESIS AND CHARACTERIZATION METHODS

All compounds presented and discussed in this dissertation have been formed by the self-assembly of designed thin-film precursors. Precursors are comprised of thin elemental layers deposited from the vapor phase that are gently heated to form a metastable product.¹ Unlike typical solid state reaction, short diffusion lengths move the formation of the product into the nucleation-limited regime, which in turn allows for investigations in previously inaccessible regions of the synthetic landscape.² This synthetic platform has led to the discovery of several new metastable single-phase compounds,³⁻⁵ but has been especially useful for its ability to form astounding numbers of new layered materials in several chemical systems.⁶⁻⁸

Figure 2.1. shows both a detailed and block schematic of the precursor deposition chamber. Precursors are deposited using physical vapor deposition of elemental sources from either electron beam guns or Knudsen effusion cells at a pressure below 5×10^{-7} torr. Sources reside at the lower portion of the deposition chamber and are monitored by quartz crystal microbalances. Computer controlled shutters above each source allow for substrates to be controllably and sequentially exposed to the plumes of evaporating atoms. Thus, the precursor is sequentially built from the bottom up, allowing for an order and thickness of layers that can be arbitrarily chosen within the limits of the equipment.

Precursors must first be calibrated to form the targeted product. For example, many binary chemical precursors form a metastable product when layers are deposited below a critical thickness and within a critical composition regime, which provides a favorable nucleation environment without a composition gradient where thermodynamic products will form as shown in Figure 2.2. The Fe-Sb chemical system is an example where these products may be formed. Understanding how deposition affects each of the thickness and composition parameters is critical.

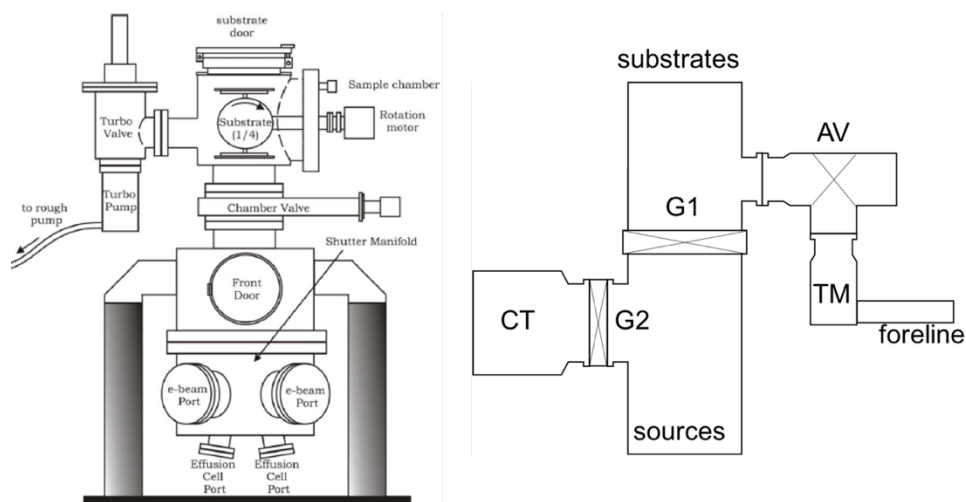


Figure 2.1. Schematic of physical vapor deposition chamber used for the synthesis of thin-film layered precursors. The simplified schematic (right) highlights the vacuum pump system and uses the acronyms CT for cryogenic entrapment pump, G1 and G2 for gate valves, AV for angle valve, and TM for turbo-molecular pump.

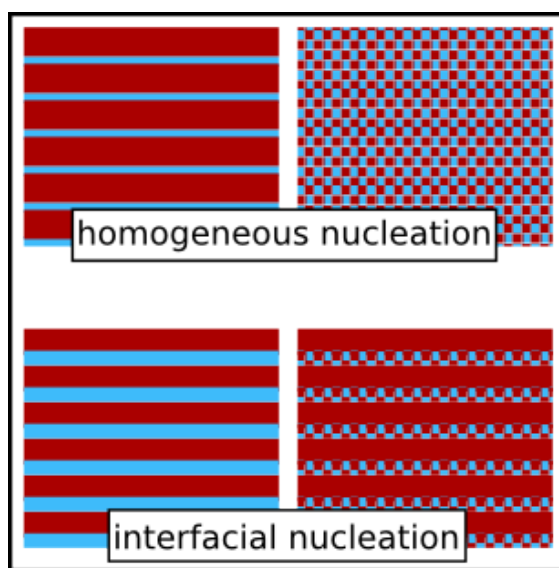


Figure 2.2. Schematic of the homogeneous nucleation environment that can be created in thin layers deposited from the vapor phase and the interfacial nucleation environment found in thicker layers or bulk reactions. While the local composition of the homogeneous precursor can be controlled with the layers, the chemical gradient present in the thick layers necessarily provides regions of compositional favorability for the formation of thermodynamic products.

A suite of binary precursors may be used to determine tooling factors and composition ratios from a set of elements. By varying the thickness of one layer while keeping the other constant, a precise determination of the thickness of material deposited onto the substrate relative to the thickness of material deposited onto the quartz crystal microbalance (QCM) deposition rate monitor may be determined. This is called the tooling factor. Figure 2.3. shows the tooling factor calibrations for a set of 2 elements – Fe and Sb. The blue(red) data points correspond to varying Fe(Sb) layer thicknesses while holding the other constant. The slope corresponds to the tooling factor of the varied element, while the intercept should correspond to the tooling factor of the constant element. For Fe(Sb) the constant value measured at the QCM was 5.1(58.8) Å with an intercept of 0.83(15.33), corresponding to a tooling factor of 0.16(0.26), which is reasonably close to tooling factor determined from the slope. The larger deviation in the suite of films with constant Fe thickness is likely due to the very thin layers, where small offsets due to shutter actuation become increasingly influential.

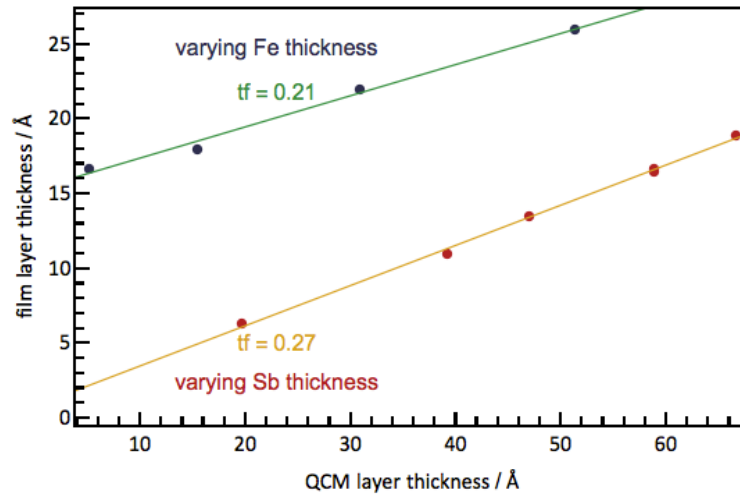


Figure 2.3. Calibration of the deposition tooling factors for a laminate system consisting of thin Fe and Sb layers. One elemental layer thickness is varied as the other is held constant. Slopes correspond to the tooling factor of the varied constituent while intercepts correspond to the constant constituent.

Once tooling factors are determined, the compositional ratio of elements relative to the layer thicknesses must be determined. In this case, it is not necessary to keep either layer thickness constant. Figure 2.4. shows a

calibration curve for the ratio of Fe:Sb thickness that has been measured at the QCM versus the measured composition of the thin film precursor. Since the tooling factors are similar it is clear that the atomic density of Fe in the Fe-Sb precursor is much greater than Sb – for a film with 50% atomic Fe density, Fe should only make up ca. 20% of the bilayer thickness. Having completed these calibrations, with a small amount of algebra a precursor with Fe-Sb bilayers with a targeted thickness and composition can be obtained.

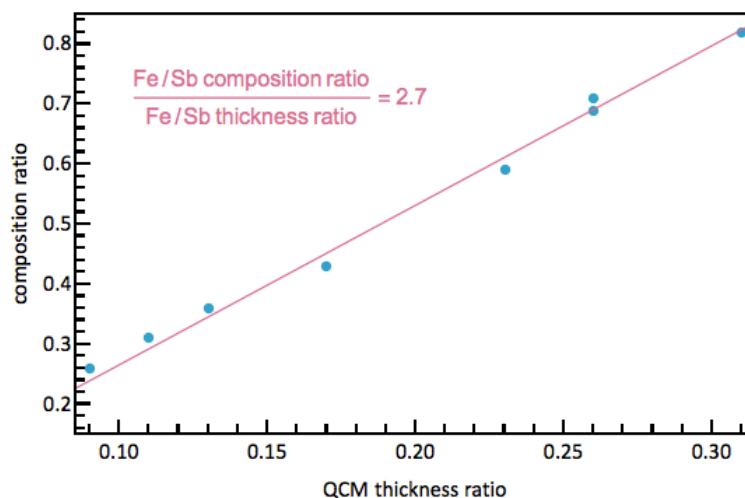


Figure 2.4. Composition ratios (Fe/Sb) of layered precursors plotted against the layer thickness ratios measured at the QCM during deposition. The Fe layers have much higher atomic packing density relative to Sb layers.

More complicated precursors may also be made, where the precise layering is designed to persist after gentle heating and crystallization in the form of a composite nanolaminate, schematically shown in Figure 2.5. The same calibration procedures are used, with the caveat that the bilayer thicknesses are then targeted to crystallize a single layer of the nanolaminate. By altering the sequence of layers deposited in the precursor, several nanolaminate products can be formed.

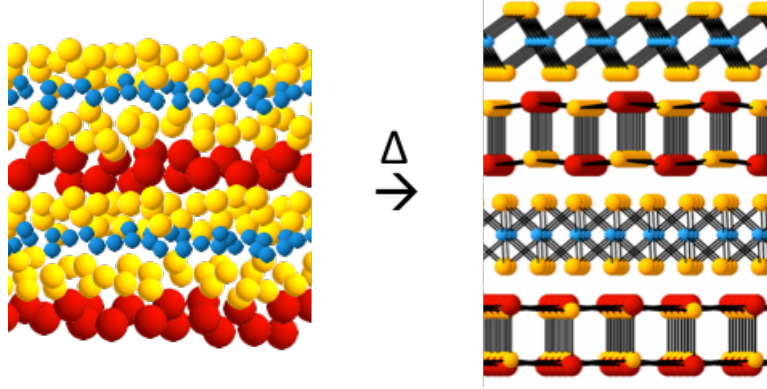


Figure 2.5. Schematic of a ternary layered precursor that is calibrated such that when gently heated the layers self-assemble into multicomponent layered heterostructures.

In a ternary system with a common element, measuring the global composition will not help determine which layers the common element belong to. However, assuming a common anion, the deposited precursor is given by the following chemical formula: $[(MX_x)_y]_p[TX_z]_q$ or $M_{py}T_qX_{pxy+qz}$. Where X is the common anion, M and T are the two cations, and x and z being the respective anion/cation ratios. y is the ratio between the two layer types and p and q are the number of layers deposited in the structure. Given the above formula the following equations are obtained:

$$q \left(\frac{X}{T} \right) = zq + pxy, \quad \frac{M}{T} = \frac{py}{q}$$

Thus, measuring composition ratios (and substituting in for M/T and X/T) while systematically changing p and q allow for all parameters to be found with simple linear regression. Once well-calibrated precursors are obtained, the temperature profiles that best activate self-assembly without forming decomposition products must be determined, which is simply an iterative process in finding the optimal temperature, time, and environment. In discussion of the precursor's product, p and q are replaced with the actual number of crystallized layers, *m* and *n*. Figure 2.6. illustrates several structures with varying *m:n* that may be formed in a system of distorted rock-salt and octahedral transition metal dichalcogenide layers.

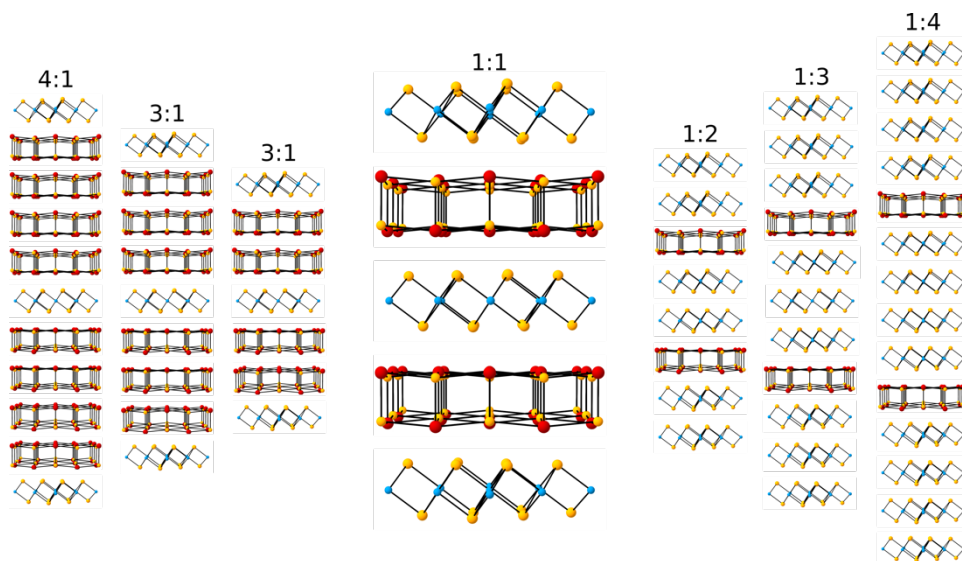


Figure 2.6. Examples of several layered structures that may be formed from the self-assembly of designed layered precursors. Well-calibrated precursor parameters can be scaled as necessary to form any of the above structures.

Structural characterization of the thin films in this dissertation is predominantly done with X-ray scattering techniques. This includes bulk and thin-film analysis of both textured and non-oriented materials. Standard X-ray diffraction (XRD) techniques from laboratory sources are predominantly used, but synchrotron radiation and less common analysis techniques at both very low and very high Q are also used in the form of X-ray reflectometry (XRR) and atomic pair distribution function analysis (PDF), respectively. Specifics on analysis techniques and experimental geometries can be found within the following chapters. Local characterization in real-space is done on small lamellas of the thin films using high angle annular dark field scanning tunneling electron microscopy (HAADF-STEM). Compositions have been measured with a variety of techniques, including electron probe microanalysis (EPMA), X-ray fluorescence (XRF), and scanning tunneling electron microscope energy dispersive spectroscopy (STEM-EDS/EDX). All techniques synergistically provide a detailed picture of the local and global structures and compositions of the metastable thin film compounds discussed herein.

Hall, resistivity, and cryogenic Seebeck coefficient measurements have been performed on a custom-built Hall system with a closed-cycle He cryostat cycling between ca. 15-295 K. Data collection is automated by a LabVIEW

program controlling several Keithley benchtop measurement devices. These measurements were made on insulating substrates, typically polished fused silica deposited through a shadow mask to form a van der Pauw cross. Measurement of the Seebeck coefficient at room-temperature is done by cooling half of a film slightly below room-temperature ($\Delta T < 2\text{K}$) and measuring both the temperature difference and thermopower with type T thermocouples.

CHAPTER III

SYNTHETIC CONSIDERATIONS FOR METASTABLE THIN-FILM THERMOELECTRIC MATERIALS FROM AMORPHOUS PRECURSORS

Chapter III is comprised of two publications both coauthored by myself, Kirsten Jensen, Anders Blichfeld, Suzannah Wood, Bo Iversen, Simon Billinge, and David Johnson. Suzannah Wood and Anders Blichfeld assisted with sample preparation, data collection and analysis, Kirsten Jensen assisted with data collection at NSLS and NSLS-II as well as analysis and manuscript preparation, and Bo Iversen, Simon Billinge, and David Johnson are our group leaders and advisors. The first part, Structural Evolution of Iron Antimonides from Amorphous Precursors to Crystalline Products Studied by Total Scattering Techniques (DOI: 10.1021/jacs.5b04838), was accepted for publication in *Journal of the American Chemical Society* on 2015-07-10 and I am the primary author. The second manuscript, Demonstration of Thin Film Pair Distribution Function Analysis (tfPDF) for the Study of Local Structure in Amorphous and Crystalline Thin Films (DOI: 10.1107/S2052252515012221), was accepted for publication on 2015-06-25 in *IUCrJ* and Kirsten Jensen is the primary author. I assisted with sample preparation, data collection, data analysis, and writing of the manuscript.

3.1. Structural Evolution of Iron Antimonides from Amorphous Precursors to Crystalline Products Studied by Total Scattering Techniques

3.1.1. Introduction

Traditional solid-state synthesis requires high heat and long reaction times to drive the formation of a thermodynamic product.¹ During this process, atoms must diffuse over long distances, which is typically rather slow in solids and even on solid surfaces. Due to the concentration gradient at the reacting interfaces, a rich combination of compounds form as interdiffusion, nucleation and growth occur.² However, the elevated temperature and long reaction times ultimately limits the product to the thermodynamically stable mix of com-

pounds at the temperature and composition of reaction. Moreover, the intermediate products and structural changes during the diffusion and crystallization process are difficult to follow. A general lack of a mechanistic understanding or even a description of the evolving structure during the formation of these compounds, as well as commercial interest in the functionality of inorganic materials, has moved solid-state synthesis from the realm of chemistry toward the domain of materials science.³

While many predictions of novel materials can be made, unlike the synthesis of organic compounds there is currently no clear-cut path to direct the formation of specific metastable inorganic products from reactants. Various guidelines, such as Ostwald's step rule that states crystallization from a solution proceeds stepwise through increasingly favorable intermediates, may be applied to inorganic and solid systems, but use of them tends to be retrospective as opposed to predictive.⁴ Recently however, in-situ monitoring of inorganic reactions has shown the formation of many metastable intermediate products as well as promising and controllable methods to synthesize them. For example, a clever in-situ diffraction experiment recently identified and isolated several new ternary sulfide phases in otherwise ordinary inorganic flux reactions.⁵ Our knowledge of how inorganic reactions proceed has also been enhanced by x-ray total scattering studies of local structure during the formation of inorganic frameworks. Recent work on nanoparticle formation under hydrothermal conditions demonstrates the insights obtained from these studies.⁶ The topic of in-situ studies of the structural evolution of inorganic compounds was recently reviewed.⁷ For the most part these (and similar) reports are from systems where the chemistry, at least in part, is occurring outside the solid-state. However, recently there has been considerable interest in better understanding the formation of inorganic compounds during solid-state reaction, hopefully leading to a renaissance in the field from a chemist's perspective.⁸⁻¹¹

A fruitful approach to the discovery of new solid state materials has been in vapor depositing thin films that are compositionally controlled at an atomic level, allowing for constituents to react at modest temperatures without the need for long range solid state diffusion.^{1,12-16} This approach has been utilized

in the synthesis of several new binary and ternary compounds.^{17–20} Furthermore, by depositing constituents in layers that are thin enough, compounds not readily synthesizable by conventional solid-state techniques are formed.¹⁴ It was proposed that under heating only thin layers would completely interdiffuse prior to nucleation. The homogeneous compositional environment was hypothesized to prevent nucleation of thermodynamically stable phases, as the systems lack a compositional gradient and would thus need to disproportionate to nucleate a thermodynamic compound with a different composition.²¹ In this case, the slow diffusion rates become a synthetic advantage and can be used to help control the formation of kinetic products.²² Particularly exciting is the possibility of “designing precursors” to yield desired products by controlling the deposition process. To realize the full potential of this method it is essential to be able to characterize in detail not only the reaction products but also the amorphous precursors and the reaction pathways to the resulting product.

Here we have applied the atomic pair distribution function (PDF) analysis of x-ray diffraction data to study the local structure of a series of precursors that yield distinct products in the FeSb_x ($x = 2, 3$) chemical system. Surprisingly, we see evidence of atomic scale interdiffusion and local metal coordinations representative of the final metastable product even in precursors compositionally unfavorable for its nucleation. The approach of coupling careful local structural measurements on homogeneous amorphous reaction intermediates represents a powerful approach that has extensions to the designed synthesis of a broad range of solid-state chemical systems.

3.1.2. Structures in FeSb_x Chemical System

The iron-antimony phase diagram contains only two thermodynamic compounds – an Fe_{1+x}Sb phase in which excess Fe resides interstitially in an otherwise NiAs-type structure and an FeSb₂ marcasite-type phase.²³ The marcasite structure can be thought of as rutile with a larger rotation between distorted FeSb₆ octahedra: octahedra are corner-sharing in the a - b plane and edge-sharing as they are translated down the c -axis. This results in a loss of symmetry, a stabilizing anion dimer, and an orthorhombic unit cell. An FeSb₃

phase that is always thermodynamically unstable relative to $\text{FeSb}_2 + \text{Sb}$ has also been synthesized using modulated thin film precursors.²⁴ This compound adopts a skutterudite structure, which is related to the ReO_3 structure but with 4 anions along parallel edges of the unit cell displaced inward, creating a four-fold ring. This doubles the edge length along each direction of the unit cell, with $\frac{1}{4}$ of the octants containing an open “cage”. In each of these compounds Fe is octahedrally coordinated with differing connectivity between octahedra, as expected by the changes in stoichiometry. In Fe_{1+x}Sb the octahedra share faces. In FeSb_2 each corner Sb of the octahedra are shared by three octahedra, which are rotated to create a short Sb-Sb bonding pair. In FeSb_3 , two octahedra share each corner. Figure 3.1. shows representations of the structures of both FeSb_2 and FeSb_3 . There has been much discussion on bonding within both the skutterudite and marcasite structural families. In each case, one could imagine a bonding scheme wherein formation of the FeSb_6 octahedral unit is the dominating interaction, followed by stabilization from dimerization (FeSb_2) or tetramerization (FeSb_3) of antimony. Similarly, the opposite case could reasonably occur and historically much of the literature has centered around discussion of the Sb-Sb dimer and tetramer formation.^{25–27} However, recent studies of both FeS_2 marcasites and CoSb_3 skutterudites show the metal octahedron plays a large role in the bonding.^{28,29}

3.1.3. Experimental Methods

Precursors were deposited using the modulated elemental reactants (MER) synthesis method on a custom-built deposition system.³⁰ Antimony was deposited from a Knudsen effusion cell whereas an iron source was evaporated using an electron gun. A pressure below 5×10^{-7} torr was maintained during deposition. Deposition rates were monitored from quartz crystal microbalances and shutters installed above each source were sequentially opened and closed to achieve a layered precursor of the desired thickness. Deposition parameters were calibrated to allow for targeted composition ratios and bilayer thicknesses between Fe and Sb. Samples used for calibrating the depositions had targeted total thicknesses of approximately 36 nm whereas samples for further analysis had a targeted total thickness of approximately 360 nm. While calibrating the

system, thicknesses were confirmed with x-ray reflectivity. Cumulative roughness combined with high-frequency Kiessig fringes prevented determining total thickness by this method on the thick films. The FeSb_3 samples were deposited with excess Sb as stoichiometric precursors (with 25 atomic % Fe) formed mixtures of the diantimonide and triantimonide phases as reported previously.³¹

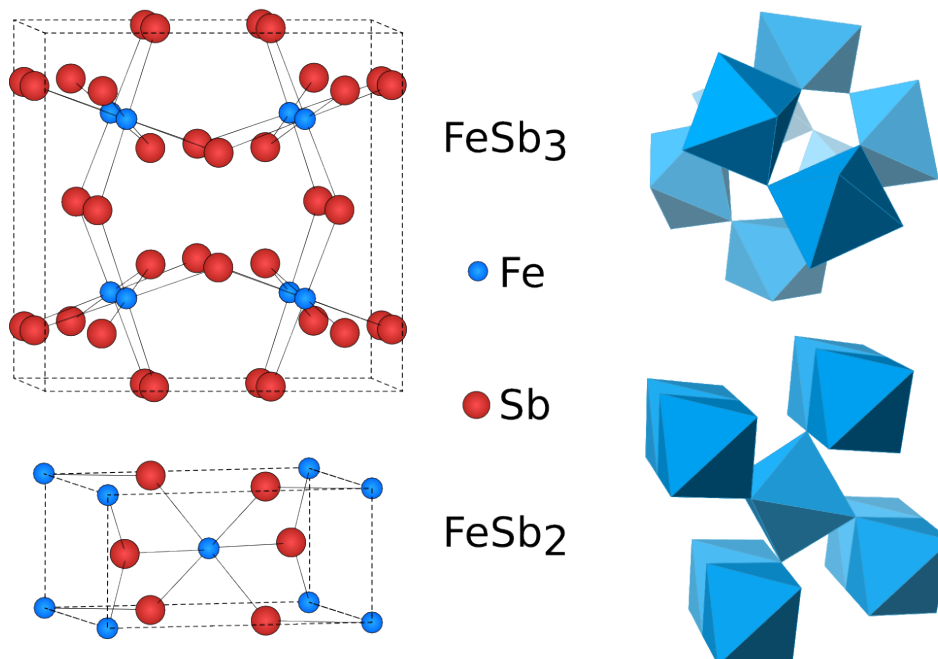


Figure 3.1. Crystalline phases of (top) FeSb_3 and (bottom) FeSb_2 in both ball-and-stick and polyhedral representations, generated from available crystallographic data.^{24,32} The FeSb_2 polyhedral representation shows 2 unit-cells along each lattice vector (8 unit cells total). The FeSb_3 polyhedral representation has an offset origin relative the ball-and-stick model.

The precursors discussed herein were deposited on adjacent substrates: polished (100) Si wafers and (100) Si wafers coated in poly(methyl methacrylate) (PMMA). Films on PMMA were then floated off of the support wafer by dissolving in acetone, washed to remove excess PMMA, and collected on a Teflon filter. This resulted in delicate flat metallic flakes with an approximate maximum diameter of 0.5 mm, which were removed from the filter and packed into a 1.0 mm kapton capillary. PDF data were taken on samples in three states: as-deposited with no high temperature treatment, interdiffused wherein precursors

are kept at 100 °C for 30 minutes in order to drive diffusion of the layers, and annealed in which precursors are held at a temperature that activates crystallization of the desired phase for 30 minutes. FeSb₃ samples were crystallized at 200 °C and FeSb₂ samples at 300 °C. All sample annealing was done on a hot plate in a nitrogen atmosphere after transfer to capillaries. No differences in capillary tubes were observed after thermal treatment.

Composition was measured from samples on bare Si using an electron probe micro analysis technique where the k-ratios are collected as a function of accelerating voltage.³³ Diffraction data for Rietveld refinement was collected from the samples deposited on bare polished Si using a Rigaku Smartlab diffractometer in grazing-incidence geometry and Cu-K α radiation. Rietveld refinements were done using the GSAS³⁴ software package and EXPGUI³⁵ interface.

Room temperature x-ray total scattering data was collected at a wavelength of 0.185970 Å at beamline X17A of the National Synchrotron Light Source, Brookhaven National Laboratory, from samples in filled kapton capillaries. The RA-PDF setup was used, with a Perkin Elmer amorphous silicon detector.³⁶ The total scattering data were integrated using Fit2D³⁷ and PDFs were generated with PDFgetX3³⁸ using a Qmin of 0.85 Å⁻¹, Qmax of 25 Å⁻¹, and an *rpoly* of 0.9. Real-space modeling of crystalline phases was done in PDFgui.³⁹

3.1.4. Results and Discussion

Following previous reports, we were able to design precursors such that they nucleate either the FeSb₂ or FeSb₃ phase.³¹ Both precursors contained partially interdiffused elemental layers of Sb and Fe with thicknesses below the critical thickness for nucleation of the triantimonide. Thus, selectivity was achieved by adjusting elemental composition. Sb layer thickness was kept nearly constant between precursors. Table 3.1. summarizes the samples used in the PDF investigation.

Table 3.1. Summary of precursors

Phase	Fe th. (Å)	Sb th. (Å)	Repeats	Fe/Sb
FeSb ₂	2.4	16.8	188	0.49
FeSb ₃	1.1	17.0	200	0.21

Figure 3.2. shows powder X-ray diffraction data from annealed thin-films of each sample and associated Rietveld refinements, which confirm the formation of the expected FeSb₂ and FeSb₃ phases. On annealing, the FeSb₃ samples remained as smooth films whereas the FeSb₂ sample forms visible crystallites on the surface. Diffraction data collected at several incidence angles and in the plane of the film indicate scattering from powder-like samples. The diffraction data from the FeSb₂ sample contains a small Sb signal (as seen from e.g. the Sb (012) peak at 2 Å⁻¹), though inclusion of Sb does not appreciably improve refinements. The FeSb₃ sample shows 34% Sb impurity by mass.

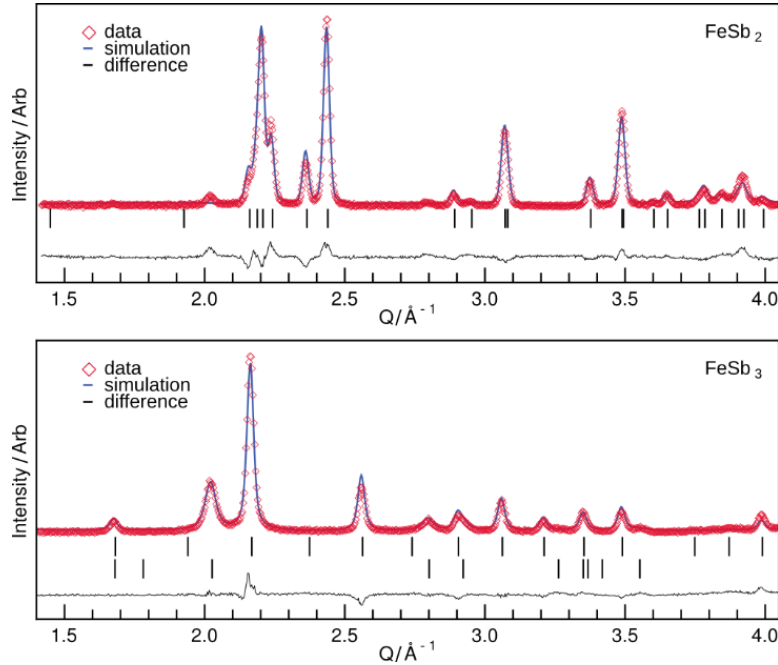


Figure 3.2. Diffraction patterns taken from iron antimonide samples. In the triantimonide phase, the above markers correspond to the marked phase and the lower markers correspond to antimony. The markers in the diantimonide pane refer to the marked phase.

Figure 3.3. shows a portion of the PDFs from crystalline samples, along with their least-squares fits (r -range fit from 5-60 Å). Also shown are theoretical PDFs of the constituent phases, which were generated with lattice parameters obtained from the refined diffraction data shown in Figure 3.2. For the metastable sample, a 2-phase fit including Sb and FeSb₃ was used. The FeSb₂ sample was fit with a single FeSb₂ phase as addition of Sb to the model resulted in no practical improvement. In both cases, fits were done preserving cell symmetry with the fitted parameters being lattice parameters, scaling, correlated motion, particle diameter, and isotropic Debye-Waller factors. The correlated motion parameters were constrained to match between phases. The difference curve shows the model does not completely capture the short-range ($r < 5$ Å) order, with agreement improving at higher r . The FeSb₃ mass percentage relative to Sb from PDF refinement is slightly lower than from Rietveld refinement but probably within the limit of the error – 62% (PDF) vs. 66% (Rietveld). Examination of the difference curve shows the strongest disagreement at ca. 2.9 Å. This corresponds to the nearest Sb pair distance in bulk Sb and indicates the misfit at low r -values is likely due to the presence of additional amorphous Sb that is not included in the model of crystalline Sb and FeSb₃. Any additional disagreement at low r may be due to remaining amorphous material or artifacts from data reduction. The results from the PDF refinements regarding the crystalline phases agree well with the structural models determined from prior results based on powder x-ray diffraction analysis. Interestingly, our data suggests that in this system the densities do not evolve according to the Ostwald rule. In fact, the refinement of the FeSb₃ sample shows a slightly higher density than for the marcasite structure. Further details of these refinements are provided in the supplementary information.

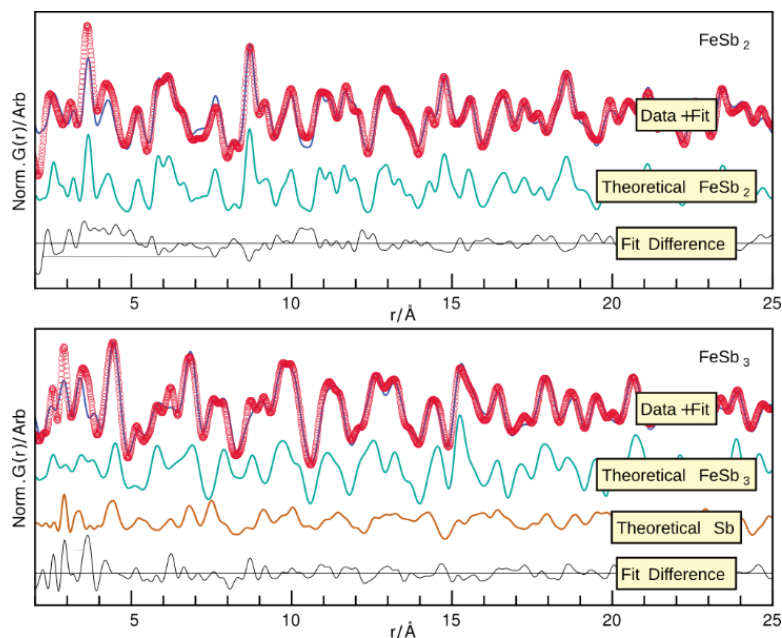














Figure 3.3. PDFs of FeSb_2 and FeSb_3 compounds with models, as well as theoretical PDFs of constituent phases. The difference between data and fit is shown below in black. Fits were performed with an r range of 5-60 Å. For the full fit-range of the PDFs see the supporting information.

Table 3.2. summarizes the pairs seen in the PDFs of each crystalline phase up to about 5 Å. This r -range contains all intra-octahedral distances, as well as the first few inter-octahedral pairs. The schematic showing pair distances denotes Fe in carmine and Sb in cyan. Both PDFs contain sharp peaks in the lowest r -range, while broader peaks are seen at ca. 3.5 Å and 4.4 Å from multiple pairs in close proximity around these distances. There is a ~ 1 Å difference in Sb-Sb pair distances along the various FeSb_6 octahedral edges in FeSb_2 . The shortest and longest pair distances belong to the translated and shared edges, respectively. Multiple electronic arguments have been previously proposed to account for the structural distortion of the metal octahedra in marcasites.^{40,41}

Table 3.2. Summary of pair distances that correspond to the first peaks in the FeSb₂ and FeSb₃ PDFs.

FeSb ₂ pair distances			FeSb ₃ pair distances		
Position / Å	Description	Schematic	Position / Å	Description	Schematic
2.6	Fe-Sb within FeSb ₆ octahedra		2.6	Fe-Sb within FeSb ₆ octahedra	
2.9	Sb-Sb dimers between corner sharing octahedra		2.9	Sb-Sb in Sb metal and Sb tetramers between FeSb ₆ octahedra	
3.2	Fe-Fe, Sb-Sb along translation direction of edge-sharing octahedra		3.3-3.5	Sb-Sb along short octahedral edges	
3.6-3.7	Sb-Sb along medium octahedral edges		3.8	Sb-Sb along long octahedral edges	
4.1-4.4	Various inter-octahedral Fe-Sb and Sb-Sb along longest octahedral edges		4.5-4.6	Various pairs (Fe-Fe, Fe-Sb, Sb-Sb) between octahedra	
5.2	Sb-Sb along opposite corners of FeSb ₆ octahedra		5.1	Sb-Sb along opposite corners of FeSb ₆ octahedra	

In previous work, Williams et al. attributed an exotherm at 140 °C in precursor films to the crystallization of FeSb₃, while an exothermic signal before the nucleation event has been associated with interdiffusion of the elemental layers.³¹ Diffraction data from as-deposited and interdiffused (heat treated at 100 °C in a nitrogen environment for 30 minutes to drive solid-state diffusion of the layers) samples show an order of magnitude decrease in intensity from the (001) superlattice reflection, indicating significant intermixing has occurred, though some modulation in electron density remains (see supplemental information). To follow structural changes as the samples evolve from the as-deposited state to the final annealed phases, X-ray total scattering data were collected on powders in the as-deposited, interdiffused, and annealed states. The total

scattering data were used to generate PDFs, which are shown in Figure 3.4. for both the FeSb_2 and FeSb_3 compounds. For both the as-deposited and interdiffused samples, only short-range order is seen, while long range order from crystalline compounds is only seen in the annealed samples. Interestingly, the PDFs obtained on the as deposited and interdiffused samples are very similar, as shown by the difference curves. This implies that the local structure of both the FeSb_3 and FeSb_2 precursors does not change significantly during the initial heating of the samples, and that significant interdiffusion between the Fe and Sb layers happens during deposition, at room temperature, or during the removal of the films from the substrate. For all four amorphous samples, a series of sharp peaks are seen at the lowest r -values, showing well-ordered local structures. The distance at which a highly ordered structure terminates is consistent between both the FeSb_2 and FeSb_3 precursors with the last high-frequency peak at *ca.* 5.1 Å followed by an intense, broad signal centered at 6.4 Å and regular oscillations to higher r . The domain size for mid-range order is given by these oscillations and appears very similar between the two precursors. The pair-distances and r -value where sharp peaks disappear in the amorphous FeSb_3 samples correspond well to the residuals in the fit of the crystalline FeSb_3 sample (Figure 3.3.), indicating that some amorphous FeSb_6 octahedra remain. No similar correlations with the residuals of the FeSb_2 residuals could be made. Cursory examinations of the PDFs show that the local structure in the two precursors are different from one another, as might be expected from the difference in average composition.

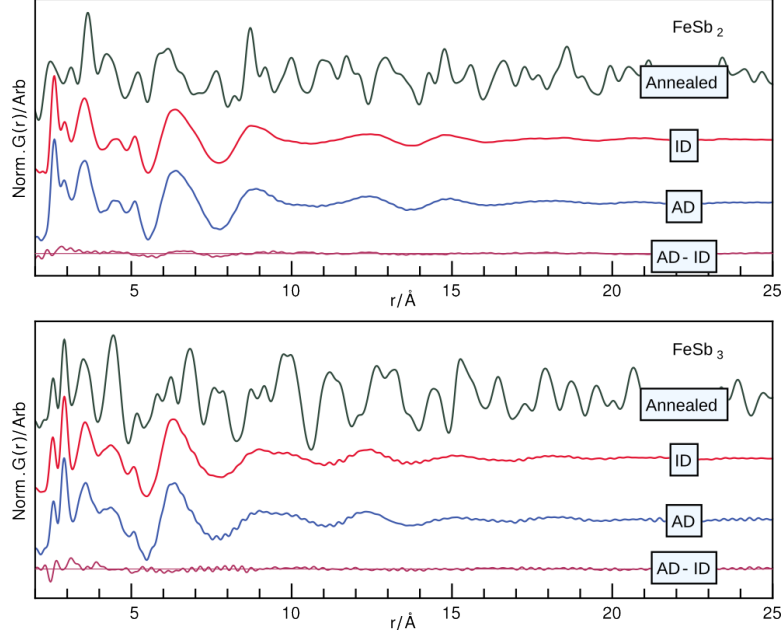


Figure 3.4. Pair distribution functions of as-deposited (AD), interdiffused (ID), and annealed samples generated from total scattering data. The difference curves between the as-deposited and interdiffused samples (AD-ID) show little structural change during the diffusion process, as seen by the small deviations from the lines showing zero change.

Panes a and b of Figure 3.5. show PDFs of the crystalline samples overlaid with their as-deposited amorphous precursors, with each curve normalized to its maximum intensity. The FeSb_3 data show large similarities between amorphous and crystalline PDFs in the local structure. Up to about 5 Å, vestiges of the FeSb_3 product can be seen, with contributions from excess Sb also clearly manifested by a sharp narrow peak at 2.9 Å. This suggests the presence of amorphous Sb with only very short range order as well as corner sharing FeSb_6 octahedra without the regular orientation found in the crystalline structure. By comparing to the atomic pairs giving rise to PDF peaks from the crystalline phases (summarized in Table 3.2.), the structural motifs in the amorphous samples can be identified, as illustrated in Figure 3.5.c. The relative intensities of peaks from Sb pairs within an octahedron (3.5 Å for pairs along an edge and 5.1 Å through the center, indicated in Figure 3.5. by blue and red, respectively) are approximately the same between as-deposited and annealed FeSb_3 samples. However, the pair intensity around 4.5 Å, which corresponds to multiple pairs

across octahedra in the crystalline structure, is broad and low in the amorphous PDF due to the large number of inter-octahedral distances which may occur between disordered corner-sharing octahedra (Figure 3.5.d., shown in magenta). Notably, no vestiges of edge-sharing octahedra, which produces multiple pairs at 3.2 Å as seen in the crystalline FeSb₂ sample (see Table 3.2.), are apparent in the FeSb₃ precursor. The similarity between the FeSb₃ precursor and product helps explain the low nucleation temperature. The data suggest that reorientation of existing corner-sharing octahedra into a regular extended network is the predominant mechanism of crystallization on heating.

Conversely, Figure 3.5.a. shows that the PDF of the precursor that nucleates to FeSb₂ does not match the crystalline phase well, even at low r . In fact, while relative intensities differ, the local structure only shows motifs of corner-sharing Fe-Sb octahedra similar to the FeSb₃ phase and precursor. This is clear in Figure 3.5.c., where the PDFs from the two precursors are overlaid. Comparing precursors, a large increase in the relative amplitude of the 2.6 Å peak corresponding to the Fe-Sb distance (in FeSb₆ octahedra) is apparent and attributable to the increased iron content in the sample. The 3.2 Å pair-distance, which corresponds to adjacent edge-sharing octahedra translated along the c -direction in FeSb₂, is not observed in the as-deposited PDFs. If the marcasite edge-sharing motif were present in the FeSb₂ precursor, additional intensity manifested as a narrow peak would be expected at this pair distance, due to every atom having an inter-octahedral pair along the translation direction. This is observed in the crystalline FeSb₂ PDF, but from the lack of this feature in the precursor we conclude edge sharing is absent. Without edge-sharing, the FeSb₂ sample does not have enough antimony to fully coordinate each iron octahedrally. However, the similarities in the as-deposited precursor and interdiffused precursor PDFs suggest that Fe in FeSb₃ and Sb in FeSb₂ are completely coordinated on deposition. With this in mind, the presence of a small signal at the characteristic 2.9 Å Sb-Sb pair distance in the FeSb₂ precursor is at first puzzling. However, this pair distance is explained by inter-octahedral Sb dimers. Notably, both the FeSb₂ and FeSb₃ precursors exhibit an inherent stability in the FeSb₆ structural unit. Unlike the FeSb₃ sample in which existing building blocks primarily need to arrange themselves into a regular structure, extra iron must be

incorporated into the edge-sharing marcasite structure of FeSb_2 . The large differences between the precursor and product help explain the higher energy required to nucleate the FeSb_2 phase relative to FeSb_3 .

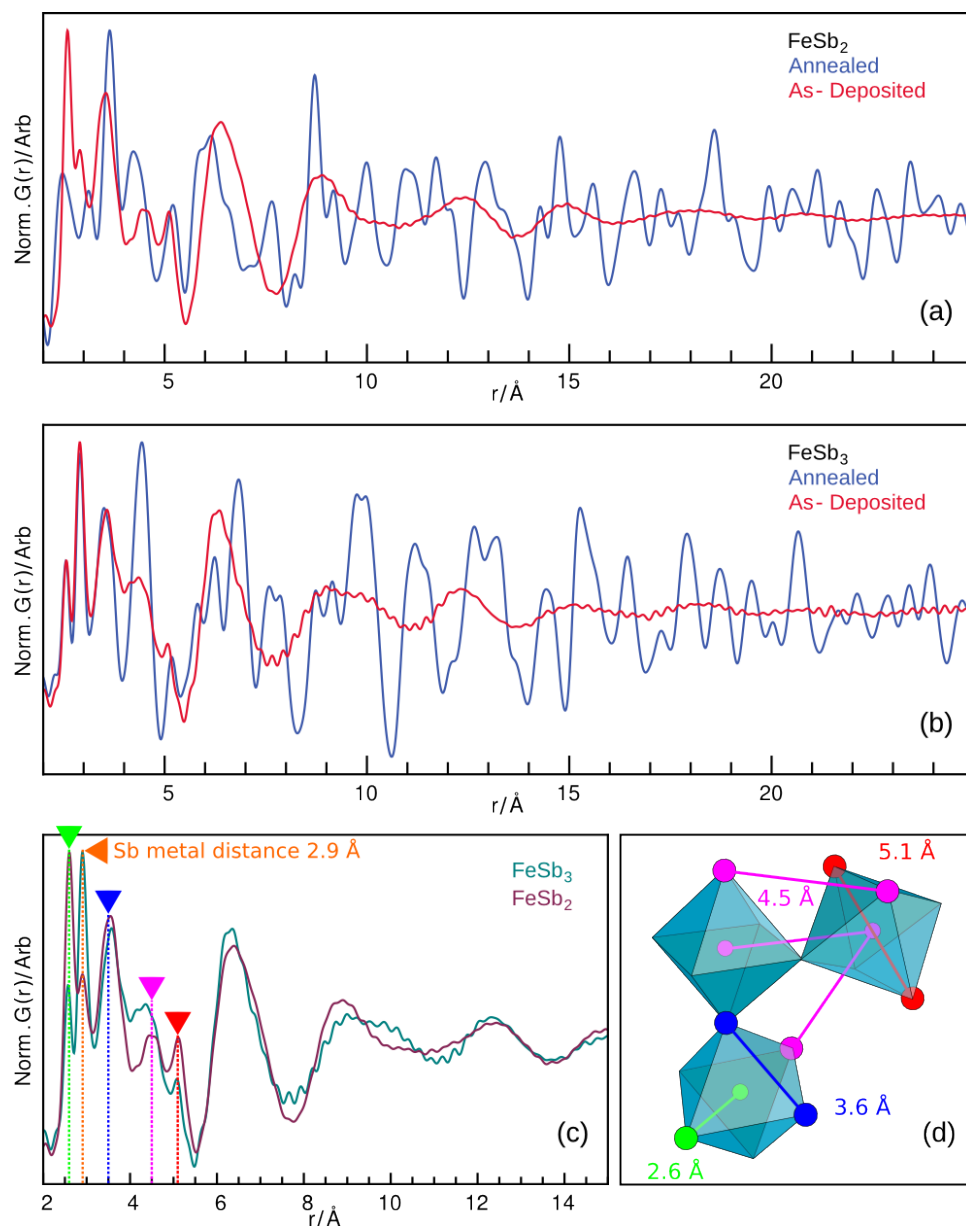


Figure 3.5. PDFs of precursors overlaid with annealed samples for (a) FeSb_2 and (b) FeSb_3 . (c) Overlaid FeSb_2 and FeSb_3 precursors show similar peak positions but varying relative intensities. Peak positions corresponding to pairs in the FeSb_3 PDF are shown by colored triangles. (d) Similar pair distances from a disordered arrangement of corner sharing octahedra are shown in corresponding colors.

Previous investigations have suggested that nucleation of metastable products from well-mixed precursors is driven by forcing a local environment of similar structure and composition to the kinetic phase. Somewhat surprisingly, the results summarized in Figure 3.5. indicate that even without the excess Sb, the local structure of the FeSb_2 precursor is more similar to FeSb_3 . It then appears that in these systems there is an inherent kinetic favorability towards adopting a structure similar to the metastable phase, which can then be nucleated in precursors with appropriate composition. The idea that similarity in the local structure of a precursor to the phase that it nucleates is something we may be able to extend to other metastable solid-state compounds, and suggests in general that homogenous amorphous intermediates might be very useful synthetic tools. Probing local structure of reaction intermediates using PDF might allow for rational changes to be made in composition to avoid local structure similar to known compounds and/or to tune composition of the amorphous precursor to obtain local structures similar to targeted compounds to promote nucleation. The observation of the same structures in both as-deposited and interdiffused states illustrates the stability of the corner-sharing FeSb_6 structural motif. If this approach proves to be general for the formation of metastable structures from amorphous reaction intermediates, it will be especially valuable when combined with *ab-initio* calculation of stable local structures.

3.1.5. Conclusions

Local structural similarities of homogeneous amorphous iron and antimony precursors to a skutterudite crystal help to nucleate a low-temperature metastable FeSb_3 phase. Significant interdiffusion of the precursors, which are deposited in layers on the Å scale, occurs even at room temperature, leading to a nucleation-limited crystallization event. On deposition, constituents form an amorphous network of corner-sharing FeSb_6 octahedra similar to AX_3 structures, even in precursors with a 1:2 Fe:Sb ratio. This indicates preferential low-temperature formation towards the metastable phase is somewhat contrary to previous reports, where it was surmised the excess Sb drove the reaction towards the metastable product. The higher temperatures necessary for the crys-

tallization of the thermodynamic FeSb_2 phase are most likely due to a major re-orientation of local environment. In further studies it will be insightful to investigate this further and see at which point compositional disagreement overcomes the observed preference to form the corner-sharing FeSb_6 octahedra.

Continued use of PDF analysis in solid-state systems nucleated from homogeneous amorphous precursors will provide insightful information correlating precursor structures with final products. This will be particularly helpful in systems where many phases could form or systems wherein ternary or quaternary phases form instead of binary phases. Ultimately, similar analysis could be potentially used as a screening mechanism to optimize a precursor to have local structure similar to a predicted, but unrealized compound. Given the appropriate synthetic control, a range of structural and compositional “designed precursors” could be formed and their local structures tested for motifs of a targeted phase. This would provide valuable insight, greatly enhance the likelihood of synthetic success, and reduce the number of required experiments when exploring additional unknowns.

3.2. Demonstration of thin Film Pair Distribution Function analysis (tfPDF) for the study of the local structure of amorphous and crystalline thin films

3.2.1. Introduction

Thin films are fundamental in applications from electronics to catalysis to tribology in structural materials.^{42–45} Even in basic science the thin-film geometry allows the generation of structures that are normally metastable. For example, advanced methods in thin film preparation such as chemical vapor deposition,^{46,47} atomic layer deposition⁴⁸ and molecular beam epitaxy⁴⁹ have in recent years made it possible to prepare new, advanced functional materials with applications in e.g. thermoelectrics, semiconductors, and multiferroics.^{42,50–52} Compounds, which are unstable or metastable in the bulk state, can by means of these atomic-layer engineering techniques be prepared as thin films, opening for a whole new realm of materials. When films are single crystalline, powerful

methods such as Coherent Bragg Rod Analysis⁵³ and x-ray standing wave analysis⁵⁴ can yield significant quantitative information about the ordered structure at the surface.⁵⁵ However, if the films are nanocrystalline or amorphous the situation becomes much more difficult. Here we describe a straightforward approach to obtain quantitative atomic pair distribution functions (PDF) from nanocrystalline and amorphous thin films yielding important local and intermediate-range structural information from films.

When preparing thin films (10-1000 nm), the precursor compounds are typically deposited on a much thicker substrate of e.g. Si, SiO₂ or Al₂O₃. This sample geometry challenges the conventional methods for structural analysis using x-ray diffraction, as data collected using standard scattering configurations (i.e. Debye-Scherrer or Bragg-Brentano setups) are dominated by scattering from the substrate. To avoid this, grazing incidence (GI) x-ray diffraction methods are generally applied for thin film structure analysis.⁵⁶ GI measurements are done with an incident x-ray angle close to the critical angle for total external reflection, which allows the beam to illuminate as much of the thin film as possible whilst minimizing penetration of the beam into the substrate, maximizing the signal from the film. However, not only are the experiments very challenging because of the very small critical angles for hard x-rays, the grazing incidence geometry complicates analysis of the data as angular dependent corrections for the penetration depth and the amount of illuminated sample/substrate must be made before quantitative information can be extracted. While e.g. Rietveld analysis can be done after careful corrections and provide valuable structural insight,^{57,58} most of the x-ray analysis done for thin films is qualitative and used mainly for identification of crystalline phases by considering the Bragg peak position. This approach is not adequate to characterize e.g. the complex nanostructures present in modern materials, which may not possess long-range order.⁵⁹

In recent years, PDF analysis has become a standard technique for characterization of local structure and nanomaterials. PDF allows the extraction of structural information from amorphous, nanostructured and crystalline materials, and PDF studies have led to a breakthrough in our understanding of materials structure and reactions in materials chemistry.⁶⁰ For thin films, local

structural analysis could in the same way help to understand things such as the crystallization processes and modifications from bulk structure of films. However, for PDF data corrections, the grazing incidence geometry highly complicates the data analysis.⁶¹ So far, to the best of our knowledge, PDF has therefore not been successfully applied to analysis of thin films in grazing incidence. We therefore set out to develop a method that can be used to do quick, routine PDF analysis of thin films, here referred to as tfPDF. We show that by using high flux, high energy x-rays from third generation synchrotron sources, standard normal incidence total scattering measurements can be used to extract reliable PDFs from thin films on amorphous substrates. The measurements can be done in transmission through both the sample and the substrate using the standard rapid acquisition PDF (RA-PDF) setup with a large area detector,³⁶ making tfPDF readily available to use for a range of thin film materials.

Here, we have investigated amorphous and crystalline FeSb_x films to illustrate the feasibility of tfPDF. Deposition of alternating ultra-thin Fe and Sb layers on a flat substrate gives an amorphous film, which upon annealing crystallizes to form FeSb₂ or FeSb₃, depending on the thickness of the alternating Fe/Sb layers as described by Williams *et al.*³¹ The FeSb₃ skutterudite structure is metastable, and consists of corner-sharing FeSb₆ octahedra only (Figure 3.6.A.), whereas the thermodynamically stable FeSb₂ structure has both corner and edge-sharing octahedra.²⁴ (Figure 3.6.B.). We set out to use tfPDF to study the local structure in the as-deposited films that leads to the metastable phase FeSb₃, to study the diffusion between the Fe/Sb layers, and the relation between the precursor layering and the final, crystalline product. Our studies give new insight into the crystallization of the metastable FeSb₃ phase and open for a range of new investigations of film materials.

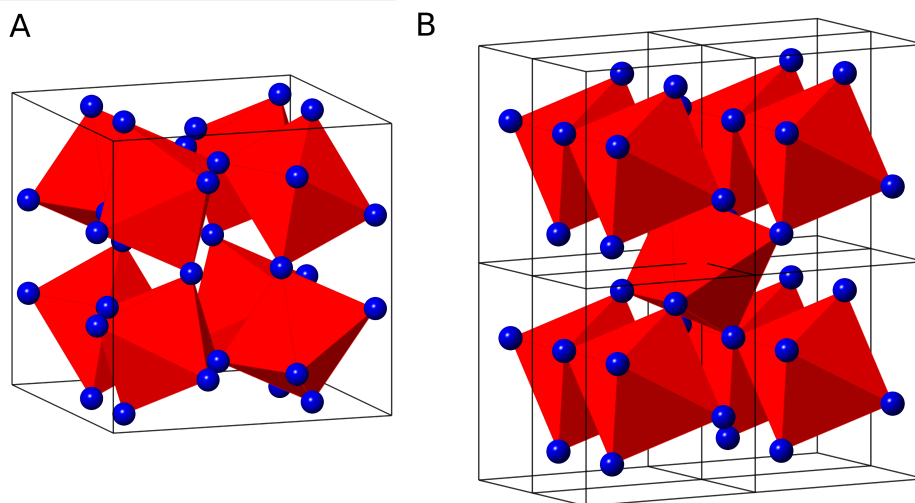


Figure 3.6. Crystal structure of A) FeSb₃ and B) FeSb₂ (4 unit cells). The red polyhedra show FeSb₆ octahedra, with Sb marked as blue spheres in the corners.

3.2.2. Experimental details

3.2.2.1. Preparation of FeSb_x

The FeSb₃ samples were synthesized using layered deposition as described in detail elsewhere.³¹ The Sb and Fe precursors were deposited on 170 μm thick amorphous borosilicate glass slips using the Modulated Elemental Reactant (MER) synthesis method on a custom-built deposition system.⁶² Antimony was deposited from a Knudsen effusion cell whereas an iron source was evaporated using an electron gun. A pressure below 5×10^{-7} torr was maintained during deposition. Deposition rates were monitored from quartz crystal microbalances and shutters installed above each source were sequentially opened and closed to achieve a layered precursor of the desired thickness. The deposition parameters were calibrated to allow for targeted composition ratios and bilayer thicknesses between Fe and Sb. After precursor layer deposition, the films were annealed in nitrogen for 30 minutes at 200 $^{\circ}\text{C}$. Compositional data was obtained with an electron probe microanalyzer, using a thin-film technique. Two sets of samples were prepared with varying Fe/Sb ratio, as listed in Table 3.3. The as-deposited samples are marked A for amorphous (i.e. sample 1A and 2A) whereas annealed samples are marked C for crystalline (i.e. 1C and 2C).

Table 3.3. Sample list

Sample name	Structure	Layer thickness	Fe/Sb ratio	Film Thickness
1A	As-deposited, amorphous	Fe: 1.1 Å Sb: 17.0 Å	0.21	3600 Å
1C	Annealed, crystalline	Fe: 1.1 Å Sb: 17.0 Å	0.21	3600 Å
2A	As-deposited, amorphous	Fe: 1.0 Å Sb: 12.0 Å	0.33	3600 Å
2C	Annealed, crystalline	Fe: 1.0 Å Sb: 12.0 Å	0.33	3600 Å

3.2.2.2. *tfPDF measurements*

Figure 3.7. shows the setup used for normal incidence thin film PDF measurements. The films are mounted perpendicular to the beam in a simple sample holder for flat plate samples, using Kapton tape to hold the film and substrate in place. The holder was mounted and centered in the goniometer so that the beam passes through the substrate before hitting the thin film.

Data collection was carried out at the XPD beamline (ID28) at the NSLS-II synchrotron, Brookhaven National Laboratory, USA, with a photon wavelength of 0.235 Å and a Perkin Elmer amorphous silicon detector, measuring 40 by 40 cm² i.e. in a setup similar to the usual RA-PDF geometry, making the experiments especially straightforward.³⁶ In addition to the thin films, the scattering pattern from a clean substrate of the same materials was measured, allowing background subtraction to be done. This approach has not been possible before because of the very low signal-background ratio in the signal. However,

through the use of the high-fluxes of hard x-rays available at modern synchrotrons, and of the latest data reduction methods that allow very dilute signals to be successfully separated from large host signals,⁶³ we show that this approach is now possible.

Calibration of detector distance, beam center etc. was carried out using a standard CeO_2 sample on Kapton tape, mounted in the sample holder. Data collection took 15 minutes for each sample, and was made with careful correction for the dark current signal. Total scattering data were also measured for reference samples of powders of amorphous and crystalline FeSb_3 packed in a Kapton capillary as described in the supplementary information.

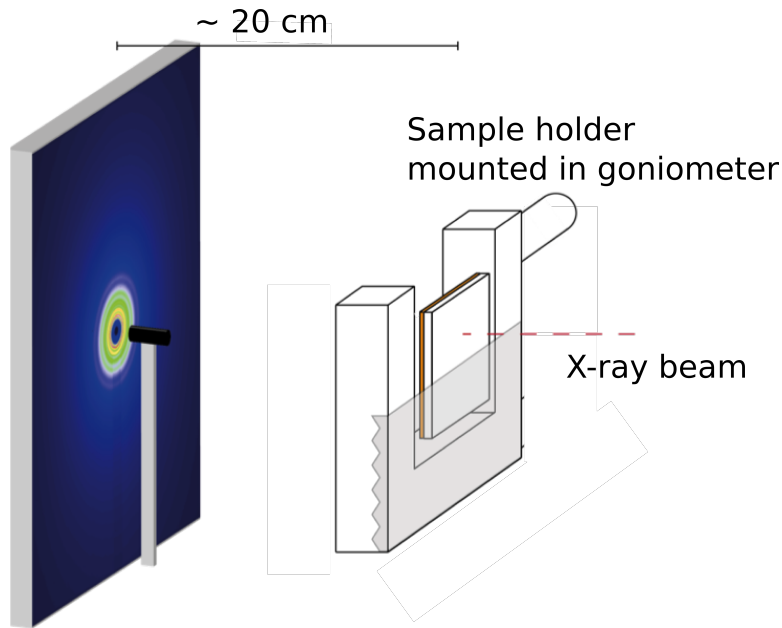


Figure 3.7. Setup used for tfPDF measurements. The x-ray beam hit the substrate before the film.

3.2.2.3. Data analysis

The PDFs were obtained from the 2D data using *SrXgui*⁶⁴ and *PDFgetX*³⁸ in *xPDFsuite*⁶⁵ as described below, with $Q_{min}=0.8 \text{ \AA}^{-1}$, $Q_{max}=17.5 \text{ \AA}^{-1}$, $Q_{max-instrument}$

$= 17.5 \text{ \AA}^{-1}$ and $r_{poly} = 0.9 \text{ \AA}$. Modeling of the PDFs was done using *PDFgui*,³⁹ where the FeSb_3 structure was refined in space group $Im-3$,²⁴ FeSb_2 in space group $Pnnm$ and Sb in space group $H-3m$. For each phase, a scale factor was refined along with unit cell parameters and symmetry allowed atomic positions. Isotropic Debye-Waller factors were also refined for Fe and Sb in each phase and correlated motion was taken into account by including the *delta2* parameter in the model. The coherence lengths of the crystalline phases were modeled by applying a spherical envelope to the model after taking instrumental dampening into account by modeling of a bulk Ni standard.

3.2.3. Results and discussion

3.2.3.1. Obtaining the *tfPDF*: Amorphous and crystalline FeSb_3 films

We firstly illustrate that reliable PDFs can be obtained from thin films on amorphous substrates, using the data obtained for sample 1A (amorphous) and sample 1C (crystalline) as an example. Figure 3.8.A. (black line) shows the total x-ray scattering pattern from sample 1C, i.e. a 360 nm thin crystalline FeSb_x film. The thickness of the borosilicate substrate was 170 μm and thus, at normal incidence, the irradiated FeSb_x film only corresponds to *ca.* 0.21% by volume of the total sample in the x-ray beam. Accordingly, the scattering pattern shows only a very weak signal from the crystalline film while the majority of the scattered intensity is from amorphous borosilicate. In order to isolate the contribution from the FeSb_x film, the substrate contribution was determined by measuring the scattering pattern from a clean substrate, shown by the red line in Figure 3.8.A. The Bragg peaks from the film are barely visible on top of the large substrate contribution, but become clearer after subtracting the background signal as shown in the difference between the two signals, plotted as the green curve in Figure 3.8.A. As shown on the expanded scale in Figure 3.8.B., sharp Bragg peaks from FeSb_3 are visible in the difference curve to Q -values at *ca.* 10 \AA^{-1} .

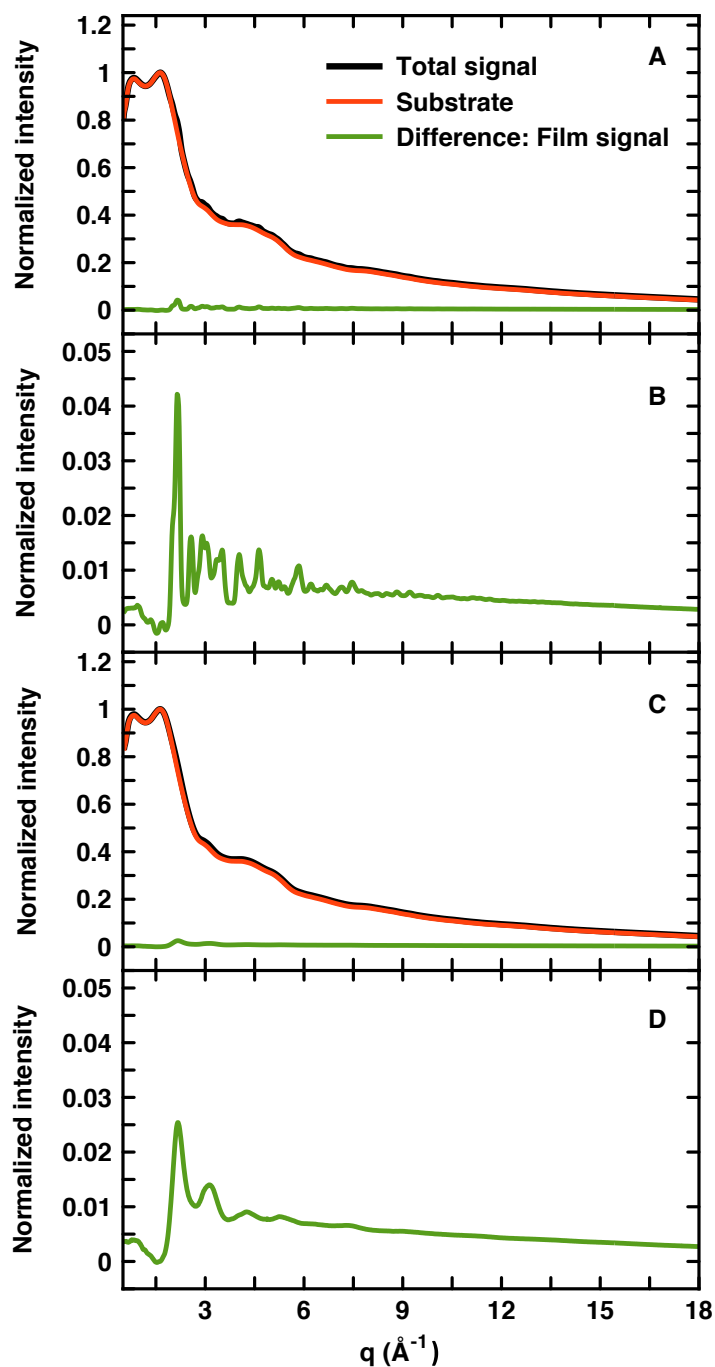


Figure 3.8. A) Normalized data collected for sample 1C (black) and a clean substrate (red). The difference curve is shown in green and is plotted on an expanded scale in B. C) Normalized data collected for sample 1A (black) and the clean substrate (red), and difference between the two (green), also shown on an expanded scale in D.

The scattering pattern from the amorphous precursor to the crystalline film is plotted in Figure 3.8.C-D., again showing the total signal including the background contribution (C), as well as the weak signal from the amorphous FeSb₃ precursor (D). Here, only diffuse scattering features from the amorphous film are present, but despite this, careful background subtraction was still sufficient to isolate the broad peaks from the Fe/Sb signal.

PDFs from the total scattering data were obtained using *PDFgetX3* in *xPDFsuite*.⁶⁵ The program uses an *ad hoc* data reduction algorithm, making fast, reliable data processing possible as individual corrections for e.g. Compton scattering and fluorescence are not needed. Instead, corrections for all long wavelength effects in the total scattering signal are accounted for by polynomial fitting as described in detail in Juhas *et al.*³⁸ This approach to data analysis makes *PDFgetX3* very well suited for data where background scattering constitutes the majority of the total signal as was previously shown for nanoparticles in very dilute systems.⁶³ Apart from correcting for the physical effects as mentioned above, the polynomial fitting applied in *PDFgetX3* can eliminate small differences between the measured background (in this case the clean substrate) and the background contribution in the sample pattern, if they are sufficiently low frequency oscillations. For standard PDF samples, these effects are on a much smaller scale than the actual signal in question and do not pose any problems in the resulting PDF. However, for small signals, such as from thin films on thick substrates, deviations such as these can be on the same scale or larger than the signal from the sample and dominate the signal after taking the difference. The *PDFgetX3* algorithm proves to be a powerful method to make these corrections that are crucial to obtain a reliable PDF from the film.

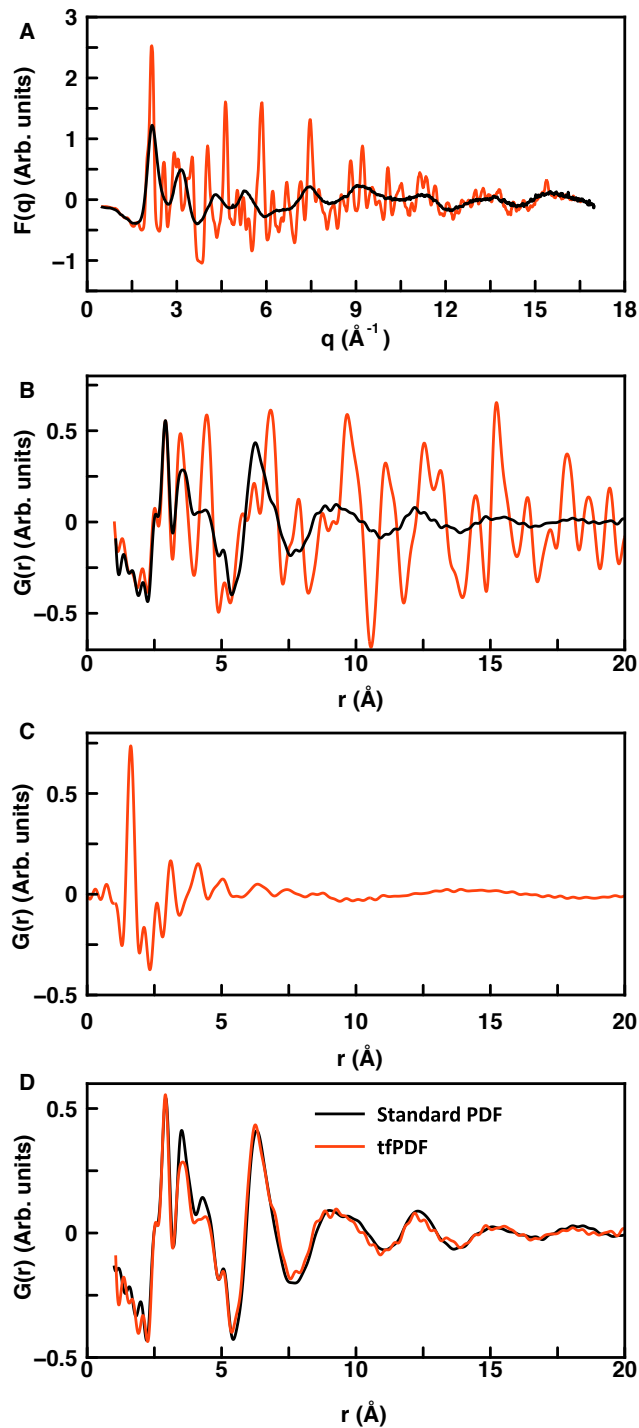


Figure 3.9. A) Reduced total scattering function $F(Q)$ for sample 1A (black) and 1C (red). B) Reduced pair distribution function $G(r)$ for 1A (black) and 1C (red). C) $G(r)$ obtained for clean substrate. D) Comparison between the tfPDF for sample 1A and similar sample, where the data were obtained for a sample measured in a standard capillary.

The corrected, reduced total scattering functions $F(Q) = Q(S(Q) - 1)$ are shown in Figure 3.9.A., for the crystalline and amorphous FeSb₃ thin films. The substrate contribution was subtracted in Q -space and the $F(Q)$ thus represents the signal just from the film. Clear signals with a very low noise level even at relatively high Q -values are seen for both the crystalline and amorphous samples. The good data quality leads to high quality PDFs for both the amorphous and crystalline films as shown in Figure 3.9.B., which were obtained by Fourier transforming the Q -range from 0.8-17.5 Å⁻¹. The PDF arising from a clean substrate is seen in Figure 3.9.C. Here, a very intense peak is observed at *ca.* 1.7 Å, corresponding to the Si-O bond distance in the borosilicate glass. Inadequate background subtraction would lead to a peak at this position in the final PDF (or a negative peak when over-subtracting), but no clear features are seen. Minor ripples are observed which may arise from small difference between the substrates, but these are easily distinguished from the film signal.

Figure 3.9. compares the tfPDF for the amorphous FeSb₃ samples obtained from a similar sample, measured in a standard PDF setup as described in the supplementary information. Clearly, the tfPDF reproduces the features from the high quality capillary PDFs, showing that reliable PDFs are being obtained even from the 360 nm thick thin-films. The tfPDF has a higher noise level than that from the capillary data, but the structural features can easily be distinguished. Minor differences between peak intensities are observed in the 3-5 Å range, but this may be real, due to differences in Fe/Sb composition.

3.2.3.2. Structures in the FeSb_x system: Sample 1

After having established the reliability of the tfPDFs by comparison with the PDF from a capillary setup, structural information can be extracted from the data. Firstly, we analyze the tfPDFs obtained from sample 1C, i.e. the annealed film discussed above. Figure 3.10.A. shows a fit of the FeSb₃ phase to the PDF from the crystalline film. The fit gives a R_w value of 32%, showing large discrepancies between the model and data. By including crystalline Sb into the model, the R_w value is reduced to 22%, and as can be seen in Figure 3.10.B., the model now agrees well with the experimental PDF in the high r -range. The

refined parameters are given in Table 3.4. and the unit cell parameters and atomic positions are within the uncertainties for the expected values for Sb and FeSb₃. The fit shows that the crystalline fraction of the sample contains 73% FeSb₃ and 27% of elemental antimony. However, Figure 3.10.B. also illustrates differences between the experimental and calculated PDF in the low r region. Especially, the high intensity of the peak at 2.9 Å is not fitted well, and smaller disagreements are also seen up to ca. 7 Å. Considering the structure of the Sb, the peak at 2.9 Å corresponds to the shortest Sb-Sb distance as illustrated in the supplementary information. The PDF thus indicates that apart from crystalline FeSb₃ and Sb included in the model, a fraction of amorphous Sb with only short-range order is also present in the sample. This agrees well with the elemental composition: In the total sample, the Fe/Sb ratio is 0.21 whereas in the model including only the crystalline phases, this ratio is ca. 0.30.

The range of structural coherence of both the crystalline Sb component and the FeSb₃ phases are 7-8 nm i.e. well beyond the separation of the initial amorphous Fe/Sb layers, which alternated at ca. 20 Å. While Williams *et al.* describe that the layered structure is preserved in the amorphous phase; the layering is thus largely removed after annealing despite the remaining amorphous Sb component.

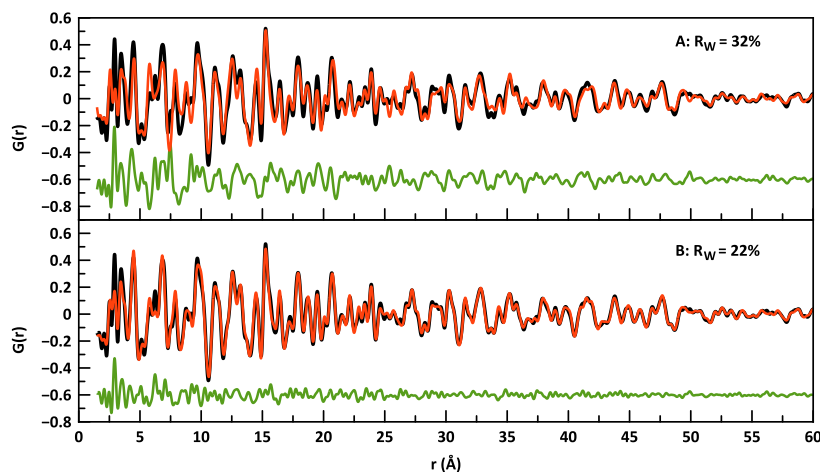


Figure 3.10. Fits (red) to the experimental PDF from sample 1C (black). The green line shows the difference curve. A) Only FeSb₃ included in the model. B) FeSb₃ and crystalline Sb included in the model.

Table 3.4. Refined parameters for the crystalline

R_w	23.7%
Weight percent, FeSb_3	73%
a , FeSb_3	9.185 Å
Crystallite size, FeSb_3	7.7 nm
y_{Sb} , FeSb_3	0.337
z_{Sb} , FeSb_3	0.159
$U_{\text{iso, Fe}}$, FeSb_3	0.0174 Å ²
$U_{\text{iso, Sb}}$, FeSb_3	0.0171 Å ²
Weight percent, crystalline Sb	27%
a , Sb	4.299 Å
c , Sb	11.291 Å
Crystallite size, Sb	6.7 nm
z , Sb	0.767
$U_{\text{iso, Sb}}$, Sb	0.0098 Å ²
$\text{delta}2^*$	4.08 Å

*The *delta2* parameters for the two phases, expressing correlated motion, were constrained to the same value.

Having analyzed the structure of the crystalline 1C film, we can now use the structure models to gain a better understanding of the atomic arrangement in the as-deposited precursor film, i.e. 1A. Figure 3.11.A. shows a comparison between the low r regions of the tfPDFs from both films. Interestingly, the local structure of the amorphous film is closely related to the crystalline structure as the first 4 main peaks overlap. By considering the atomic pairs leading to the peaks in the crystalline structure, we can identify the local structural motifs in the amorphous film. As seen in Figure 3.6.A., the FeSb_3 structure consists of

corner sharing FeSb_6 octahedra, making up the full skutterudite lattice. A cut-out of the FeSb_3 unit cell is shown in Figure 3.11.B. with selected interatomic distances marked and listed in the supplementary information. The nearest neighbor Fe-Sb distance in FeSb_3 is *ca.* 2.6 Å, (marked in magenta in Figure 3.11.B.) which is seen as a clear peak in the PDFs from both the crystalline and amorphous phases. After deposition of the individual Fe/Sb layers, the metals thus immediately diffuse at room temperature to form an alloyed, amorphous structure between the Fe/Sb layers rather than staying as separate phases. The nearest Sb-Sb distances in the FeSb_3 structure, arising from the edge length in the FeSb_6 octahedra make up the broad peak centered at 3.5 Å, marked in orange in Figure 3.11.B. Again, this peak can clearly be found in the PDF from the amorphous sample, largely overlapping with that from the crystalline PDF. The longest Sb-Sb distance in the FeSb_6 octahedra is at 5.1 Å (marked in green), where a small peak can also be identified, thus illustrating how all intra-octahedral distances can be found in the PDF from the as-deposited sample.

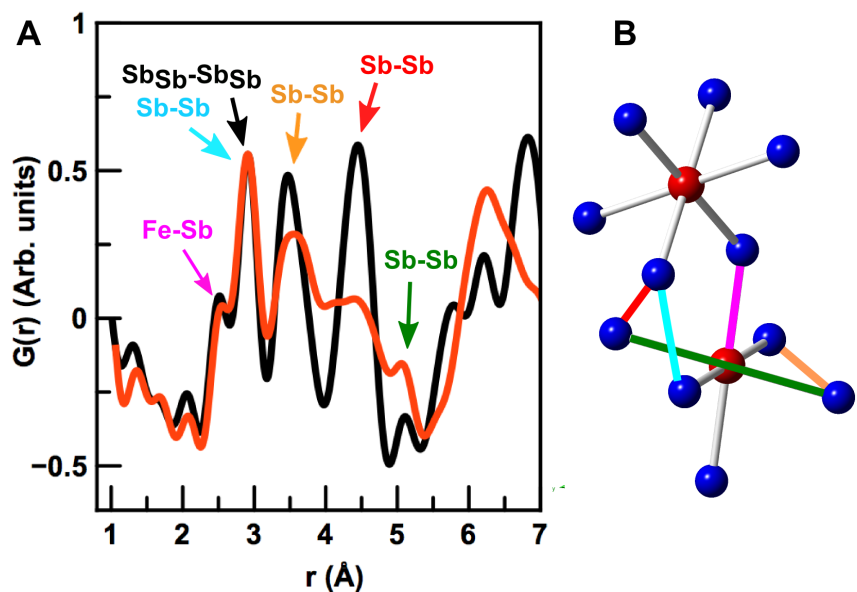


Figure 3.11. A) Comparison between the PDF obtained from sample 1A (red) and sample 1C (black). Pairs contributing to the low r region are indicated with errors, and color coded with the bond illustrated in B) showing a cut-out from the FeSb_3 unit cell, with corner-sharing FeSb_6 octahedra. Iron is shown in red and antimony in blue.

The intense PDF peak at 2.9 Å originates from the shortest Sb-Sb distances in the elemental Sb phase as described above. This peak is clearly present in the amorphous phase, so apart from the interdiffused Fe-Sb structures, the amorphous phase appears to also contain a fraction of amorphous Sb not atomically coordinated to Fe. In crystalline Sb, the 2nd nearest neighbor Sb-Sb distance is at 3.34 Å, and from the theoretical PDF from Sb metal, this peak should have ca. 80% of the intensity of the peak at 2.9 Å. However, this peak is not clear in the PDF from sample 1A, indicating that the local structure of the amorphous Sb fraction in the as-deposited sample does not resemble that of crystalline Sb, where the atoms are arranged in layers of 6-membered rings.

As indicated in Figure 3.11.A., the PDF peak at 4.3 Å in crystalline FeSb₃ arises from a number of inter-octahedral correlations, one shown in red in Figure 3.11.B. A broad peak in the same region is seen in the PDF from the amorphous phase. In crystalline FeSb₃, an inter-octahedral Sb—Sb distance marked in cyan in Figure 3.11. furthermore gives rise to a weak peak at ca. 2.9 Å. However, compared with the Sb—Sb distance in crystalline Sb metal, this is only a minor contribution to the total PDF of the crystalline sample, and we cannot distinguish this from the elemental Sb—Sb peak in sample 1A.

The observation of the existence of FeSb₆ octahedra as well as amorphous Sb points to a structure where amorphous Sb structures with only short-range order coexist with disordered, corner-sharing FeSb₆ octahedra. The local structure of the amorphous precursor before thermal annealing thus highly resembles that of the metastable FeSb₃ phase, explaining the possibility to synthesize it from the layered precursors.

3.2.3.3. Structures in the FeSb_x system: Sample 2

Sample 2 was prepared with slightly lower antimony content than sample 1. Figure 3.12. compares the PDFs from sample 1A and 2A, i.e. the two amorphous samples. While some of the peaks discussed above are also evident in the 2A PDF, we also observe clear differences in the local structure. The first peak

at 2.6 Å again corresponds to the Fe-Sb distance in FeSb₆ polyhedra and peaks from the Sb-Sb distances in the octahedra (at *ca.* 3.5 Å and 5.1 Å, see Figure 3.11.) are also seen. Furthermore, a contribution at 2.9 Å is also present, corresponding to the first Sb-Sb distance in metallic Sb as discussed above. However, compared to 1A, this peak is much less dominant, indicating a smaller contribution of Sb not coordinated to Fe. This agrees with the measured compositions, where the Fe/Sb is 0.33. We also see a difference in the width and position of the peak at *ca.* 4.6 Å, which we above ascribed to correlations between the individual octahedra.

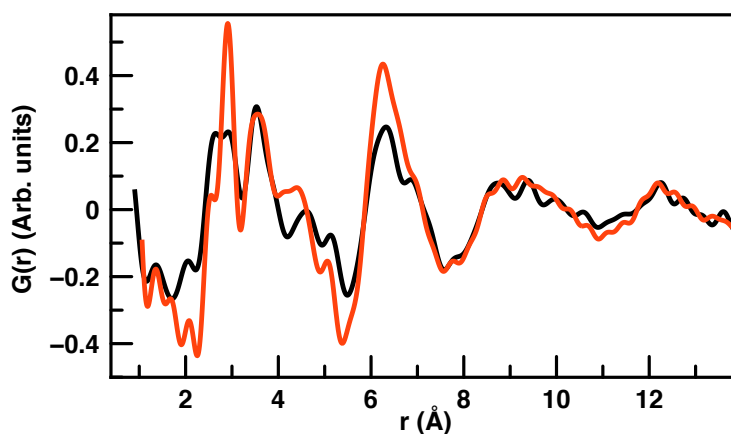


Figure 3.12. Comparison between the PDFs from sample 1A (red) and 2A (black).

The appearance of the PDF from sample 2P indicates that the corresponding annealed sample 2C will contain a smaller Sb content than sample 1C. This is confirmed when modeling the PDF, as a two-phase fit with FeSb₃ and Sb results in phase fractions of 99% and 1%, respectively, thus effectively suppressing the Sb phase completely. However, interestingly, the fit of the FeSb₃ phase is still of poor quality, giving $R_w=35\%$ and large deviations as seen in Figure 3.13. When introducing the thermodynamic phase in the phase diagram, FeSb₂, the fit improves considerably (Figure 3.13. giving R_w of 25%. The refined parameters for this fit are given in Table 3.5. The refined phase fractions are 80% FeSb₃ and 20% FeSb₂, with the coherence length in the FeSb₂ phase

being *ca.* 7 nm. The coherence length of the FeSb₃ phase refines to *ca.* 50 nm, which is well above the reliable limit for size determination but indicates that this component forms very large crystallites. The lower Sb content in the precursor thus has two effects: Suppression of crystalline Sb while forming a phase mixture between the thermodynamic FeSb₃ phase and the metastable FeSb₂ as well as allowing the FeSb₃ to grow into a bulk phase.

Table 3.5. Refined parameters for modeling of sample 2C.

R _W	23.8%
Phase fraction, FeSb ₃	73.2%
Phase fraction, FeSb ₂	26.8%
<i>a</i> , FeSb ₃	9.219 Å
Particle diameter, FeSb ₃	47 nm
y _{Sb} , FeSb ₃	0.334
z _{Sb} , FeSb ₃	0.158
U _{iso, Fe} , FeSb ₃	0.0073 Å ²
U _{iso, Sb} , FeSb ₃	0.0100 Å ²
<i>a</i> , FeSb ₂	5.836 Å
<i>b</i> , FeSb ₂	6.572 Å
<i>c</i> , FeSb ₂	3.221 Å
Particle diameter, FeSb ₂	7.8 nm
x _{Sb} , FeSb ₃	0.187
y _{Sb} , FeSb ₃	0.357
z _{Sb} , FeSb ₃	0.030
u _{iso, Fe} , FeSb ₃	0.0086 Å ²
u _{iso, Sb} , FeSb ₃	0.0046 Å ²

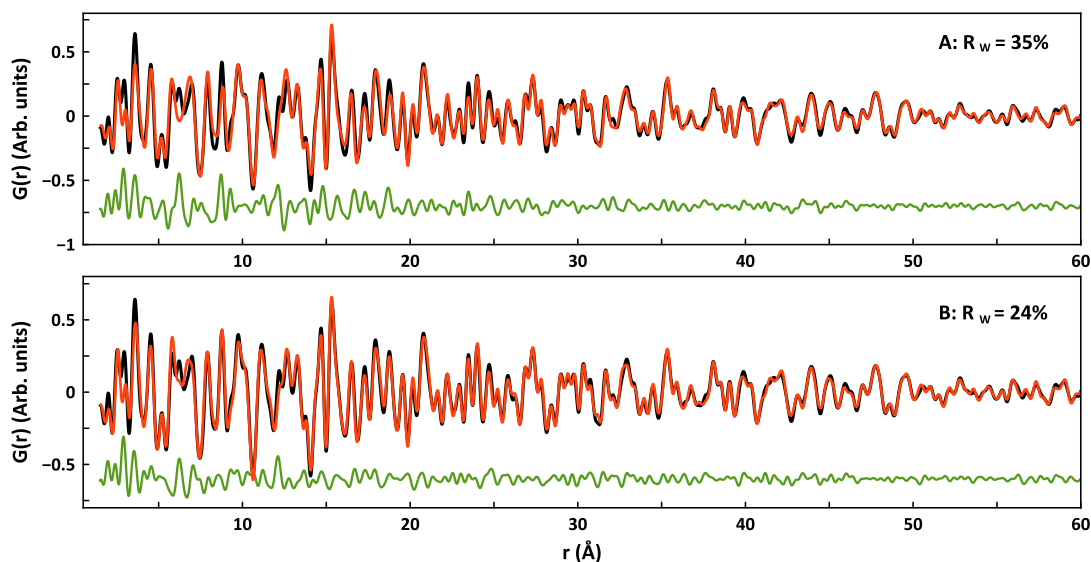


Figure 3.13. A) Fit of FeSb_3 and Sb to the PDF from sample 2C. B) Fit of FeSb_3 and FeSb_2 to the PDF from sample 2C. The experimental PDF is shown in black, the fit in red and the difference in green.

3.2.4. Conclusion

PDFs have been obtained from supported thin film samples, using normal incidence x-ray diffraction measurements in a standard RA-PDF setup. The use of high flux, high energy x-rays and careful background subtraction make it possible to get a clear scattering signal from amorphous, nanocrystalline and polycrystalline films down to a thickness of at least a few hundred nanometers, which by use of *xPDFsuite* and *PDFgetX3* can be Fourier transformed into PDFs of very high quality.²⁸

All films studied were deposited on amorphous substrates, as this allows for simple subtraction of the substrate scattering signal without the need to mask intense, orientation dependent scattering signals from single crystal substrates, e.g. silicon wafers. No angular dependent corrections are needed, as would be the case for grazing incidence measurements. By use of *PDFgetX3*, where *ad hoc* corrections for fluorescence, Compton scattering and any other non-structural effects are done, PDFs can be obtained quickly in a robust manner. The thin films that have been studied here are all *ca.* 360 nm thick, but

PDFs from even thinner films may also be obtained, as long as careful background subtraction is done.

The characterization of thin films has so far been limited by the need for grazing incidence techniques, which is still to be reported for PDF analysis. In some cases, the film can be isolated from the substrate and standard characterization techniques can be used, but most often, this is not possible due to the small mass of sample present as film. tfPDF thus opens the way for many new possibilities in materials characterization for thin films. As shown in the case of the FeSb_x samples, tfPDF can be used to understand the relation between the local structure in amorphous films and the final crystalline product, which will help chemists in controlled synthesis of new, advanced materials, in thin film form. We now plan to use tfPDF for *in situ* studies, where a much deeper understanding of processes like this (diffusion, nucleation, crystallization) can be understood. While the time resolution is limited by longer counting times required for the small amount of sample present in the beam, the new, high flux beamlines at 3rd generation synchrotrons suitable for PDF analysis will allow these studies to be feasible.

3.3. Bridge

Chapter III explores formation mechanisms of metastable materials from amorphous precursors and presents tfPDF, a new analytical technique for the investigation of local structure in intact thin films without removal from the substrate. These experiments were carried out in the FeSb_x chemical system, which is highly chemically relevant as both low and medium temperature thermoelectric materials. The remaining chapters move on to discuss composite thermoelectric materials formed from similar precursors as presented in chapter III, but where the diffusion-controlled synthesis allows for precisely layered nanocomposite structures to be formed.

CHAPTER IV

PHASE WIDTH OF KINETICALLY STABLE $([\text{PbSe}]_{1+\delta})_1(\text{TiSe}_2)_1$ FERECRYSTALS AND THE EFFECT OF PRECURSOR COMPOSITION ON ELECTRICAL PROPERTIES

The work in this chapter was accepted on 2015-04-30 for publication in *Journal of Alloys and Compounds* (DOI: 10.1016/j.jallcom.2015.04.228) and is coauthored with Daniel Moore, Jeffrey Ditto, and David Johnson. Daniel Moore assisted with sample preparation and structural, compositional, and electrical characterization. Jeffrey Ditto assisted with collection of scanning tunneling electron microscopy data. David Johnson is my advisor and I am the primary author.

4.1. Introduction

The high temperatures and long times used in most solid state reactions lead to equilibrium products and an equilibrium distribution of impurity atoms.^{1,2} This leads to the common practice of reporting the properties of a new compound based on the measurement of a single sample, ideally a single crystal that has been structurally characterized. For metallic compounds with a narrow phase width, subsequent reports usually agree with the initial report, as metallic properties are usually not significantly affected by small changes in the concentration of defects or impurities except for at low temperatures.³ For semiconducting compounds properties often vary significantly between preparations, especially preparations from different groups and even when using near equilibrium synthesis conditions, as small differences in impurity levels and/or defects can significantly vary carrier concentration.³ An especially large variation in properties is observed when there is a range of compositions within which compounds are stable.⁴ As the number of elements within a compound is increased or the structure becomes more complicated, obtaining agreement on properties becomes even more difficult due to the varying distributions of the elements within the ideal composition, impurity atoms, and defects of different crystallographic sites.

The challenges in determining the base properties of ternary intergrowth compounds is especially difficult. An example of this is ternary misfit layer

compounds of the form $([MX]_{1+\delta})(TX_2)_n$, which consist of an intergrowth of a rock salt structure, MX, where M = Sn, Pb, Bi, or RE, and a transition metal dichalcogenide, TX_2 where T = Ti, V, Cr, Nb, or Ta.⁵ The chalcogen, X, is either S or Se. The misfit parameter, δ , represents the difference in area per cation of the two different structures, which is required to accurately describe these compounds since the individual MX and TX_2 layers will not necessarily have the same area per formula unit in the plane perpendicular to the stacking direction of the intergrowth. The integer n ($n = 1, 2$) may be included to express compounds with multiple TX_2 layers per MX. Electrical properties for nominally the same compound vary considerably from group to group, even for metallic samples. For example, the resistivity of single crystals of $([PbS]_{1.18})(TiS_2)$ as reported from different groups^{6,7} differs by a factor of 5 and the resistivity of $([SmS]_{1.18})(TaS_2)$ as reported from different groups^{8,9} varies by a factor of 7. The differences in properties of these misfit layer compound crystals is thought to be a consequence of different growth conditions used during vapor transport leading to different amounts of incorporated iodine, other impurities, and/or defects, as has been widely reported for binary constituents.^{5,10,11} Recently a new synthesis approach was shown capable of preparing intergrowth compounds $([MX]_{1+\delta})_m(TX_2)_n$, where m and n , which respectively denote the integer number of rock salt bilayers and dichalcogenide trilayers, can be systematically controlled by design of a precursor.¹² The structures are different from misfit layer compounds in that there is rotational (turbostratic) disorder between basal planes of the constituents and hence no systematic cooperative structural distortion of the layers. The synthesis route to these compounds is kinetically controlled and the kinetics of the formation reaction should determine the concentration and distribution of defects and impurity atoms.

It is important to understand the reproducibility of the kinetically controlled synthesis of these turbostratically disordered misfit layer compounds, or ferecrystals, before considering the difference between compounds with different stacking sequences, because small deviations in the product could potentially cause the properties to vary more within different preparations of the same compound relative to compounds with different m and n values. Here we investigate two sets of $([PbSe]_{1+\delta})_1(TiSe_2)_1$ samples prepared

from a range of different starting precursors and deposited over several months. Although a large variation of precursor composition was used, we find that they crystallize to nominally the same product, with a small range of *c*-axis lattice parameters (defined to be along the stacking direction of the intergrowth). It is difficult to determine the precise composition of the majority compound as different trace amounts of secondary phases may form, and so the $1+\delta$ nomenclature is used to discuss compounds synthesized as part of the current contribution. We find that electrical behavior in the form of resistivity values, Seebeck coefficients, and carrier densities vary from sample to sample and cluster into discreet regions within deposition cycles. The changes in electrical properties correlate with changes in overall composition. There is a narrower distribution in both the composition and the transport properties of compounds formed from precursors deposited in the same equipment cycle. To minimize contribution from repeatability limitations, the most meaningful comparisons of trends in ferecrystal properties as *m* or *n* are varied can be made with precursors from the same deposition cycle.

4.2. Materials and methods

Thin films of the amorphous precursor were deposited on silicon and quartz substrates using a custom built physical vapor deposition system.¹³ Selenium was deposited using a Knudsen effusion cell, whereas lead and titanium were deposited using electron beam guns. The thickness of each elemental layer was monitored using quartz crystal microbalances. Background pressure inside the chamber during film deposition was maintained between 5×10^{-8} and 5×10^{-7} torr for all reported samples. The first set of depositions produced thin films that were approximately 50 nm thick, which consisted of repetitions of the layer sequence Ti-Se-Pb-Se. A second set of samples, prepared much later than the first set, was made with a total thickness of 35 nm. The precursors were calibrated to contain an excess of 2% Se, as this has previously been shown to produce samples with more intense diffraction patterns.¹² The thickness of each layer in the repeating sequence was calibrated via a method described previously such that each layer self assembles into a

$(\text{PbSe})_{1+\delta}(\text{TiSe}_2)_1$ unit cell upon annealing.¹⁴ Samples were annealed on a hot plate at 350 °C in a nitrogen atmosphere. Electron-probe microanalysis (EPMA) was used to determine the composition of the thin film samples.¹⁵ Specular X-ray diffraction data were collected using a Bruker D8 Discover diffractometer with Cu-K α radiation.

Cross-section specimens for high angle annular dark field scanning transmission electron microscopy (HAADF-STEM) investigations were prepared with in-situ lift-out and gallium focused ion beam (FIB) milling methods on an FEI Helios 600 Nanolab. All specimens were thinned to 300nm using wedge premilling methods¹⁶ with a 30kV accelerating voltage. The subsequent thinning process was done at 5kV until 100 nm thick, followed by thinning 2kV to 40 nm thick, with final thinning at 1kV to a final thickness of 20 nm. HAADF-STEM was carried out on an FEI Titan 80-300 using a 50um condenser aperture, 300kV accelerating voltage, 0.050 nA of current, and a 240 mm camera length.

Thin film specimens for electrical transport properties were deposited on insulating fused silica substrates in order to minimize the influence of the substrate. Films were deposited through a shadow mask in a cross geometry, as well as a rectangle. Four-probe electrical resistivity (ρ) was measured from 20 K to 300 K in a custom closed-cycle He cryo-system using the van der Pauw technique on the cross.¹⁷ Electrical leads were attached using pressed Indium contacts. The Seebeck coefficient was measured on the rectangular portion. One half of the sample was cooled slightly below room temperature ($\Delta T < 2\text{K}$) and voltages were measured through thermocouples at each side as the temperature equilibrates. The Seebeck coefficient is determined from the slope of applied measured voltage difference as a function of temperature difference, corrected for the Seebeck coefficients of the copper-constantan thermocouple leads. All reported electrical data correspond to the in-plane direction.

4.3. Results and discussion

4.3.1. Structural characterization

Sample precursors were prepared in two deposition cycles to synthesize a precursor which yields a sample after annealing that is crystallographically and compositionally in agreement with the previously reported turbostratically disordered $([\text{PbSe}]_{1.16})_1(\text{TiSe}_2)_1$.¹⁴ Once a parameter-space close to optimal was found, the depositions were fine-tuned by varying the elemental layer thicknesses of the precursor, which also changes the compositions of the precursors. The full width at half maximum of the (002) Bragg reflection was used between depositions as a fast indicator of 1:1 sample quality. Data collected on the samples prepared for this study that formed the 1:1 compound, as well as the previously reported sample, are summarized in Table 4.1.

Low angle specular diffraction patterns are shown in Figure 4.1 and indicate little variation is present within deposition cycles. The small variation of critical angle from 0.62 to 0.67 degrees in 2-theta shows little change in density and no correlation was able to be drawn between small shifts in critical angle and composition. Fitting of the high-frequency Kiessig oscillations to the Bragg equation modified for refractive contributions results in film thicknesses within 2.5 nm of the targeted values of 50 nm for set A and 35 nm for set B. The angle at which the Kiessig fringes can no longer be resolved is an indicator of the roughness of the films. The increased smoothness seen in the second set of samples is due to diffraction data being collected from samples on a Si substrate as opposed to fused quartz. The changes in rate of decay of the Kiessig fringes between samples is most-likely due to a variance in different substrate's native oxide thicknesses. The first Bragg Peak is seen in all low-angle scans. The peak centers of gravity vary little from 7.27 degrees, corresponding to a d-spacing of 1.215 nm; and the (001) reflection of the 1:1 ferecrystal.

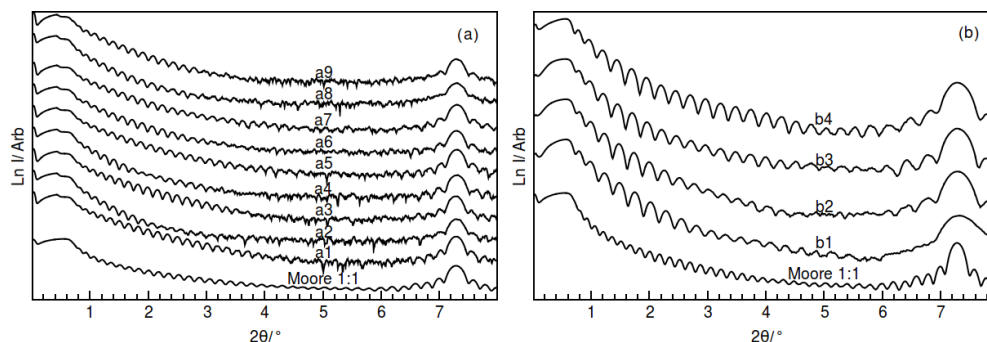


Figure 4.1. Low-angle diffraction patterns collected from samples. Data from the previously reported 1:1 compound¹⁴ (labelled Moore 1:1) is shown as the bottom curve in each pane. (a) Set A. The first loss of intensity near the critical angle is a substrate artifact. The critical angle is taken from the second loss. (b) Set B. The apparent amplitude difference is due to the stacking. The range of normalized data is comparable for all samples.

High angle coupled θ - 2θ diffraction patterns collected normal to the film surface (Figure 4.2.) also show little variation between samples or deposition cycles. The c -lattice parameters of all samples are within 0.001 nm; of the average value and within 0.25% of the previously reported value for the $([\text{PbSe}]_{1.16})_1(\text{TiSe}_2)_1$ ferecrystal. This small change in c -lattice parameter correlates weakly with composition changes, trending with the measured metal (Pb, Ti) to Se ratio. The increased FWHM of the samples from the second deposition cycle is due to fewer layers in the $(00l)$ direction in which the crystallite size is limited by the thickness of the film. The lack of any $(hk)l$ reflections with $h, k \neq 0$ in a coupled out-of-plane geometry is characteristic of ferecrystal samples due to the crystallographic alignment of the samples with the substrate. The similarity of the diffraction patterns suggests a similar average structure for all of the samples. There is some variation in the relative intensities of peaks throughout both sets of samples, with the largest variations occurring on odd $(00l)$ peaks in Pb-rich samples shrinking about 50% from the average relative intensity. These changes in relative intensity suggest a variation in the occupancy of specific locations reflecting the different compositions of the precursors.

Table 4.1. Summary of all samples as well as data from the previously reported 1:1 compound¹⁴ (labelled Moore 1:1). Samples from the first deposition cycle, set A, were deposited in order from a1 to a9. Samples from the second deposition cycle, set B, were deposited in order from b1 to b4.

Sample	c-lattice parameter (nm)	295K resistivity (m Ω -cm)	Carrier density (10 ²¹ cm ⁻³)	Composition		
				Pb/Ti	Pb/Se	Ti/Se
a1	1.2181	0.93	2.12	0.95	0.36	0.38
a2	1.2173	1.32	1.76	1.05	0.39	0.37
a3	1.2181	0.83	2.04	0.88	0.33	0.38
a4	1.2167	1.41	1.72	1.10	0.38	0.35
a5	1.2169	1.21	1.71	0.99	0.37	0.37
a6	1.2181	1.45	1.72	1.07	0.38	0.36
a7	1.2170	1.18	1.82	0.96	0.36	0.37
a8	1.2176	1.78	1.86	0.95	0.37	0.38
a9	1.2173	1.14	2.1	0.98	0.36	0.36
b1	1.2188	1.97	1.44	0.92	0.40	0.44
b2	1.2193	3.3	1.07	1.16	0.46	0.40
b3	1.2199	3.01	1.16	1.08	0.43	0.40
b4	1.2194	2.15	1.29	0.91	0.40	0.43
Moore 1:1	1.2174	3.00	2.10	1.16	0.37	0.32

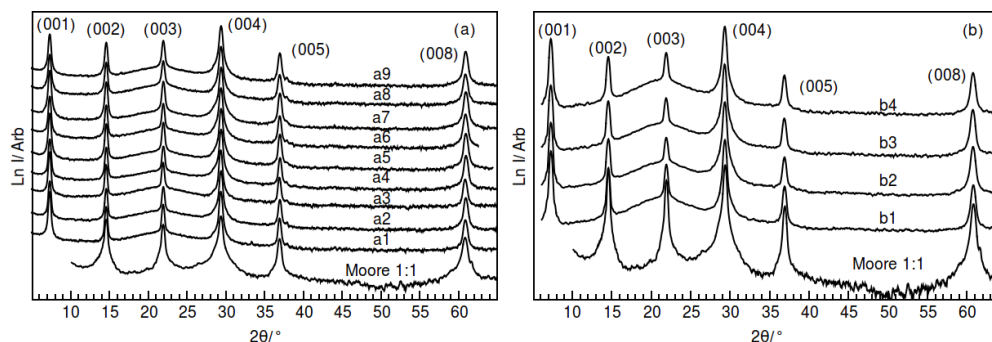


Figure 4.2. High angle specular diffraction patterns collected from samples in (a) set A and (b) set B. Data from the previously reported 1:1 compound¹⁴ (labelled Moore 1:1) is shown for comparison as the bottom curve in each pane. The apparent difference in scales is due to a reduced range in the pane with fewer curves.

4.3.2. Electrical characterization

Electrical measurements are more sensitive to impurity phases or local crystalline defects than X-ray measurements. Prior literature suggests charge transport occurs mainly in the conduction band of the transition metal dichalcogenide constituent.¹⁴ We expect changes in impurity and defect concentration would alter the carrier density of the semimetallic TiSe₂. Table 4.1. contains the room temperature resistivity of the samples. The composition and resistivity data from both sets of samples cluster in nearby but discrete regions of parameter space, distinct also from the previously published compound. The variation of the extrema from the average value is 40% within sample set A and 30% within sample set B. There is a factor of 2 difference between the averages of the resistivity values of the two data sets, with the extrema from the entire experiment spanning a 400% change. The resistivity values were found to trend with the Pb/Se ratio, as shown in Figure 4.3. The variation in room temperature resistivity (400%), however, is smaller than that reported for different single crystals of misfit layer compounds (500-700%). This is somewhat surprising, as the misfit layer compound crystals were grown under nearly equilibrium conditions while the self-assembly of our precursors is a kinetic process. This suggests that in the self-assembly, the excess material is incorporated as inclusions rather than being dispersed as local defects

throughout the film. The larger variation between depositions also suggests that it would be better to make samples with different m and n in the same set to correlate nanoarchitecture with properties.

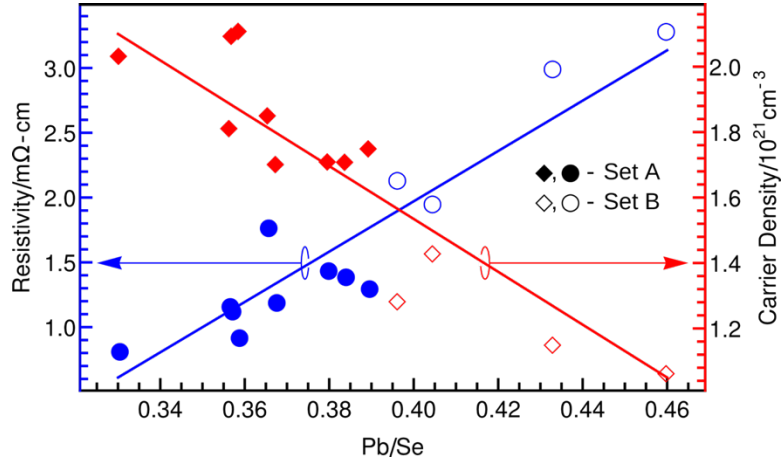


Figure 4.3. Sample resistivities and carrier concentrations. Values cluster in two regions for the two sample sets and loosely trend with the overall Pb/Se ratio measured by EPMA, which is at best only proportional to the composition of the ferecrystal. The lines are provided as a guide to the eye.

Temperature dependent resistivity data, collected for most of the compounds from set A, are shown in Figure 4.4. The temperature dependence is very similar for all samples and indicates metallic behavior. The temperature dependence of the electrical resistivity can be modeled using the Bloch-Gruneisen equation, following the Debye model for a metal, where scattering of carriers is by phonons,

$$\rho(T) = \rho_0 + \Re \left(\frac{T}{\theta_D} \right)^5 \int_0^{\theta_D} \frac{z^5}{(e^z - 1)(1 - e^{-z})} dz$$

where ρ_0 is the residual resistivity, \Re is the electron-phonon interaction constant, and θ_D is the debye temperature. Two of the fits (for a1 and a2) are shown alongside the data in Figure 4.4. with good agreement to the data. The

closest comparison of temperature-dependent resistivity we can make is to the recently reported $([\text{PbSe}]_{1.16})(\text{TiSe}_2)_2$ misfit layer compound analog.¹⁸ The 1:2 misfit layer compound was previously reported to have a room-temperature to residual resistivity ratio of 18.8 whereas our 1:1 ferecrystals are all below 1.8. The very weak temperature dependence indicates a small electron phonon interaction, reflecting the lack of long range order found for compounds prepared by self-assembling designed precursors. This disorder, and the resultant lack of phonons, results in the low lattice thermal conductivity of ferecrystals. The variation of the residual resistivity with both sample set and composition is similar to that of the room temperature values, discussed above. There is evidence for a slight upturn in the resistivity at the lowest temperatures measured, but this upturn is smaller than previously reported.¹⁴

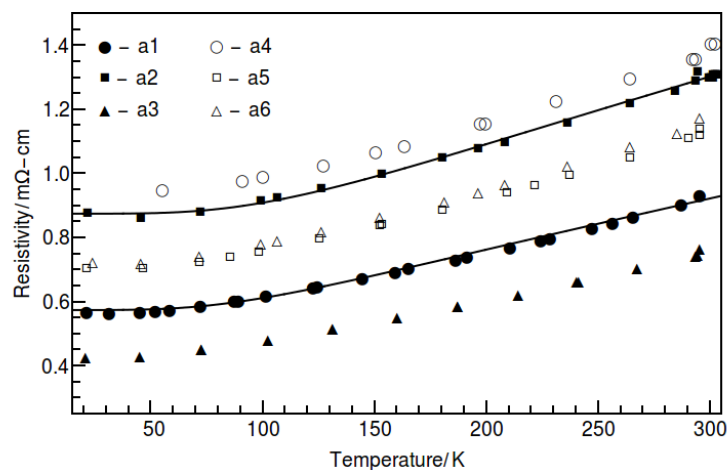


Figure 4.4. Variable temperature resistivity data for select ferecrystal samples from set A. Solid lines are from Bloch-Gruneisen fits of samples a1 and a3 and show the samples follow a metallic behavior.

To gain further information on the electrical properties, Hall coefficients were measured at room temperature for all samples. All samples exhibit a negative Hall coefficient indicating conduction via electrons, which is consistent with prior suggestions of charge donation to TiSe_2 from PbSe . Following prior literature reports, the Hall coefficients were converted to carrier concentration

assuming a single band model.⁶ Carrier concentrations are reported for all samples in Figure 4.3. and in Table 4.1., and are shown as a function of temperature on a subset of samples (Figure 4.5.). Room temperature carrier concentration for each deposition varies by 15% from the average value and there is a factor of 1.5 between sets. Room temperature carrier concentration has a linear downward trend with cation impurity (Figure 4.3.), suggesting reduced donation of charge into the dichalcogenide layer. The variation of the carrier concentration with temperature may be a consequence of assuming a single band model to calculate carrier concentrations. A change in charge transfer with temperature would be expected and lead to the observed weak temperature dependence.

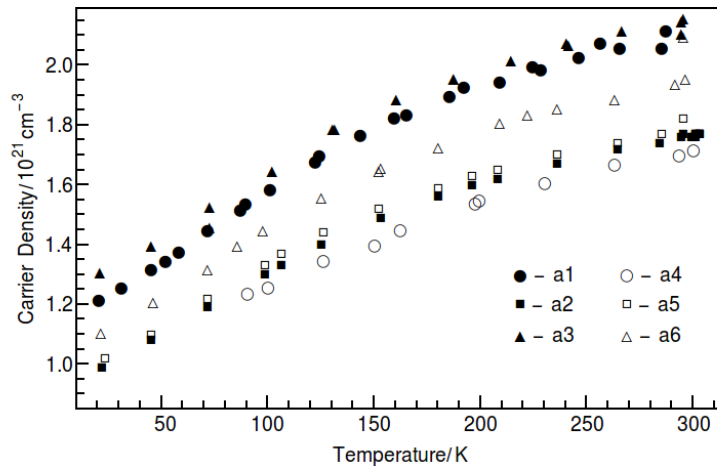


Figure 4.5. Carrier concentration as a function of temperature for a subset of samples.

Hall mobilities calculated from carrier concentration and resistivity measurements vary between 1.8 and 3.8 cm² V⁻¹s⁻¹. The mobility increases with carrier concentration, which is unusual for doping because dopant atoms usually cause scattering. However, this is consistent with charge donation from PbSe to TiSe₂, where conduction occurs in a location spatially separated from the dopant. The mobility decreases as the Pb/Se ratio increases, perhaps due to defects in the dichalcogenide layer from the excess rock-salt cation acting as scattering centers.

Seebeck coefficients were all negative, consistent with Hall coefficient in indicating that electrons are the majority carrier. The magnitude of the Seebeck coefficients vary by about $2.5 \text{ V } \mu\text{V K}^{-1}$ within a set of samples with the values of each set clustered around averages $5 \text{ } \mu\text{V K}^{-1}$ apart. As expected, the magnitude of the Seebeck coefficient increases as carrier density is reduced. If conduction from a single parabolic band with acoustic scattering is assumed, the carrier effective mass can be determined from the Pisarenko relationship¹⁹,

$$\alpha = \frac{8\pi^2 k_b^2}{3eh^2} m^* T \left(\frac{\pi}{3n} \right)^{\frac{3}{2}}$$

where α is the Seebeck voltage, k_b is the Boltzmann constant, e is the elementary charge, h is Planck's constant, m^* is the effective mass, T is the absolute temperature, and n is the carrier concentration. The average carrier mass was found to be $4.4 m_e$ and $3.6 m_e$ for sets A and B respectively, both lower than calculated from data on the previously reported 1:1 compound ($5.5 m_e$). The variations in m^* indicate the band assumptions are imperfect in describing the ferecrystal as we change precursor composition. However, the relative insensitivity of the Seebeck coefficient to changes in carrier concentration from compositional modulation may bode well for future studies of using dopants to influence ferecrystal transport properties, for example the thermoelectric power factor.²⁰ Coupled with the inherent tunability due to flexibility in synthetic control of the MER synthesis method for ferecrystals,²¹ this could offer an additional degree of freedom in controlling the transport properties of these compounds. Figure 4.6. graphs the correlation between the effective mass as calculated from the Pisarenko equation as a function of the cation concentrations measured for each sample. The lowest effective masses correspond to samples with a high cation (Pb, Ti)/Se ratio, as expected from their reduction in carrier density. The magnitude of the Seebeck coefficient (all values were measured to be negative) is relatively insensitive to changes in the carrier concentration, as shown by the inset in Figure 4.6. The data from both set A and set B once again cluster into discrete regions, with the single data

point from the previously published compound in a different space as well. Moore also reported Seebeck measurements from three other data points with magnitudes of 66-69 $\mu\text{V K}^{-1}$, though no carrier concentration data was provided for these samples.¹⁴ This once again reinforces that systematic studies of ferecrystal compound stacking sequences would be best done within a deposition cycle.

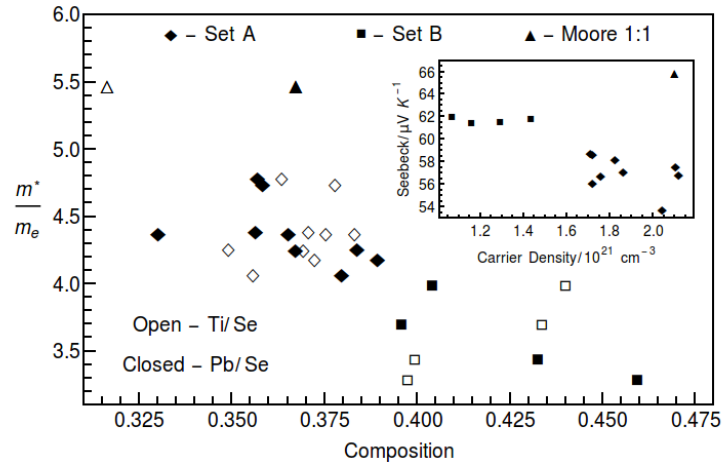


Figure 4.6. Effective masses determined from the Pisarenko relationship plotted against cation ratios for all samples and the previously reported 1:1 compound¹⁴ (labelled Moore 1:1). A general trend of decreasing effective with cation concentrations is apparent. The inset shows the magnitude of the Seebeck coefficients as a function of carrier concentration. Symbol allocation is consistent between the main figure and inset.

4.3.3. Defect characterization

To gain further insight on any structural changes due to the variation in the composition of the precursors, and how they might influence the electrical properties discussed above, cross sections of two samples were prepared for STEM imaging. From Set A, sample a5 was chosen as its intermediate composition should be representative of the set. From Set B, sample b2 was chosen as it is the most Pb-rich sample in the study. STEM images of the 2 samples are shown in Figure 4.7. The bright PbSe rock salt layers and dimmer TiSe₂ dichalcogenide layers are visible in both samples. Surprisingly, the a5

sample shows a capping layer of PbSe at the surface, even though the composition from EPMA does not indicate excess Pb relative to the previously published ferecrystal. The excess PbSe appears excluded from the bulk compound and only appears on the surface. The highly Pb-rich b2 sample shows that excess lead is incorporated into the film, replacing the dichalcogenide layer in regions as PbSe inclusions. Unlike sample a5 where excess PbSe is excluded, defects are instead trapped during the growth of the crystal front. Even with the inclusions, the layering of the ferecrystal is not severely disturbed, hence the narrow range of c-lattice parameters still observed from the lead-rich samples. However, the difference in scattering power of PbSe defect regions relative to the TiSe_2 helps to explain the previously noted changes in diffraction intensity between samples. Crystallization of excess lead first on the surface, then as nanoscale PbSe inclusions within the dichalcogenide layer also offers insight as to why the transport properties are not severely affected by changing the composition of the sample. Following behavior of well-known semimetallic and narrow band gap materials,^{4,22} one might expect a highly dispersed defect distribution to cause a severe perturbation to the transport properties of the ferecrystal relative to discrete inclusions of a wider band-gap compound.

The MER deposition method ensures a similar composition throughout the film, so this implies that the buried excess lead is ‘pushed’ towards the surface prior to the formation of the ferecrystal. It remains to be seen if annealing conditions can be used to further promote exclusion of excess rock-salt to the ferecrystal surface, enhancing purity without destroying the bulk metastable structure. Temperature ramps, Se vapor annealing, or excess dwell time are all avenues to explore.

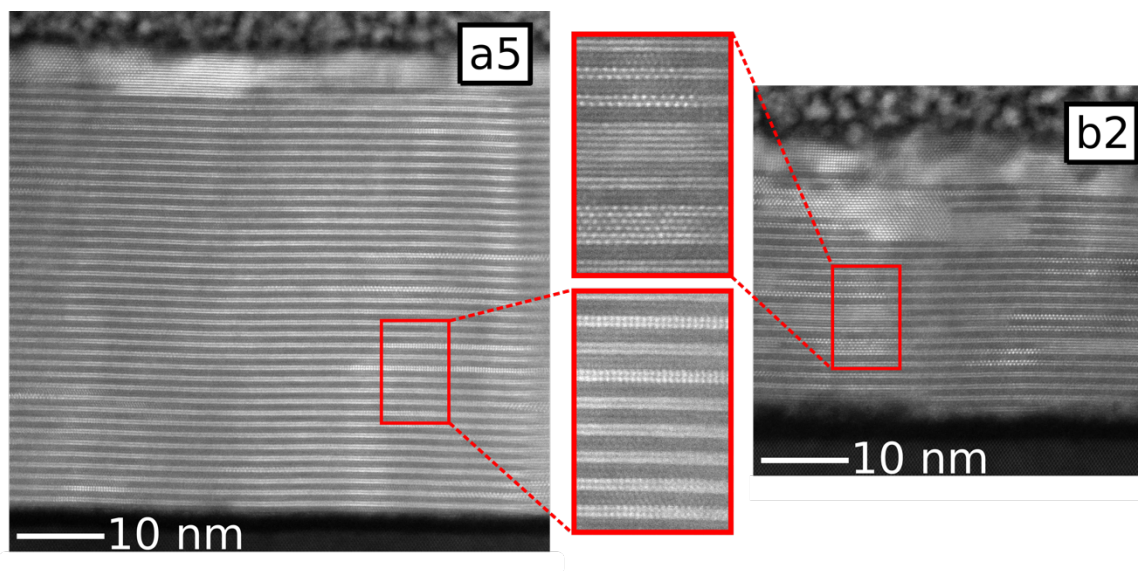


Figure 4.7. HAADF-STEM images of sample a5 and b2. In both cases, excess PbSe can be seen on the surface. Regular, uninterrupted layering is visible in a5, whereas the highly lead-rich b2 sample shows excess lead incorporates itself as PbSe inclusions rather than dispersed Pb, however the global layering scheme is hardly interrupted.

4.4. Conclusions

Turbostratically disordered $([\text{PbSe}]_{1+\delta})_1(\text{TiSe}_2)_1$ forms over a range of initial precursor compositions resulting in a very narrow range of c-axis lattice parameters. STEM images showed excess rock salt in a typical sample was excluded from the bulk and instead formed on the surface of the ferecrystals, and then eventually as nanoscale inclusions when the Pb content became high enough. The resistivity between samples was found to vary by a factor of two, with the change correlating with the Pb/Se ratio. The Seebeck coefficient was consistent within a set of samples prepared in the same deposition cycle. The unusual temperature dependence of the carrier concentration and unusual variation in the effective mass calculated from the Seebeck coefficients and the carrier concentration suggest a more complicated band structure than often assumed. The small change in electrical properties between ferecrystal samples relative to the large difference between reports of single crystals of misfit layer compounds, especially from a set of samples in the same deposition cycle, is

encouraging for future experiments that explore how properties vary as compounds with different values of n and m are prepared.

4.5. Bridge

This initial work in exploring the $([\text{PbSe}]_{1+\delta})_l(\text{TiSe}_2)_l$ compounds first reported by Moore¹⁴ establishes the degree by which structurally and compositionally unfavorable precursors affect the properties of the product. Much of the power in studying nanolaminates from designed precursors is the availability of phase homologies – similar structures that may be systematically and controllably changed. However, due to the kinetically controlled formation, one must be careful to consider the measurement of potentially varying defect distributions along with the changes in structure. The results of this chapter provide important insight moving forward with studying various families of nanoarchitectures within the $([\text{PbSe}]_{1+\delta})_m(\text{TiSe}_2)_n$ chemical system (Chapters V-VII).

CHAPTER V

STRUCTURE-PROPERTY RELATIONSHIPS IN NON-EPITAXIAL CHALCOGENIDE HETEROSTRUCTURES: THE ROLE OF INTERFACE DENSITY ON CHARGE EXCHANGE

The work in the following chapter was accepted 2016-07-14 for publication in *Nanoscale* (DOI: 10.1039/C6NR04274K). It is coauthored by Jeffrey Ditto, Daniel Moore, and David Johnson. Jeffrey Ditto assisted with sample preparation for and collection of scanning tunneling electron microscopy data. Daniel Moore assisted with sample preparation and structural characterization. David Johnson is my advisor and I am the primary author.

5.1. Introduction

The discovery of graphene and its extraordinary properties has generated a significant interest in other 2D and quasi-2D materials, such as planar boron nitride, puckered-planar black phosphorous, and few-layer compounds such as transition metal dichalcogenides.¹⁻³ Interest in designing properties with these ‘nanosheets’ has segued into research on nanolayered heterostructures, which are made by stacking two or more distinct 2D materials together.⁴⁻⁶ By incorporating 2D layers into heterostructures, or even growing them onto a substrate rather than as a suspended layer, both the augmentation of existing properties has been observed as well as emerging behaviors absent from both their bulk and isolated analogues.^{4,7,8} Thus, the synergistic relationships between constituents due to their interfacial interactions can be used as a tool to effectively optimize functionality in heterostructures. Thermoelectric performance is an example of a material property which has can be enhanced by incorporating materials into both single-phase and heterostructure low dimensional environments.⁹⁻¹² Unlike less-intimately mixed chemical systems low-dimensional heterostructures have significant interfacial areas relative to their volumes, which fundamentally changes the composite material’s behavior and stability. These effects can be due to exotic electronic coupling between constituents or in simpler cases large internal electric fields from charge exchange. An example is in nanometer length scale semiconducting

heterojunctions, such as quantum dots or epitaxial superlattices, where size and hence interface/volume ratio directly influences the electronic structure of the nanocomposite material.^{13–15} These emerging behaviors show that simplified physical models typically used to describe constituent interactions in bulk materials are distinctly different to systems mixed at the atomic scale.

Heterostructures comprised of non-epitaxial nanosheets offer the opportunity to study and build models for nanocomposite systems in a characterizable planar geometry while introducing structural change in a systematic fashion at the unit-cell scale and outside of epitaxial growth requirements.

Self-assembled heterostructure nanolaminates, which are made up of several iterations of a repeated heterostructure, have been recently reported in several material systems.^{16,17} One of the most heavily studied has been TiSe_2 layers interleaved with MSe ($\text{M}=\text{Sn, Pb, Bi}$) rock-salt like bilayers.^{18–20} The PbSe-TiSe_2 based family of these structures has been previously used as a platform for studying how systematic nanoscale structural changes affect the composite's thermoelectric performance.^{21–23} These can be described by the general formula for a single repeat of the heterostructure, $([\text{PbSe}]_{1+\delta})_m(\text{TiSe}_2)_n$, where $1+\delta$ is the misfit parameter that describes the difference in formula units per layer per unit area of the two constituents, and m and n are the number of layers of each constituent per repeating unit. Here, we investigate the case where $m=n$ (here forward referred to as m) and $1 \leq m \leq 4$, effectively changing the PbSe-TiSe_2 interface density of the heterostructure nanolaminate while maintaining the global composition. Contrary to the expectation from the rigid band model previously used to describe charge transfer between the layers, we observe a marked decrease in mobile carrier density with increasing m , and attribute this loss to reduced charge transfer between constituents due to band-bending in thick layers.

5.2. Materials and Methods

Heterostructures were crystallized on 100 Si and fused SiO_2 substrates by heating designed precursors consisting of a repeating sequence of several vapor-deposited elemental layers as described previously.²⁴ Ti and Pb layers

were deposited from electron guns and Se layers from a Knudsen cell (all elemental sources >99.99% pure). The substrates were sequentially exposed to each source, building each precursor from the bottom up. Each $(\text{TiSe}_2)_m$ structure consisted of m Ti-Se repeats and each $([\text{PbSe}]_{1+\delta})_m$ structure consisted of m Pb-Se repeats. This sequence was repeated until the precursor was on the order of 50 nm thick. The precursors were calibrated such that each bilayer contained the correct amount of material to nucleate either a single TiSe_2 trilayer or a single PbSe bilayer, with a slight excess of Se to account for loss due to crystallizing in an open environment. Precursors were heated at 350 °C for 30 minutes in an N_2 environment to self-assemble each heterostructure nanolaminate. The process of calibrating the heterostructure precursors has been discussed in detail elsewhere.²⁴

All structural measurements were made on samples deposited on Si substrates. Out-of-plane diffraction patterns were taken with parallel beam Cu- α radiation from a commercial diffractometer in a locked-coupled theta/2-theta geometry. In-plane diffraction patterns were also collected with Cu- α radiation but in a grazing-incidence geometry with the source elevated 0.5° from the sample plane and the detector elevated 4° from the sample plane. High angle annular dark-field scanning transmission electron microscopy (HAADF-STEM) images of the $m=4$ compound were collected using a probe aberration corrected FEI Titan 80-300 TEM/STEM (300kV, 120 mm camera length, $C_s < 1$ μm). HAADF-STEM images of the $m=3$ compound were collected on an FEI Titan 80-300 TEM/STEM (300kV, 240 mm camera length, $C_s = 1.2$ mm). Cross-sectional lamellae for STEM were prepared using an FEI Helios 600 Nanolab dual-beam FIB and thinned using wedge premilling methods.²⁵

Electrical measurements were made on samples deposited on fused SiO_2 substrates through a shadow mask forming a van der Pauw cross pattern. Indium contacts were used for both resistivity and Hall measurements. All measurements were made sourcing a current ≤ 0.001 A and Hall measurements were made in a field between 0 and 16 kG. Seebeck coefficients were measured at room temperature using two sets of type T thermocouples. Half of the sample was cooled ($\Delta T \leq 2\text{K}$) before measuring the voltage between like-material thermocouple leads as a function of ΔT . Each slope was corrected for the

Seebeck coefficient of the metal with which it was measured, with values measured on Cu and Constantan agreeing to $<1 \mu\text{V K}^{-1}$.

5.3. Results

5.3.1. Structure

A homologous series of $([\text{PbSe}]_{1+\delta})_m(\text{TiSe}_2)_m$ heterostructures were crystallized from amorphous thin film precursors designed such that the integer m of the final product systematically changed from 1 to 4. A single repeat of each heterostructure is schematically shown in Figure 5.1. To facilitate analytical characterization each precursor was designed to form several repeats of the heterostructure, creating a nanolaminate thin film during a low temperature anneal. Out-of-plane diffraction patterns of the $([\text{PbSe}]_{1+\delta})_m(\text{TiSe}_2)_m$ nanolaminates are shown in Figure 5.2. Due to the layered nature of the precursor, the intergrowths crystallize with highly textured layers parallel to the substrate so only $00l$ peaks are observed in the out-of-plane diffraction patterns. Indexing the reflections and calculating the c -axis lattice parameters for each m leads to the observation that the c -axis lattice parameter systematically increases by $1.215(6)$ nm as m is increased (shown in the inset of Figure 5.2.). This systematic increase is slightly smaller than the c -axis lattice parameter of previously published $m=1$ samples,¹⁸ and close inspection of Figure 5.1. shows a slight shift of the overlapping peaks (highlighted by dashed boxes) to lower angle of the $m=1$ diffractogram compared to the higher m samples. $([\text{PbSe}]_{1+\delta})_1(\text{TiSe}_2)_1$ has a larger unit cell than the systematic increase because the $m=1$ nanolaminate is made entirely of PbSe bilayer and TiSe_2 trilayer interfaces, whereas the $m>1$ heterostructures all incorporate additional layers into an existing block of like material – either an additional bonding bilayer in the PbSe structure or a van der Waals gap in the TiSe_2 structure.

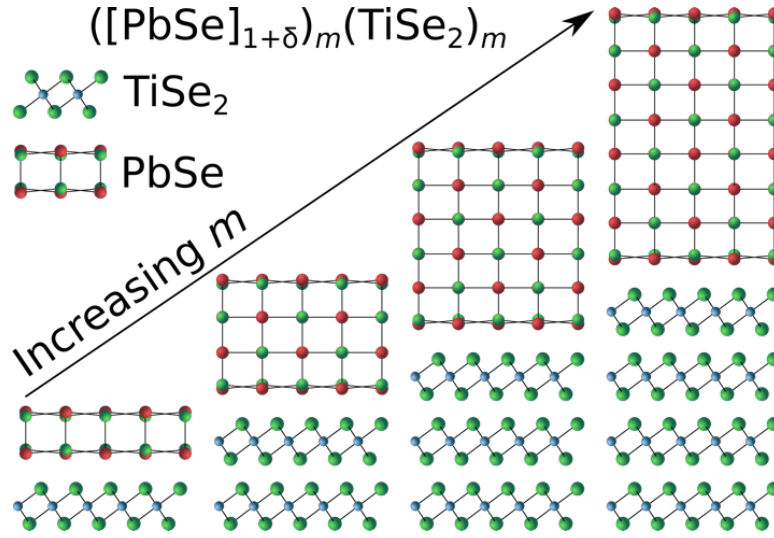


Figure 5.1. Schematic of $([\text{PbSe}]_{1+\delta})_m(\text{TiSe}_2)_m$ heterostructure nanolaminates for $1 \leq m \leq 4$. Each structure has the same composition and only one interface per repeating unit, but decreasing interface density with increasing m .

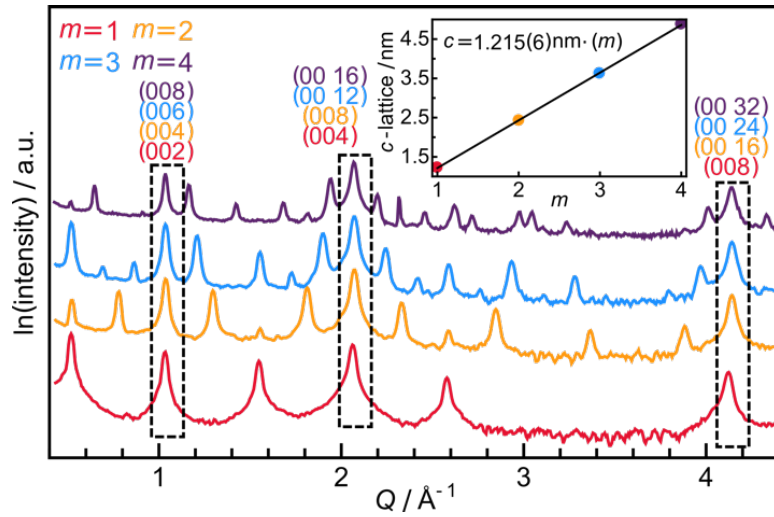


Figure 5.2. Out-of-plane diffraction patterns for $([\text{PbSe}]_{1+\delta})_m(\text{TiSe}_2)_m$ nanolaminates for $1 \leq m \leq 4$. The outlined peaks correspond to the adjacent indices of the same color. The inset shows the c -lattice parameter, which also corresponds to the PbSe-TiSe₂ interface density in the out-of-plane direction, as a function of m .

Because out-of-plane diffraction scans only contain information regarding the atomic planes parallel to the substrate, in-plane diffraction patterns were also taken to verify the structure of the constituent layers and are

shown in Figure 5.3. All nanolaminates show similar diffraction patterns, with peak positions and relative intensities being similar across samples. The peaks can be indexed as 2D powders of $hk0$ reflections from the parent PbSe and TiSe₂ compounds (space groups $Fm-3m$ and $P-3m1$, respectively). From these reflections the in-plane lattice parameters of the constituents crystallized in each compound are determined and reported in Table 5.1. along with the c -lattice parameter and calculated compositional misfit parameter. As shown by the inset of Figure 5.3., for each constituent a decrease in the full-width at half-maximum of the peaks is observed with increasing m , indicating the in-plane crystallite size increases with m . Impurity phases are also seen, especially in the $m=2$ nanolaminate. However, the signal is small relative to the majority compound. The diffraction patterns and calculated parameters indicate that the constituent structures are consistent as m is increased and the compositional misfit parameter is 1.17 for all m , which is striking as the interplay between interface and volume energies often require structural distortions to reach a local minimum in free energy.

Table 5.1. Lattice parameters and compositional misfit of PbSe and TiSe₂ found in the $([\text{PbSe}]_{1+\delta})_m(\text{TiSe}_2)_m$ heterostructures.

m	c (nm)	a -PbSe (nm)	a -TiSe ₂ (nm)	$1+\delta$
1	1.215(1)	0.6137(1)	0.357(1)	1.17
2	2.4232(6)	0.6134(3)	0.357(1)	1.17
3	3.6323(5)	0.6140(1)	0.357(1)	1.17
4	4.8723 (9)	0.6139(2)	0.357(1)	1.17

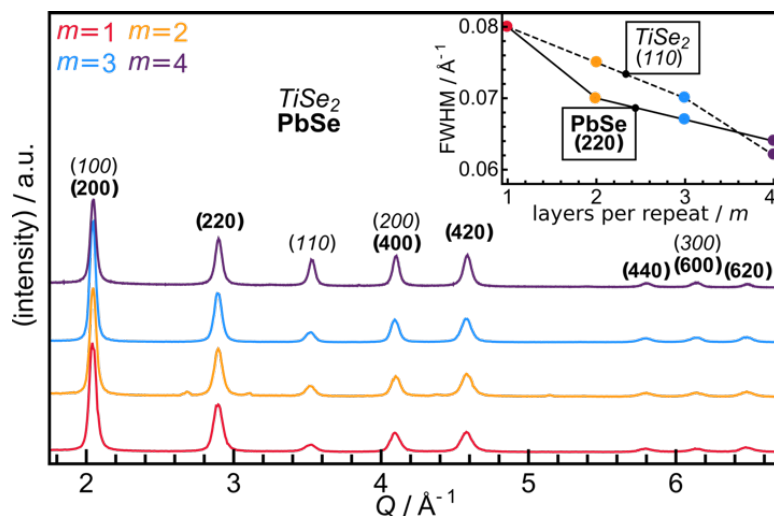


Figure 5.3. In-plane diffraction patterns for $([\text{PbSe}]_{1+\delta})_m(\text{TiSe}_2)_m$ nanolaminates for $1 \leq m \leq 4$. Peaks correspond to PbSe (Fm-3m) and TiSe_2 (P-3m1) $hk0$ planes, showing the nanolaminates crystallize as 2D powders of these phases. Inset is the full-width at half-maximum (FWHM) of the PbSe (220) and TiSe_2 (110) peaks. The systematic decrease is indicative of increasing crystallite size. The $m=2$ sample shows traces of an impurity phase alongside the majority compound. Calculations from the measured lattice parameters indicate a formula-unit mismatch ($1+\delta$) of 1.17 between PbSe to TiSe_2 for all m .

To further characterize the nanolaminate structures, HAADF-STEM images were taken of the $m=3$ and $m=4$ members as shown in Figure 5.4. The HAADF intensity is sensitive to the Z-contrast of the atoms in the layers, so the PbSe layers are much brighter than the TiSe_2 layers. The left-most $m=4$ image shows the thickness of the film in its entirety. Regular layering is present throughout the sample. Ten $([\text{PbSe}]_{1+\delta})_4(\text{TiSe}_2)_4$ repeats are present as opposed to the eleven repeats deposited in the precursor, most likely due to surface oxidation and/or a loss of material during the self-assembly process. The right images show higher magnification of the layers where the bright spots correlate to atomic columns. The various patterns of bright spots indicate changing zone orientations and highlight a rotational misregistration between the non-epitaxial constituents.

The structural characterization shows that each product shares similar global structure and stoichiometry, consisting of interleaved blocks of PbSe and TiSe_2 with a compositional misfit ($1+\delta$) of 1.17 due to the differences in basal

plane area per formula unit. However, the local structure and composition varies between products. As m is increased the thickness of the constituent blocks, and hence the c -axis lattice parameter increases while the interface density within the laminate structure decreases.

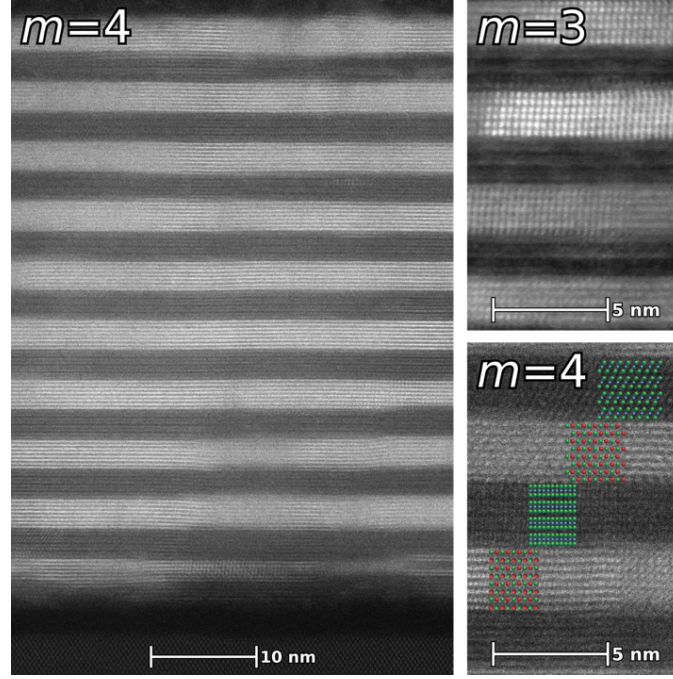


Figure 5.4. HAADF-STEM images of $([\text{PbSe}]_{1+\delta})_m(\text{TiSe}_2)_m$ nanolaminates for $m=3, 4$. The leftmost image shows 10 $([\text{PbSe}]_{1+\delta})_4(\text{TiSe}_2)_4$ structures, which indicates a loss of one $([\text{PbSe}]_{1+\delta})_4(\text{TiSe}_2)_4$ repeat unit from the precursor with 11 repeats and is believed to occur on annealing. The high-magnification right images show changing lattice faces between constituents highlighting the rotational misregistration in the layers.

5.3.2. Transport

The normalized temperature dependent in-plane resistivity values for the four $([\text{PbSe}]_{1+\delta})_m(\text{TiSe}_2)_m$ compounds are shown in Figure 5.5. The room-temperature normalization factors are given in Table 5.2. The resistivity values systematically increase as m is increased. All samples show a decreasing resistivity as they are cooled, with an upturn below 100 K. The magnitude of the ratio between the room temperature and minimum resistivity systematically increases with m . In metals, the resistivity generally increases with temperature

due to electron-phonon interaction. The larger constituent blocks allow for more coherent vibrational modes, and hence more carrier scattering as phonon modes are activated. The upturn at low temperatures, which has been attributed to correlated electron behavior and/or localization in 2D systems,²⁶ systematically moves to lower temperatures until the $m=4$ structure, at which point the temperature of the resistivity minima increases again. Previous work indicates conduction occurs within the TiSe_2 layers by charge donated from the PbSe . Given the heterostructures have constant compositions and only the interface density varies, results from prior studies suggest that the carrier concentration and carrier type should not change as m increases. However, carrier mobility might be expected to increase with increasing m due to the larger constituent blocks and reduced interfacial scattering. The trend in the resistivity data is inconsistent with expectations from prior studies of TiX_2 chalcogenide intergrowth compounds.^{20,22,27}

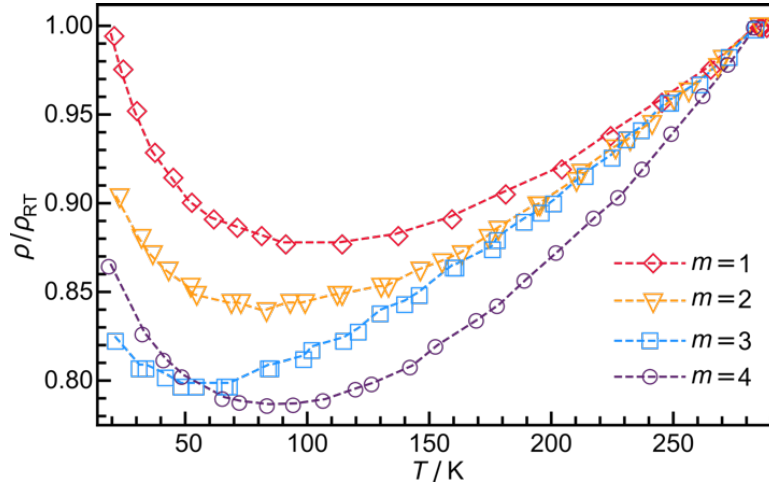


Figure 5.5. In-plane temperature-dependent resistivity for $([\text{PbSe}]_{1+\delta})_m(\text{TiSe}_2)_m$ nanolaminates with $1 \leq m \leq 4$. Each curve is normalized to the room temperature value (see Table 5.2.). The size of the data points is a conservative estimate of the error in the measurement. Between 100K and room temperature, resistivity generally increases with temperature, as expected for metallic behavior. In this range the relative change in resistivity with temperature increases with m due to increasing phonon scattering. The upticks below 100K are attributed to electron localization.

Table 5.2. Room-temperature in-plane transport properties of $([\text{PbSe}]_{1+\delta})_m(\text{TiSe}_2)_m$ heterostructures. Estimates of error are given in parentheses for the last digit reported.

m	R_H ($10^{-11}\Omega\text{-cm G}^{-1}$)	n_e (10^{21}cm^{-3})	S ($\mu\text{V K}^{-1}$)	ρ ($10^{-5}\Omega\text{-m}$)	$S^2\rho^{-1}$ ($10^{-4}\text{WK}^{-2}\text{m}^{-1}$)	μ ($\text{cm}^2\text{V}^{-1}\text{s}^{-1}$)
1	-2.7(1)	2.3(1)	-57(3)	1.5(1)	2.2(3)	1.8(1)
2	-3.3(1)	1.9(1)	-78(3)	2.1(1)	2.9(3)	1.6(1)
3	-4.5(1)	1.4(1)	-85(3)	2.4(1)	3.0(3)	1.9(1)
4	-8.3(1)	0.75(10)	-89(3)	3.0(1)	2.6(3)	2.8(1)

To gain insight into the resistivity changes, temperature-dependent Hall coefficients were measured and room-temperature values are shown in Table 5.2. A linear V/B response was observed for all samples and temperatures and negative Hall coefficients suggest transport is dominated by n -type conduction. Hall coefficients were converted to carrier concentrations using a single band model, which are shown in Figure 5.6. The carrier densities consistently decrease as m increases, contrary to the constant value expected from prior studies. The carrier concentration steadily decreases with temperature until ca. 150 K. Around this temperature the carrier concentration begins to decrease faster with T , suggesting a reduction in mobile carriers is responsible for the low-temperature resistivity increases that are seen in Figure 5.5. The rate of carrier loss decreases with both m and room-temperature carrier concentration. The temperatures of the accelerated carrier loss do not appear to trend with m and are higher than the resistivity upturn temperatures. An increase in resistivity due to carrier reduction would be expected to compete with a decrease due reduced phonon scattering, which may account for the difference in temperatures between these observations.

Room-temperature carrier concentration consistently decreases with m and is shown in Table 5.2. and the right-axis of Figure 5.7. Because previous work showed that thick TiSe_2 blocks readily accept charge from a single PbSe

bilayer,²² the decreased carrier density observed in the high m samples of the present study suggests that doping efficiency from PbSe decreases with layer thickness. The unexpected decrease in carrier density explains the resistivity increase. Table 5.2. also shows the electron mobility calculated from the single band carrier density and resistivity. The mobility generally increases as m increases, with the $m=2$ sample having a lower value presumably due to the presence of trace impurity phases (seen in the in-plane XRD data) that reduce the mobility below the value of a phase-pure sample. Reduction in mobility would be expected from the thinner layers, due to the high interface densities that truncate a structure. On the other hand, increasing dimensionality of layered compounds might drastically alter the band structure, and hence the mobility of either or both constituents as well.⁷ Decoupling the interplay between defects and nanostructure in kinetically stabilized heterostructures, and how these affect the properties, is an ongoing area of active research.^{28,29}

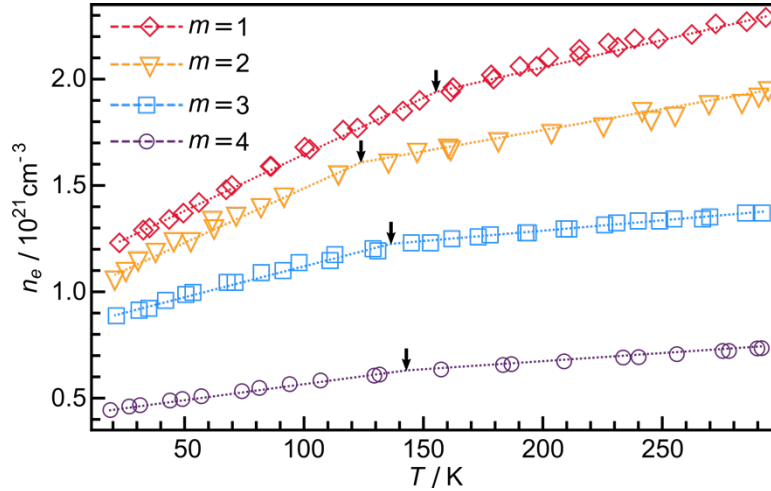


Figure 5.6. In-plane temperature-dependent carrier concentration for $([\text{PbSe}]_{1+\delta})_m(\text{TiSe}_2)_m$ nanolaminates with $1 \leq m \leq 4$. The size of the data points is a conservative estimate of the error in the measurement. The carrier concentration consistently decreases with increasing m . The decrease appears to accelerate at lower temperatures. This behaviour is qualitatively indicated by the dashed lines and black arrows, which are both added to serve as a guide to the eye.

In parabolic conduction bands of band mass m^* , the Seebeck coefficient is inversely related to the carrier density.³⁰ $([\text{PbSe}]_{1+\delta})_l(\text{TiSe}_2)_n$ nanolaminates have been previously shown to roughly follow this trend.²² The higher mobility and lower carrier concentrations suggest that raising m might be an efficient means to optimizing the thermoelectric performance of the heterostructures. Figure 5.7. shows the room temperature Seebeck coefficients and carrier concentrations for the $([\text{PbSe}]_{1+\delta})_m(\text{TiSe}_2)_m$ nanolaminates as a function of m . In agreement with the Hall coefficients and previous measurements on $([\text{PbSe}]_{1+\delta})_m(\text{TiSe}_2)_n$ compounds the Seebeck coefficients are negative, indicating electrons dominate the transport. The Seebeck coefficient consistently increases in magnitude with m , though the differences in value between the $m=2$, $m=3$, and $m=4$ heterostructures is small, increasing from -78 to -85 to -89 $\mu\text{V K}^{-1}$ as m is increased. The power factor generally increases along with the Seebeck coefficient with the exception of the $m=4$ sample, which has an appreciable increase in resistivity but negligible change in Seebeck coefficient over both the $m=2$ and $m=3$ samples. Changing the interface density of the $([\text{PbSe}]_{1+\delta})_m(\text{TiSe}_2)_m$ heterostructures does not appear to significantly raise the power factor relative to other changes to the nanostructure such as increasing the number of TiSe_2 layers. However, a more complicated layering structure that combines the effects of increased mobility from the $m=n$ heterostructure family and the high Seebeck coefficient from the $m=1$ with high- n heterostructure family is an obvious next step. Further enhancement of the thermoelectric transport in $([\text{PbSe}]_{1+\delta})_m(\text{TiSe}_2)_n$ and other nanolaminates with similar structure might be achieved by introduction of f electrons into the structure, which are well known to introduce sharp features into the density of states and significantly enhancing the Seebeck coefficient.³¹ In the bottom-up synthesis employed here, this might be possible either with chemical substitutions with mixed-valence rare-earth elements within the rock-salt layers or by intercalation of the dichalcogenide.^{32,33}

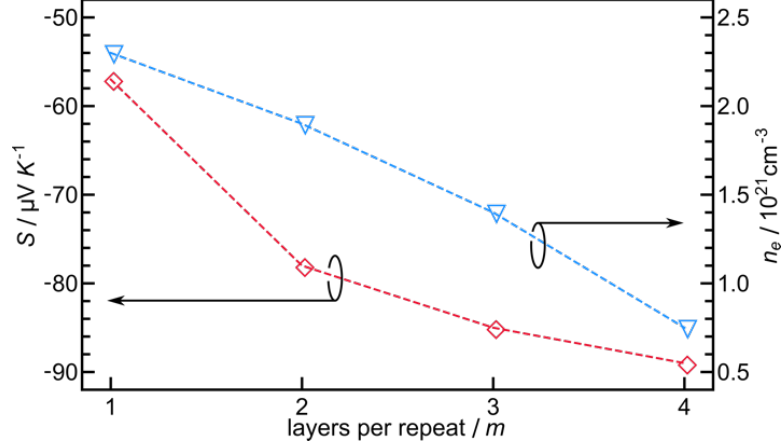


Figure 5.7. Seebeck coefficients (left axis, red diamond symbols) and carrier concentrations (right axis, blue triangle symbols) of $([\text{PbSe}]_{1+\delta})_m(\text{TiSe}_2)_m$ nanolaminates for $1 \leq m \leq 4$. The size of the data points is a conservative estimate of the error in the measurement. The Seebeck coefficient systematically decreases and appears to be saturating with increasing m . The decreasing carrier concentration with m is not expected from the rigid-band model.

5.4. Discussion

As defect-free bulk compounds, both PbSe and TiSe_2 are narrow gap semiconductors with direct and indirect band gaps, respectively. However, defects in TiSe_2 often result in finite filling of the conduction band.³⁴ PbSe has been extensively researched due to its size-tunable band gap in quantum-confined systems.¹³ Previous studies of intergrowth compounds between these constituents suggest the heterostructures have type II broken-gap band alignment such that the bottom of the TiSe_2 conduction band falls below the top of the PbSe valence band.^{27,35} The difference in the chemical potential of electrons (μ) within the layers will result in charge exchange from the valence band of PbSe into the conduction band of TiSe_2 . This partial filling and emptying of the bands serves to spatially separate electrons and holes into the TiSe_2 and PbSe layers, respectively. The band-bending diagrams in Figure 5.8. illustrate this behavior.

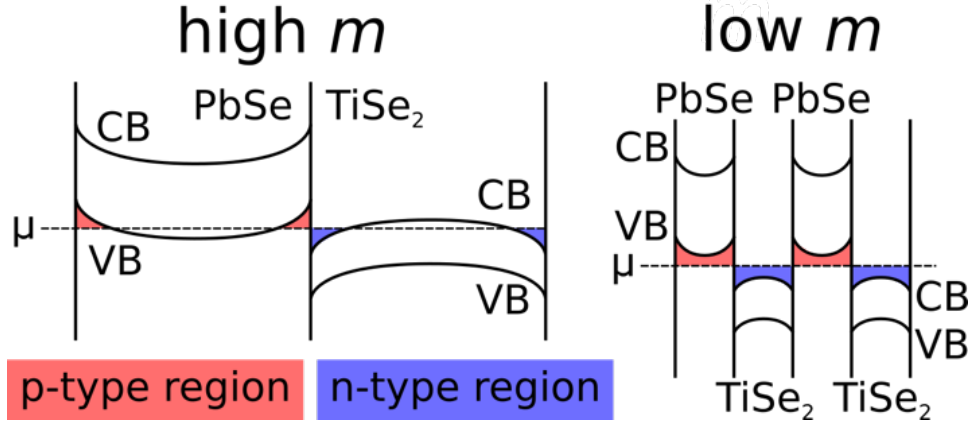


Figure 5.8. Schematic of proposed band-bending that occurs in the heterostructures. The low interface density of the high m samples leads to the valence (conduction) band of PbSe (TiSe₂) crossing back over the chemical potential as the bulk band positions are re-established, which does not occur in the low m samples with high interface density

In light of these considerations, the reduced carrier density in $([\text{PbSe}]_{1+\delta})_m(\text{TiSe}_2)_m$ can be intuitively understood. The change in band positions relative to the chemical potential occurs at the PbSe-TiSe₂ interfaces. For low m heterostructures these positions are approximately maintained, but as m increases the band positions will move towards the bulk values within the constituent layers and the exchanged charge will remain primarily at the interfaces, as shown in Figure 5.8. This limits the extent to which charge exchange is possible deep within the layers, lowering the average carrier concentration over the entire heterostructure. Thus, absent of other size-induced changes to the electronic structure, the *charge per interface* should asymptotically increase with m and might be considered to be a natural size-dependent parameter in the discussion of nanoscale heterostructures with similar band alignment.

Within the framework of the charge per interface parameter, we can make insights as to why structurally similar misfit compounds have only been stabilized thermodynamically at high temperatures with $m=1$.³⁶ The charge exchange creates two oppositely charged layers that attract, which can be thought of in similar terms to an ionic bond. The stabilization from the formation of an ionic bond depends on the ionization potential of the cation and

the electron affinity of the anion, which influence how much charge is transferred, as well as the separation distance and resulting coulomb potential, ϕ , between charged species. Lead chalcogenides have been observed to have low ionization potentials³⁷ and TiX_2 is well known to form intercalation compounds with both alkali and transition metals, which are stabilized by charge exchange between the electronegative chalcogenide ions and the intercalated metal.³⁸ As the amount of intercalation increases the charge transfer from the intercalated ions reduces the TiX_2 host lattice's effective electronegativity, which limits how much charge can be intercalated into the system.³⁹ A similar behavior should occur when considering stabilization of $([\text{PbSe}]_{1+\delta})_n(\text{TiSe}_2)_m$ heterostructures by charge exchange between the PbSe “cations” and TiSe_2 “anions”.

Charge exchanged in layered compounds is well known to reside at or near the interfaces.⁴⁰ This forms the coulomb potential of the interlayer “ionic bond,” which is directly related to the energetic gain of its formation. Under a rigid band condition, as is often used for similar assemblies of nanosheets, the total coulomb potential (ϕ_{total}) between a volume of layers would be constant with m , but the potential across an individual interface ($\phi_{interface}$) would increase with m , as shown in Figure 5.9. by triangle markers. For the $1 \leq m \leq 4$ nanolaminates studied the charge per interface, calculated from the carrier density, generally increases with m (given by $n_e \times c$ -lattice see Table 5.1. and Table 5.2.). However, as shown by Figure 5.9. the total coulomb energy is greatest in the $m=1$ structure, with a systematic decrease as m is increased, indicating the most stabilization from charge exchange. In the $m=1$ case, the bands will exhibit the least bending (i.e. be the most rigid) and thus maximize the degree of charge transfer that can be accommodated. This lowers the total electron energy relative to any higher m nanolaminate or the bulk constituents. These effects should also be taken into account when considering the stabilization of other nanolayered systems. The interlayer coulomb interaction, the degree of band-bending that can be accommodated in nanoscale layers, and the chemical potential difference of the constituents all play a role in the stability of 2D heterostructures. These will be important considerations as heterostructures with increased complexity and functionality continue to be made.

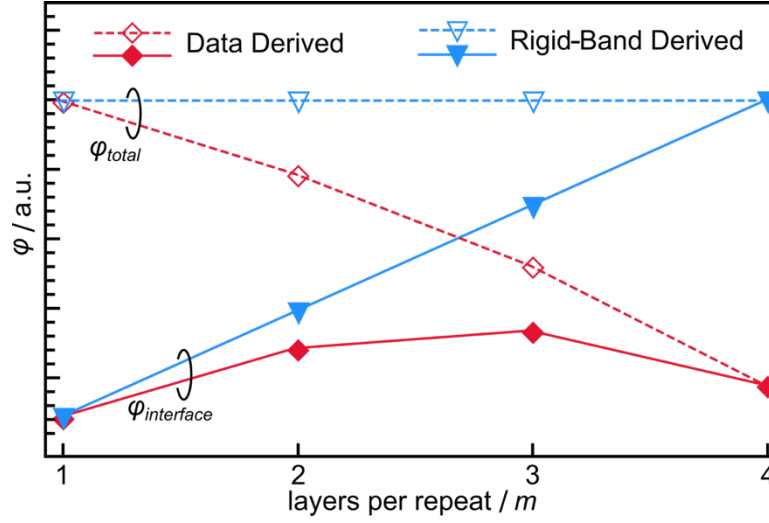


Figure 5.9. Calculated coulomb potential per interface (closed markers, solid lines) and per total volume (open markers, dashed lines) across PbSe-TiSe₂ interfaces. Data is presented both using the measured carrier densities from the $1 \leq m \leq 4$ nanolaminates (red diamond markers) and also assuming charge is separated in rigid-bands and normalized to the $m=1$ value from the data-derived calculation (blue triangle markers).

5.5. Conclusions

A series of $([\text{PbSe}]_{1+\delta})_m(\text{TiSe}_2)_m$ heterostructures were made with $1 \leq m \leq 4$. In-plane and out-of-plane diffraction and HAADF-STEM investigations showed that the compounds consisted of intergrowths between PbSe and TiSe₂. In-plane electrical transport measurements show all samples to be n-type conductors with carrier concentrations on the order of 10^{21} cm^{-3} , and the carrier concentration decreases as m increases due to reduced charge exchange between the thicker layers. This behavior is explained by considering how the layers are stabilized and how the bulk band positions are restored far from the interfaces. Since mobility increases as m increases, when combined with further nanostructural control this form of ‘modulation doping’ may be an effective means of improving thermoelectric performance through obtaining higher power factors. These results highlight how in-plane electrical measurements can be a useful probe of the stabilization mechanisms of nanoscale layered structures by interaction in the out-of-plane direction. This is achieved through the use of a

homologous series of structures rather than using gated or other device geometries. Furthermore, the results show that these mechanisms may have a direct impact on the transport behavior of the composite structure. As research in heterostructures of 2D layers continues to progress towards the design of functionalized materials, interlayer interactions and accessible means of probing them will continue to be an important consideration.

5.6. Bridge

As the interface density of compositionally identical nanolaminates of PbSe and TiSe₂ is changed, the assumption of rigid bands does not appear to hold and the degree of inter-constituent charge transfer lessens. However, the nanoarchitecture was changed such that the smallest repeating unit in the structure was varied along with the interface density. The following chapter addresses this by implementing structural isomers that bury interfaces within a series of 8 layers while holding both the repeating length scale and composition constant.

CHAPTER VI

BURIED INTERFACES IN THE UNIT CELL OF $[(\text{PbSe})_{1+\delta}]_4(\text{TiSe}_2)_4$ NANOLAMINATE THIN FILMS AND THEIR EFFECT ON THE THERMOELECTRIC TRANSPORT PROPERTIES.

At the time of writing the work in this chapter is unpublished, but a manuscript is planned and will be coauthored with Danielle Hamann, Jeffrey Ditto, Daniel Moore, and David Johnson. Danielle Hamann assisted with preparation, Jeffrey Ditto assisted with sample preparation for and collection of scanning tunneling electron microscopy data. Daniel Moore assisted with sample preparation and characterization. David Johnson is my advisor and I am the primary author.

6.1. Introduction

In molecular and especially organic chemistry, to some degree the local arrangement of atoms can be controlled by piecewise substitutions and kinetically favorable exchanges to an existing structure. On the other hand, rational control of the nanoarchitecture in solid-state materials is inherently difficult because not only must local coordination be controlled, but so too does the global arrangement into a particular extended structure.^{1,2} The necessary reaction conditions for driving solid-state diffusion at the reacting interfaces will typically bypass any tricks the experimentalist might play to drive the formation of a specific extended structure.^{3,4} In a sense and using the vernacular of molecular chemists, the reaction of solids is typically limited to ‘one-pot’ methods.⁵ Composite materials are one method by which structures, compositions, and properties of solids can be controlled.⁶⁻⁹ For example, miscibility gaps between compounds can be used to form nanocomposites of embedded inclusions of secondary phases within a host matrix.⁹ However, under typical growth conditions, there is still little opportunity for rationally tailoring the final composite structure at the nanoscale.

Thermoelectric materials research is an example of a field that has seen significant progress come from the approach of making nanostructured composites.¹⁰ Designing thermoelectric materials over several length scales with

defects, dopants, or strained inclusions significantly reduces thermal conductivity, which is the denominator of the thermoelectric material figure of merit (zT).⁹⁻¹¹ By choosing appropriate materials, these structures can also be used to enhance the power factor, or the numerator of zT .¹¹ However, at the nanoscale electronic transport properties are highly dependent on size and structure, which cannot be readily either controlled or probed in the bulk in a high-throughput manner. Further confounding, it is unknown how these features, which are directly responsible for the augmented behavior relative to their bulk counterparts, change with annealing and in a temperature gradient for long times - the environment of a thermoelectric device. The ability to reliably control the nanostructures within a host compound can provide subtle feedback as to these effects.

It was recently shown that the constituent layers in $([\text{PbSe}]_{1+\delta})_m(\text{TiSe}_2)_m$ nanolaminates undergo little structural change as their sizes increase.¹²⁻¹⁴ This layered system thus serves as an ideal test case for probing the effects of size and interface density in nanocomposite materials absent of size-induced structural distortion. Because of the synthetic flexibility when making these nanolaminate materials, several homologous series of compounds can be systematically formed and studied while rationally controlling the nanoscale structure and composition.^{12,15-17} Here, we utilize structural isomers of layered $([\text{PbSe}]_{1+\delta})_4(\text{TiSe}_2)_4$ to systematically investigate the effects of introducing buried interfaces into 6 compounds that are identical in composition and with repeating structure length scales that vary by <0.05 nm. We find that the nanoscale interface density influences the transport behavior of the composite nanolaminate and that the structures with intermediate interface density exhibit a $\sim 10\%$ enhancement of the power factor over the endmembers, despite their global likeness both structurally and compositionally. This highlights the role that actively designing the nanoarchitecture of composite materials might play in properties optimization.

6.2. Experimental Methods

Chemical precursors were made from vapor deposition of elemental layers onto silicon and silica substrates. Pb and Ti were evaporated from electron guns operating at 6 kV and Se from a Knudsen effusion cell. All source material was purchased from Alfa Aesar and >99.95% purity. Shutters above each evaporating source were programmed to sequentially open and deposit amorphous layers onto the substrates of appropriate thickness to nucleate either bilayers of PbSe (one-half rock salt unit cell thick) or trilayers of TiSe₂ (one transitional metal dichalcogenide unit cell thick). PbSe bilayers were deposited with a Pb-Se shutter sequence and TiSe₂ trilayers with a Ti-Se shutter sequence. These sequences between layers were controlled such that the amorphous precursor layers resembled the structure of the targeted nanolaminate and repeated 11 times to build a film approximately 50 nm thick.¹⁸ Precursors were gently annealed at 350 °C for 30 minutes in an N₂ atmosphere to promote self-assembly into a crystalline nanolaminate.

Locked-coupled θ -2 θ out-of-plane diffraction data and grazing-incidence in-plane diffraction data were both collected using laboratory Cu-K α radiation with parallel beam optics on a Bruker D8 Discover and Rigaku Smartlab, respectively. Grazing-incidence scans were carried out with an incident angle of 1.0° and the detector 4.0° above the sample plane. Ab-initio reflectivity patterns from the idealized targeted structures were generated with the Bede REFS modeling software assuming bulk densities and 0.1 nm of roughness at all interfaces. High angle annular dark-field scanning transmission electron microscopy (HAADF-STEM) data were collected using a probe aberration corrected FEI Titan 80-300 (300kV, 120 mm camera length, C_s<1 μ m). Energy dispersive X-ray spectroscopy (EDS) data were acquired with a 2.3 ms dwell time per pixel and summed over several drift-corrected frames. Cross-sectional lamellae for STEM imaging were made using an FEI Helios 600 Nanolab dual-beam FIB.¹⁹

Electrical measurements were carried out on a house built closed-cycle He cryostat using a 1.5 T magnet. Van der Pauw resistivities and Hall resistivities both were collected on cross-pattern films through Cu wires and In contacts. Reported values were calculated using thicknesses from reflectivity

measurements of the annealed films. Seebeck coefficients were also measured using a house built system. One-half of the film was cooled slightly and both S and ΔT were measured between two type-T thermocouples.

6.3. Results

6.3.1. Synthesis/Structure

Crystallization of PbSe-TiSe₂ nanolaminate structures from designed layered precursors results in crystallographically aligned 2D powders with the c -axis perpendicular to the substrate.²⁰ The modulation waveform of the two constituents, a and b is defined by the thickness of each of the blocks and the stacking order (k). For example, $k=44$ for the stacking sequence **aaaabbbb** and $k=3212$ for the stacking sequence **aaabbabb**. While each repeating unit contains 4 layers of a and b , the stacking and hence the diffraction patterns are different due to the different varying electron density profiles along the stacking direction. In the convention used here, the largest PbSe component is given first and is in normal typeface whereas the TiSe₂ is second in bold typeface. The atomically sharp interfaces between constituent structures results in k taking the form of a square-wave that represents cation density, electron density, or another property unique to each constituent. For the compounds prepared in this study, the modulation wavelength, λ_k (which can be expressed as the c -lattice parameter for the nanolaminate), is approximately constant as each structure is made up of the same number and type of individual layers, with the only changes being the number of buried PbSe-TiSe₂ interfaces ('nodes' in k) within the repeating structure.

A schematic representation of the modulation waveforms, where we assume that the modulation wavelength is constant and that the interfaces occur along intervals of $\frac{\lambda_k}{8}$, the specular out-of-plane, and the grazing incidence in-plane diffraction for each structural isomer is shown in Figure 6.1. From the k profiles it is seen that **221111** and **211211** profiles will have 5 interfaces within λ_k , **3311**, **3212**, and **2321** profiles will have 3 interfaces within λ_k , and the **44** profile has 1 interface within λ_k . The positions of the 001 reflections remain relatively unchanged in the specular scan, due to the similar c -axis

lattice parameter between all nanolaminate structures. However, differences in the modulation waveforms result in 00l reflections with varying amplitude as the Fourier transform of the electron density is different for each structural isomer. This results in each isomer carrying a unique ‘fingerprint’ of relative peak intensities, observable even in the first few Bragg reflections. The measured patterns are compared with ab-initio theoretical curves from the ideal isomeric structures and assuming k consists of eight equal-width blocks summing to the thickness λ_k calculated from the Bragg peak positions. The low intensity reflections correlate well between the models and experimental data, with small deviations expected due to the simplicity of the models relative to the samples (the thickness of a Se-Ti-Se trilayer and a Pb-Se bilayer are not exactly equal and the electron density does not have abrupt changes). The small oscillations between Bragg peaks are a consequence of the finite number of unit cells in the films. One to two less fringes are visible between Bragg reflections in the measured data relative to the models indicating that layers (or parts of the top and/or bottom layers) are lost during the self-assembly of the precursors into crystalline samples. The value of λ_k (or c -lattice parameter of the nanolaminate) is consistent between all nanolaminates, with a repeat period of 48.6(2) Å. Also shown in Figure 6.1, in-plane diffraction patterns support the formation of similar relative amounts of PbSe and TiSe₂ between samples, as the relative intensities of reflections from each constituent is maintained across the suite of samples. The (110) peak from the PbSe structure is expected to be systematically absent from the $Fm-3m$ rock-salt space group and can possibly be explained by a shift of the interfacial ions from special sites in the bulk rock salt unit cell, or if each sheet is unique, it can be indexed as the 2D wallpaper group $p4gm$ wherein this reflection is allowed.²¹ The low intensity peaks above 5 Å⁻¹ in Q increase in intensity in samples with fewer buried interfaces, likely due to more nucleation events resulting in smaller crystallites in the thinner layers.

To further confirm the stacking sequences, HAADF-STEM images were taken of all structural isomers, as well a high resolution EDS profile of the **2321** sample, as shown in Figure 6.2. Rock-salt layers containing high-Z Pb show up as bright regions whereas TiSe₂ layers are darker. Distinct bright atomic columns of atoms can be seen when looking down a crystallite’s zone axis. The

2321 nanolaminate has examples of layers looking down several zone axis of the structures, which highlights rotational disorder at interfaces within the structures. The images show that the nanolaminate films consist of precisely stacked layers with sharp planar interfaces between constituents, consistent with the persisting Kiessig fringes in Figure 6.1. All layering schemes can be clearly identified, and as expected the unit cells between the 6 are practically the same. Intensity traces from the EDS signal of both Pb and Ti taken from the **2321** sample are shown at the top of Figure 6.2 and further confirm the composition and structure of the layers, with distinct maxima visible from the planes of atoms as expected by layers with the **2321** modulation.

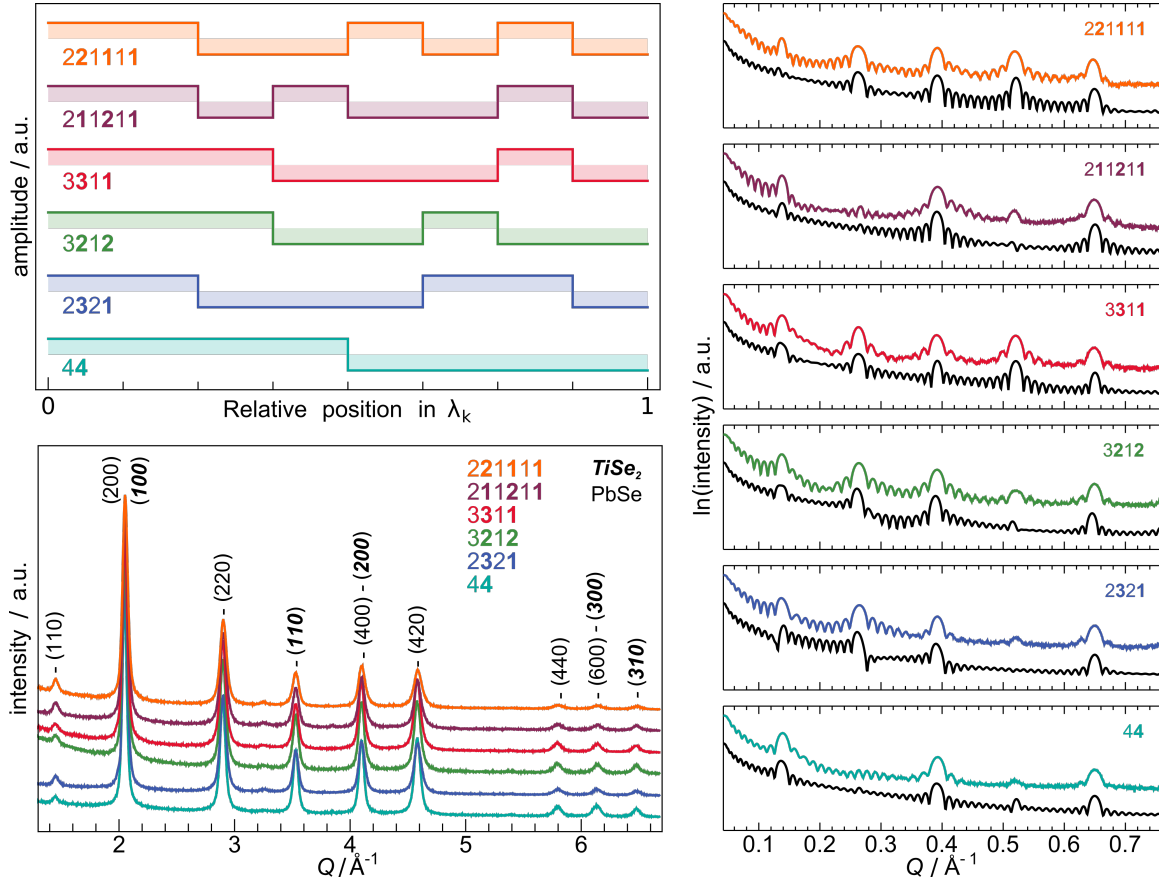


Figure 6.1. (top-left) Schematic representation of the modulation profile of PbSe and TiSe₂ within λ_k for each nanolaminate. (right) X-ray reflectivity patterns (in color) shown against idealized models of the targeted nanolaminate (in black). (bottom-left) Grazing incidence in-plane diffraction pattern showing $hk0$ lattice planes.

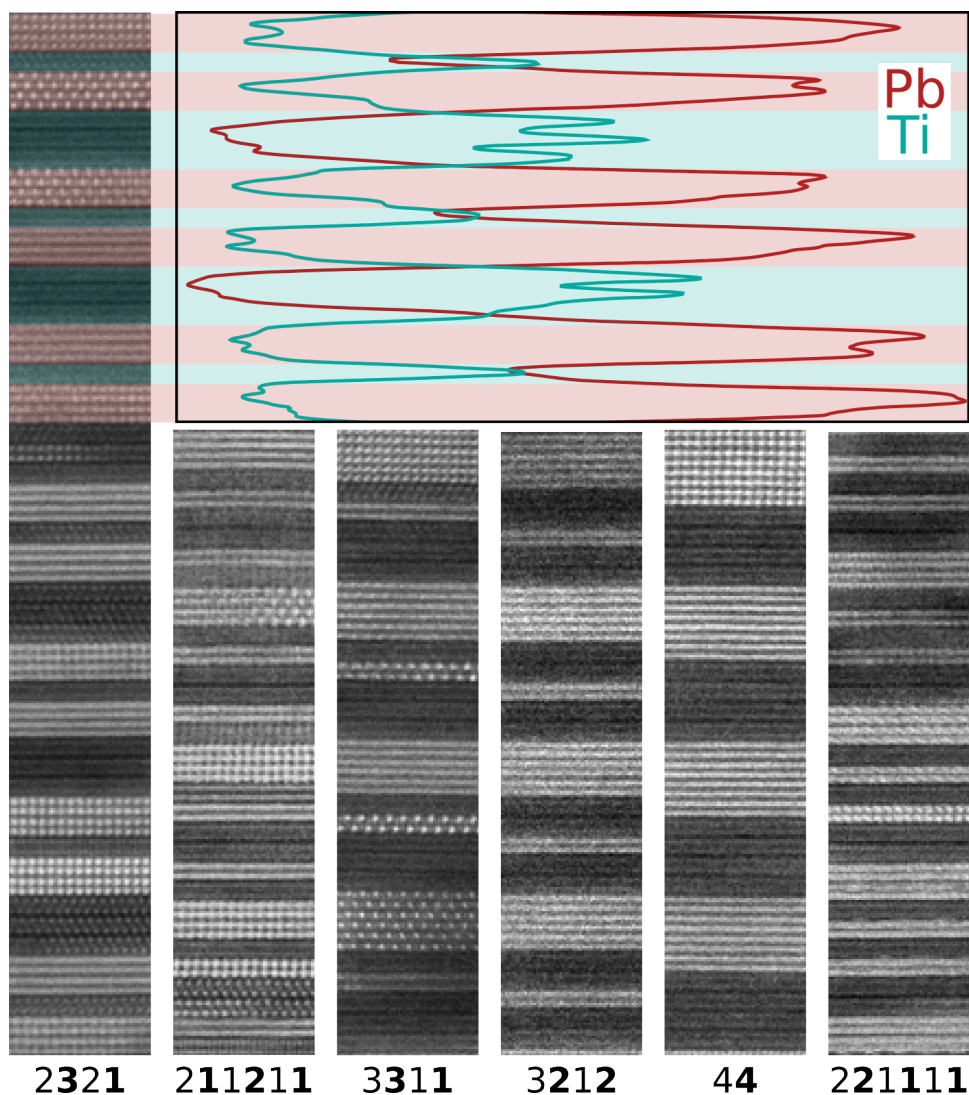


Figure 6.2. HAADF-STEM images of each nanolaminate highlighting the formation of the targeted nanoarchitecture, sharp interfaces between constituents, and rotational misregistration between layers. The colored traces show the relative intensity of characteristic X-ray signals from Pb and Ti when moving down the $k=2\mathbf{321}$ structure.

6.3.2. Transport Properties

Shown in Figure 6.3 is the temperature-dependent resistivity of the 6 nanolaminate samples. The upturn observed at low temperature is similar to those observed in $[(\text{PbSe})_{1+\delta}]_m(\text{TiSe}_2)_n$ compounds previously reported.^{12–14,22}

While most isomers have similar resistivity, it is immediately apparent that the **44** isomer stands out with a higher resistivity and the **221111** appears to have slightly lower resistivity relative to the other five. Additionally, the **3212** isomer, which is the only compound beside the **44** that doesn't contain TiSe_2 monolayers, also has higher resistivity than the other samples with buried interfaces in the unit cell. This could still be explained by variation in defect levels between samples as, in the semimetallic transport regime seen here, relatively small defect densities might significantly affect the mobility or carrier concentration and hence the conductivity.²³ To account for this potential variation, resistivity values can be normalized to their room-temperature values, as seen in Figure 6.3. In this arrangement we see that the ratio of $\frac{\rho}{\rho_{295K}}$ trends the same way as the absolute resistivity values, with the **44** and **221111** nanolaminates representing the highest and lowest normalized residual resistivity values, respectively. Generally, the upturn at low temperatures is seen to shift to lower temperatures in samples with a larger resistivity ratio $\frac{\rho_{295K}}{\rho_{min}}$, which also corresponds to a higher number of buried interfaces. The band alignment in PbSe-TiSe_2 nanolaminates has been previously proposed to result in charge transfer from PbSe into TiSe_2 and a resulting modulated p-n-p-n carrier type profile, in which the n-type bands in TiSe_2 dominate. The upturns have been associated with localization of carriers. The data suggests the localization occurs at lower temperatures in nanolaminates with more buried interfaces.

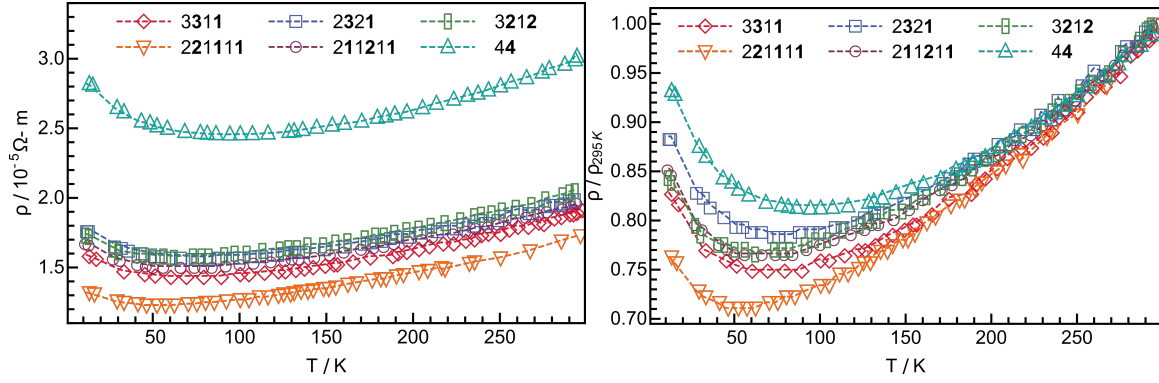


Figure 6.3. Temperature dependent resistivity of 6 [(PbSe)_{1+δ}]₄(TiSe₂)₄ nanolaminates. Both (left) measured values and (right) normalized values are shown.

Figure 6.4 shows carrier concentrations measured as a function of temperature for each isomer. The carrier concentrations were determined from the negative Hall coefficients assuming conduction from a single parabolic band. Nanolaminates with the same number of buried interfaces in k have similar carrier concentrations, with the **44** structure having by far the least and the **221111** representing the other bound. This suggests that charge exchange from the PbSe to the TiSe₂, which is assumed to be the source of mobile carriers in the nanolaminate, occurs most with maximum interfacial density of constituents. These data imply that the differences in absolute resistivity between structures with different numbers of buried interfaces are primarily due to carrier density fluctuation. However, as evidenced by the **221111** and **211211** nanolaminates which have the same number of interfaces, mobility differences account for their distinct resistivity values but similar carrier concentrations. While the carrier densities differ between structures with varying interface density, the normalized temperature dependent carrier concentrations, shown above the main plot, are very similar, suggesting the large difference in resistivity ratios is not due to the carrier concentration.

Using the resistivity and Hall data, the carrier mobilities were determined and are shown in Figure 6.5. The data have little variation between the various k , especially near room temperature. There is a steady increase in mobility with decreasing temperature that follows the trend of increasing resistivity ratio,

$\frac{\rho_{295K}}{\rho_{min}}$. This indicates the change in the resistivity ratio is due to an increase in mobility of the samples as opposed to changes in freeze-out of mobile carriers. As temperature decreases, the mobilities deviate from one another, arranging themselves such that those with highest resistivity suffer lowest mobility. Contrary to the room temperature values, higher low temperature mobilities correlate with increasing buried interface density. This is somewhat surprising as more interfacial scattering from the layers, which should be relatively temperature independent unlike other mechanisms (e.g. electron-electron or electron-phonon scattering), would intuitively be present in the structures with high interface density. The thinner layers of the high interface density laminates also typically show greater changes in mobility, which suggests they are likely able to accommodate a greater number coherent phonon modes.

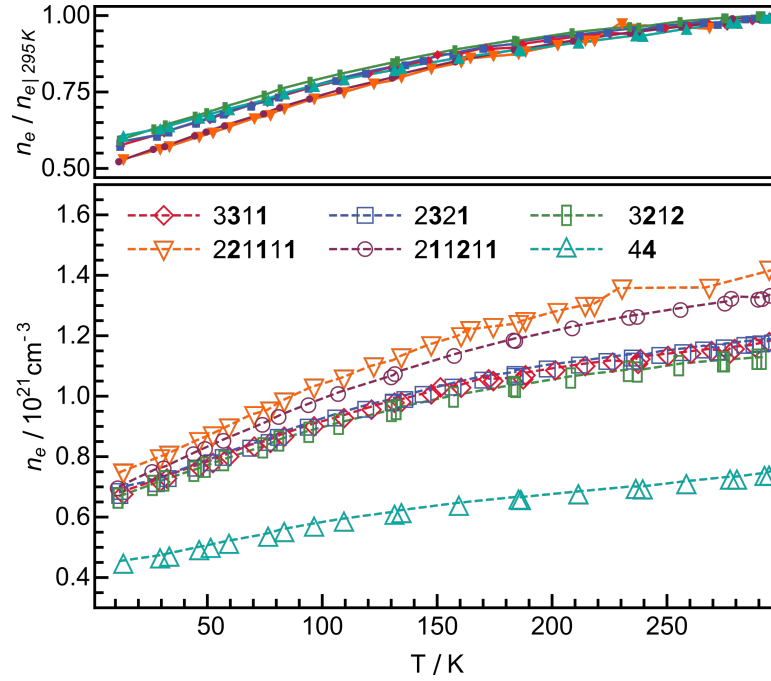


Figure 6.4. Temperature dependent carrier concentration of 6 $[(\text{PbSe})_{1+\delta}]_4(\text{TiSe}_2)_4$ nanolaminates. Values are calculated from Hall coefficients assuming a single n-type band. Both (bottom) measured values and (top) normalized values are shown.

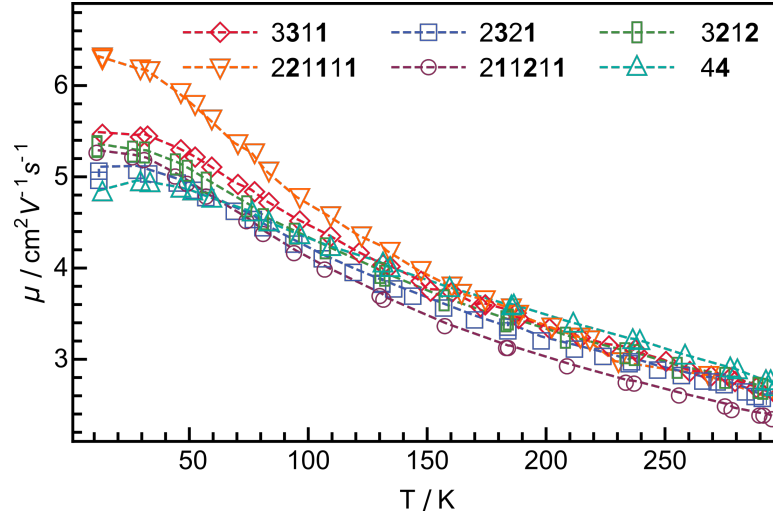


Figure 6.5. Temperature dependent mobility of 6 $[(\text{PbSe})_{1+\delta}]_4(\text{TiSe}_2)_4$ nanolaminates calculated from resistivity and carrier concentration data.

The room temperature Seebeck coefficient was also taken on each compound presented. These values are shown in Figure 6.6. Additional $[(\text{PbSe})_{1+\delta}]_4(\text{TiSe}_2)_4$ nanolaminates with various k that are not included in the bulk of this study were also prepared for room-temperature transport measurements. The specific samples chosen for full analysis were synthesized during the same equipment cycle and set of precursor deposition parameters in order to target a similar distribution of kinetically trapped defects. The additional samples are included to help assess the repeatability of results. The negative Seebeck coefficients agree with the Hall measurements that electrons are the majority carriers. Furthermore, they systematically decrease (increase in magnitude) as the interface density decreases in the $[(\text{PbSe})_{1+\delta}]_4(\text{TiSe}_2)_4$ nanolaminates.

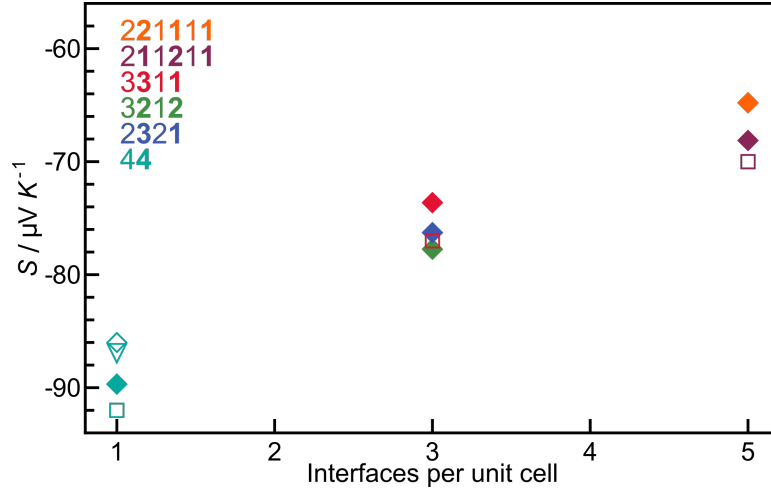


Figure 6.6. Room-temperature Seebeck coefficient of $[(\text{PbSe})_{1+\delta}]_4(\text{TiSe}_2)_4$ nanolaminates. Colors correspond to nanoarchitecture and symbols correspond to precursor parameters.

The room-temperature power factor is shown in Figure 6.7. This parameter depends on both the Seebeck coefficient and the electrical resistivity of the material ($S^2\rho^{-1}$ or $S^2\sigma$). Introducing interfaces into the $[(\text{PbSe})_{1+\delta}]_4(\text{TiSe}_2)_4$ unit cell systematically lowers both the resistivity and the magnitude of the Seebeck coefficient resulting in a region of optimal performance, as seen in the structures with an intermediate number of buried interfaces.

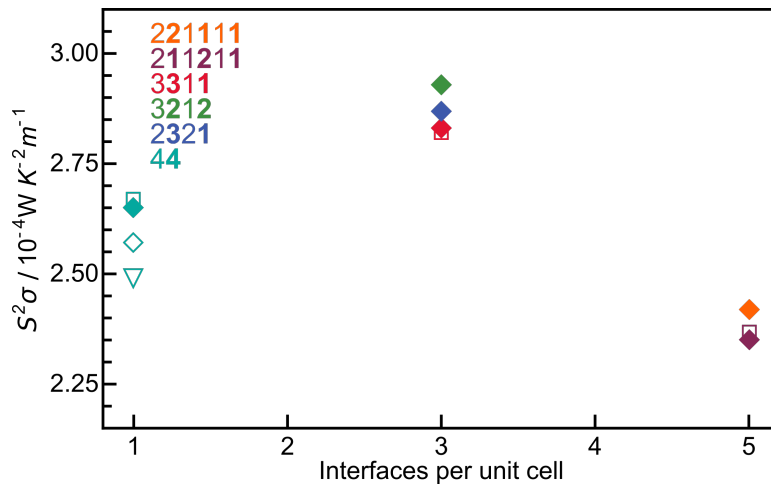


Figure 6.7. Room-temperature power factor of $[(\text{PbSe})_{1+\delta}]_4(\text{TiSe}_2)_4$ nanolaminates. Colors correspond to nanoarchitecture and symbols correspond to precursor parameters.

While no specific nanostructure with a particular stacking sequence stands out, the number of buried interfaces consistently appears to affect the transport properties of the compound. This observation provides opportunity for course-grain surveying the parameter space when optimizing the thermoelectric performance of a nanolaminate system. As the number of layers per repeating unit increases, so to do the number of available combinations. For example, while the current study has 6 unique sequences and 3 options for buried interface density, increasing the number of layers by just 1 unit of each constituent allows for 15 unique sequences and 4 options for buried interface density.²⁴ As the number of layers in the repeating unit further increases, the number of unique stacking sequences increases far more rapidly than the number of interfaces. By first selectively synthesizing and probing a single structure with each interface density, the parameters near which the optimal compound within the series might be determined without having to survey all possible combinations.

6.4. Conclusion

We investigated the transport properties of $[(\text{PbSe})_{1+\delta}]_4(\text{TiSe}_2)_4$ nanolaminates undergoing local nanoarchitectural changes by the introduction buried interfaces into the unit cell, while maintaining the global composition and structure. X-ray diffraction, HADDF-STEM, and STEM-EDS confirm the formation of the nanolaminate structures. The compounds exhibit similar transport properties to each other owing to the similarities in the composition and structure, but small variation trending with the number of buried interfaces in the repeat unit is present. This highlights that rationally controlling the nanoarchitecture of nanocomposite materials allows for further optimization of the transport behavior beyond the choice of chemical composition and global arrangement.

6.5. Bridge

As seen in chapter VI, the isomerism available in nanolaminate structures allows for exploring the details of subtle structural change on the transport properties. Composition of a nanolaminate can also be modified by changing the relative ratio of each constituent. Chapter VII investigates the case of increasing the relative amount of TiSe_2 layers in $[(\text{PbSe})_{1+\delta}]_l(\text{TiSe}_2)_n$ nanolaminates as a means to control the mobile carrier concentration and enhance the thermoelectric power factor.

CHAPTER VII

CARRIER DILUTION IN TiSe₂ BASED INTERGROWTH COMPOUNDS FOR ENHANCED THERMOELECTRIC PERFORMANCE

The work in the following chapter was accepted 2015-07-16 for publication in *Journal of Materials Chemistry C* (DOI: 10.1039/C5TC01570G). It is coauthored with Devin Merrill, Daniel Moore, and David Johnson. Devin Merrill assisted with sample preparation and manuscript preparation. Daniel Moore assisted with sample preparation and characterization. David Johnson is my advisor and I am the primary author.

7.1. Introduction

The figure of merit for thermoelectric materials $zT = \frac{\alpha^2 \sigma}{\kappa} T$ consists of three terms – the thermovoltage (α), electrical conductivity (σ), and thermal conductivity (κ). The material parameters for the optimization of these factors are often contradictory (both structurally and electrically), making the discovery compounds with of high values of zT particularly difficult. A productive approach has been synthesizing nanocomposite materials, where electronic interactions between constituents provide favorable electronic gains (high $\alpha^2 \sigma$, called the power factor) while the interfaces between them or the nanoparticle inclusions scatter phonons, resulting in a low thermal conductivity.¹⁻⁴ A subset of composite thermoelectric materials are nanolaminates.^{5,6} The regular interfaces in these materials enables the structure to be determined, aiding in the development of structure-property relationships essential to understanding the cause of high zT values.⁷

A promising family of naturally occurring nanolaminates are chalcogenide misfit layered compounds (MLCs) – thermodynamically stable crystalline materials consisting of an intergrowth between a transition metal dichalcogenide, TX₂, and a distorted rock-salt, MX. These two constituents stack along the *c*-axis such that an MX bilayer is interleaved with either one or two TX₂ trilayers. The general formula for these compounds is (MX)_{1+ δ} (TX₂)_{*n*}, where 1+ δ is the ratio of the in-plane areas per cation of each constituent, and *n* is the number of TX₂ layers per unit cell along the *c*-axis. This unique class of

compounds have been extensively studied and reviewed.⁸ They have low lattice conductivities for crystalline solids, due to phonon mass mismatch and the large number of interfaces between constituents.^{2,9,10} Several mechanisms have been suggested to account for the surprising stability of the MLC structure, with stabilization from charge transfer between constituents the leading hypothesis.¹¹ In-plane electrical transport is dominated by the high-mobility TX_2 layer⁸, so charge transfer from the stabilization is effectively modulation doping the dichalcogenide layers. Systems with identical TX_2 layers but different MX exhibit notably different transport properties as evidenced in the $(\text{MS})_{1+\delta}(\text{TiS}_2)_2$ ($\text{M} = \text{Sn, Pb, Bi}$) compounds.¹²

The low thermal conductivities and promising electrical properties of misfit compounds make them interesting candidates as thermoelectric materials. The most promising thermoelectric chalcogenide MLCs are RE/Nb sulfides⁹ and Pb, Sn/Ti sulfides¹², with zT values of close to 0.4 reported for $(\text{SnS})_{1.2}(\text{TiS}_2)_2$. The TiX_2 based compounds have unusually high Seebeck coefficients given carrier concentrations of 10^{21} cm^{-3} . The band structures of both TiS_2 and TiSe_2 have several pockets and steep density of state gradients near EF, both of which result in high thermovoltages.^{13,14} However, it has not been possible to control composition or structure of MLCs beyond the thermodynamic phase width using classical synthetic approaches, which hinders their utility as model systems and their optimization as potential high performance materials. An additional difficulty in evaluating layered compounds as thermoelectric materials is determining zT , as the anisotropy makes it difficult to comparably make each of the necessary measurements. In-plane electrical properties and cross-plane thermal properties are relatively simple to determine, but measuring cross-plane electrical properties and in-plane thermal properties is challenging.

Recently, a new class of kinetically stabilized thin-film materials closely related to misfit layered compounds has been synthesized. These intergrowth compounds, called ferecrystals, also consist of MX and TX_2 layers but do not have registration between constituents, with independent lattice parameters and rotational (turbostratic) disorder observed across interfaces.¹⁵ The turbostratic disorder is very effective at disrupting phonons causing these

compounds to have even lower lattice conductivities than MLCs.¹⁵ In-plane total thermal conductivities of insulating ferecrystals have been measured to be on the order of $0.5 \text{ W m}^{-1} \text{ K}^{-1}$, which is quite low for a crystalline solid.¹⁶ In-plane thermal conductivities of promising MLCs for thermoelectric applications are about twice as large.² This suggests that zT enhancement in these systems will most likely occur by increasing the power factor, the numerator in the expression for zT . Low electron-phonon coupling interactions have also been observed, resulting in the reduction of the temperature dependence of electrical conductivity by about an order of magnitude over analogous MLCs, which are already quite low.^{17,18} The kinetic synthesis route of ferecrystals also allows for designed layering schemes, with increasing MX units¹⁹, increasing TX₂ units²⁰, and even inorganic structural isomers²¹ all being reported. A similar chemical formula to MLCs is used for ferecrystals, but an integer, m , may be added to express the number of rock-salt bilayers present in the repeating unit. The synthetic control allows for systematic exploration of how several structural changes may affect material properties.

The $[(\text{PbSe})_{1+\delta}]_m(\text{TiSe}_2)_n$ ferecrystals have been one of the most-studied systems in the ferecrystal class of compounds. The $m = 1$, $n = 1, 2$ compounds have been previously reported in detail,^{18,22} with a brief overview of all compounds with m , $n \leq 3$ also recently discussed.⁷ Encouraging results from these first reports prompted our systematic investigation of these thermoelectric materials as reported here. The strong correlations between the thermovoltage, electrical conductivity, and thermal conductivity makes optimization of thermoelectric materials inherently difficult. Each of these factors depends differently on carrier concentration, leading to an optimal carrier concentration for maximization of the figure of merit. Assuming the donor-acceptor model in PbSe-TiSe₂ ferecrystals, carrier concentration is an inherently tunable property by varying m and n . Calculations from previously reported data show the power factor increases with additional TiSe₂ layers from a decrease in carrier density. Here, we report the synthesis and transport properties of several $(\text{PbSe})_{1+\delta}(\text{TiSe}_2)_n$ ferecrystals with $1 \leq n \leq 18$. A decrease in carrier concentration is observed as n is increased, as the charge donated by the PbSe bilayer is diluted over more TiSe₂ layers. An increase in the Seebeck coefficient results,

increasing the power factor by over 600% when increasing n from 1 to 18. Finally, while charge dilution appears to be an effective means of raising the power factor, a correlation in high power factor with mobility is also observed, independent of the thickness of the TiSe_2 constituent.

7.2. Experimental

Samples were deposited on (100) oriented Si and amorphous quartz substrates using the modulated elemental reactants (MER) technique.²³ Pressure was kept under 5×10^{-7} torr and deposition rates were under 0.1 nm s^{-1} . Pb and Ti sources were evaporated using electron guns and Se using a Knudsen effusion cell. Substrates were held approximately 1 meter above the sources and were sequentially exposed to sources to build a layered precursor. Samples were generally 50 nm thick, though some variation is necessary to build an integer number of unit cell repeats. The TiSe_2 constituent was deposited first. As an example, deposition for a $(\text{PbSe})_{1+8}(\text{TiSe}_2)_3$ sample would consist of repeating a Ti-Se-Ti-Se-Ti-Se-Pb-Se sequence until the desired total thickness is reached. While not explicitly characterized in the present work, a small excess of Se has previously resulted in the best final samples.²⁴ Prior to thermal treatment, precursor thin-films consisted of precisely stacked amorphous layers. Each precursor was heated at 350°C for 30 minutes in a N_2 atmosphere to self-assemble the desired ferecrystal compound.

Out-of-plane diffraction patterns were taken in a coupled θ - 2θ geometry on a Bruker D8 Discover diffractometer using Cu-K α radiation. In-plane diffraction patterns were collected at the Advanced Photon Source, beamline 33BM-C, using 12.49 keV radiation on a stationary sample with the source held at a small constant incident angle (0.2 - 0.5°) in the out-of-plane direction, to increase illumination volume. The cross-section used for high angle annular dark field scanning transmission electron microscopy (HAADF-STEM) was prepared with focused ion beam milling on an FEI Helios 600 Nanolab. The HAADF-STEM images were collected with an FEI Titan 80–300 using 300 kV accelerating voltage, 50 pA of current, and a 240 mm camera length.

Electrical measurements were carried out on samples deposited on amorphous quartz substrates in cross patterns. All measurements were made

on a characterization system built in-house with a closed-cycle He cryo system capable of operating from 20-300 K. Resistivity measurements were made using the van der Pauw method with indium leads attached to the ends of the crosses. Hall measurements were made in the same geometry. The thermovoltage was measured with copper-constantan thermocouple leads by cooling one half of the sample slightly below room temperature ($\Delta T < 2$ K) and letting it relax back. During this process, temperature was measured on each side of the sample and then thermovoltage deduced from the corrected dV/dT slopes between like thermocouple junctions.

7.3. Results and Discussion

7.3.1. Structural

Out-of-plane diffraction patterns of the $(\text{PbSe})_{1+\delta}(\text{TiSe}_2)_n$ ferecrystals prepared in this study are shown in Figure 7.1. In this geometry the highly oriented ferecrystal samples only show peaks corresponding to the $00l$ direction, which corresponds to the stacking of layers. A systematic increase in the c -axis lattice parameter is apparent as n is increased, indicating the formation of a growing superstructure. The c -axis lattice parameters increase by 0.603(1) nm for each n , from the insertion of additional TiSe_2 layers into the stacking sequence. This increase is very close to the bulk c -axis lattice parameter of TiSe_2 , 0.6008 nm.²⁵ This increase also corresponds well with the previously published values for PbSe-TiSe_2 containing intergrowths, which grew by 0.608 nm when the number of TiSe_2 layers within a repeat was increased from 1 to 2.^{18,22} Extrapolating the trend in lattice parameter to $n = 0$ gives a value of 0.61(1) nm for the PbSe bilayer thickness, as seen in Figure 7.1b. This corresponds well with thicknesses previously reported for PbSe containing ferecrystal compounds, where an increase in c -axis lattice parameter of 0.612 nm was reported per addition of PbSe bilayer in $[(\text{PbSe})_{1.14}]_m(\text{NbSe}_2)_{1.19}$. While this is consistent with the expected structures of the repeating units along the stacking direction, the $00l$ scans provide no information as to the in-plane structures of the constituent phases.

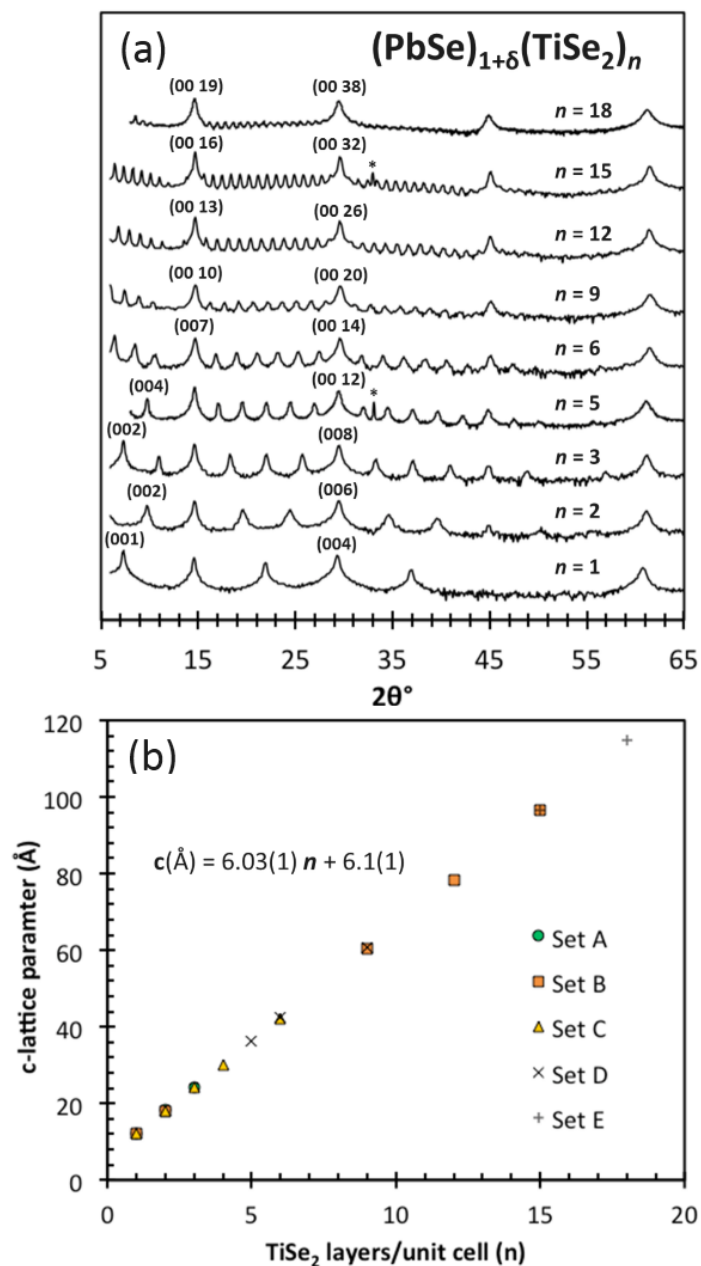


Figure 7.1. Data corresponding to the 00 l reflections of the $(\text{PbSe})_{1+\delta}(\text{TiSe}_2)_n$ ferecrystals. (a) Diffraction patterns plotted on a log scale and (b) c -lattice parameters as a function of n . Different sets correspond to samples prepared in different deposition cycles.

To confirm the formation of the targeted constituent phases, in-plane diffraction was taken on samples with n up to 4 at the APS, as shown in Figure 7.2. Due to the texture in the samples, only $hk0$ reflections are observed.

The random $hk0$ orientation of crystallites within the a - b plane of the samples results in all expected $hk0$ reflections being observed. This lack of in-plane texture is characteristic of ferecrystal films, which can be thought of as precise layers of separate 2D powders. The relative intensities of the reflections from each constituent roughly correspond to the fraction of that phase. Due to many overlapping reflections, this is easiest to observe in the distinct peaks arising from the PbSe (220) and TiSe_2 (110) planes. A systematic increase in the relative intensity from the TiSe_2 is apparent as n is increased. Increasing the number of TiSe_2 layers does not appear to shift the reflections of either constituent suggesting in-plane distortions are either absent or unchanging as n is increased.

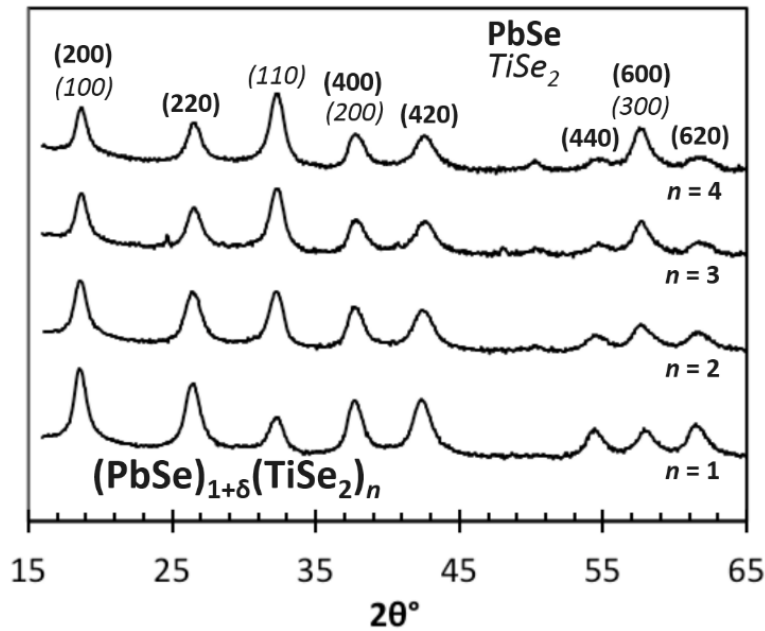


Figure 7.2. Log-scale in-plane diffraction patterns corresponding to $hk0$ reflections.

HAADF-STEM imaging was used to further verify the structure of the desired compounds. Figure 7.3. contains an image of an $n = 12$ sample. The bright spots correspond to atomic columns of Se atoms along the (110) zone-axis of TiSe_2 and the bright ‘smears’ are PbSe layers which are off of a zone-

axis. As expected for TiSe_2 in general (including when synthesized from MER), the TiSe_2 layers within each block of 12 TiSe_2 are stacked in a 1-T arrangement.²⁶ The off-axis orientations in the TiSe_2 blocks above and below are evidence of turbostratic disorder between layers and the off zone axis orientation of PbSe reflects the turbostratic disorder between constituents.

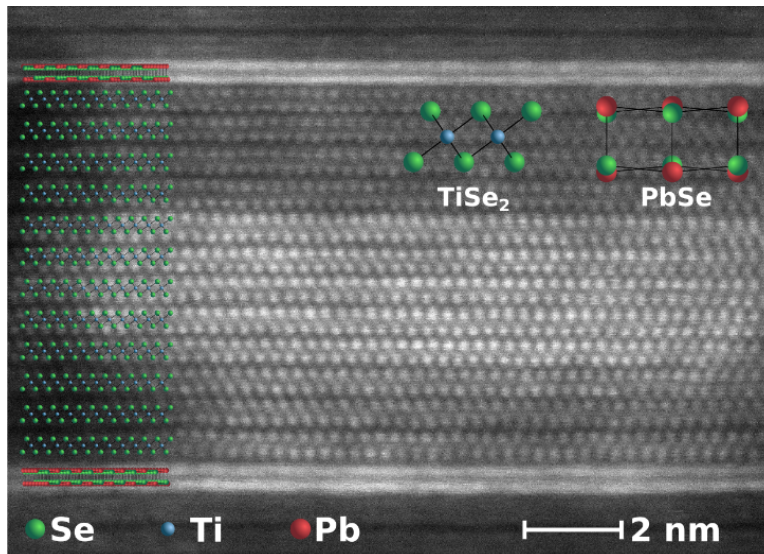


Figure 7.3. HAADF-STEM image of the $(\text{PbSe})_{1+6}(\text{TiSe}_2)_{12}$ sample showing the 1-T polymorph for the block of 12 TiSe_2 layers.

7.3.2. Electrical

There has been extensive discussion in intergrowth literature suggesting that charge donation between constituents is an important stabilizing mechanism.¹¹ In the case of TiSe_2 compounds, electrons are transferred from the MSe layer to unoccupied Ti-3d states. A simple rigid band picture suggests the donated charge would partially deplete the Pb-6p band in PbSe as shown in Figure 7.4., which schematically outlines the expected behavior of the $(\text{PbSe})_{1+6}(\text{TiSe}_2)_n$ system. As the number of TiSe_2 layers increases the donated charge is spread across more $(n + 1)$ layers, resulting in a lower carrier density in the Ti-3d band. Diagrams similar to Figure 7.4. are often used in the discussion of stacked monolayers or bilayers.^{8,17} For thin layers, it is reasonable to consider charge to be spread approximately evenly throughout a constituent

block as distances are short enough for considerable wavefunction overlap across layers. On the other hand, for high n compounds one can begin to consider charge depletion regions within the TiSe_2 constituent. In this regime, conventional band-bending diagrams become meaningful and calculations of absolute band energies would prove invaluable for further analysis. However, at present we consider a homogeneous distribution of carriers within the TiSe_2 constituent for all values of n .

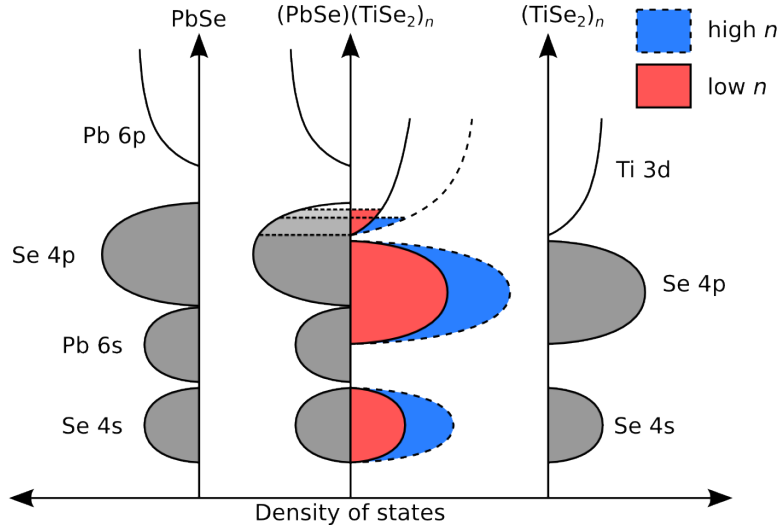


Figure 7.4. Density of state schematic for $(\text{PbSe})_{1+\delta}(\text{TiSe}_2)_n$ intergrowths for both low (red) and high (blue) values of n . As seen in the central portion, the charge donated from the PbSe layers increases with n but the number of populated bands in TiSe_2 decreases, effectively reducing the carrier density relative to a low n compound. From top to bottom, the horizontal black lines illustrate the filled levels for low, high, and infinite n .

Assuming band structure is not heavily perturbed by incorporation into the superlattice, electron conduction through the light TiSe_2 bands should dominate over hole conduction through the heavy PbSe bands. This is supported by the observation of negative Hall coefficients for all samples (not shown), indicating electrons are the majority carrier. Assuming a single carrier through a simple parabolic band, the carrier concentration can be determined from Hall coefficient by the relationship $n_e = -\frac{1}{R_H e}$. Figure 7.5a. shows the dependence of carrier concentration on the number of TiSe_2 layers in the unit

cell. The scatter in the data is caused in part by the samples being prepared in different deposition cycles, resulting from larger variation in the Pb to Ti ratio compared to samples deposited in the same cycle.²⁷ The trend suggests that charge is being diluted as more TiSe₂ layers are added, and the decrease roughly follows the expected functional form of $n_e = n_i + \frac{n_d}{n+1}$, where n_e is the total carrier concentration, n_d is a constant expressing the infinite limit of charge donated to TiSe₂ (spread among n TiSe₂ trilayers and 1 PbSe bilayer), and n_i is the existing carrier density in TiSe₂ due to defects. A fit of this form with $n_i = 9.4 \times 10^{20}$ and $n_d = 2.8 \times 10^{21}$, shown by a solid line in Figure 7.5a., indicates that for an $n = 1$ compound the amount of donated charge from PbSe and the intrinsic carriers in TiSe₂ are of the same order. The reduction of carrier density in the conducting TiSe₂ layers with increasing n is promising for thermoelectric applications. Further reduction of n_e by lowering n_i (by increasing sample quality) and/or n_d (by appropriately alloying or doping the PbSe layers) may both be possible^{28,29}, though reduction of the intrinsic component would result in the highest gains. Figure 7.5b. shows the temperature dependence of the carrier concentration for a subset of samples, each normalized to its value at 295K. For all samples the number of carriers gradually increases as temperature increases. The samples with large TiSe₂ blocks increase much more steeply at high temperatures, suggesting that carriers might be thermally activated into a conducting state. The change in carrier density is not as abrupt as in most semiconductors because TiSe₂ has a very narrow band-gap and very little thermal energy would be required to promote electrons into a conducting band.³⁰ In contrast, the low n samples follow behavior expected from a heavily doped or metallic system where carrier promotion is not an activated process.

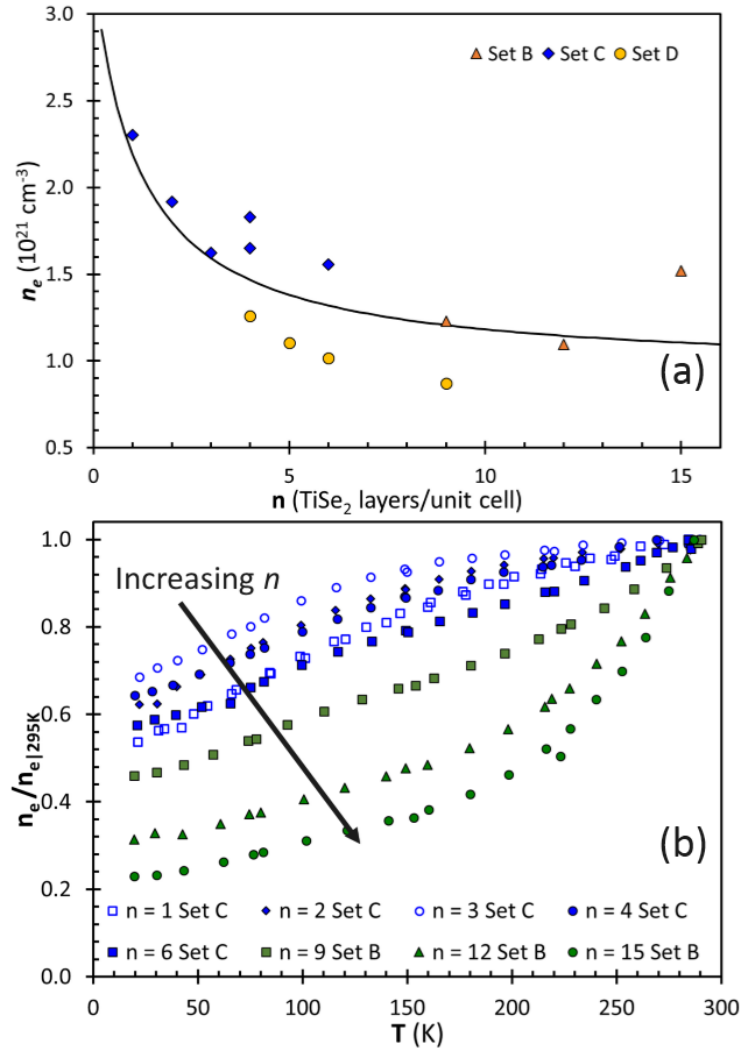


Figure 7.5. (a) Room temperature carrier concentrations for the $(\text{PbSe})_{1+\delta}(\text{TiSe}_2)_n$ samples determined from van der Pauw Hall measurements assuming a single band model. The black line shows a fit of the expected functional form, $n_e = n_i + \frac{n_d}{n+1}$. (b) Temperature dependence of the normalized carrier concentration for the $(\text{PbSe})_{1+\delta}(\text{TiSe}_2)_n$ samples showing the change as a function of increasing thickness of the TiSe_2 layer. The arrow indicates the general trend.

The measured room temperature values of the Seebeck coefficient are shown in Figure 7.6a. All samples have a negative thermovoltage, agreeing with the Hall coefficient in showing electrons are the majority carrier. The magnitude of the Seebeck coefficient increases as n is increased, with some variation between depositions. The Pisarenko relationship, which assumes simple

parabolic bands and a single carrier, predicts an increase in the thermovoltage magnitude as carrier concentration is decreased. Figure 7.6b. shows the Seebeck coefficient as a function of carrier concentration. The solid line shows the Pisarenko relationship assuming an effective mass of $6.3 m_e$ (calculated effective masses range from $5-7 m_e$). The samples at low n deviate from the curve, due to a loss of dimensionality and band degeneracy when approaching (and reaching) a stack of repeating PbSe-TiSe₂ monolayers or to increased deviations associated with assuming a single band model.

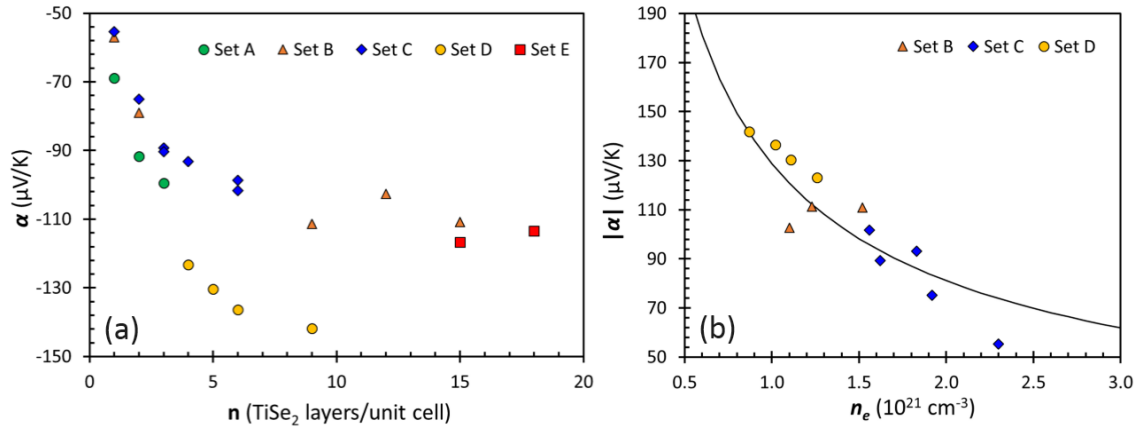


Figure 7.6. (a) Room temperature Seebeck coefficients for the $(\text{PbSe})_{1+\delta}(\text{TiSe}_2)_n$ samples. (b) Seebeck coefficient versus carrier concentration shown as a Pisarenko plot with $m^*=6.3m_e$.

In-plane resistivity is shown for all samples in Figure 7.7. The magnitudes are typical for conduction in a semimetal. At room temperature, the resistivity of the $n = 2$ ferecrystal is lower than for the analogous MLC, due to reduced electron-phonon scattering. However, as phonon modes are frozen in the MLC by reducing the temperature, the resistivity of the extended crystal drops below that of the nearly temperature independent ferecrystal. Samples with the thinnest TiSe₂ layers have an upturn in resistivity at low temperatures suggesting localization of carriers. As the TiSe₂ thickness increases, the temperature dependence becomes more metallic like, with resistivity decreasing as temperature is decreased. There is no clear trend in the magnitude of the resistivity as the number of TiSe₂ layers is increased. This could be due to a

carrier concentration reduction being cancelled by an increased mobility and may bode well for thermoelectric applications, as both would positively affect the power factor. However, both of these quantities are defect sensitive and ferecrystals have been shown to form with wide degrees of defect incorporation.²⁷

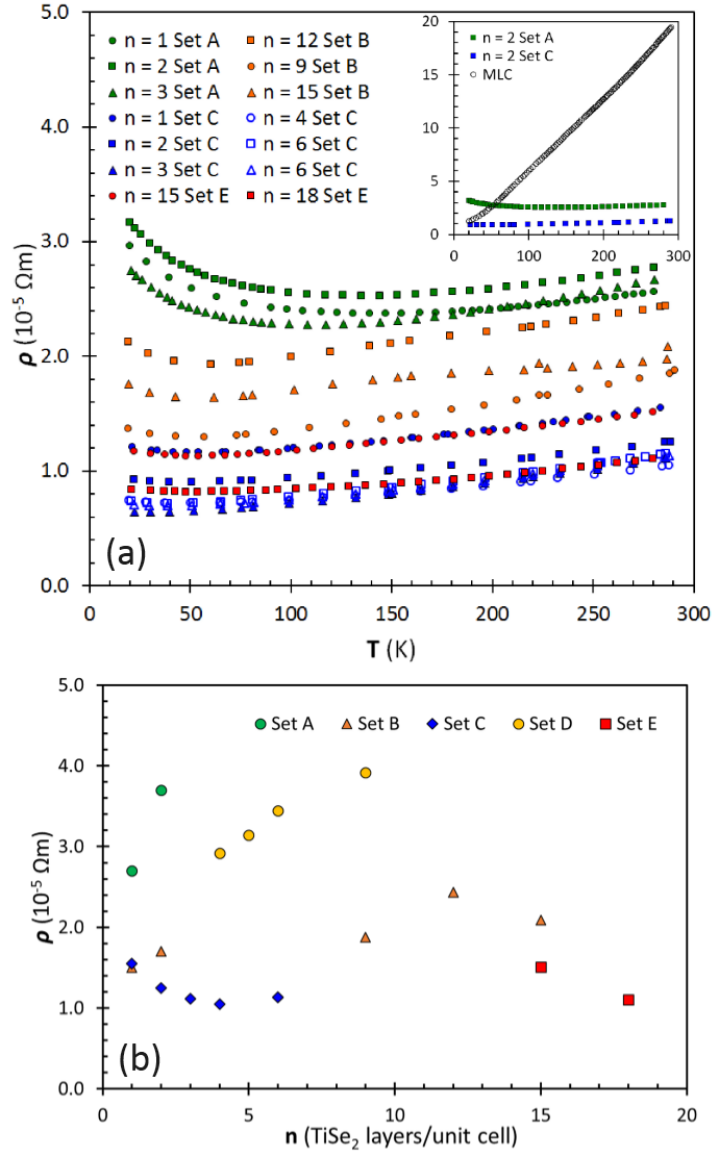


Figure 7.7. (a) Temperature dependent resistivity for the $(PbSe)_{1+\delta}(TiSe_2)_n$ samples. (b) Room temperature resistivity versus n , with the variation between sample sets highlighted.

The single-band approximation allows for calculation of Hall mobility from the Hall coefficient and resistivity. An increase in mobility may be expected from high n compounds, as charge is diluted over larger volumes resulting in more conducting states per carrier and less carrier interaction. Additionally, higher mobility might be expected from reduced interface scattering from carriers with velocity components in the cross-plane direction. However, even with these considerations, no trending in mobility is observed as a function of n . While this may be an indicator that modulation doping of ferecrystals does not have an effect on mobility, the more likely scenario is that mobility is dominated by defects and controlling these defects to maximize mobility is the next synthetic step in improving thermoelectric performance.

The room-temperature power factor, calculated from the thermovoltages and resistivity values discussed above ($\alpha^2 \rho^{-1}$), increases as a function of n , as shown in Figure 7.9. When referring back to the trends of n with resistivity (Figure 7.7.) and Seebeck coefficient (Figure 7.6.), it appears an increase in power factor predominantly comes about through an increase in the magnitude of the thermovoltage, since no clear trending between resistivity and n was observed. This is somewhat contrary to many systems, where increasing the Seebeck coefficient comes at the expense of raising band mass, severely affecting mobility and reducing the overall power factor.³¹ The $n = 18$ sample has a power factor of $11.6 \text{ mW K}^{-2} \text{ cm}^{-1}$, which to the authors' knowledge is the highest reported value in the chalcogenide MLC and ferecrystal families (summarized in Table 7.1.). This is particularly encouraging as measurements were made at 300K, lower than the typical peak performance regime, especially considering the weak electron-phonon coupling of ferecrystals. However, it must be mentioned that the $(\text{PbSe})_{1+\delta}(\text{TiSe}_2)_n$ ferecrystals begin to decompose above approximately 650 K.

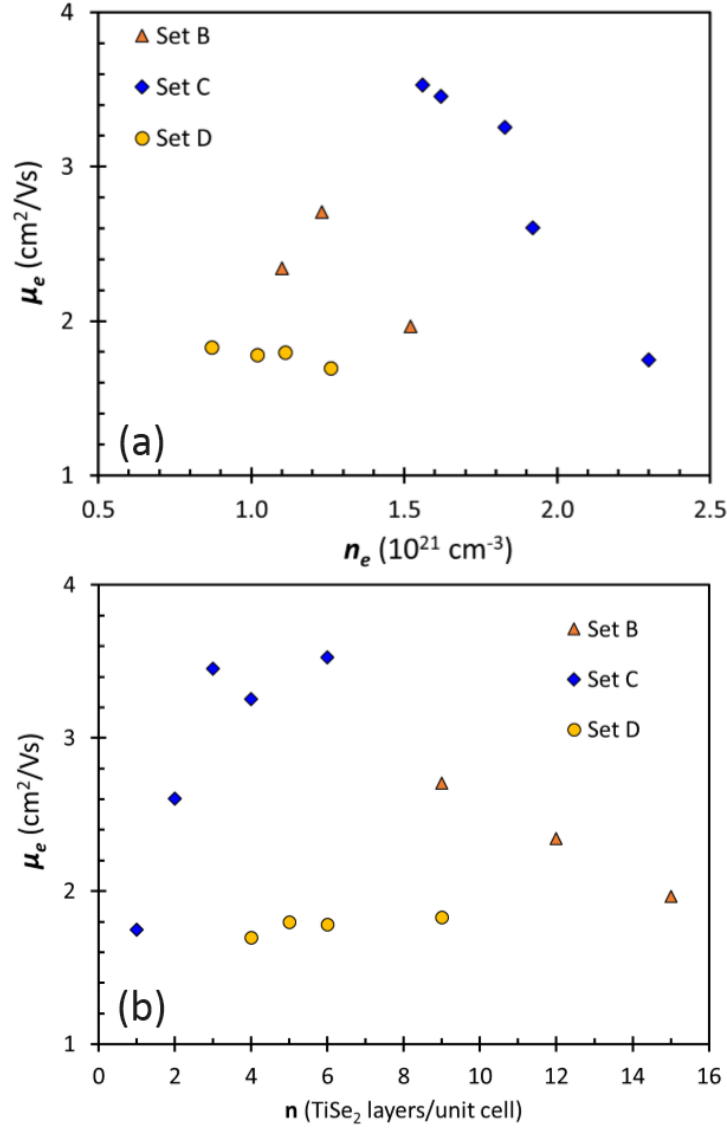


Figure 7.8. (a) Room temperature mobility values as a function of carrier concentration for the $(\text{PbSe})_{1+\delta}(\text{TiSe}_2)_n$ samples. (b) Room temperature mobility values plotted versus the thickness of the TiSe_2 layer in the unit cell.

Mobility, which affects the power factor through the resistivity, appeared uncorrelated with n . However, plotting power factor against carrier mobility shows a monotonically increasing relationship, indicating high power factor in these samples is a result of a simultaneous increase in both the thermovoltage and conductivity. This is illustrated in Figure 7.9b. The labels next to each point denote n for that sample. The mobility plot strongly suggests future

optimization of ferecrystal materials for thermoelectric applications should focus on tuning mobility. Previous studies from similar materials synthesized from designed precursors and the MER process have shown an order of magnitude mobility increase is possible by the reduction of defects through vapor annealing.²⁸ These treatments also considerably lowered carrier densities, suggesting a potential route for considerable materials improvement in the PbSe-TiSe₂ ferecrystal system.

Table 7.1. Summary of room-temperature power factors for published ferecrystal and misfit layered compounds.

Compound	ρ (10 ⁻⁵ Ω -m)	α (μ V K ⁻¹)	$\alpha^2\rho^{-1}$ (mW K ⁻² cm ⁻¹)	Reference
(PbSe)_{1+δ}(TiSe₂)₁₈	1.11	-114	11.6	*
(PbSe)_{1+δ}(TiSe₂)₁₅	1.51	-117	9.0	*
(PbSe)_{1+δ}(TiSe₂)₆	1.14	-102	9.1	*
(SnSe)_{1.2}(TiSe₂)	1.16	-77	5.1	32
(SnS) _{1.2} (TiS ₂) ₂	0.59	-70	8.3	12
(PbS) _{1.18} (TiS ₂) ₂	0.53	-56	6.0	12
(BiS) _{1.2} (TiS ₂) ₂	0.37	-45	5.5	12
(LaS) _{1.14} (NbS ₂)	0.5	34	2.3	2
(LaS) _{1.20} (CrS ₂)	14.5	-60	1.8	2
(BiSe) _{1.09} (TaSe ₂)	0.28	-18	1.2	33
(BiSe) _{1.10} (NbSe ₂) ³³	0.20	-8	0.3	33
(TbS) _{1.21} (NbS ₂)	0.25	-5	0.1	34
(TbS) _{1.20} (TaS ₂)	0.098	0.5	0.003	34
(DyS) _{1.22} (NbS ₂)	0.16	-14	1.2	34
(DyS) _{1.21} (TaS ₂)	0.07	2	0.06	34

Bold – ferecrystal compounds

* – this work

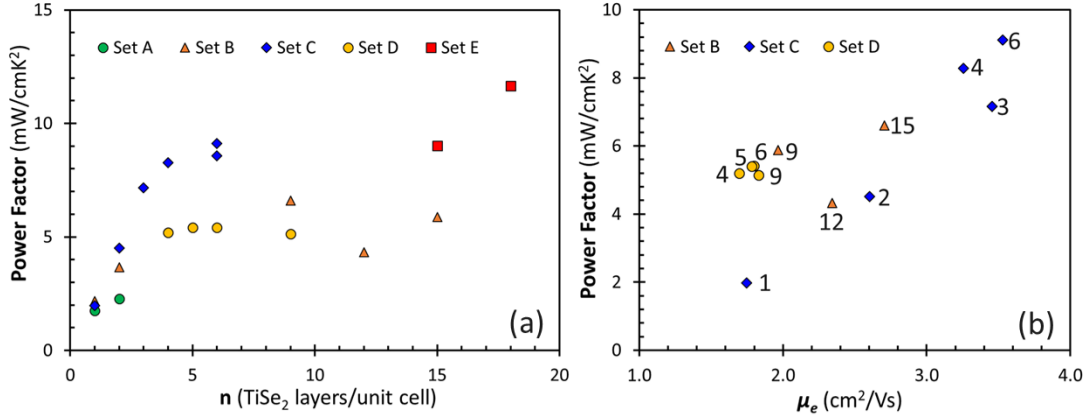


Figure 7.9. (a) Room temperature power factor as a function of the thickness of the TiSe₂ layer in the unit cell for the (PbSe)_{1+δ}(TiSe₂)_n samples. (b) Room temperature power factor plotted versus room temperature mobility values. The adjacent numbers indicate n .

7.4. Conclusions

The synthesis of (PbSe)_{1+δ}(TiSe₂)_n with $1 \leq n \leq 18$ is reported and characterized. Charge donated from the PbSe layers is diluted across the conducting TiSe₂ layers as n is increased. This leads to higher Seebeck coefficients without an adverse effect on the resistivity of the compounds. The power factor increases with increasing n , showing that carrier dilution through modulation doping is an effective means of enhancing transport properties in nanolaminate thermoelectric materials. However, for ferecrystal systems increasing the carrier mobility by decreasing incorporated defects appears to be the best path forward. Annealing samples in Se vapor is one approach that might help.

7.5. Bridge

Chapters IV-VII have investigated the effects of adjusting the nanoarchitecture of ([PbSe]_{1+δ})_m(TiSe₂)_n materials on the transport behavior, generating several structure-property relationships along the way. Chapters VIII and IX move forward with similar experiments in the ([SnSe]_{1+δ})_m(TiSe₂)_n chemical system, which is similar but undergoes significant structural distortion in SnSe as the layer size changes.

CHAPTER VIII

HIGH THERMOELECTRIC POWER FACTOR AT CRYOGENIC TEMPERATURES IN $([\text{SnSe}]_{1+\delta})_1(\text{TiSe}_2)_n$ HETEROSTRUCTURE NANOLAMINATES

At the time of writing the work in this chapter is unpublished, but a manuscript is planned to be coauthored with Danielle Hamann, Devin Merrill, and David Johnson. Danielle Hamann and Devin Merrill assisted with sample preparation and characterization. David Johnson is my advisor and I am the primary author.

8.1. Introduction

Thermoelectric generators passively convert temperature differences across a material into usable power, and thermoelectric coolers can run this process in reverse.¹⁻³ The performance of a thermoelectric material is given by the dimensionless parameter, $zT = \frac{S^2\sigma}{\kappa_L + \kappa_e}T$, where S is the Seebeck coefficient, σ is the electrical conductivity, and κ_L and κ_e are the lattice and electronic components of the thermal conductivity. This figure can be viewed as an ‘electronic gain’ in the numerator, called the power factor, balanced by a parasitic ‘thermal loss’ in the denominator, which is the total thermal conductivity. Optimization is difficult due to these interrelated transport parameters in the Figure – σ and κ_e are directly related by the Wiedemann-Franz law and S and σ are inversely related by the Pisarekno relationship (and $\sigma = ne\mu$). Several promising thermoelectric materials have been discovered or engineered with lattice thermal conductivity (κ_L), near the predicted theoretical limits. In these cases, increasing the Seebeck coefficient is the likeliest method for further enhancing the figure of merit.⁴

High Seebeck coefficients arise in compounds with sharp features present in the density of states near the chemical potential.⁵ Several approaches have been taken to introducing these features, such as low-dimensional structures and working in systems with correlated electron behavior.⁶⁻⁹ Cobalt oxide intergrowths, epitaxial pnictide superlattices, and non-epitaxial chalcogenide nanolaminates are all examples of layered structures

that have been investigated with aim to take advantage of these effects.^{10–12} Many of these approaches have limited degrees of synthetic flexibility available, with bulk synthesis techniques having little opportunity for tuning the structure and composition due to thermodynamic constraints, and kinetic growth approaches (epitaxy and self-assembly of vapor-deposited layers) representing the other bound, where literally billions of unique layering sequences can be made in a system of only four constituents.^{13–15}

Within the large family of non-epitaxial nanolaminate materials, those comprised of interleaved layers of MSe (M=Sn, Pb, Bi) and TiSe₂, have exhibited the most promising thermoelectric properties found to date.^{12,16,17} The nanostructures (layer order), the number of capacitive interfaces (number of times the laminate is repeated), and the local and global compositions (chemical system and constituent ratios) can be utilized to tune the properties.^{12,18–21} These materials exhibit ultralow thermal conductivities for dense solids, making them good candidates for focusing on enhancement of zT by increasing the Seebeck coefficient.^{22–24} In the compounds comprised of stacked single layers, the SnSe containing nanolaminate exhibits a higher Seebeck coefficient than the PbSe or BiSe analogues.^{16,25,26} In the $([\text{PbSe}]_{1+\delta})_1(\text{TiSe}_2)_n$ series of compounds, which have increasing numbers of TiSe₂ layers (n) and a single PbSe layer, the magnitude of the Seebeck coefficient increases with n .¹² This is assumed to be because electrons donated from PbSe into lower energy TiSe₂ bands are ‘spread’ across more layers.

Here, we present a series of $([\text{SnSe}]_{1+\delta})_1(\text{TiSe}_2)_n$ nanolaminates with $2 \leq n \leq 15$ and similar to $([\text{PbSe}]_{1+\delta})_1(\text{TiSe}_2)_n$ we report enhancement of the Seebeck coefficient with increasing n . Exchanging the Pb atoms in PbSe for isovalent Sn in high- n was expected to result in similar behavior, but perhaps with even greater enhancement if the offset seen in the $n=1$ compounds holds or increases. For low n , similar behavior is observed as to the PbSe-containing laminates. At higher n however, strikingly different behavior is observed in the transport between compounds, with mobile carriers quickly freezing out. Furthermore, at cryogenic temperatures ($T \sim 100$ K) large enhancement of the Seebeck coefficient is seen in the $n=15$ compound relative to $n=3$. This results

in a power factor near $13 \mu\text{W K}^{-1}\text{cm}^{-2}$ which gives reasonable values of zT at these temperatures with conservative estimates of thermal conductivity.

8.2. Experimental Methods

All compounds were formed from the self-assembly of designed thin film precursors. This process is described in detail elsewhere.^{16,27,28} Precursors were deposited at high vacuum (pressure $<5 \times 10^{-7}$ torr) from vaporized plumes onto Si and fused silica substrates. Sn and Ti were vaporized using electron guns and Se from a Knudsen cell (all sources $>99.95\%$ elemental purity). Substrates were sequentially exposed to each plume in the order of the layered product, forming a layered but amorphous precursor with similar local structure and composition. Self-assembly of the precursors was activated by heating to 350°C for 30 minutes in an N_2 environment. Diffraction patterns were collected on laboratory instruments using Cu- $\text{K}\alpha$ radiation in both locked-coupled out-of-plane and grazing-incidence in-plane geometries. Grazing-incidence scans were performed with the source elevated 0.4° above the sample plane and the detector elevated 4° above the sample plane. Compositions, which were used in the calibration process, were made with an electron microprobe analyzer using a thin-film technique.²⁹

Electrical measurements were taken with a house built cryostat using films deposited on silica through a cross patterned shadow mask. Contacts were made with In pressed onto the corners of the films at room temperature. Both cryogenic and room-temperature Seebeck coefficients were measured with heat-sunk type-T thermocouples. Room-temperature measurements were made by cooling half of a film slightly, measuring temperature at each side and voltages on like thermocouple leads. Cryogenic Seebeck coefficients were measured similarly, but one half of the sample was passively heated/cooled with good thermal contact with the cold finger. The other half was isolated by stainless steel standoffs and making thermal contact to a different copper block.

8.3. Results and Discussion

8.3.1. Structural Characterization

Several $([\text{SnSe}]_{1+\delta})_1(\text{TiSe}_2)_n$ heterostructure nanolaminates were made with $2 \leq n \leq 15$ by nucleation from designed thin-film precursors. Briefly, each binary constituent was calibrated such that stoichiometric layers of amorphous SnSe and TiSe_2 could be formed. Further calibrations were done such that the Sn:Ti ratio gave the targeted misfit parameter established for the $n=1$ compound by Merrill et al. ($1+\delta=1.20$). By this procedure, deposition parameters were established to correctly achieve both the necessary inter-layer and intra-layer compositions in the nanolaminate. Next, these parameters were scaled to ensure the thicknesses of the layers were appropriate such that each Ti-Se or Sn-Se repeat contained the appropriate amount of material to nucleate a TiSe_2 trilayer or SnSe bilayer respectively. In the thickness scaling process, deposition parameters were slightly moved from the ‘ideal’ ratios established in the first step to yield the crystalline $n=1$ film with the best diffraction pattern (narrowest peaks and highest intensity odd reflections in the $00l$ plane). The number of TiSe_2 layers in the unit cell was then increased from $n=1$ to $n=3$, making small adjustments to the deposition parameters to maximize the quality of the diffraction patterns. Once satisfactory results were obtained for both $n=1$ and $n=3$, these parameters were used for the remaining compounds in this study.

Each precursor was made such that identical units heterostructures were stacked until the nanolaminate was approximately 50 nm thick. Specifically, the structure was repeated 28, 21, 17, 9, 7, and 5 times for the $n=2, 3, 4, 8, 11$, and 15 nanolaminate, respectively. The repeating structure allows for analysis by conventional diffraction techniques. Figure 8.1. shows locked-coupled out-of-plane diffraction patterns, which probe atomic planes aligned with the stacking direction of the nanolaminate. As n increases the intensity of most peaks from the superlattice diminish. However, for all samples, the broader peaks at ca. 14° , 30° , and 62° have large intensity. These correspond to d -spacings that can be found within the constituent blocks and relatively more of these Fourier components are required with increasing thickness of the TiSe_2 blocks. As n increases, the thickness of the repeating unit of the nanolaminate increases, which manifests as increasing peak frequency in

the diffraction pattern. These peaks can be indexed and used to determine size of each repeating unit in the superstructure. A linear regression fit of this thickness against n gives a slope (corresponding to the thickness of a single TiSe_2 trilayer) of $6.02(4) \text{ \AA}$ and an intercept (corresponding to a single SnSe bilayer) of $6.0(3) \text{ \AA}$, which are in agreement with previous reports of both $([\text{SnSe}]_{1+\delta})_1(\text{TiSe}_2)_1$ when extrapolated and with the TiSe_2 layer thickness found in $([\text{PbSe}]_{1+\delta})_1(\text{TiSe}_2)_n$.

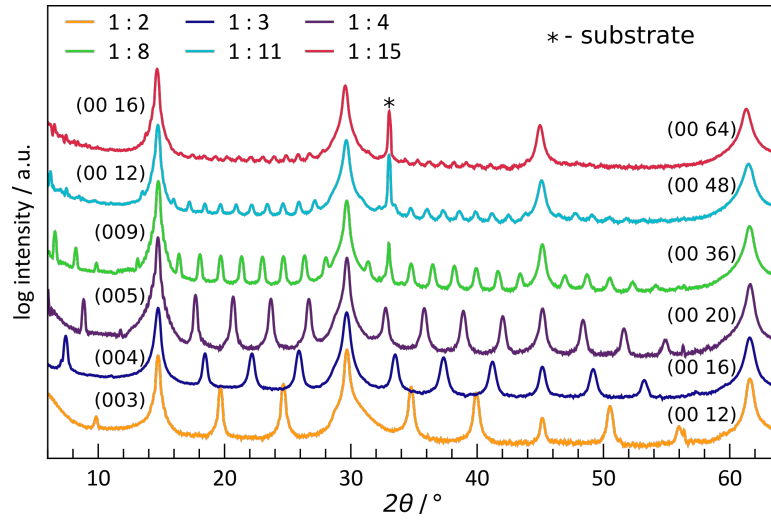


Figure 8.1. Out-of-plane diffraction patterns of samples. All reflections can be indexed to $(00l)$ reflections from the superlattice. The asterisk marks a Si reflection.

In-plane diffraction patterns taken on a subset of samples and shown in Figure 8.2. probe the $hk0$ lattice planes of the crystallites and confirm the formation of the constituent phases. The in-plane diffraction shows that the SnSe bilayer distorts from the bulk Pcmn phase and can instead be indexed to P2gg for all n . Because each SnSe layer resides at an interface, the surface energetics should dominate and this distortion is possibly due to an energetic gain by forming a commensurate axis with TiSe_2 . Peak positions are relatively unchanged between the patterns, indicating structural distortions are minimal as the number of TiSe_2 layers increases. However, as n increases reflections from the SnSe constituent become relatively weaker due to the ratio of

diffracting crystallites more heavily favoring TiSe_2 . For the case of $n=11$ that has fewest repeating units in the patterns shown, only 7 SnSe bilayers are present in the nanolaminate as opposed to 28 bilayers for $n=2$.

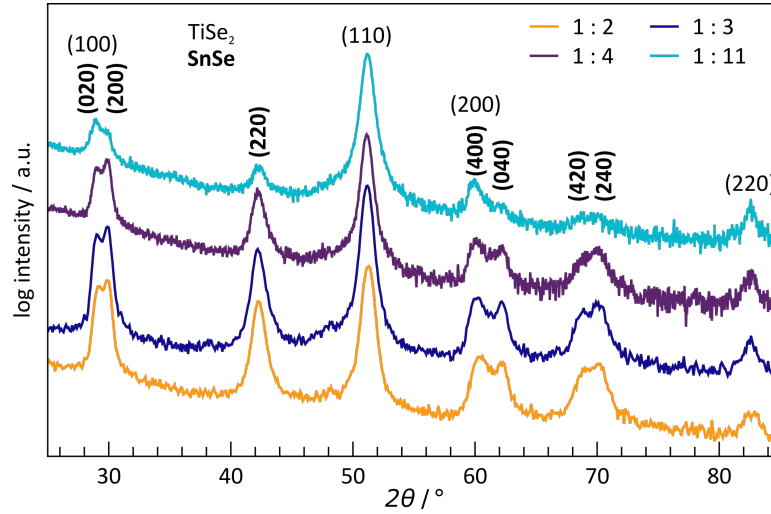


Figure 8.2. In-plane diffraction patterns of select samples. All reflections can be indexed to $(hk0)$ planes of either TiSe_2 or distorted SnSe, with the relative intensity of TiSe_2 reflections increasing with n , as expected.

8.3.2. Electrical Characterization

Seebeck coefficients taken near room-temperature are shown in Figure 8.3. Error bars reflect uncertainty in both the $V/\Delta T$ fit as well as the difference in values between Cu and constantan measuring junctions. To ascertain the degree of repeatability in accessing the same region of the kinetic nucleation landscape, a second $n=3$ sample was made and measured. Both $n=3$ samples give similar values. As with the previously reported $([\text{PbSe}]_{1+\delta})_1(\text{TiSe}_2)_n$ nanolaminates, the negative Seebeck coefficient systematically increases in magnitude with n . In general, the magnitudes are higher than in Pb-containing compounds of similar n , but the variation is likely within the limit of possible values that can be achieved by varying the kinetic defect density while globally maintaining the structure of the majority compound.

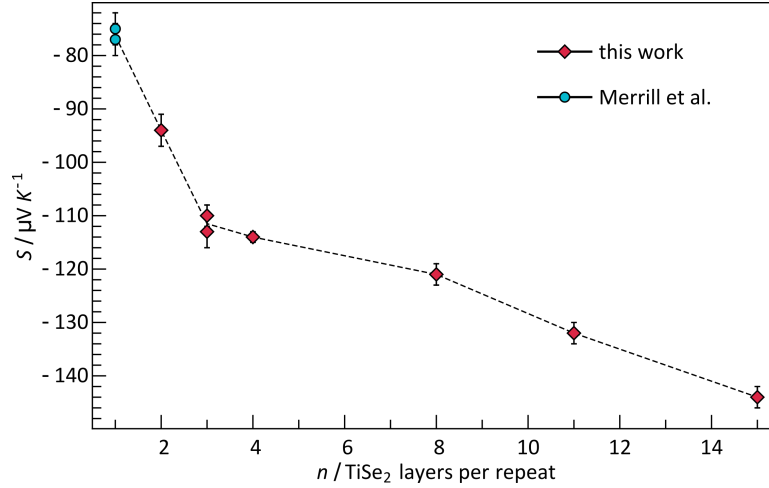


Figure 8.3. Room-temperature Seebeck coefficients of $([\text{SnSe}]_{1+\delta})_1(\text{TiSe}_2)_n$ nanolaminates. The values for $n=1$ are from previous work of Merrill et al.¹⁶ Error bars correspond to the precision of the measurement.

Temperature dependent hall-effect and resistivity data were taken to further investigate the transport properties and underlying mechanism for enhancement of the Seebeck coefficient. The resistivity data are shown in Figure 8.4. and inset is the data normalized to the value at room temperature. Previous investigations of $([\text{MSe}]_{1+\delta})_m(\text{TiSe}_2)_n$ ($\text{M}=\text{Sn}, \text{Pb}, \text{Bi}$) nanolaminates have all shown metallic behavior in their temperature-dependent resistivity curves with upturns at low temperatures attributed to carrier localization in the layers. The $n=8, 11, 15$ nanolaminates all have increasing resistivity as they are cooled from room-temperature. This is the first time $([\text{SnSe}]_{1+\delta})_m(\text{TiSe}_2)_n$ nanolaminates with m or $n>1$ have been reported and also the first time no initial drop in resistivity with temperature has been observed in the TiSe_2 based heterostructures. The increasing resistivity is similar to what would be expected from a semiconducting compound, but does not increase quickly enough with decreasing temperature to be modeled as a simple semiconductor. Generally, the resistivity increases with n , with the exception of the $n=15$ sample, which is lower than expected. This is contrary to the $([\text{PbSe}]_{1+\delta})_1(\text{TiSe}_2)_n$ series, where the resistivity did not systematically trend with n . However, in the prior report samples were crystallized from precursors that likely had different numbers of incorporated defects due to being made at different times, which convoluted

trends in resistivity. If the precursor is calibrated in a low n nanolaminate such that a slight excess or lack of material is deposited in each layer, then diffusion might still occur across the thin blocks allowing for correction by the formation of layering defects during self-assembly. However, in the thicker blocks of high n nanolaminates nonstoichiometry in the SnSe precursor layers might be more constrained during crystallization and less self-healing of the compound occurs. Thus a systematic increase in defect density, and hence resistivity, may be expected with n .

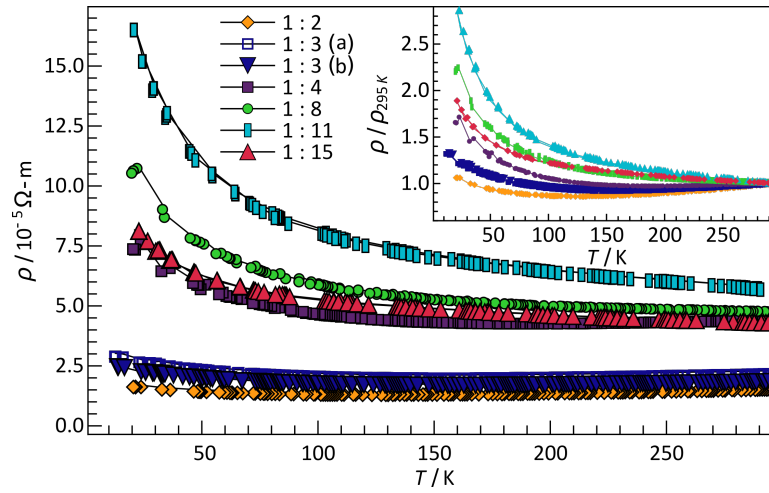


Figure 8.4. Temperature-dependent resistivity of $([\text{SnSe}]_{1+\delta})_l(\text{TiSe}_2)_n$ nanolaminates. Inset are values normalized to room-temperature.

Temperature-dependent carrier concentrations for all samples except $n=4$, calculated from their negative Hall coefficients, are shown in Figure 8.5. Contrary to the $([\text{PbSe}]_{1+\delta})_l(\text{TiSe}_2)_n$ nanolaminates, where electrons donated from PbSe into TiSe_2 were ‘diluted’ across more layers, a systematic trend is not observed for all n . This is striking as the systematic increase in the magnitude of the Seebeck coefficient would suggest, in the absence of significant changes to the band structure, that the carrier concentration is being systematically reduced. For the $([\text{SnSe}]_{1+\delta})_l(\text{TiSe}_2)_n$ nanolaminates shown here the low n samples exhibit behavior consistent with the Pb-containing analogues, with room temperature carrier concentration decreasing from 1.9 to 1.4 cm^{-3} when n

is increased from 2 to 3 (with the previously published $n=1$ nanolaminates being between 2.0-2.4 cm^{-3}). As n is increased, as seen by the $n=8$ and $n=11$ curves, the room temperature carrier concentration increases, but the carriers also quickly freeze-out with decreasing temperature. Surprisingly, both the magnitude and temperature dependence of carrier concentration in these two nanolaminates are nearly identical. For the $n=15$ nanolaminate the room temperature carrier density is on the order found in the low n samples, but a steep decay, similar to the intermediate n samples, is observed. This suggests that defect levels alone don't account for all behaviors seen, and that the underlying transport mechanisms are changing with n .

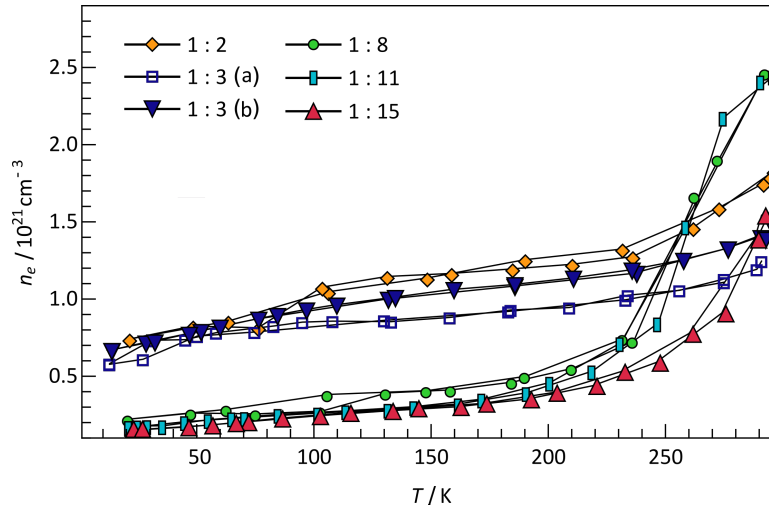


Figure 8.5. Temperature-dependent carrier concentrations of $([\text{SnSe}]_{1+\delta})_1(\text{TiSe}_2)_n$ nanolaminates calculated from Hall coefficients assuming a single n -type band.

To further investigate the changes in transport behavior, variable-temperature Seebeck coefficient measurements were taken on a low- and high- n compound. Figure 8.6. shows the measurements taken on the $n=3$ and $n=15$ nanolaminates, as well as a simplified schematic of the measurement system. The $n=3$ sample behaves like a typical poor metal – gradually decreasing in magnitude from the room temperature value. On the other hand, the $n=15$ sample shows drastically different behavior. Due to the surprising behavior and the inherent difficulty in accurately measuring the Seebeck coefficient of thin

films the $n=15$ sample was measured several times, hence the smaller error bars. The Seebeck coefficient of the $n=15$ nanolaminate increases in magnitude quickly as the temperature is decreased, in agreement with the freeze-out behavior observed in the carrier concentration data (by the Pisarenko relationship). It then increases towards 0 with further cooling until it increases in magnitude again to ca. $-250 \mu\text{V K}^{-1}$ near 100 K. Given there are no abrupt changes in carrier concentration near this temperature, the cause for enhancement is likely more exotic than moving the Fermi level within a band. In bulk TiSe_2 the Seebeck coefficient exhibits an abrupt minimum near 150K and broad plateau at lower temperatures, only rising to 0 below ca. 50 K, which has been attributed to a phonon-drag effect.³⁰ However, this also correlates with the onset of a charge density wave (CDW) in the material, which may be the mechanism for the enhancement. There are no signatures of a CDW transition in the resistivity data of the $n=15$ sample, so this is also an unlikely mechanism for the observed enhancement. Even with the relatively high resistivity at 100K, when coupled with the high-magnitude Seebeck coefficient the power factor, $\frac{S^2}{\rho}$, is ca. $13 \mu\text{W K}^{-1}\text{cm}^{-2}$, which should give quite high zT values given the low thermal conductivity expected from the nanolaminate. For example, assuming a Lorenz number of $2.45 \times 10^{-8} \text{ V}^2 \text{ K}^{-2}$, the best-case zT value ($\kappa_L = 0$) is >2.5 for a Seebeck coefficient of $-250 \mu\text{V K}^{-1}$. For insulating nanolaminates with similar structure (e.g. $([\text{PbSe}]_{0.99})_4(\text{WSe}_2)_4$, the total in-plane thermal conductivity at room temperature was measured to be ca. $0.4 \text{ W m}^{-1} \text{ K}^{-1}$. Conservatively assuming this value for the lattice conductivity at 100 K and a typical Lorenz number of $2.45 \times 10^{-8} \text{ V}^2 \text{ K}^{-2}$, the calculated zT value would be about 0.3 for the $n=15$ nanolaminate. Further temperature-dependent study of the Seebeck coefficient in nanolaminates both within and outside of the TiSe_2 family of compounds will hopefully further inform as to the onset and cause of this behavior.

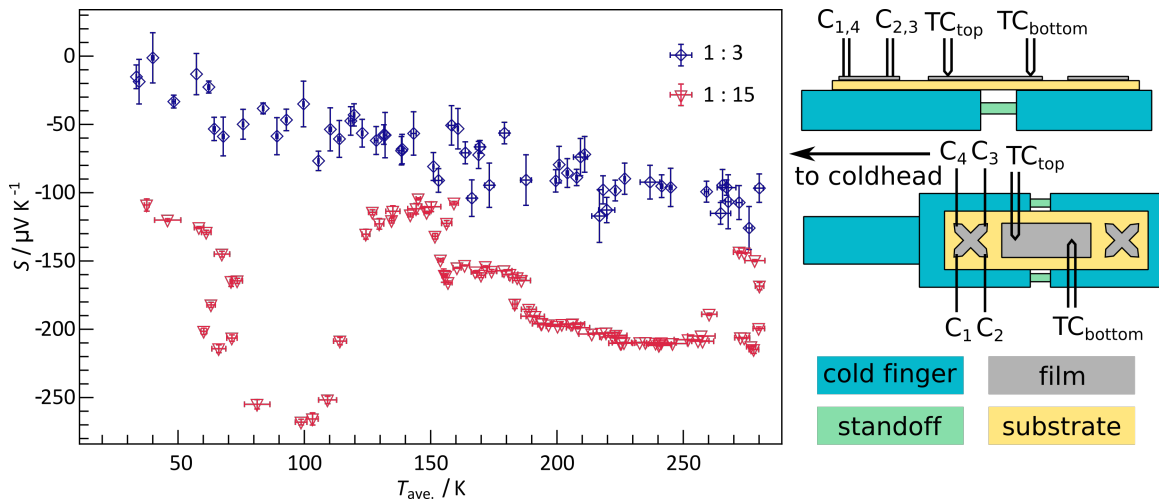


Figure 8.6. (left) Temperature-dependent Seebeck coefficient measurements on $([\text{SnSe}]_{1+\delta})_1(\text{TiSe}_2)_n$ ($n=3, 15$) nanolaminates. (right) Schematic showing side and top view of measurement stage with Cu cold finger, stainless steel standoffs, silica substrate and nanolaminate film. Hall and resistivity measurements are made using C_1 - C_4 and Seebeck coefficients using the top and bottom thermocouples ($\text{TC}_{\text{top/bottom}}$). Thermocouple wires run along Cu blocks to reduce hot/cold finger effects.

8.4. Conclusion

$([\text{SnSe}]_{1+\delta})_1(\text{TiSe}_2)_n$ nanolaminates from designed precursors were used to investigate the effects of increasing the TiSe_2 constituent relative to SnSe . Similar to $([\text{PbSe}]_{1+\delta})_1(\text{TiSe}_2)_n$ nanolaminates, the Seebeck coefficient of the composite structure is decreased. However, whereas nanolaminates containing PbSe did not show radically different behavior when increasing the relative amounts of TiSe_2 , the SnSe compounds drastically change. Thus, the underlying transport mechanisms appear to be different between the two chemical systems, which is surprising given the TiSe_2 bands have been assumed to dominate the transport behavior. Cryogenic Seebeck coefficient measurements further illustrate considerable differences between low- and high- n nanolaminates, with $([\text{SnSe}]_{1+\delta})_1(\text{TiSe}_2)_{15}$ having a reasonably high Seebeck coefficient of $-250 \mu\text{V K}^{-1}$ at 100K. This is promising for functionality as a leg in thermoelectric coolers, as an ultralow thermal conductivity would be expected based on measurement of similar nanolaminates.

8.4. Bridge

The changing behavior in $([\text{SnSe}]_{1+\delta})_1(\text{TiSe}_2)_n$ nanolaminates relative to the PbSe-containing counterparts is surprising given the consistent structure of the constituent layers. When the thickness of SnSe layers is increased, size-dependent structural distortions³¹ likely further change the properties. In the following chapter, a homologous series of $([\text{SnSe}]_{1+\delta})_m(\text{TiSe}_2)_n$ nanolaminates with $m=n$ are explored, similar to those in Chapter V of this dissertation, but with substitution of PbSe for SnSe. Considerable structural change in the SnSe layers results in a wildly changing electrical properties with bipolar carrier effects – behaviors that are not readily explainable by rigid- or single-band models.

CHAPTER IX

DIVERSE AND BIPOLAR TRANSPORT BEHAVIOR IN $([\text{SnSe}]_{1+\delta})_m(\text{TiSe}_2)_n$ NANOLAMINATES UNDERGOING STRUCTURAL DISTORTIONS

At the time of writing the work in this chapter is unpublished, but a manuscript is planned to be coauthored with Danielle Hamann and David Johnson. Danielle assisted with sample preparation, sample characterization, and manuscript preparation. David Johnson is my advisor and I am the primary author.

9.1. Introduction

Thin-films comprised of two or more interleaved structures have held significant interest over the last several decades. Much of this interest was initially ignited by the development of new epitaxial deposition techniques, which allowed for the synthesis of high quality superlattices and became a fruitful hunting ground for several emerging areas of condensed matter physics.¹⁻³ The crux of these techniques, for example molecular beam epitaxy (MBE), relies on designing experiments such that atoms adsorbed onto the substrate or the previous layer will have a low 'surface tension' and preferentially spread over the substrate as opposed to forming agglomerates.⁴ As the packing of these atoms increases, they tend to form atomically smooth strained monolayers templated off of the layers beneath.⁴ However, at some critical thickness the complex interplay between surface energy, volume energy, strain, and other physical properties will tend to destabilize the film and instead new material will coalesce into distinct islands.⁵ The introduction of an interface prior to the point of instability often preserves the energetic favorability of the thin-film structure and a superlattice of thin strained layers can be created.⁶

More recently, a remarkable degree of research effort has been devoted towards the investigation of the stabilization and properties of 2D sheets and their heterostructures.^{7,8} Contrary to epitaxial films, these are built from the isolation and assembly of individual layers, which comes with the requirements that individual layers be stabilized outside of surface interaction with the substrate or preceding layers. While this severely limits the scope of chemical

systems, it allows for the formation of superlattices that do not structurally interact as a necessity for their stabilization. Furthermore, due to small flakes of material being manually stacked to form the layered structure, a regular angular registration between the materials is not a prerequisite of growth.⁹

A third approach that has seen less interest devoted to it has been in the formation of nanolaminate thin films from layered amorphous precursors.¹⁰ Perhaps falling between the extremes of strained epitaxial superlattices and quasi 2D heterostructures, these films form from several nucleation points as the self-assembling precursors crystallize while balancing the various volume, surface, and diffusive energetic terms within a complex multidimensional energy landscape with multiple phases.¹¹ While the layers may crystallize congruently or step-wise, varying degrees of templating along the layers may occur further complicating the crystallization process.¹² As long as a local free energy minimum exists within the targeted layered system there is a high likelihood they can be stabilized, but when several nearby minima exist then stabilizing a single phase may be difficult.

Recently, nanolaminates made from designed precursors consisting of SnSe rocksalt-like layers paired with several transition metal dichalcogenide layers have been shown to undergo structural distortion between the high-temperature β -SnSe and low-temperature α -SnSe phases as the size of the SnSe layers are changed.¹³⁻¹⁵ These distortions were determined to be driven by size as opposed to interfacial interactions with the dichalcogenides.¹³ Also recently reported was that SnSe bilayers when paired with TiSe₂ exhibit a different structure altogether, which is likely due to interfacial interactions owing to the unique behavior and larger lattice parameter of TiSe₂.^{16,17} Here, we investigate the changes in structure and transport properties of $([\text{SnSe}]_{1+\delta})_m(\text{TiSe}_2)_n$ as m and n are increased. While the TiSe₂ layers maintain their structure, the SnSe exhibit rich structural change as their size increases, including coexistence of multiple phases and defect structures in the same compound. These result in changing transport behavior unexplained by previous models in this and similar chemical systems.^{18,19}

9.2. Materials and Methods

Precisely layered but amorphous designed precursors were prepared by physical vapor deposition. Elemental layers were deposited from source material either by an effusion cell or electron beam guns onto silicon wafers with native SiO₂. The deposition sequence was computer programmed and controlled. Pneumatic shutters were used to control the thickness of each sequentially deposited elemental layer. Layer thickness was monitored by quartz crystal microbalances located near the shutter. Locked θ -2 θ diffraction patterns were used to determine the optimal parameters for building the $m=n$ nanolaminate structures and briefly, varying one constituent's number of layers while monitoring the change in superlattice period and total film thickness was the strategy employed in optimizing to the correct precursor and subsequent crystalized product.

The layered structures were analyzed by coupled θ -2 θ diffraction on a Bruker D8 Discover diffractometer equipped with Cu K-alpha radiation. These patterns were used to get total thickness, individual layer thickness (*c*-lattice parameter), and the number of layers in both the precursor and crystalized product. In-plane diffraction was used to determine what crystal phases are present in the layered structure. These data were collected using a Rigaku Smartlab diffractometer equipped with Cu K-alpha radiation and an in-plane detector arm. Both the source and detector were elevated slightly above the sample plane in a grazing-incidence geometry (at 0.5 and 4.0°, respectively). The precise angles were chosen by moving the in-plane drive to a Bragg position and iteratively adjusting both the source and detector in the out-of-plane direction to achieve maximum intensity.

Electrical data were collected on films deposited in parallel to those used for structural analysis, but on fused silica substrates through a shadow mask in a van der Pauw cross pattern. Measurements were made in a closed-cycle He cryostat between 15 and 295 K using a house-built Hall measurement system. For Hall coefficients, V_H /B-field slopes were averaged between 4 sets of contacts with a maximum field strength of 1.6 T and sourcing a constant current ≤ 0.001 A. Resistivity measurements were made using the van der Pauw method sourcing a current between 0 and 0.001 A. Seebeck coefficients were measured

at room-temperature using a house-built system. One half of the sample was cooled slightly ($\Delta T \leq 2$ °C) and $V/\Delta T$ curves were collected as the temperature equilibrated across the sample. Type-T thermocouples were used to measure each temperature and the individual metal junctions were used to measure voltages across the films. The measured $V/\Delta T$ slopes were then corrected for the Seebeck coefficients of the copper and constantan measurement junctions, with the two corrected values being in agreement to within $3 \mu\text{V K}^{-1}$

9.3. Results and Discussion

9.3.1. Synthesis

A series of precursors consisting of vapor deposited layers of Ti, Sn, and Se were calibrated to form $([\text{SnSe}]_{1+\delta})_m(\text{TiSe}_2)_n$ nanolaminates such that $m=n$. For $m=n \leq 5$, the target thickness was 50nm, with some rounding so as to form an integer number of repeating structures. For $m=n > 5$, precursors were designed to crystallize 8 repeats of the target heterostructure, which results in thicknesses of ca. 57 nm and 76 nm for $m=n$ of 6 and 8, respectively. A small amount of selenium loss upon annealing is calibrated into the 50 nm thick precursor. The increased thickness in the $m=n$ of 6 and 8 will have a decreased amount of selenium loss because of the larger distance the selenium would have to diffuse through, potentially impacting the transport properties. Precursors were gently heated at 350 °C for 30 minutes to promote the self-assembly of several $([\text{SnSe}]_{1+\delta})_m(\text{TiSe}_2)_n$ superlattice thin-films, which can be described as alternating sheets of each structure with each sheet being comprised of m SnSe bilayers and n TiSe_2 trilayers. Thus, m and n describe thickness of each distinct sheet within the repeating nanolaminate structure and herein we discuss a homologous series where they are simultaneously increased in the range of $1 \leq m=n \leq 8$.

9.3.2. Structure

Figure 9.1. shows locked-coupled θ - 2θ diffraction patterns of the $([\text{SnSe}]_{1+\delta})_m(\text{TiSe}_2)_n$ ($2 \leq m=n \leq 8$) heterostructure superlattices. Due to the texture of the films, peaks in this geometry correspond uniquely to planes of atoms in

the stacking direction of the layers. As m and n are increased, the number of reflections increases, as expected from the thicker layers (and hence larger unit cell) found in the nanolaminate. Indexing these peaks as $00l$ lattice planes gives the thickness of a single repeat of m SnSe layers and n TiSe₂ layers. Table 9.1. shows these thicknesses which regularly increase by approximately 11.89 Å each time m and n are increased by 1. This is in good agreement with previous data, with the $m=n=1$ compounds being approximately 12.05 Å thick.¹⁸ The small discrepancy has been previously noted in ([PbSe]_{1+δ})_{*m*}(TiSe₂)_{*n*} nanolaminates and attributed to thickening of existing structures as opposed to forming additional rock-salt dichalcogenide interfaces.¹⁹ The regular increase in layer thicknesses and sharp diffraction peaks indicate the superlattice layering is preserved in the form of precisely stacked crystallites but does not inform on the structure of the constituent phases.

Table 9.1. Lattice parameters of SnSe, TiSe₂, and the superlattice period (c) the ([SnSe]_{1+δ})_{*m*}(TiSe₂)_{*n*} nanolaminates from Le Bail fits of the diffraction patterns.

$m=n$	c (Å)	SnSe a (Å)	SnSe b (Å)	TiSe ₂ a (Å)
1	12.0582(7)	6.094(3)	5.974(4)	3.52(3)
2	23.8412(4)	4.266(1)	4.257(4)	3.52(3)
3	35.5890(2)	4.27(1)	4.248(3)	3.51(3)
4	47.3549(6)	4.301(6)	4.26(3)	3.51(3)
5	59.5935(8)	4.311(6)	4.233(4)	3.52(2)
6	71.4519(5)	4.328(1)	4.235(8)	3.566(3)
8	95.1122(3)	4.344(3)	4.233(2)	3.569(1)

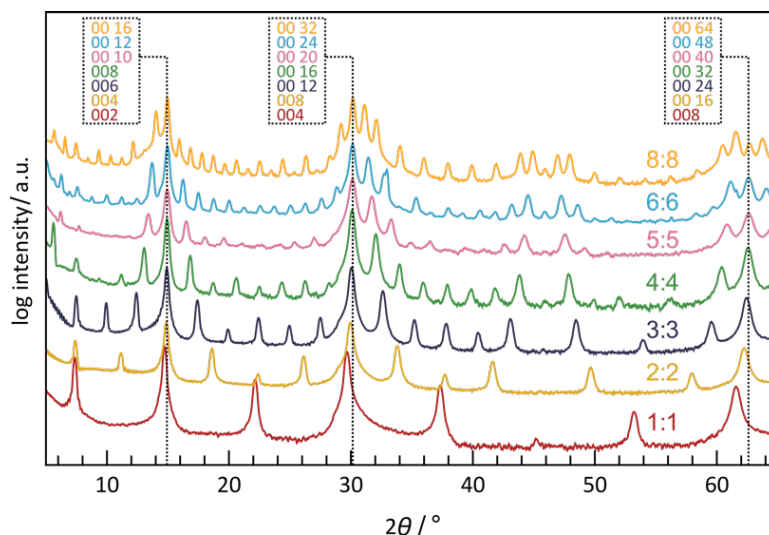


Figure 9.1. Coupled θ - 2θ out-of-plane diffraction patterns of $([\text{SnSe}]_{1+\delta})_m(\text{TiSe}_2)_n$ ($1 \leq m=n \leq 8$). A systematic increase in the c -lattice parameter of 11.89 Å, corresponding to a single TiSe_2 unit cell and half SnSe unit cell, is seen as m and n are increased.

In-plane diffraction data were collected for the $([\text{SnSe}]_{1+\delta})_m(\text{TiSe}_2)_n$ ($1 \leq m=n \leq 8$) nanolaminates to begin to characterize the structures of the layers, and are shown in Figure 9.2. The peaks in each pattern can be indexed to reflections of either of distorted SnSe or TiSe_2 , with an impurity reflection from SnSe_2 appearing in higher $m=n$ samples. The SnSe_2 is marked by an asterisk and can likely be eliminated by longer annealing time. $hk0$ lattice parameters determined from the in-plane scans are given in Table 9.1. The TiSe_2 constituent parameters are consistent with other TiSe_2 -containing nanolaminates, and exhibit negligible structural change with size. The $m=n=1$ compound shows a tetragonal basal plane as indicated by the split peaks in the diffraction pattern. This pattern must be indexed to a larger unit cell than bulk SnSe , with a - and b - lattice parameters of 6.094 and 5.974 Å, respectively. This distortion is distinct to nanolaminates with TiSe_2 and SnSe , with other systems containing SnSe typically converging to a single lattice parameter as m approaches 1.¹⁶ For $([\text{SnSe}]_{1+\delta})_m(\text{TiSe}_2)_n$ ($2 \leq m=n \leq 4$) the basal plane becomes very nearly square and the splitting into distinct $hk0$ peaks where $h \neq k$ is no longer observed. These patterns can still be fit to a tetragonal basal plane but are indexed to a smaller unit cell and inset in Figure 9.2. (top-right) are the a - and

b -lattice parameters and a/b . In the compounds with $([\text{SnSe}]_{1+\delta})_m(\text{TiSe}_2)_n$ ($5 \leq m=n \leq 8$) splitting of the SnSe peaks reappears, but the smaller unit cell and symmetry shift are maintained, appearing similar to the bulk α -SnSe phase. As $m=n$ increases in this regime, the peaks split further towards the bulk lattice parameters, but do not yet reach the bulk values for the case of $m=n=8$ as seen here. Notably, the tetragonal basal plane seen in the thicker compounds ($5 \leq m=n \leq 8$) has different lattice parameters than the compound with where $m=n=1$. This is best explained by a face-centered to body-centered symmetry shift (see schematic in Figure 9.2. bottom-right) and a corresponding $\sim \frac{1}{\sqrt{2}}$ ratio between lattice parameters which, as Figure 9.3. is indexed, also fits the expected systematic absences.

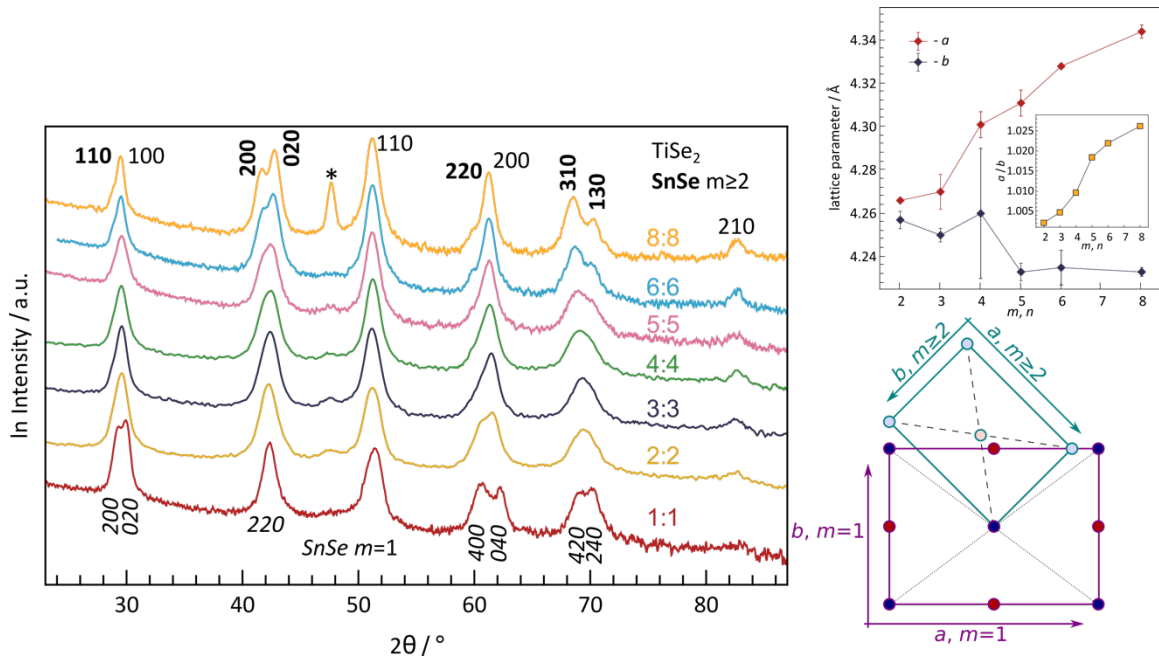


Figure 9.2. (left) In-plane diffraction patterns of $([\text{SnSe}]_{1+\delta})_m(\text{TiSe}_2)_n$ nanolaminates. The SnSe must be indexed differently as the layers thicken. The asterisk marks the location expected from SnSe_2 . (top-right) Lattice parameters of SnSe for $m=n \geq 2$ and ratio of a/b . (bottom-right) Schematic of face-to-body centering symmetry shift of SnSe.

HAADF-STEM micrographs of $m=n$ of 1, 2, and 3 nanolaminates provide a real-space representation of the nanolaminate structure, shown in Figure 9.3.

A-C, D-H, and E, respectively. Initial inspection shows regular layering with sharp interfaces between rock salt and dichalcogenide layers. The global layering reflects the structure expected from each precursor with periodic layering defects due to slight precursor non-stoichiometry (for example in the lower-right of the $m=n=3$ image, Figure 9.3.E.). Zone axis of the constituent lattices manifest as bright distinct points in the image with the brighter layers corresponding to the heavier Sn-containing constituent. Within each structure multiple zone axis orientations are visible indicating some degree of interlayer rotational misregistration.

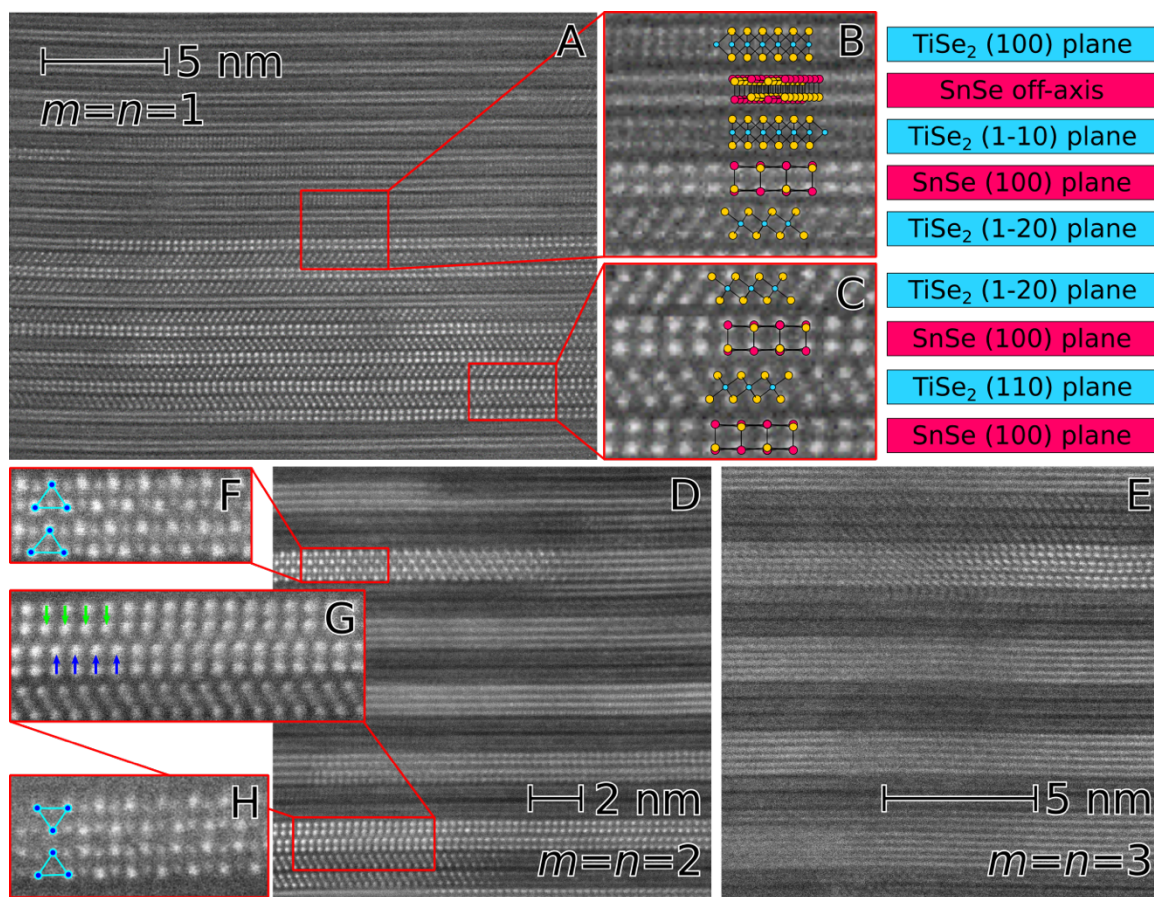


Figure 9.3. HAADF-STEM images of $[\text{SnSe}]_{1+6}(\text{TiSe}_2)_n$ nanolaminates showing templated interfaces for $m=n=1$ and several stabilized structures for $m=n=2$.

However, the $m=n=1$ structure exhibits far less misregistration instead appearing nearly epitaxial several layers. Focusing on this structure, two

primary regions can be seen in the film with apparent templating between constituents. As seen in the top-right of Figure 9.3., with labels corresponding to the adjacent planes in panes B and C, the octahedrally coordinated TiSe_2 can be seen as a dumbbell like structure when looking across the (110) and (1-20) planes. On the other hand, this structure appears as vertical bars when looking across the (100) and (1-10) planes. The SnSe structure in this image manifests as either indistinguishable ‘smears’ due to being off-axis or distinct points corresponding to looking across the (100) plane. The off-axis SnSe is regularly seen adjacent to the TiSe_2 (100)/(1-10) planes whereas the (100) SnSe plane is seen adjacent to the TiSe_2 (110)/(1-20) planes. An interfacial region where the layers cleanly change from one sequence to the next is also visible. This layering can be understood by considering the templating mechanism between TiSe_2 and SnSe . The measured lattice parameters of SnSe and TiSe_2 for $m=n=1$ (Table 9.1.) show a $\sqrt{3}$ ratio between a -lattice parameters. This corresponds exactly with the ratio that would be expected from the formation of a commensurate interface between tetragonal and hexagonal structures along the $\langle 100 \rangle$ and $\langle 1-10 \rangle$ directions, respectively. This also agrees with the STEM image seen in Figure 9.3.C. Considering the distortion and alignment of the SnSe lattice to accommodate this orientation, the region in Figure 9.3.B. is also understood by considering looking down the TiSe_2 $\langle 100 \rangle$ axis, which would appear as off zone-axis in SnSe . The TiSe_2 interface between the two may occur both looking along the TiSe_2 (1-10) plane or TiSe_2 (100) plane, which would result in SnSe on or off zone axis as observed in the lower and upper SnSe layers, respectively. These distortions are likely driven by interface energetics and unique to ‘soft’ SnSe layers paired with TiSe_2 , which has a larger a -lattice parameter than other dichalcogenides.¹⁶

In the $m=n=2$ nanolaminate, several structural details can be seen within the SnSe layers. Looking down the $\langle 110 \rangle$ axis of SnSe in Figure 9.3.F., the typical α - SnSe structure is observed, highlighted by the stacked triangle pointing in the same direction.²⁰ On the other hand, Figure 9.3.H. shows another region of the film where β - SnSe is seen looking down the same axis, as highlighted by the stacked triangles pointing in opposite directions.²⁰ Figure 9.3.G. highlights a slip plane occurring along the $\langle 100 \rangle$ axis in which one

bilayer of SnSe is offset from the bilayer below it so the atoms lie in between each other. This misalignment could be due to the SnSe layers trying to align with the TiSe₂ layers on either side of it forcing the SnSe layers to shift. In fact, looking the TiSe₂ layers above and below, both the dumbbell and vertical bar structures corresponding to (110) and (1-10) planes can be seen, both of which could be visible when forming the commensurate interface with SnSe. The various structures seen in the $m=n=2$ structure point to the complicated environment the compounds nucleate in. Unlike the $m=n=1$ compound, the introduction of interior atoms allows for entirely new behavior due to a complication of the free energy landscape and balancing of interface and volume terms in approximately equal amounts.

9.3.3. Transport

Previous work in similar $([\text{SnSe}]_{1+\delta})_m(\text{TiSe}_2)_n$ nanolaminates suggests that the effective density of states (DOS) in the composite material is given by a superposition of the partial DOS (pDOS) from each constituent and an equilibrium chemical potential set by the chemical composition and layer ratios.²¹ However, recent work in $([\text{PbSe}]_{1+\delta})_m(\text{TiSe}_2)_n$ nanolaminates suggests that some band-bending away from the interfaces occurs.¹⁹ The two separate pDOS are combined assuming the shape, location, and size of the bands do not change in the composite structure. The 4p orbitals of Se are fully filled in the isolated SnSe layer. When interleaved with the TiSe₂ layers at the nanoscale, electrons from the Se-4p band in SnSe are donated to the empty Ti-3d band. This exchange causes the $([\text{SnSe}]_{1+\delta})_m(\text{TiSe}_2)_n$ nanolaminate heterostructures to have a both a mostly empty (n-type) band in the TiSe₂ constituent and a mostly full (p-type) band in the SnSe constituent with the Fermi level lying within the bands. This suggests a likely metallic behavior as well as the opportunity for bilpolar transport with both holes and electrons as mobile carriers that could impact the transport behavior of the material. Given the strong interfacial interaction, the structural changes and symmetry shifts, and significantly changing interface to volume ratios within the SnSe layers, a similarly rich electronic behavior might also be seen, despite the typical dominance of the TiSe₂ bands. To this end it is not known whether this predicted density of states

or previously used simple physical models are accurate in describing the behavior that occurs in thicker $([\text{SnSe}]_{1+\delta})_m(\text{TiSe}_2)_n$ nanolaminate heterostructures.

Increasing the layer thickness of the compounds has an impact on the resistivity that is measured at various temperatures as seen in Figure 9.4. Previous research showed that $([\text{SnSe}]_{1+\delta})_m(\text{TiSe}_2)_n$ where $m=n=1$ showed a low resistivity that had temperature dependent behavior of what was expected for a metal. As the layer thickness is increased from $m=n=1$ the resistivity increases and as opposed to metallic behavior, an increasing resistivity is seen as temperature is decreased. This behavior looks closer to that of thermally activated carriers in a semiconductor and becomes more pronounced as the layers reach larger numbers of $m=n$.

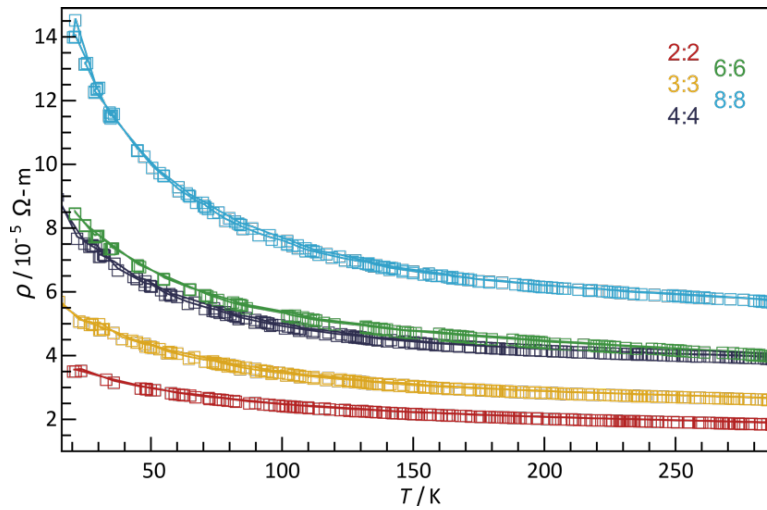


Figure 9.4. Temperature-dependent resistivity of $([\text{SnSe}]_{1+\delta})_m(\text{TiSe}_2)_n$ nanolaminates.

Each of the parent materials in these layered nanolaminates are narrow-gap semiconductors in the bulk, though self-doping due to slight non-stoichiometry in the narrow-gap TiSe_2 tends to result in weakly metallic transport behavior. With increasing layer thickness the SnSe starts to adopt the structure that it has in the bulk, so it is possible that it will display the electronic properties that it has in the bulk. If this were true, it might be

expected that SnSe in thicker layer compounds, adopts a DOS similar to discussed above. On the other hand, TiSe₂ does not undergo any structural distortion with increasing layer thickness and its transport behavior is expected to remain relatively unperturbed with size.

Hall coefficients of the $([\text{SnSe}]_{1+\delta})_m(\text{TiSe}_2)_n$ nanolaminates are shown in Figure 9.5. Strikingly different to the $m=n=1$ compound which exhibits negative Hall coefficients at all temperatures¹⁸, the $m=n\geq 2$ nanolaminates all show positive Hall coefficients at room-temperature. For $m=n<6$, decreasing Hall coefficients with temperature are observed. While $m=n=2, 4$ exhibit a sign change at ca. 200K, the $m=n=3$ does not. Whether this is due to defect levels in the compounds or heretofore unexplored or unexplained behavior from, for example, the energetics of stabilization of the nanolaminates, is yet to be determined. The $m\geq 6$ nanolaminates show increasing Hall coefficients as the temperature is decreased. While further structural characterization is necessary via STEM, this is likely the point at which the bulk α -SnSe structure is established and the intermediate structures cease to appreciably affect the transport, as indicated by the in-plane diffraction patterns. Despite the positive Hall coefficients, negative Seebeck coefficients are measured for all compounds as shown in Table 9.2. This points to a complicated Fermi surface in the composite material that cannot be described by a single electronic band or carrier type as has typically been done in other nanolaminates containing TiSe₂.

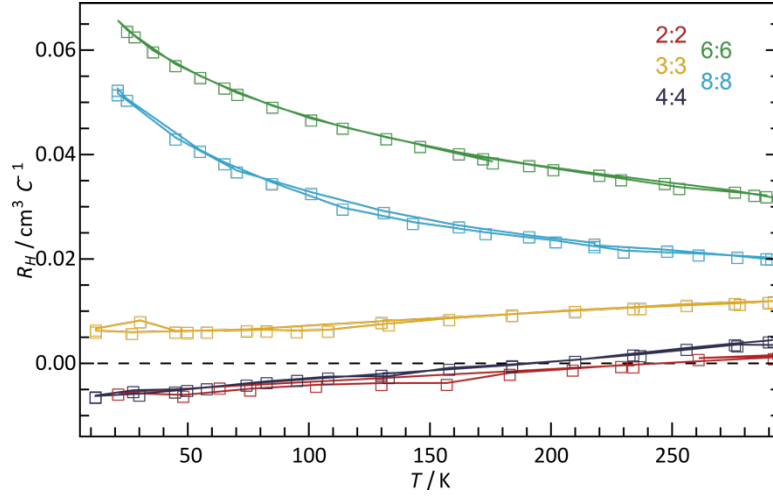


Figure 9.5. Temperature dependent Hall coefficients of $([\text{SnSe}]_{1+\delta})_m(\text{TiSe}_2)_n$ nanolaminates.

Table 9.2. Room-temperature transport measurements for $([\text{SnSe}]_{1+\delta})_m(\text{TiSe}_2)_n$ nanolaminates.

$m=n$	S ($\mu\text{V K}^{-1}$)	R_H ($10^{-3} \text{ cm}^3 \text{ C}^{-1}$)	ρ ($10^{-5} \Omega\text{-m}$)
1	-75	-0.0031	1.52
2	-52	0.0017	1.89
3	-75	0.012	2.63
4	-75	0.0035	3.93
5	-92	0.0041	5.71
6	-40	0.032	4.03
8	-40	0.02	5.72

9.4. Conclusion

The complicated energy landscape of $([\text{SnSe}]_{1+\delta})_m(\text{TiSe}_2)_n$ nanolaminates allows for the formation of epitaxial interfaces and several different structures in the SnSe constituent prior to stabilization of the bulk structure in thick layers. In the $m=n=2$ nanolaminate with equal amounts of interfacial and interior atoms, several structures exist simultaneously in the SnSe layers. This

diverse structural change allows for a rich suite of electronic properties including a more complicated bipolar behavior than has been observed in either the $[(\text{SnSe})_{1+\delta}]_l(\text{TiSe}_2)_l$ nanolaminates or nanolaminates with TiSe_2 in other material systems. Future work on the details of the electronic structure will be necessary in these compounds to fully realize the power of the predictive/synthetic loop available to nanolaminate structures.

CHAPTER X

CONCLUSIONS, SUMMARY, AND OUTLOOK FOR FUTURE WORK

The structure and properties of several kinetically stabilized compounds formed from the self-assembly of designed precursors are reported and discussed. All precursors were formed as thin films by vapor deposition of amorphous elemental layers onto substrates, then subsequently heated to promote the formation into metastable products. The compounds in this dissertation all show interest as thermoelectric materials, with significant discussion devoted to their optimization as such.

The formation mechanism of the metastable FeSb_3 phase over thermodynamically stable FeSb_2 was investigated by atomic pair distribution analysis (PDF). It was found that the local structure of the metastable phase is present in precursors even when compositionally unfavorable. When provided a nucleation environment locally free of chemical gradients favoring the thermodynamically stable compound and globally favorable in composition for the FeSb_3 phase, the metastable phase can be formed as a polycrystalline thin film. Furthermore, the first reports of PDF on thin films in a transmission geometry was reported, with results closely matching data collected from powders of the same material.

Self-assembly of layered materials from designed precursors allows for the investigation of an unprecedented amount of new compounds using the concept of phase homology. By defining distinct ‘building blocks’ that can be predictably introduced into a material, relationships between composition, structure, and properties can be explored. Several homologous and isomeric series of compounds within the $([\text{MSe}]_{1+\delta})_m(\text{TiSe}_2)_n$ ($\text{M}=\text{Pb}, \text{Sn}$) family of nanolaminate compounds were investigated with systematic variation in m and n . These series allow for controllably modifying the chemical system, relative composition, nanoarchitecture, and structure in a controllable fashion.

In order to determine the effects of defects on $([\text{PbSe}]_{1+\delta})_m(\text{TiSe}_2)_n$ nanolaminates, precursors with deliberate nonstoichiometry were investigated. The laminates tend to ‘self-heal’ during self-assembly, but inclusionary defects form with high compositional unfavorability of the precursor. Even so, the transport and global layered structure

was relatively insensitive to these defects despite the large compositional mismatch. Increasing the thickness of the layers by increasing m and n congruently has little effect on the structure of either compound beside nucleation of larger crystallites within the layers. However, it does all for band-bending away from the PbSe-TiSe₂ interfaces and decreases the degree of charge exchange within the layers. This also suggests that the reduced coulombic stabilization from thick layers is the basis for the thermodynamically stable, but structurally similar, misfit compounds only being found with $m, n \leq 2$. The introduction of buried interfaces into compounds where $m=n=4$ by reducing the thick blocks into smaller constituents while maintaining the same number of layers in the nanolaminate unit cell can be achieved forming solid state structural isomers. The readily characterizable platform of repeating nanolayered systems is especially well highlighted in these materials as, despite them being structurally and compositionally indistinguishable at the global scale, the nanoarchitectures can still be confirmed with laboratory tools. These compounds highlight a method whereby the vast synthetic space might be course-grained towards the optimal compound for an end-use, such as thermoelectric materials. Compounds with an intermediate number of buried interface exhibit enhanced thermoelectric performance relative to the other nanoarchitectures. Finally, by increasing n while maintaining m at 1, the mobile electrons exchanged between the PbSe constituent into the TiSe₂ can be ‘diluted’ across more layers, providing a controllable means of enhancing the Seebeck coefficient and thermoelectric performance of the nanolaminate. These results fit well to simple physical models of charge exchange between ridged bands and when taken with the results of previous chapters, suggest the band-bending within the interior of the TiSe₂ layers is less severe than in PbSe. For $n=18$, the highest thermoelectric power factor ever in the broader family of chalcogenide nanolaminates was reported, which is especially exciting considering the measurement was made at room-temperature, the thermal conductivity is expected to be near the amorphous limits, and the opportunity for further optimization. Combining the effects from buried interfaces and a high relative ratio of TiSe₂ is an obvious next step for further optimizing the transport in this chemical system.

The substitution of Pb atoms for isovalent Sn to form $([\text{SnSe}]_{1+\delta})_m(\text{TiSe}_2)_n$ nanolaminates wouldn’t be thought to dramatically alter the transport behavior. In fact, the transport between compounds with $m=n=1$ is qualitatively quite similar.

However, SnSe undergoes significant structural distortions as the size of the layers are changed and complex behavior and interactions between constituents are observed. In the case of increasing n as m is held at 1, similar behavior is initially seen as to the PbSe-containing compounds. However, and somewhat surprisingly as the SnSe layer size is maintained and the TiSe₂ structure does not change with size, highly divergent behavior is seen beyond $n=4$. In these cases, the temperature dependence and values of both the resistivity and carrier densities differ drastically from the lower n and PbSe-containing compounds. Furthermore, the Seebeck coefficient at cryogenic temperatures significantly increases in magnitude for $n=15$ relative to the expected behavior seen in $n=3$. This results in a noteworthy cryogenic thermoelectric power and estimated values of the thermoelectric figure of merit near unity. Increasing m and n concomitantly shows significantly changing structure in the SnSe layers while maintaining the TiSe₂ structure. Unlike PbSe, the ‘soft’ SnSe layers distort and appear to form commensurate axis with TiSe₂. As the layers thicken and interior atoms are introduced a complicated energy landscape allows for the formation of several intermediate structures before the bulk SnSe phase is observed. The varying structures result in radically changing transport properties, including the first signs of bipolar behavior observed in TiSe₂ nanolaminates. The results are unprecedented and currently no physical explanation has been developed that describes the observed behavior. While work in this chemical system seems to initially decrease the inherent value of using it with phase homologues, the ability to synthesize the compounds remains and further experimentation will help build understanding of the changing structures, which will aid in development of new physical models, and finally allow for prediction to be made but in a much richer chemical environment.

REFERENCES CITED

CHAPTER I

- (1) Mott, N.; Jones, H. *The Theory of the Properties of Metals and Alloys*; Oxford University Press: Oxford, 1936.
- (2) Snyder, G. J.; Toberer, E. S. Complex Thermoelectric Materials. *Nat. Mater.* **2008**, 7 (2), 105–114.
- (3) Pei, Y.; Wang, H.; Snyder, G. J. Band Engineering of Thermoelectric Materials. *Adv. Mater.* **2012**, 24 (46), 6125–6135.
- (4) Pei, Y.; LaLonde, A. D.; Wang, H.; Snyder, G. J. Low Effective Mass Leading to High Thermoelectric Performance. *Energy Environ. Sci.* **2012**, 5 (7), 7963.
- (5) Pei, Y.; Shi, X.; LaLonde, A.; Wang, H.; Chen, L.; Snyder, G. J. Convergence of Electronic Bands for High Performance Bulk Thermoelectrics. *Nature* **2011**, 473 (7345), 66–69.
- (6) DiSalvo, F. J. Thermoelectric Cooling and Power Generation. *Science*. **1999**, 285 (5428), 703–706.
- (7) Morelli, D. T.; Jovovic, V.; Heremans, J. P. Intrinsically Minimal Thermal Conductivity in Cubic I-V-VI₂ Semiconductors. *Phys. Rev. Lett.* **2008**, 101 (3), 035901.
- (8) Slack, G. A. New Materials and Performance Limits for Thermoelectric Cooling. In *CRC Handbook of Thermoelectrics*; Rowe, D. M., Ed.; CRC Press, Boca Raton, FL, USA, 1995; pp 407–440.
- (9) Kleinke, H. New Bulk Materials for Thermoelectric Power Generation: Clathrates and Complex Antimonides †. *Chem. Mater.* **2010**, 22 (3), 604–611.
- (10) Toberer, E. S.; May, A. F.; Snyder, G. J. Zintl Chemistry for Designing High Efficiency Thermoelectric Materials † ‡. *Chem. Mater.* **2010**, 22 (3), 624–634.
- (11) Sales, B. C.; Mandrus, D.; Williams, R. K. Filled Skutterudite Antimonides: A New Class of Thermoelectric Materials. *Science*. **1996**, 272 (5266), 1325–1328.

- (12) Shi, X.; Yang, J.; Salvador, J. R.; Chi, M.; Cho, J. Y.; Wang, H.; Bai, S.; Yang, J.; Zhang, W.; Chen, L. Multiple-Filled Skutterudites: High Thermoelectric Figure of Merit through Separately Optimizing Electrical and Thermal Transports. *J. Am. Chem. Soc.* **2011**, *133* (20), 7837–7846.
- (13) Snyder, G. J.; Christensen, M.; Nishibori, E.; Caillat, T.; Iversen, B. B. Disordered Zinc in Zn_4Sb_3 with Phonon-Glass and Electron-Crystal Thermoelectric Properties. *Nat. Mater.* **2004**, *3* (7), 458–463.
- (14) Hsu, K. F.; Loo, S.; Guo, F.; Chen, W.; Dyck, J. S.; Uher, C.; Hogan, T.; Polychroniadis, E. K.; Kanatzidis, M. G. Cubic $\text{AgPb}(m)\text{SbTe}(2+m)$: Bulk Thermoelectric Materials with High Figure of Merit. *Science* **2004**, *303* (5659), 818–821.
- (15) Poudeu, P. F. P.; D'Angelo, J.; Downey, A. D.; Short, J. L.; Hogan, T. P.; Kanatzidis, M. G. High Thermoelectric Figure of Merit and Nanostructuring in Bulk P-Type $\text{Na}[1-x]\text{Pb}[m]\text{Sb}[y]\text{Te}[m+2]$. *Angew. Chemie* **2006**, *118* (23), 3919–3923.
- (16) Biswas, K.; He, J.; Zhang, Q.; Wang, G.; Uher, C.; Dravid, V. P.; Kanatzidis, M. G. Strained Endotaxial Nanostructures with High Thermoelectric Figure of Merit. *Nat. Chem.* **2011**, *3* (2), 160–166.
- (17) Biswas, K.; He, J.; Wang, G.; Lo, S.-H.; Uher, C.; Dravid, V. P.; Kanatzidis, M. G. High Thermoelectric Figure of Merit in Nanostructured P-Type PbTe-MTe ($M = \text{Ca, Ba}$). *Energy Environ. Sci.* **2011**, *4* (11), 4675.
- (18) Biswas, K.; He, J.; Blum, I. D.; Wu, C.-I.; Hogan, T. P.; Seidman, D. N.; Dravid, V. P.; Kanatzidis, M. G. High-Performance Bulk Thermoelectrics with All-Scale Hierarchical Architectures. *Nature* **2012**, *489* (7416), 414–418.
- (19) Zhao, L.-D.; Hao, S.; Lo, S.-H.; Wu, C.-I.; Zhou, X.; Lee, Y.; Li, H.; Biswas, K.; Hogan, T. P.; Uher, C.; et al. High Thermoelectric Performance via Hierarchical Compositionally Alloyed Nanostructures. *J. Am. Chem. Soc.* **2013**, *135* (19), 7364–7370.

- (20) Poudel, B.; Hao, Q.; Ma, Y.; Lan, Y.; Minnich, A.; Yu, B.; Yan, X.; Wang, D.; Muto, A.; Vashaee, D.; et al. High-Thermoelectric Performance of Nanostructured Bismuth Antimony Telluride Bulk Alloys. *Science* **2008**, 320 (5876), 634–638.
- (21) Zhao, L.-D.; Lo, S.-H.; Zhang, Y.; Sun, H.; Tan, G.; Uher, C.; Wolverton, C.; David, V. P.; Kanatzidis, M. G. Ultralow Thermal Conductivity and High Thermoelectric Figure of Merit in SnSe Crystals. *Nature* **2014**, 508 (7496), 373–377.
- (22) Rhyee, J.-S.; Lee, K. H.; Lee, S. M.; Cho, E.; Kim, S. Il; Lee, E.; Kwon, Y. S.; Shim, J. H.; Kotliar, G. Peierls Distortion as a Route to High Thermoelectric Performance in In(4)Se(3- δ) Crystals. *Nature* **2009**, 459 (7249), 965–968.
- (23) Heremans, J. P.; Wiendlocha, B.; Chamoire, A. M. Resonant Levels in Bulk Thermoelectric Semiconductors. *Energy Environ. Sci.* **2012**, 5 (2), 5510–5530.
- (24) Mahan, G. D.; Sofo, J. O. The Best Thermoelectric. *Proc. Natl. Acad. Sci.* **1996**, 93 (15), 7436–7439.
- (25) Heremans, J. P.; Jovovic, V.; Toberer, E. S.; Saramat, A.; Kurosaki, K.; Charoenphakdee, A.; Yamanaka, S.; Snyder, G. J. Enhancement of Thermoelectric Efficiency in PbTe by Distortion of the Electronic Density of States. *Science* **2008**, 321 (5888), 554–557.
- (26) Pei, Y.; LaLonde, A.; Iwanaga, S.; Snyder, G. J. High Thermoelectric Figure of Merit in Heavy Hole Dominated PbTe. *Energy Environ. Sci.* **2011**, 4 (6), 2085.
- (27) Singh, D. J. Doping-Dependent Thermopower of PbTe from Boltzmann Transport Calculations. *Phys. Rev. B* **2010**, 81 (19), 195217.
- (28) Hicks, L. D.; Dresselhaus, M. S. Effect of Quantum-Well Structures on the Thermoelectric Figure of Merit. *Phys. Rev. B* **1993**, 47 (19), 12727–12731.
- (29) Hicks, L. D.; Dresselhaus, M. S. Thermoelectric Figure of Merit of a One-Dimensional Conductor. *Phys. Rev. B* **1993**, 47 (24), 16631–16634.
- (30) Hicks, L. D.; Harman, T. C.; Sun, X.; Dresselhaus, M. S. Experimental Study of the Effect of Quantum-Well Structures on the Thermoelectric Figure of Merit. *Phys. Rev. B* **1996**, 53 (16), R10493–R10496.

- (31) Harman, T. C.; Spears, D. L.; Manfra, M. J. High Thermoelectric Figures of Merit in PbTe Quantum Wells. *J. Electron. Mater.* **1996**, 25 (7), 1121–1127.
- (32) Heremans, J.; Thrush, C. M. Thermoelectric Power of Bismuth Nanowires. *Phys. Rev. B* **1999**, 59 (19), 12579–12583.
- (33) Rabina, O.; Lin, Y.-M.; Dresselhaus, M. S. Anomalous High Thermoelectric Figure of Merit in Bi[1-x] Sb[X] Nanowires by Carrier Pocket Alignment. *Appl. Phys. Lett.* **2001**, 79 (1), 81.
- (34) Heremans, J. P.; Thrush, C. M.; Morelli, D. T.; Wu, M.-C. Thermoelectric Power of Bismuth Nanocomposites. *Phys. Rev. Lett.* **2002**, 88 (21), 216801.
- (35) Teweldebrhan, D.; Goyal, V.; Balandin, A. A. Exfoliation and Characterization of Bismuth Telluride Atomic Quintuples and Quasi-Two-Dimensional Crystals. *Nano Lett.* **2010**, 10 (4), 1209–1218.
- (36) Touzelbaev, M. N.; Zhou, P.; Venkatasubramanian, R.; Goodson, K. E. Thermal Characterization of Bi₂Te₃/Sb₂Te₃ Superlattices. *J. Appl. Phys.* **2001**, 90 (2), 763.
- (37) Winkler, M.; Liu, X.; König, J. D.; Buller, S.; Schürmann, U.; Kienle, L.; Bensch, W.; Böttner, H. Electrical and Structural Properties of Bi₂Te₃ and Sb₂Te₃ Thin Films Grown by the Nanoalloying Method with Different Deposition Patterns and Compositions. *J. Mater. Chem.* **2012**, 22 (22), 11323.
- (38) Mahan, G. D. Rare Earth Thermoelectrics. In *XVI ICT "97. Proceedings ICT"97. 16th International Conference on Thermoelectrics (Cat. No.97TH8291)*; IEEE, 1997; pp 21–27.
- (39) MAHAN, G. D. Good Thermoelectrics. *Solid state Phys.* 51, 81–157.
- (40) Rowe, D. M.; Kuznetsov, V. L.; Kuznetsova, L. A.; Min, G. Electrical and Thermal Transport Properties of Intermediate-Valence Yb Al₃. *J. Phys. D. Appl. Phys.* **2002**, 35 (17), 2183–2186.
- (41) Lee, S. J.; Park, J. M.; Canfield, P. C.; Lynch, D. W. Optical Properties and Electronic Structures of Single Crystalline R Al₃ (R = Sc , Yb, and Lu). *Phys. Rev. B* **2003**, 67 (7), 075104.

- (42) Bonten, A.; Johnsen, S.; Madsen, G. K. H.; Iversen, B. B.; Steglich, F. Colossal Seebeck Coefficient in Strongly Correlated Semiconductor FeSb₂. *Europhys. Lett.* **2007**, *80* (1), 17008.
- (43) Wang, Y.; Rogado, N. S.; Cava, R. J.; Ong, N. P. Spin Entropy as the Likely Source of Enhanced Thermopower in Na_xCo₂O₄. *Nature* **2003**, *423* (6938), 425–428.
- (44) Imai, H.; Shimakawa, Y.; Kubo, Y. Large Thermoelectric Power Factor in TiS₂ Crystal with Nearly Stoichiometric Composition. *Phys. Rev. B* **2001**, *64* (24), 241104.
- (45) Gaby, J. H.; DeLong, B.; Brown, F. C.; Kirby, R.; Lévy, F. Origin of the Structural Transition in TiSe₂. *Solid State Commun.* **1981**, *39* (11), 1167–1170.
- (46) Guilmeau, E.; Bréard, Y.; Maignan, A. Transport and Thermoelectric Properties in Copper Intercalated TiS₂ Chalcogenide. *Appl. Phys. Lett.* **2011**, *99* (5), 052107.
- (47) Bhatt, R.; Basu, R.; Bhattacharya, S.; Singh, A.; Aswal, D. K.; Gupta, S. K.; Okram, G. S.; Ganesan, V.; Venkateshwarlu, D.; Surger, C.; et al. Low Temperature Thermoelectric Properties of Cu Intercalated TiSe₂: A Charge Density Wave Material. *Appl. Phys. A* **2013**, *111* (2), 465–470.
- (48) Bhatt, R.; Bhattacharya, S.; Patel, M.; Basu, R.; Singh, A.; Sürger, C.; Navaneethan, M.; Hayakawa, Y.; Aswal, D. K.; Gupta, S. K. Thermoelectric Performance of Cu Intercalated Layered TiSe₂ above 300 K. *J. Appl. Phys.* **2013**, *114* (11), 114509.
- (49) Wiegers, G. . Misfit Layer Compounds: Structures and Physical Properties. *Prog. Solid State Chem.* **1996**, *24* (1-2), 1–139.
- (50) Koumoto, K.; Terasaki, I.; Funahashi, R. Complex Oxide Materials for Potential Thermoelectric Applications. *MRS Bull.* **2011**, *31* (03), 206–210.
- (51) Limelette, P.; Hébert, S.; Hardy, V.; Frésard, R.; Simon, C.; Maignan, A. Scaling Behavior in Thermoelectric Misfit Cobalt Oxides. *Phys. Rev. Lett.* **2006**, *97* (4), 046601.

- (52) Wan, C.; Wang, Y.; Wang, N.; Koumoto, K. Low-Thermal-Conductivity (MS)[1+x](TiS₂)₂ (M = Pb, Bi, Sn) Misfit Layer Compounds for Bulk Thermoelectric Materials. *Materials (Basel)*. **2010**, 3 (4), 2606–2617.
- (53) Jood, P.; Ohta, M.; Nishiate, H.; Yamamoto, A.; Lebedev, O. I.; Berthebaud, D.; Suekuni, K.; Kunii, M. Microstructural Control and Thermoelectric Properties of Misfit Layered Sulfides (LaS)[1+ M] TS₂ (T = Cr, Nb): The Natural Superlattice Systems. *Chem. Mater.* **2014**, 26 (8), 2684–2692.
- (54) Wiegers, G. A. Charge Transfer between Layers in Misfit Layer Compounds. *J. Alloys Compd.* **1995**, 219 (1-2), 152–156.
- (55) Fang, C. M.; Ettema, A. R. H. F.; Haas, C.; Wiegers, G. A.; van Leuken, H.; de Groot, R. A. Electronic Structure of the Misfit-Layer Compound (SnS)_{1.17}NbS₂ Deduced from Band-Structure Calculations and Photoelectron Spectra. *Phys. Rev. B* **1995**, 52 (4), 2336–2347.
- (56) Cario, L.; Lafond, A.; Palvadeau, P.; Deudon, C.; Meerschaut, A. Evidence of a Mixed-Valence State for Europium in the Misfit Layer Compound [(EuS)_{1.5}]_{1.15}NbS₂ by Means of a Superspace Structural Determination, Mössbauer Spectroscopy, and Magnetic Measurements. *J. Solid State Chem.* **1999**, 147 (1), 58–67.
- (57) Nong, N. V.; Liu, C.-J.; Ohtaki, M. Improvement on the High Temperature Thermoelectric Performance of Ga-Doped Misfit-Layered Ca₃Co_{4-x}Ga_xO_{9+δ} (x=0, 0.05, 0.1, and 0.2). *J. Alloys Compd.* **2010**, 491 (1-2), 53–56.
- (58) Shen, J. J.; Liu, X. X.; Zhu, T. J.; Zhao, X. B. Improved Thermoelectric Properties of La-Doped Bi₂Sr₂Co₂O₉-Layered Misfit Oxides. *J. Mater. Sci.* **2009**, 44 (7), 1889–1893.
- (59) Venkatasubramanian, R.; Siivola, E.; Colpitts, T.; O’Quinn, B. Thin-Film Thermoelectric Devices with High Room-Temperature Figures of Merit. *Nature* **2001**, 413 (6856), 597–602.
- (60) Harman, T. C.; Taylor, P. J.; Walsh, M. P.; LaForge, B. E. Quantum Dot Superlattice Thermoelectric Materials and Devices. *Science* **2002**, 297 (5590), 2229–2232.

- (61) Winkler, M.; Liu, X.; Schürmann, U.; König, J. D.; Kienle, L.; Bensch, W.; Böttner, H. Current Status in Fabrication, Structural and Transport Property Characterization, and Theoretical Understanding of Bi₂Te₃ / Sb₂Te₃ Superlattice Systems. *Zeitschrift für Anorg. und Allg. Chemie* **2012**, 638 (15), 2441–2454.
- (62) Hansen, A.-L.; Dankwort, T.; Winkler, M.; Ditto, J.; Johnson, D. C.; Koenig, J. D.; Bartholomé, K.; Kienle, L.; Bensch, W. Synthesis and Thermal Instability of High-Quality Bi₂Te₃ /Sb₂Te₃ Superlattice Thin Film Thermoelectrics. *Chem. Mater.* **2014**, 26 (22), 6518–6522.
- (63) Böttner, H.; Chen, G.; Venkatasubramanian, R. Aspects of Thin-Film Superlattice Thermoelectric Materials, Devices, and Applications. *MRS Bull.* **2011**, 31 (03), 211–217.
- (64) Cui, H.; Bhat, I.; O’Quinn, B.; Venkatasubramanian, R. In-Situ Monitoring of the Growth of Bi₂Te₂ and Sb₂Te₃ Films and Bi₂Te₃-Sb₂Te₃ Superlattice Using Spectroscopic Ellipsometry. *J. Electron. Mater.* **2001**, 30 (11), 1376–1381.
- (65) Peranio, N.; Eibl, O.; Nurnus, J. Structural and Thermoelectric Properties of Epitaxially Grown Bi₂Te₃ Thin Films and Superlattices. *J. Appl. Phys.* **2006**, 100 (11), 114306.
- (66) Wang, G.; Endicott, L.; Uher, C. Recent Advances in the Growth of Bi–Sb–Te–Se Thin Films. *Sci. Adv. Mater.* **2011**, 3 (4), 539–560.
- (67) Banga, D.; Lensch-Falk, J. L.; Medlin, D. L.; Stavila, V.; Yang, N. Y. C.; Robinson, D. B.; Sharma, P. A. Periodic Modulation of Sb Stoichiometry in Bi₂Te₃ /Bi₂- X Sb X Te₃ Multilayers Using Pulsed Electrodeposition. *Cryst. Growth Des.* **2012**, 12 (3), 1347–1353.
- (68) Zeipl, R.; Walachová, J.; Pavelka, M.; Jelínek, M.; Studnička, V.; Kocourek, T. Power Factor of Very Thin Thermoelectric Layers of Different Thickness Prepared by Laser Ablation. *Appl. Phys. A* **2008**, 93 (3), 663–667.
- (69) It’s Still All about Graphene. *Nat. Mater.* **2011**, 10 (1), 1.
- (70) Novoselov, K. S.; Geim, A. K.; Morozov, S. V; Jiang, D.; Zhang, Y.; Dubonos, S. V; Grigorieva, I. V; Firsov, A. A. Electric Field Effect in Atomically Thin Carbon Films. *Science* **2004**, 306 (5696), 666–669.

- (71) Pacilé, D.; Meyer, J. C.; Girit, C. O.; Zettl, A. The Two-Dimensional Phase of Boron Nitride: Few-Atomic-Layer Sheets and Suspended Membranes. *Appl. Phys. Lett.* **2008**, *92* (13), 133107.
- (72) Xia, F.; Wang, H.; Jia, Y. Rediscovering Black Phosphorus as an Anisotropic Layered Material for Optoelectronics and Electronics. *Nat. Commun.* **2014**, *5*, 4458.
- (73) Min, Y.; Moon, G. D.; Kim, B. S.; Lim, B.; Kim, J.-S.; Kang, C. Y.; Jeong, U. Quick, Controlled Synthesis of Ultrathin Bi₂Se₃ Nanodiscs and Nanosheets. *J. Am. Chem. Soc.* **2012**, *134* (6), 2872–2875.
- (74) Mas-Ballesté, R.; Gómez-Navarro, C.; Gómez-Herrero, J.; Zamora, F. 2D Materials: To Graphene and Beyond. *Nanoscale* **2011**, *3* (1), 20–30.
- (75) Huang, X.; Zeng, Z.; Zhang, H. Metal Dichalcogenide Nanosheets: Preparation, Properties and Applications. *Chem. Soc. Rev.* **2013**, *42* (5), 1934–1946.
- (76) Coleman, J. N.; Lotya, M.; O'Neill, A.; Bergin, S. D.; King, P. J.; Khan, U.; Young, K.; Gaucher, A.; De, S.; Smith, R. J.; et al. Two-Dimensional Nanosheets Produced by Liquid Exfoliation of Layered Materials. *Science* **2011**, *331* (6017), 568–571.
- (77) Zeng, Z.; Sun, T.; Zhu, J.; Huang, X.; Yin, Z.; Lu, G.; Fan, Z.; Yan, Q.; Hng, H. H.; Zhang, H. An Effective Method for the Fabrication of Few-Layer-Thick Inorganic Nanosheets. *Angew. Chem. Int. Ed. Engl.* **2012**, *51* (36), 9052–9056.
- (78) Splendiani, A.; Sun, L.; Zhang, Y.; Li, T.; Kim, J.; Chim, C.-Y.; Galli, G.; Wang, F. Emerging Photoluminescence in Monolayer MoS₂. *Nano Lett.* **2010**, *10* (4), 1271–1275.
- (79) Radisavljevic, B.; Radenovic, A.; Brivio, J.; Giacometti, V.; Kis, A. Single-Layer MoS₂ Transistors. *Nat. Nanotechnol.* **2011**, *6* (3), 147–150.
- (80) Goyal, V.; Teweldebrhan, D.; Balandin, A. A. Mechanically-Exfoliated Stacks of Thin Films of Bi₂Te₃ Topological Insulators with Enhanced Thermoelectric Performance. *Appl. Phys. Lett.* **2010**, *97* (13), 133117.

- (81) Wu, J.; Schmidt, H.; Amara, K. K.; Xu, X.; Eda, G.; Özyilmaz, B. Large Thermoelectricity via Variable Range Hopping in Chemical Vapor Deposition Grown Single-Layer MoS₂. *Nano Lett.* **2014**, *14* (5), 2730–2734.
- (82) Fei, R.; Faghaninia, A.; Soklaski, R.; Yan, J.-A.; Lo, C.; Yang, L. Enhanced Thermoelectric Efficiency via Orthogonal Electrical and Thermal Conductances in Phosphorene. *Nano Lett.* **2014**, *14* (11), 6393–6399.
- (83) Huang, W.; Da, H.; Liang, G. Thermoelectric Performance of MX₂ (M = Mo, W; X = S, Se) Monolayers. *J. Appl. Phys.* **2013**, *113* (10), 104304.
- (84) Geim, A. K.; Grigorieva, I. V. Van Der Waals Heterostructures. *Nature* **2013**, *499* (7459), 419–425.
- (85) Lin, Q.; Smeller, M.; Heideman, C. L.; Zschack, P.; Koyano, M.; Anderson, M. D.; Kykyneshi, R.; Keszler, D. A.; Anderson, I. M.; Johnson, D. C. Rational Synthesis and Characterization of a New Family of Low Thermal Conductivity Misfit Layer Compounds [(PbSe) 0.99] M (WSe₂) N⁺. *Chem. Mater.* **2009**, *22* (3), 1002–1009.
- (86) Atkins, R.; Wilson, J.; Zschack, P.; Grosse, C.; Neumann, W.; Johnson, D. C. Synthesis of [(SnSe) 1.15] M (TaSe₂) N Ferrecrystals: Structurally Tunable Metallic Compounds. *Chem. Mater.* **2012**, *24* (23), 4594–4599.
- (87) Beekman, M.; Cogburn, G.; Heideman, C.; Rouvimov, S.; Zschack, P.; Neumann, W.; Johnson, D. C. New Layered Intergrowths in the Sn-Mo-Se System. *J. Electron. Mater.* **2012**, *41* (6), 1476–1480.
- (88) Beekman, M.; Heideman, C. L.; Johnson, D. C. Ferrecrystals: Non-Epitaxial Layered Intergrowths. *Semicond. Sci. Technol.* **2014**, *29* (6), 064012.
- (89) Moore, D. B.; Beekman, M.; Disch, S.; Johnson, D. C. Telluride Misfit Layer Compounds: [(PbTe)1.17]m(TiTe₂)n. *Angew. Chem. Int. Ed. Engl.* **2014**, *53* (22), 5672–5675.
- (90) Heideman, C. L.; Tepfer, S.; Lin, Q.; Rostek, R.; Zschack, P.; Anderson, M. D.; Anderson, I. M.; Johnson, D. C. Designed Synthesis, Structure, and Properties of a Family of Ferrecrystalline Compounds [(PbSe)(1.00)](m)(MoSe₂)(n). *J. Am. Chem. Soc.* **2013**, *135* (30), 11055–11062.

- (91) Falmbigl, M.; Alemayehu, M. B.; Merrill, D. R.; Beekman, M.; Johnson, D. C. In-Plane Structure of Ferecrystalline Compounds. *Cryst. Res. Technol.* **2015**, 50 (6), 464–472.
- (92) Chiritescu, C.; Cahill, D. G.; Nguyen, N.; Johnson, D.; Bodapati, A.; Koblinski, P.; Zschack, P. Ultralow Thermal Conductivity in Disordered, Layered WSe₂ Crystals. *Science* **2007**, 315 (5810), 351–353.
- (93) Chiritescu, C.; Cahill, D. G.; Heideman, C.; Lin, Q.; Mortensen, C.; Nguyen, N. T.; Johnson, D.; Rostek, R.; Böttner, H. Low Thermal Conductivity in Nanoscale Layered Materials Synthesized by the Method of Modulated Elemental Reactants. *J. Appl. Phys.* **2008**, 104 (3), 033533.
- (94) Mavrokefalos, A.; Lin, Q.; Beekman, M.; Seol, J. H.; Lee, Y. J.; Kong, H.; Pettes, M. T.; Johnson, D. C.; Shi, L. In-Plane Thermal and Thermoelectric Properties of Misfit-Layered [(PbSe)_{0.99}]_x (WSe₂)_x Superlattice Thin Films. *Appl. Phys. Lett.* **2010**, 96 (18), 181908.
- (95) Moore, D.; Stolt, M.; Atkins, R.; Sitts, L.; Jones, Z.; Disch, S.; Beekman, M.; Johnson, D. Structural and Electrical Properties of (PbSe)_{1.16} TiSe₂. *Emerg. Mater. Res.* **2012**, 1 (6), 292–298.
- (96) Moore, D. B.; Beekman, M.; Disch, S.; Zschack, P.; Haßler, I.; Neumann, W.; Johnson, D. C. Synthesis, Structure, and Properties of Turbostratically Disordered (PbSe)_{1.18} (TiSe₂)₂. *Chem. Mater.* **2013**, 25 (12), 2404–2409.
- (97) Merrill, D. R.; Moore, D. B.; Ditto, J.; Sutherland, D. R.; Falmbigl, M.; Winkler, M.; Pernau, H.-F.; Johnson, D. C. The Synthesis, Structure, and Electrical Characterization of (SnSe)_{1.2} TiSe₂. *Eur. J. Inorg. Chem.* **2014**.
- (98) Merrill, D.; Moore, D.; Bauers, S.; Falmbigl, M.; Johnson, D. Misfit Layer Compounds and Ferecrystals: Model Systems for Thermoelectric Nanocomposites. *Materials (Basel)*. **2015**, 8 (4), 2000–2029.
- (99) Bauers, S. R.; Merrill, D. R.; Moore, D. B.; Johnson, D. C. Carrier Dilution in TiSe₂ Based Intergrowth Compounds for Enhanced Thermoelectric Performance. *J. Mater. Chem. C* **2015**, 3 (40), 10451–10458.

- (100) Giang, N.; Xu, Q.; Hor, Y. S.; Williams, A. J.; Dutton, S. E.; Zandbergen, H. W.; Cava, R. J. Superconductivity at 2.3 K in the Misfit Compound (PbSe) 1.16 (TiSe 2) 2. *Phys. Rev. B* **2010**, 82 (2), 24503.
- (101) Ohno, Y. Electronic Structure of the Misfit-Layer Compounds PbTiS₃ and SnNbS₃. *Phys. Rev. B* **1991**, 44 (3), 1281–1291.
- (102) Wiegers, G. A.; Haange, R. J. Electrical Transport Properties of the Misfit Layer Compounds (SnS) 1.20 TiS₂ and (PbS) 1.18 TiS₂. *Eur. J. solid state Inorg. Chem.* **1991**, 28 (5), 1071–1078.
- (103) Merrill, D. R.; Sutherland, D. R.; Ditto, J.; Bauers, S. R.; Falmbigl, M.; Medlin, D. L.; Johnson, D. C. Kinetically Controlled Site-Specific Substitutions in Higher-Order Heterostructures. *Chem. Mater.* **2015**, 27 (11), 4066–4072.
- (104) Merrill, D. R.; Moore, D. B.; Coffey, M. N.; Jansons, A. W.; Falmbigl, M.; Johnson, D. C. Synthesis and Characterization of Turbostratically Disordered (BiSe) 1.15 TiSe 2. *Semicond. Sci. Technol.* **2014**, 29 (6), 064004.
- (105) Wood, S. R.; Merrill, D. R.; Falmbigl, M.; Moore, D. B.; Ditto, J.; Esters, M.; Johnson, D. C. Tuning Electrical Properties through Control of TiSe 2 Thickness in (BiSe) 1+ δ (TiSe 2) N Compounds. *Chem. Mater.* **2015**, 27 (17), 6067–6076.
- (106) Bauers, S. R.; Moore, D. B.; Ditto, J.; Johnson, D. C. Phase Width of Kinetically Stable ([PbSe]1+ δ)1(TiSe₂)1 Ferecrystals and the Effect of Precursor Composition on Electrical Properties. *J. Alloys Compd.* **2015**, 645, 118–124.

CHAPTER II

- (1) Noh, M.; Johnson, C. D.; Hornbostel, M. D.; Thiel, J.; Johnson, D. C. Control of Reaction Pathway and the Nanostructure of Final Products through the Design of Modulated Elemental Reactants. *Chem. Mater.* **1996**, 8, 1625–1635.
- (2) Fischer, D.; Jansen, M. Low-Activation Solid-State Syntheses by Reducing Transport Lengths to Atomic Scales As Demonstrated by Case Studies on AgNO₃ and AgO. *J. Am. Chem. Soc.* **2002**, 124 (14), 3488–3489.
- (3) Hornbostel, M. D.; Hyer, E. J.; Thiel, J.; Johnson, D. C. Rational Synthesis of Metastable Skutterudite Compounds Using Multilayer Precursors. *J. Am. Chem. Soc.* **1997**, 119, 2665–2668.

- (4) Anderson, M. D.; Thompson, J. O.; Johnson, D. C. Avoiding Binary Compounds as Reaction Intermediates in Solid State Reactions. *Chem. Mater.* **2013**, *25*, 3996–4002.
- (5) Fukuto, M.; Hornbostel, M. D.; Johnson, D. C. Use of Superlattice Structure To Control Reaction Mechanism: Kinetics and Energetics of Nb₅Se₄ Formation. *J. Am. Chem. Soc.* **1994**, *116*, 9136–9140.
- (6) Esters, M.; Alemayehu, M. B.; Jones, Z.; Nguyen, N. T.; Anderson, M. D.; Grosse, C.; Fischer, S. F.; Johnson, D. C. Synthesis of Inorganic Structural Isomers By Diffusion-Constrained Self-Assembly of Designed Precursors: A Novel Type of Isomerism. *Angew. Chemie* **2015**, *127* (4), 1146–1150.
- (7) Merrill, D. R.; Sutherland, D. R.; Ditto, J. J.; Moore, D. B.; Falmbigl, M.; Medlin, D. L.; Johnson, D. C. The Synthesis of $\{[(\text{PbSe})_{1+\delta}]_m (\text{TiSe}_2)_n [(\text{SnSe}_2)_{1+\gamma}]_m (\text{TiSe}_2)_n\}$ Heterostructures with Designed Nanoarchitectures by Self Assembly of Amorphous Precursors. *Nanoscale* **2016**, *8* (28), 13646–13651.
- (8) Beekman, M.; Heideman, C. L.; Johnson, D. C. Ferecrystals: Non-Epitaxial Layered Intergrowths. *Semicond. Sci. Technol.* **2014**, *29* (6), 064012.

CHAPTER III

- (1) Stein, A.; Keller, S. W.; Mallouk, T. E. Turning down the Heat: Design and Mechanism in Solid-State Synthesis. *Science*. **1993**, *259*, 1558–1564.
- (2) West, A. R. *Solid State Chemistry and Its Applications*; John Wiley & Sons, 2007.
- (3) DiSalvo, F. J. Solid-State Chemistry: A Rediscovered Chemical Frontier. *Science*. **1990**, *247*, 649–655.
- (4) Chung, S.-Y.; Kim, Y.-M.; Kim, J.-G.; Kim, Y.-J. Multiphase Transformation and Ostwald's Rule of Stages during Crystallization of a Metal Phosphate. *Nat. Phys.* **2008**, *5*, 68–73.
- (5) Shoemaker, D. P.; Hu, Y.-J.; Chung, D. Y.; Halder, G. J.; Chupas, P. J.; Soderholm, L.; Mitchell, J. F.; Kanatzidis, M. G. In Situ Studies of a Platform for Metastable Inorganic Crystal Growth and Materials Discovery. *Proc. Natl. Acad. Sci.* **2014**, *111*, 10922–10927.

- (6) Jensen, K. M. Ø.; Christensen, M.; Juhas, P.; Tyrsted, C.; Bøjesen, E. D.; Lock, N.; Billinge, S. J. L.; Iversen, B. B. Revealing the Mechanisms behind SnO₂ Nanoparticle Formation and Growth during Hydrothermal Synthesis: An in Situ Total Scattering Study. *J. Am. Chem. Soc.* **2012**, *134*, 6785–6792.
- (7) Pienack, N.; Bensch, W. In-Situ Monitoring of the Formation of Crystalline Solids. *Angew. Chemie Int. Ed.* **2011**, *50*, 2014–2034.
- (8) Chen, Z.; Ren, Y.; Qin, Y.; Wu, H.; Ma, S.; Ren, J.; He, X.; Sun, Y.-K.; Amine, K. Solid State Synthesis of LiFePO₄ Studied by in Situ High Energy X-Ray Diffraction. *J. Mater. Chem.* **2011**, *21*, 5604.
- (9) Lebreton, F.; Belin, R. C.; Prieur, D.; Delahaye, T.; Blanchart, P. In Situ Study of the Solid-State Formation of U(1-x)Am(x)O(2±δ) Solid Solution. *Inorg. Chem.* **2012**, *51*, 9369–9375.
- (10) Sarkar, S.; Peter, S. C. Structural Phase Transitions in a New Compound Eu₂AgGe₃. *Inorg. Chem.* **2013**, *52*, 9741–9748.
- (11) Martinolich, A. J.; Neilson, J. R. Pyrite Formation via Kinetic Intermediates through Low-Temperature Solid-State Metathesis. *J. Am. Chem. Soc.* **2014**, *136*, 15654–15659.
- (12) Johnson, D. C. Controlled Synthesis of New Compounds Using Modulated Elemental Reactants. *Curr. Opin. Solid State Mater. Sci.* **1998**, *3*, 159–167.
- (13) Behrens, M.; Kiebach, R.; Bensch, W.; Häussler, D.; Jäger, W. Synthesis of Thin Cr₃Se₄ Films from Modulated Elemental Reactants via Two Amorphous Intermediates: A Detailed Examination of the Reaction Mechanism. *Inorg. Chem.* **2006**, *45*, 2704–2712.
- (14) Fukuto, M.; Hornbostel, M. D.; Johnson, D. C. Use of Superlattice Structure To Control Reaction Mechanism: Kinetics and Energetics of Nb₅Se₄ Formation. *J. Am. Chem. Soc.* **1994**, *116*, 9136–9140.
- (15) Fischer, D.; Jansen, M. Low-Activation Solid-State Syntheses by Reducing Transport Lengths to Atomic Scales As Demonstrated by Case Studies on AgNO₃ and AgO. *J. Am. Chem. Soc.* **2002**, *124* (14), 3488–3489.

- (16) Bach, A.; Fischer, D.; Jansen, M. Metastable Phase Formation of Indium Monochloride from an Amorphous Feedstock. *Zeitschrift für Anorg. und Allg. Chemie* **2013**, 639 (3-4), 465–467.
- (17) Smalley, A. L. E.; Jespersen, M. L.; Johnson, D. C. Synthesis and Structural Evolution of rusb_3 , a New Metastable Skutterudite Compound. *Inorg. Chem.* **2004**, 43, 2486–2490.
- (18) Berseth, P. A.; Hughes, T. A.; Schneidmiller, R.; Smalley, A.; Johnson, D. C. Low Temperature Synthesis Using Modulated Elemental Reactants: A New Metastable Ternary Compound, Ni_3MoSe_2 . *Solid State Sci.* **2002**, 4, 717–722.
- (19) Regus, M.; Kuhn, G.; Polesya, S.; Mankovsky, S.; Alemayehu, M.; Stolt, M.; Johnson, D. C.; Ebert, H.; Bensch, W. Experimental and Theoretical Investigation of the New, Metastable Compound Cr_3Sb . *Zeitschrift für Krist. - Cryst. Mater.* **2014**, 229.
- (20) Bach, A.; Fischer, D.; Mu, X.; Sigle, W.; van Aken, P. A.; Jansen, M. Structural Evolution of Magnesium Difluoride: From an Amorphous Deposit to a New Polymorph. *Inorg. Chem.* **2011**, 50 (4), 1563–1569.
- (21) Fister, L.; Novet, T.; Grant, C. A.; Johnson, D. C. Controlling Solid State Reactions via Rational Design of Superlattice Reactants. *ChemInform* **1994**, 25.
- (22) Anderson, M. D.; Thompson, J. O.; Johnson, D. C. Avoiding Binary Compounds as Reaction Intermediates in Solid State Reactions. *Chem. Mater.* **2013**, 25, 3996–4002.
- (23) Richter, K. W.; Ipser, H. Reinvestigation of the Binary Fe-Sb Phase Diagram. *J. Alloys Compd.* **1997**, 247, 247–249.
- (24) Hornbostel, M. D.; Hyer, E. J.; Thiel, J.; Johnson, D. C. Rational Synthesis of Metastable Skutterudite Compounds Using Multilayer Precursors. *J. Am. Chem. Soc.* **1997**, 119, 2665–2668.
- (25) Goodenough, J. B. Energy Bands in TX_2 Compounds with Pyrite, Marcasite, and Arsenopyrite Structures. *J. Solid State Chem.* **1972**, 5, 144–152.

- (26) A Papoian G; Hoffmann, R. Hypervalent Bonding in One, Two, and Three Dimensions: Extending the Zintl-Klemm Concept to Nonclassical Electron-Rich Networks. *Angew. Chem. Int. Ed. Engl.* **2000**, 39, 2408–2448.
- (27) Jung, D.; Whangbo, M. H.; Alvarez, S. Importance of the X4 Ring Orbitals for the Semiconducting, Metallic, or Superconducting Properties of Skutterudites MX₃ and RM₄X₁₂. *Inorg. Chem.* **1990**, 29, 2252–2255.
- (28) Schmøkel, M. S.; Bjerg, L.; Cenedese, S.; Jørgensen, M. R. V.; Chen, Y.-S.; Overgaard, J.; Iversen, B. B. Atomic Properties and Chemical Bonding in the Pyrite and Marcasite Polymorphs of FeS₂: A Combined Experimental and Theoretical Electron Density Study. *Chem. Sci.* **2014**, 5, 1408.
- (29) Stokkebro Schmøkel, M.; Bjerg, L.; Overgaard, J.; Krebs Larsen, F.; Hellerup Madsen, G. K.; Sugimoto, K.; Takata, M.; Brummerstedt Iversen, B. Pushing X-Ray Electron Densities to the Limit: Thermoelectric CoSb₃. *Angew. Chemie Int. Ed.* **2013**, 52, 1503–1506.
- (30) Noh, M.; Johnson, C. D.; Hornbostel, M. D.; Thiel, J.; Johnson, D. C. Control of Reaction Pathway and the Nanostructure of Final Products through the Design of Modulated Elemental Reactants. **1996**, 4756, 1625–1635.
- (31) Williams, J. R.; Johnson, M.; Johnson, D. C. Composition Dependence of the Nucleation Energy of Iron Antimonides from Modulated Elemental Reactants. *J. Am. Chem. Soc.* **2001**, 123, 1645–1649.
- (32) Holseth, H.; Kjekshus, A. Compounds With The Marcasite Type Crystal Structure. IV. The Crystal Structure Of FeS₂. *Acta Chem. Scand.* **1969**, 23, 3043–3050.
- (33) Phung, T. M.; Jensen, J. M.; Johnson, D. C.; Donovan, J. J.; McBurnett, B. G. Determination of the Composition of Ultra-Thin Ni-Si Films on Si: Constrained Modeling of Electron Probe Microanalysis and X-Ray Reflectivity Data. *X-Ray Spectrom.* **2008**, 37, 608–614.
- (34) Larson, A. C.; Von Dreele, R. B. Gsas. *Gen. Struct. Anal. Syst. LANSCE, MS-H805, Los Alamos, New Mex.* **1994**.
- (35) Toby, B. H. EXPGUI, A Graphical User Interface for GSAS. *J. Appl. Crystallogr.* **2001**, 34, 210–213.

- (36) Chupas, P. J.; Qiu, X.; Hanson, J. C.; Lee, P. L.; Grey, C. P.; Billinge, S. J. L. Rapid-Acquisition Pair Distribution Function (RA-PDF) Analysis. *J. Appl. Crystallogr.* **2003**, 36, 1342–1347.
- (37) Hammersley, A. P.; Svensson, S. O.; Hanfland, M.; Fitch, A. N.; Hausermann, D. Two-Dimensional Detector Software: From Real Detector to Idealised Image or Two-Theta Scan. *Int. J. High Press. Res.* **1996**, 14, 235–248.
- (38) Juhas, P.; Davis, T.; Farrow, C. L.; Billinge, S. J. L. PDFgetX3: A Rapid and Highly Automatable Program for Processing Powder Diffraction Data into Total Scattering Pair Distribution Functions. *J. Appl. Crystallogr.* **2013**, 46, 560–566.
- (39) Farrow, C. L.; Juhas, P.; Liu, J. W.; Bryndin, D.; Božin, E. S.; Bloch, J.; Proffen, T.; Billinge, S. J. L. PDFfit2 and PDFgui: Computer Programs for Studying Nanostructure in Crystals. *J. Phys. Condens. Matter* **2007**, 19, 335219.
- (40) Hulliger, F.; Mooser, E. Semiconductivity in Pyrite, Marcasite and Arsenopyrite Phases. *J. Phys. Chem. Solids* **1965**, 26, 429–433.
- (41) Brostigen, G.; Kjekshus, A. Relationships between the Structure Types Pyrite, Marcasite, and Arsenopyrite. *Acta Chem Scand* **1970**, 24 (), 2983–2992.
- (42) Nomura, K.; Ohta, H.; Takagi, A.; Kamiya, T.; Hirano, M.; Hosono, H. Room-Temperature Fabrication of Transparent Flexible Thin-Film Transistors Using Amorphous Oxide Semiconductors. *Nature* **2004**, 432 (7016), 488–492.
- (43) Tang, C. W.; VanSlyke, S. A.; Chen, C. H. Electroluminescence of Doped Organic Thin Films. *J. Appl. Phys.* **1989**, 65 (9), 3610.
- (44) O'Regan, B.; Grätzel, M. A Low-Cost, High-Efficiency Solar Cell Based on Dye-Sensitized Colloidal TiO₂ Films. *Nature* **1991**, 353 (6346), 737–740.
- (45) Ginley, D. S.; Bright, C. Transparent Conducting Oxides. *MRS Bull.* **2000**, 25 (08), 15–18.
- (46) Hampden-Smith, M. J.; Kudas, T. T. Chemical Vapor Deposition of Metals: Part 1. An Overview of CVD Processes. *Chem. Vap. Depos.* **1995**, 1 (1), 8–23.
- (47) Hunt, A. T.; Carter, W. B.; Cochran, J. K. Combustion Chemical Vapor Deposition: A Novel Thin-Film Deposition Technique. *Appl. Phys. Lett.* **1993**, 63 (2), 266.

- (48) George, S. M. Atomic Layer Deposition: An Overview. *Chem. Rev.* **2010**, *110* (1), 111–131.
- (49) Panish, M. B. Molecular Beam Epitaxy. *Science* **1980**, *208* (4446), 916–922.
- (50) Chiritescu, C.; Cahill, D. G.; Nguyen, N.; Johnson, D.; Bodapati, A.; Koblinski, P.; Zschack, P. Ultralow Thermal Conductivity in Disordered, Layered WSe₂ Crystals. *Science* **2007**, *315* (5810), 351–353.
- (51) Ramesh, R.; Spaldin, N. A. Multiferroics: Progress and Prospects in Thin Films. *Nat. Mater.* **2007**, *6* (1), 21–29.
- (52) Fortunato, E.; Barquinha, P.; Martins, R. Oxide Semiconductor Thin-Film Transistors: A Review of Recent Advances. *Adv. Mater.* **2012**, *24* (22), 2945–2986.
- (53) Yacoby, Y.; Sowwan, M.; Stern, E.; Cross, J. O.; Brewe, D.; Pindak, R.; Pitney, J.; Dufresne, E. M.; Clarke, R. Direct Determination of Epitaxial Interface Structure in Gd₂O₃ Passivation of GaAs. *Nat. Mater.* **2002**, *1* (2), 99–101.
- (54) Cowan, P. L.; Golovchenko, J. A.; Robbins, M. F. X-Ray Standing Waves at Crystal Surfaces. *Phys. Rev. Lett.* **1980**, *44* (25), 1680–1683.
- (55) Eom, C. B.; Cava, R. J.; Fleming, R. M.; Phillips, J. M.; Vandover, R. B.; Marshall, J. H.; Hsu, J. W.; Krajewski, J. J.; Peck, W. F. Single-Crystal Epitaxial Thin Films of the Isotropic Metallic Oxides Sr[1-x] Ca[x] RuO₃ (0 ≤ x ≤ 1). *Science* **1992**, *258* (5089), 1766–1769.
- (56) Lim, G.; Parrish, W.; Ortiz, C.; Bellotto, M.; Hart, M. Grazing Incidence Synchrotron X-Ray Diffraction Method for Analyzing Thin Films. *J. Mater. Res.* **1987**, *2* (04), 471–477.
- (57) Quaas, M.; Eggs, C.; Wulff, H. Structural Studies of ITO Thin Films with the Rietveld Method. *Thin Solid Films* **1998**, *332* (1), 277–281.
- (58) Simeone, D.; Baldinozzi, G.; Gosset, D.; Zalczer, G.; Béar, J.-F.; M., A. A.; K., M. M.; A., A. P.; M., A. A.; L., G. A.; et al. Rietveld Refinements Performed on Mesoporous Ceria Layers at Grazing Incidence. *J. Appl. Crystallogr.* **2011**, *44* (6), 1205–1210.

- (59) Billinge, S. J. L.; Kanatzidis, M. G.; Wagner, C. N. J.; Jeong, I.-K.; Mohiuddin-Jacobs, F.; Petkov, V.; Billinge, S. J. L.; Kycia, S.; Petkov, V.; Peterson, P. F.; et al. Beyond Crystallography: The Study of Disorder, Nanocrystallinity and Crystallographically Challenged Materials with Pair Distribution Functions. *Chem. Commun.* **2004**, 31 (7), 749.
- (60) Billinge, S. J. L.; Levin, I. The Problem with Determining Atomic Structure at the Nanoscale. *Science* **2007**, 316 (5824), 561–565.
- (61) Peterson, P. F.; Božin, E. S.; Proffen, T.; Billinge, S. J. L.; L., B. S. J.; T., E.; L., C. F.; F., S.-B.; A., M.; F., D. W. I.; et al. Improved Measures of Quality for the Atomic Pair Distribution Function. *J. Appl. Crystallogr.* **2003**, 36 (1), 53–64.
- (62) Harris, F. R.; Standridge, S.; Johnson, D. C. The Synthesis of $[(\text{Bi}_2\text{Te}_3)_x(\text{TiTe}_2)_y]_{1.36}$ Superlattices from Modulated Elemental Reactants. *J. Am. Chem. Soc.* **2005**, 127 (21), 7843–7848.
- (63) Terban, M. W.; Johnson, M.; Di Michiel, M.; Billinge, S. J. L.; Tyrsted, C.; Jensen, K. M. Ø.; Bøjesen, E. D.; Lock, N.; Christensen, M.; Billinge, S. J. L.; et al. Detection and Characterization of Nanoparticles in Suspension at Low Concentrations Using the X-Ray Total Scattering Pair Distribution Function Technique. *Nanoscale* **2015**, 7 (12), 5480–5487.
- (64) Yang, X.; Juhás, P.; Billinge, S. J. L.; IUCr; J.-F., B.; P., L.; J., C. P.; X., Q.; C., H. J.; L., L. P.; et al. On the Estimation of Statistical Uncertainties on Powder Diffraction and Small-Angle Scattering Data from Two-Dimensional X-Ray Detectors. *J. Appl. Crystallogr.* **2014**, 47 (4), 1273–1283.
- (65) Yang, X.; Juhas, P.; Farrow, C. L.; Billinge, S. J. L. xPDFsuite: An End-to-End Software Solution for High Throughput Pair Distribution Function Transformation, Visualization and Analysis. **2014**.

CHAPTER IV

- (1) Stein, A.; Keller, S. W.; Mallouk, T. E. Turning down the Heat: Design and Mechanism in Solid-State Synthesis. *Science*. **1993**, 259, 1558–1564.
- (2) Schmalzried, H. *Chemical Kinetics of Solids*; John Wiley & Sons, 2008.

- (3) Sze, S. M. *Semiconductor Devices: Physics and Technology*; John Wiley & Sons, 2008.
- (4) Popov, I. M. *Stoichiometry in Crystal Compounds and Its Influence on Their Physical Properties*; Nova Publishers, 1988; Vol. 177.
- (5) Wiegers, G. A. Misfit Layer Compounds: Structures and Physical Properties. *Prog. Solid State Chem.* **1996**, 24 (1), 1–139.
- (6) Wiegers, G. A.; Haange, R. J. Electrical Transport Properties of the Misfit Layer Compounds (SnS) 1.20 TiS₂ and (PbS) 1.18 TiS₂. *Eur. J. solid state Inorg. Chem.* **1991**, 28 (5), 1071–1078.
- (7) Auriel, C.; Meerschaut, A.; Deudon, C.; Wiegers, G. A.; Baas, J.; Chen, J.; Monceau, P. Electrical Transport Properties of Mono-and Bilayers Misfit Compounds (MX) 1+ X (TX₂) M, M. *Eur. J. solid state Inorg. Chem.* **1995**, 32 (9), 947–962.
- (8) Suzuki, K.; Enoki, T.; Bandow, S. Electronic Properties and Valence State of Sm in (SmS) 1.19 TaS₂. *Phys. Rev. B* **1993**, 48 (15), 11077.
- (9) Wiegers, G. A.; Meetsma, A.; Haange, R. J.; de Boer, J. L. Structure, Electrical Transport and Magnetic Properties of the Misfit Layer Compound (SmS)_{1.19} TaS₂ “SmTaS 3.” *J. Less Common Met.* **1991**, 168 (2), 347–359.
- (10) Di Salvo, F. J.; Waszczak, J. V. Transport Properties and the Phase Transition in Ti[1-x] M[x] Se₂ (M=Ta or V). *Phys. Rev. B* **1978**, 17 (10), 3801–3807.
- (11) Legma, J. B.; Vacquier, G.; Casalot, A. Chemical Vapour Transport of Molybdenum and Tungsten Diselenides by Various Transport Agents. *J. Cryst. Growth* **1993**, 130 (1), 253–258.
- (12) Lin, Q.; Smeller, M.; Heideman, C. L.; Zschack, P.; Koyano, M.; Anderson, M. D.; Kykyneshi, R.; Keszler, D. A.; Anderson, I. M.; Johnson, D. C. Rational Synthesis and Characterization of a New Family of Low Thermal Conductivity Misfit Layer Compounds [(PbSe) 0.99] M (WSe₂) N. *Chem. Mater.* **2009**, 22 (3), 1002–1009.
- (13) Harris, F. R.; Standridge, S.; Johnson, D. C. The Synthesis of [(Bi₂Te₃)_x((TiTe₂)_y)_{1.36}] Superlattices from Modulated Elemental Reactants. *J. Am. Chem. Soc.* **2005**, 127 (21), 7843–7848.

- (14) Moore, D. B.; Stolt, M. J.; Atkins, R.; Sitts, L.; Jones, Z.; Disch, S.; Matt, B.; Johnson, D. C. Structural and Electrical Properties of (PbSe) 1.16 TiSe₂. *Emerg. Mater. Res.* **2012**, 1 (6), 292–298.
- (15) Phung, T. M.; Jensen, J. M.; Johnson, D. C.; Donovan, J. J.; McBurnett, B. G. Determination of the Composition of Ultra-Thin Ni-Si Films on Si: Constrained Modeling of Electron Probe Microanalysis and X-Ray Reflectivity Data. *X-Ray Spectrom.* **2008**, 37, 608–614.
- (16) Schaffer, M.; Schaffer, B.; Ramasse, Q. Sample Preparation for Atomic-Resolution STEM at Low Voltages by FIB. *Ultramicroscopy* **2012**, 114, 62–71.
- (17) der Pauw, L. J. A Method of Measuring the Resistivity and Hall Coefficient on Lamellae of Arbitrary Shape. *Philips Tech. Rev.* **1958**, 20 (8), 220–224.
- (18) Giang, N.; Xu, Q.; Hor, Y. S.; Williams, A. J.; Dutton, S. E.; Zandbergen, H. W.; Cava, R. J. Superconductivity at 2.3 K in the Misfit Compound (PbSe) 1.16 (TiSe₂)₂. *Phys. Rev. B* **2010**, 82 (2), 24503.
- (19) Snyder, G. J.; Toberer, E. S. Complex Thermoelectric Materials. *Nat. Mater.* **2008**, 7 (2), 105–114.
- (20) Pei, Y.; Wang, H.; Snyder, G. J. Band Engineering of Thermoelectric Materials. *Adv. Mater.* **2012**, 24 (46), 6125–6135.
- (21) Merrill, D. R.; Moore, D. B.; Ditto, J.; Sutherland, D. R.; Falmbigl, M.; Winkler, M.; Pernau, H.-F.; Johnson, D. C. The Synthesis, Structure, and Electrical Characterization of (SnSe)_{1.2} TiSe₂. *Eur. J. Inorg. Chem.* **2014**.
- (22) Wolf, S. Silicon Processing for the VLSI Era. In *LATTICE*; 1995; pp 559–581.

CHAPTER V

- (1) Pacilé, D.; Meyer, J. C.; Girit, C. O.; Zettl, A. The Two-Dimensional Phase of Boron Nitride: Few-Atomic-Layer Sheets and Suspended Membranes. *Appl. Phys. Lett.* **2008**, 92 (13), 133107.
- (2) Liu, H.; Neal, A. T.; Zhu, Z.; Luo, Z.; Xu, X.; Tománek, D.; Ye, P. D. Phosphorene: An Unexplored 2D Semiconductor with a High Hole Mobility. *ACS Nano* **2014**, 8 (4), 4033–4041.

- (3) Wang, Q. H.; Kalantar-Zadeh, K.; Kis, A.; Coleman, J. N.; Strano, M. S. Electronics and Optoelectronics of Two-Dimensional Transition Metal Dichalcogenides. *Nat. Nanotechnol.* **2012**, 7 (11), 699–712.
- (4) Geim, A. K.; Grigorieva, I. V. Van Der Waals Heterostructures. *Nature* **2013**, 499 (7459), 419–425.
- (5) Ferrari, A. C. Science and Technology Roadmap for Graphene, Related Two-Dimensional Crystals, and Hybrid Systems. *Nanoscale* **2014**, 7 (11), 4598–4810.
- (6) Li, M.-Y.; Chen, C.-H.; Shi, Y.; Li, L.-J. Heterostructures Based on Two-Dimensional Layered Materials and Their Potential Applications. *Mater. Today* **2015**.
- (7) Jariwala, D.; Sangwan, V. K.; Lauhon, L. J.; Marks, T. J.; Hersam, M. C. Emerging Device Applications for Semiconducting Two-Dimensional Transition Metal Dichalcogenides. *ACS Nano* **2014**, 8 (2), 1102–1120.
- (8) Huang, X.; Tan, C.; Yin, Z.; Zhang, H. 25th Anniversary Article: Hybrid Nanostructures Based on Two-Dimensional Nanomaterials. *Adv. Mater.* **2014**, 26 (14), 2185–2204.
- (9) Teweldebrhan, D.; Goyal, V.; Balandin, A. A. Exfoliation and Characterization of Bismuth Telluride Atomic Quintuples and Quasi-Two-Dimensional Crystals. *Nano Lett.* **2010**, 10 (4), 1209–1218.
- (10) Fei, R.; Faghaninia, A.; Soklaski, R.; Yan, J.-A.; Lo, C.; Yang, L. Enhanced Thermoelectric Efficiency via Orthogonal Electrical and Thermal Conductances in Phosphorene. *Nano Lett.* **2014**, 14 (11), 6393–6399.
- (11) Zhang, Y.; Wang, H.; Kräemer, S.; Shi, Y.; Zhang, F.; Snedaker, M.; Ding, K.; Moskovits, M.; Snyder, G. J.; Stucky, G. D. Surfactant-Free Synthesis of Bi₂Te₃-Te Micro-Nano Heterostructure with Enhanced Thermoelectric Figure of Merit. *ACS Nano* **2011**, 5 (4), 3158–3165.
- (12) Dresselhaus, M. S.; Chen, G.; Tang, M. Y.; Yang, R. G.; Lee, H.; Wang, D. Z.; Ren, Z. F.; Fleurial, J.-P.; Gogna, P. New Directions for Low-Dimensional Thermoelectric Materials. *Adv. Mater.* **2007**, 19 (8), 1043–1053.

- (13) Pietryga, J. M.; Schaller, R. D.; Werder, D.; Stewart, M. H.; Klimov, V. I.; Hollingsworth, J. A. Pushing the Band Gap Envelope: Mid-Infrared Emitting Colloidal PbSe Quantum Dots. *J. Am. Chem. Soc.* **2004**, *126* (38), 11752–11753.
- (14) Smith, D. L.; Mailhot, C. Theory of Semiconductor Superlattice Electronic Structure. *Rev. Mod. Phys.* **1990**, *62* (1), 173–234.
- (15) Kandaswamy, P. K.; Guillot, F.; Bellet-Amalric, E.; Monroy, E.; Nevou, L.; Tchernycheva, M.; Michon, A.; Julien, F. H.; Baumann, E.; Giorgetta, F. R.; et al. GaN/AlN Short-Period Superlattices for Intersubband Optoelectronics: A Systematic Study of Their Epitaxial Growth, Design, and Performance. *J. Appl. Phys.* **2008**, *104* (9), 093501.
- (16) Beekman, M.; Heideman, C. L.; Johnson, D. C. Ferecrystals: Non-Epitaxial Layered Intergrowths. *Semicond. Sci. Technol.* **2014**, *29* (6), 064012.
- (17) Falmbigl, M.; Alemayehu, M. B.; Merrill, D. R.; Beekman, M.; Johnson, D. C. In-Plane Structure of Ferecrystalline Compounds. *Cryst. Res. Technol.* **2015**, *50* (6), 464–472.
- (18) Moore, D.; Stolt, M.; Atkins, R.; Sitts, L.; Jones, Z.; Disch, S.; Beekman, M.; Johnson, D. Structural and Electrical Properties of (PbSe) 1.16 TiSe₂. *Emerg. Mater. Res.* **2012**, *1* (6), 292–298.
- (19) Merrill, D. R.; Moore, D. B.; Coffey, M. N.; Jansons, A. W.; Falmbigl, M.; Johnson, D. C. Synthesis and Characterization of Turbostratically Disordered (BiSe) 1.15 TiSe₂. *Semicond. Sci. Technol.* **2014**, *29* (6), 064004.
- (20) Merrill, D. R.; Moore, D. B.; Ditto, J.; Sutherland, D. R.; Falmbigl, M.; Winkler, M.; Pernau, H.-F.; Johnson, D. C. The Synthesis, Structure, and Electrical Characterization of (SnSe) 1.2 TiSe₂. *Eur. J. Inorg. Chem.* **2015**, *2015* (1), 83–91.
- (21) Merrill, D.; Moore, D.; Bauers, S.; Falmbigl, M.; Johnson, D. Misfit Layer Compounds and Ferecrystals: Model Systems for Thermoelectric Nanocomposites. *Materials (Basel)*. **2015**, *8* (4), 2000–2029.
- (22) Bauers, S. R.; Merrill, D. R.; Moore, D. B.; Johnson, D. C. Carrier Dilution in TiSe₂ Based Intergrowth Compounds for Enhanced Thermoelectric Performance. *J. Mater. Chem. C* **2015**, *3* (40), 10451–10458.

- (23) Bauers, S. R.; Moore, D. B.; Ditto, J.; Johnson, D. C. Phase Width of Kinetically Stable $[(\text{PbSe})_{1+\delta}(\text{TiSe}_2)_1]$ Ferecrystals and the Effect of Precursor Composition on Electrical Properties. *J. Alloys Compd.* **2015**, *645*, 118–124.
- (24) Atkins, R.; Wilson, J.; Zschack, P.; Grosse, C.; Neumann, W.; Johnson, D. C. Synthesis of $[(\text{SnSe})_{1.15}]_M(\text{TaSe}_2)_N$ Ferecrystals: Structurally Tunable Metallic Compounds. *Chem. Mater.* **2012**, *24* (23), 4594–4599.
- (25) Schaffer, M.; Schaffer, B.; Ramasse, Q. Sample Preparation for Atomic-Resolution STEM at Low Voltages by FIB. *Ultramicroscopy* **2012**, *114*, 62–71.
- (26) Altshuler, B. L.; Khmel'nitzkii, D.; Larkin, A. I.; Lee, P. A. Magnetoresistance and Hall Effect in a Disordered Two-Dimensional Electron Gas. *Phys. Rev. B* **1980**, *22* (11), 5142–5153.
- (27) Wan, C.; Wang, Y.; Wang, N.; Koumoto, K. Low-Thermal-Conductivity $(\text{MS})_{1+x}(\text{TiS}_2)_2$ ($M = \text{Pb, Bi, Sn}$) Misfit Layer Compounds for Bulk Thermoelectric Materials. *Materials (Basel)*. **2010**, *3* (4), 2606–2617.
- (28) Falmbigl, M.; Fiedler, A.; Atkins, R. E.; Fischer, S. F.; Johnson, D. C. Suppressing a Charge Density Wave by Changing Dimensionality in the Ferecrystalline Compounds $[(\text{SnSe})_{1.15}]_1(\text{VSe}_2)_n$ with $N = 1, 2, 3, 4$. *Nano Lett.* **2015**, *15* (2), 943–948.
- (29) Falmbigl, M.; Putzky, D.; Ditto, J.; Esters, M.; Bauers, S. R.; Ronning, F.; Johnson, D. C. Influence of Defects on the Charge Density Wave of $[(\text{SnSe})_{1+\delta}]_1(\text{VSe}_2)_1$ Ferecrystals. *ACS Nano* **2015**, *9* (8), 8440–8448.
- (30) Snyder, G. J.; Toberer, E. S. Complex Thermoelectric Materials. *Nat. Mater.* **2008**, *7* (2), 105–114.
- (31) Rowe, D. M.; Kuznetsov, V. L.; Kuznetsova, L. A.; Min, G. Electrical and Thermal Transport Properties of Intermediate-Valence YbAl_3 . *J. Phys. D: Appl. Phys.* **2002**, *35* (17), 2183–2186.
- (32) Cario, L.; Lafond, A.; Palvadeau, P.; Deudon, C.; Meerschaut, A. Evidence of a Mixed-Valence State for Europium in the Misfit Layer Compound $[(\text{EuS})_{1.5}]_{1.15}\text{NbS}_2$ by Means of a Superspace Structural Determination, Mössbauer Spectroscopy, and Magnetic Measurements. *J. Solid State Chem.* **1999**, *147* (1), 58–67.

- (33) Danzenbächer, S.; Molodtsova, S. L.; Koepernik, K.; Tomm, Y.; Laubschat, C. Electronic Structure of TiSe₂ and TiSe₂ Intercalated with Eu. *Mol. Cryst. Liq. Cryst. Sci. Technol. Sect. A. Mol. Cryst. Liq. Cryst.* **2000**, *341* (2), 45–50.
- (34) Rasch, J. C. E.; Stemmler, T.; Müller, B.; Dudy, L.; Manzke, R. 1T-TiSe₂: Semimetal or Semiconductor? *Phys. Rev. Lett.* **2008**, *101* (23), 237602.
- (35) Giang, N.; Xu, Q.; Hor, Y. S.; Williams, A. J.; Dutton, S. E.; Zandbergen, H. W.; Cava, R. J. Superconductivity at 2.3 K in the Misfit Compound (PbSe)_{1.16}(TiSe₂)₂. *Phys. Rev. B* **2010**, *82* (2), 24503.
- (36) Wiegers, G. . Misfit Layer Compounds: Structures and Physical Properties. *Prog. Solid State Chem.* **1996**, *24* (1-2), 1–139.
- (37) McDonald, S. A.; Konstantatos, G.; Zhang, S.; Cyr, P. W.; Klem, E. J. D.; Levina, L.; Sargent, E. H. Solution-Processed PbS Quantum Dot Infrared Photodetectors and Photovoltaics. *Nat. Mater.* **2005**, *4* (2), 138–142.
- (38) Whittingham, M. S. Chemistry of Intercalation Compounds: Metal Guests in Chalcogenide Hosts. *Prog. Solid State Chem.* **1978**, *12* (1), 41–99.
- (39) Mendizabal, F.; Contreras, R.; Aizman, A. A Model for the Charge Capacity of 1T-TiS₂ Intercalated with Li. *Int. J. Quantum Chem.* **1995**, *56* (6), 819–823.
- (40) M.S. Dresselhaus. Intercalation In Layered Materials. *MRS Bull.* **1987**, *12* (03), 24–28.

CHAPTER VI

- (1) Stein, A.; Keller, S. W.; Mallouk, T. E. Turning down the Heat: Design and Mechanism in Solid-State Synthesis. *Science.* **1993**, *259*, 1558–1564.
- (2) DiSalvo, F. J. Solid-State Chemistry: A Rediscovered Chemical Frontier. *Science.* **1990**, *247*, 649–655.
- (3) Shoemaker, D. P.; Hu, Y.-J.; Chung, D. Y.; Halder, G. J.; Chupas, P. J.; Soderholm, L.; Mitchell, J. F.; Kanatzidis, M. G. In Situ Studies of a Platform for Metastable Inorganic Crystal Growth and Materials Discovery. *Proc. Natl. Acad. Sci.* **2014**, *111*, 10922–10927.

- (4) Bauers, S. R.; Wood, S. R.; Jensen, K. M. O.; Blichfeld, A. B.; Iversen, B. B.; Billinge, S. J. L.; Johnson, D. C. Structural Evolution of Iron Antimonides from Amorphous Precursors to Crystalline Products Studied by Total Scattering Techniques. *J. Am. Chem. Soc.* **2015**.
- (5) Kanatzidis, M. G. Structural Evolution and Phase Homologies for “Design” and Prediction of Solid-State Compounds. *Acc. Chem. Res.* **2005**, 38 (4), 359–368.
- (6) Poudeu, P. F. P.; D’Angelo, J.; Kong, H.; Downey, A.; Short, J. L.; Pcionek, R.; Hogan, T. P.; Uher, C.; Kanatzidis, M. G. Nanostructures versus Solid Solutions: Low Lattice Thermal Conductivity and Enhanced Thermoelectric Figure of Merit in $\text{Pb}_{9.6}\text{Sb}_{0.2}\text{Te}_{10-x}\text{Se}_x$ Bulk Materials. *J. Am. Chem. Soc.* **2006**, 128 (44), 14347–14355.
- (7) Makongo, J. P. A.; Misra, D. K.; Zhou, X.; Pant, A.; Shabetai, M. R.; Su, X.; Uher, C.; Stokes, K. L.; Poudeu, P. F. P. Simultaneous Large Enhancements in Thermopower and Electrical Conductivity of Bulk Nanostructured Half-Heusler Alloys. *J. Am. Chem. Soc.* **2011**, 133 (46), 18843–18852.
- (8) Makongo, J. P. A.; Misra, D. K.; Salvador, J. R.; Takas, N. J.; Wang, G.; Shabetai, M. R.; Pant, A.; Paudel, P.; Uher, C.; Stokes, K. L.; et al. Thermal and Electronic Charge Transport in Bulk Nanostructured $\text{Zr}_{0.25}\text{Hf}_{0.75}\text{NiSn}$ Composites with Full-Heusler Inclusions. *J. Solid State Chem.* **2011**, 184 (11), 2948–2960.
- (9) Biswas, K.; He, J.; Zhang, Q.; Wang, G.; Uher, C.; Dravid, V. P.; Kanatzidis, M. G. Strained Endotaxial Nanostructures with High Thermoelectric Figure of Merit. *Nat. Chem.* **2011**, 3 (2), 160–166.
- (10) Biswas, K.; He, J.; Blum, I. D.; Wu, C.-I.; Hogan, T. P.; Seidman, D. N.; Dravid, V. P.; Kanatzidis, M. G. High-Performance Bulk Thermoelectrics with All-Scale Hierarchical Architectures. *Nature* **2012**, 489 (7416), 414–418.
- (11) Zhao, L.-D.; Dravid, V. P.; Kanatzidis, M. G. The Panoscopic Approach to High Performance Thermoelectrics. *Energy Environ. Sci.* **2014**, 7 (1), 251–268.
- (12) Bauers, S.; Ditto, J.; Moore, D. B.; Johnson, D. C. Structure-Property Relationships in Non-Epitaxial Chalcogenide Heterostructures: The Role of Interface Density on Charge Exchange. *Nanoscale* **2016**.

- (13) Bauers, S. R.; Merrill, D. R.; Moore, D. B.; Johnson, D. C. Carrier Dilution in TiSe₂ Based Intergrowth Compounds for Enhanced Thermoelectric Performance. *J. Mater. Chem. C* **2015**, 3 (40), 10451–10458.
- (14) Merrill, D.; Moore, D.; Bauers, S.; Falmbigl, M.; Johnson, D. Misfit Layer Compounds and Ferecrystals: Model Systems for Thermoelectric Nanocomposites. *Materials (Basel)*. **2015**, 8 (4), 2000–2029.
- (15) Esters, M.; Alemayehu, M. B.; Jones, Z.; Nguyen, N. T.; Anderson, M. D.; Grosse, C.; Fischer, S. F.; Johnson, D. C. Synthesis of Inorganic Structural Isomers By Diffusion-Constrained Self-Assembly of Designed Precursors: A Novel Type of Isomerism. *Angew. Chemie* **2015**, 127 (4), 1146–1150.
- (16) Falmbigl, M.; Fiedler, A.; Atkins, R. E.; Fischer, S. F.; Johnson, D. C. Suppressing a Charge Density Wave by Changing Dimensionality in the Ferecrystalline Compounds ([SnSe]_{1.15})₁(VSe₂)_n with N = 1, 2, 3, 4. *Nano Lett.* **2015**, 15 (2), 943–948.
- (17) Alemayehu, M. B.; Falmbigl, M.; Ta, K.; Grosse, C.; Westover, R. D.; Bauers, S. R.; Fischer, S. F.; Johnson, D. C. Structural and Electrical Properties of ([SnSe]_{1+δ})_M(NbSe₂)₁ Compounds: Single NbSe₂ Layers Separated by Increasing Thickness of SnSe. *Chem. Mater.* **2015**, 27 (3), 867–875.
- (18) Lin, Q.; Smeller, M.; Heideman, C. L.; Zschack, P.; Koyano, M.; Anderson, M. D.; Kykyneshi, R.; Keszler, D. A.; Anderson, I. M.; Johnson, D. C. Rational Synthesis and Characterization of a New Family of Low Thermal Conductivity Misfit Layer Compounds [(PbSe)_{0.99}]_M(WSe₂)_{N+}. *Chem. Mater.* **2009**, 22 (3), 1002–1009.
- (19) Schaffer, M.; Schaffer, B.; Ramasse, Q. Sample Preparation for Atomic-Resolution STEM at Low Voltages by FIB. *Ultramicroscopy* **2012**, 114, 62–71.
- (20) Tise, P.; Moore, D. B.; Beekman, M.; Disch, S.; Zschack, P.; Ha, I.; Neumann, W.; Johnson, D. C. Synthesis , Structure , and Properties of Turbostratically Disordered. **2013**.
- (21) Falmbigl, M.; Alemayehu, M. B.; Merrill, D. R.; Beekman, M.; Johnson, D. C. In-Plane Structure of Ferecrystalline Compounds. *Cryst. Res. Technol.* **2015**, 50 (6), 464–472.

- (22) Moore, D.; Stolt, M.; Atkins, R.; Sitts, L.; Jones, Z.; Disch, S.; Beekman, M.; Johnson, D. Structural and Electrical Properties of (PbSe) 1.16 TiSe $_2$. *Emerg. Mater. Res.* **2012**, 1 (6), 292–298.
- (23) Bauers, S. R.; Moore, D. B.; Ditto, J.; Johnson, D. C. Phase Width of Kinetically Stable $[(\text{PbSe})_{1+\delta}](\text{TiSe}_2)_1$ Ferecrystals and the Effect of Precursor Composition on Electrical Properties. *J. Alloys Compd.* **2015**, 645, 118–124.
- (24) Merrill, D. R.; Sutherland, D. R.; Ditto, J. J.; Moore, D. B.; Falmbigl, M.; Medlin, D. L.; Johnson, D. C. The Synthesis of $\{[(\text{PbSe})_{1+\delta}]_m (\text{TiSe}_2)_n [(\text{SnSe}_2)_{1+\gamma}]_m (\text{TiSe}_2)_n\}$ Heterostructures with Designed Nanoarchitectures by Self Assembly of Amorphous Precursors. *Nanoscale* **2016**, 8 (28), 13646–13651.

CHAPTER VII

- (1) Dresselhaus, M. S.; Chen, G.; Tang, M. Y.; Yang, R. G.; Lee, H.; Wang, D. Z.; Ren, Z. F.; Fleurial, J.-P.; Gogna, P. New Directions for Low-Dimensional Thermoelectric Materials. *Adv. Mater.* **2007**, 19 (8), 1043–1053.
- (2) Jood, P.; Ohta, M.; Nishiate, H.; Yamamoto, A.; Lebedev, O. I.; Berthebaud, D.; Suekuni, K.; Kunii, M. Microstructural Control and Thermoelectric Properties of Misfit Layered Sulfides $(\text{LaS})_{1+M} \text{TS}_2$ ($T = \text{Cr}, \text{Nb}$): The Natural Superlattice Systems. *Chem. Mater.* **2014**, 26 (8), 2684–2692.
- (3) Biswas, K.; He, J.; Zhang, Q.; Wang, G.; Uher, C.; Dravid, V. P.; Kanatzidis, M. G. Strained Endotaxial Nanostructures with High Thermoelectric Figure of Merit. *Nat. Chem.* **2011**, 3 (2), 160–166.
- (4) Tan, G.; Shi, F.; Doak, J. W.; Sun, H.; Zhao, L.-D.; Wang, P.; Uher, C.; Wolverton, C.; Dravid, V. P.; Kanatzidis, M. G. Extraordinary Role of Hg in Enhancing the Thermoelectric Performance of P-Type SnTe. *Energy Environ. Sci.* **2015**, 8 (1), 267–277.
- (5) Jood, P.; Ohta, M. Hierarchical Architecturing for Layered Thermoelectric Sulfides and Chalcogenides. *Materials (Basel)*. **2015**, 8 (3), 1124–1149.
- (6) Venkatasubramanian, R.; Siivola, E.; Colpitts, T.; O'Quinn, B. Thin-Film Thermoelectric Devices with High Room-Temperature Figures of Merit. *Nature* **2001**, 413 (6856), 597–602.

- (7) Merrill, D.; Moore, D.; Bauers, S.; Falmbigl, M.; Johnson, D. Misfit Layer Compounds and Ferecrystals: Model Systems for Thermoelectric Nanocomposites. *Materials (Basel)*. **2015**, 8 (4), 2000–2029.
- (8) Wiegers, G. . Misfit Layer Compounds: Structures and Physical Properties. *Prog. Solid State Chem.* **1996**, 24 (1-2), 1–139.
- (9) Miyazaki, Y.; Ogawa, H.; Kajitani, T. Preparation and Thermoelectric Properties of Misfit-Layered Sulfide [Yb 1.90 S 2] 0.62 NbS 2. *Jpn. J. Appl. Phys.* **2004**, 43 (No. 9A/B), L1202–L1204.
- (10) Wan, C.; Wang, Y.; Norimatsu, W.; Kusunoki, M.; Koumoto, K. Nanoscale Stacking Faults Induced Low Thermal Conductivity in Thermoelectric Layered Metal Sulfides. *Appl. Phys. Lett.* **2012**, 100 (10), 101913.
- (11) Wiegers, G. A. Charge Transfer between Layers in Misfit Layer Compounds. *J. Alloys Compd.* **1995**, 219 (1-2), 152–156.
- (12) Wan, C.; Wang, Y.; Wang, N.; Koumoto, K. Low-Thermal-Conductivity (MS)_{1+x}(TiS₂)₂ (M = Pb, Bi, Sn) Misfit Layer Compounds for Bulk Thermoelectric Materials. *Materials (Basel)*. **2010**, 3 (4), 2606–2617.
- (13) Fang, C.; de Groot, R.; Haas, C. Bulk and Surface Electronic Structure of 1T-TiS₂ and 1T-TiSe₂. *Phys. Rev. B* **1997**, 56 (8), 4455–4463.
- (14) Sootsman, J. R.; Chung, D. Y.; Kanatzidis, M. G. New and Old Concepts in Thermoelectric Materials. *Angew. Chem. Int. Ed. Engl.* **2009**, 48 (46), 8616–8639.
- (15) Beekman, M.; Heideman, C. L.; Johnson, D. C. Ferecrystals: Non-Epitaxial Layered Intergrowths. *Semicond. Sci. Technol.* **2014**, 29 (6), 064012.
- (16) Mavrokefalos, A.; Lin, Q.; Beekman, M.; Seol, J. H.; Lee, Y. J.; Kong, H.; Pettes, M. T.; Johnson, D. C.; Shi, L. In-Plane Thermal and Thermoelectric Properties of Misfit-Layered [(PbSe)_{0.99}]_x (WSe₂)_X Superlattice Thin Films. *Appl. Phys. Lett.* **2010**, 96 (18), 181908.
- (17) Giang, N.; Xu, Q.; Hor, Y. S.; Williams, A. J.; Dutton, S. E.; Zandbergen, H. W.; Cava, R. J. Superconductivity at 2.3 K in the Misfit Compound (PbSe) 1.16 (TiSe 2) 2. *Phys. Rev. B* **2010**, 82 (2), 24503.

- (18) Moore, D. B.; Beekman, M.; Disch, S.; Zschack, P.; Ha?usler, I.; Neumann, W.; Johnson, D. C. Synthesis, Structure, and Properties of Turbostratically Disordered (PbSe) 1.18 (TiSe $_2$) 2 . *Chem. Mater.* **2013**, *25* (12), 2404–2409.
- (19) Alemayehu, M. B.; Mitchson, G.; Ditto, J.; Hanken, B. E.; Asta, M.; Johnson, D. C. Charge Transfer between PbSe and NbSe 2 in [(PbSe) 1.14] M (NbSe 2) 1 Ferecrystalline Compounds. *Chem. Mater.* **2014**, *26* (5), 1859–1866.
- (20) Falmbigl, M.; Fiedler, A.; Atkins, R. E.; Fischer, S. F.; Johnson, D. C. Suppressing a Charge Density Wave by Changing Dimensionality in the Ferecrystalline Compounds [(SnSe) 1.15] 1 (VSe $_2$) n with $N = 1, 2, 3, 4$. *Nano Lett.* **2015**, *15* (2), 943–948.
- (21) Esters, M.; Alemayehu, M. B.; Jones, Z.; Nguyen, N. T.; Anderson, M. D.; Grosse, C.; Fischer, S. F.; Johnson, D. C. Synthesis of Inorganic Structural Isomers By Diffusion-Constrained Self-Assembly of Designed Precursors: A Novel Type of Isomerism. *Angew. Chemie* **2015**, *127* (4), 1146–1150.
- (22) Moore, D.; Stolt, M.; Atkins, R.; Sitts, L.; Jones, Z.; Disch, S.; Beekman, M.; Johnson, D. Structural and Electrical Properties of (PbSe) 1.16 TiSe $_2$. *Emerg. Mater. Res.* **2012**, *1* (6), 292–298.
- (23) Noh, M.; Johnson, C. D.; Hornbostel, M. D.; Thiel, J.; Johnson, D. C. Control of Reaction Pathway and the Nanostructure of Final Products through the Design of Modulated Elemental Reactants. *Chem. Mater.* **1996**, *8*, 1625–1635.
- (24) Lin, Q.; Smeller, M.; Heideman, C. L.; Zschack, P.; Koyano, M.; Anderson, M. D.; Kykyneshi, R.; Keszler, D. A.; Anderson, I. M.; Johnson, D. C. Rational Synthesis and Characterization of a New Family of Low Thermal Conductivity Misfit Layer Compounds [(PbSe) 0.99] M (WSe $_2$) N^+ . *Chem. Mater.* **2009**, *22* (3), 1002–1009.
- (25) Huntley, D. R.; Sienko, M. J.; Hiebl, K. Magnetic Properties of Iron-Intercalated Titanium Diselenide. *J. Solid State Chem.* **1984**, *52* (3), 233–243.
- (26) Moore, D. B.; Sitts, L.; Stolt, M. J.; Beekman, M.; Johnson, D. C. Characterization of Nonstoichiometric $Ti_{1+x} Se_2$ Prepared by the Method of Modulated Elemental Reactants. *J. Electron. Mater.* **2012**, *42* (7), 1647–1651.

- (27) Bauers, S. R.; Moore, D. B.; Ditto, J.; Johnson, D. C. Phase Width of Kinetically Stable $[(\text{PbSe})_{1+\delta}(\text{TiSe}_2)_1]$ Ferecrystals and the Effect of Precursor Composition on Electrical Properties. *J. Alloys Compd.* **2015**, 645, 118–124.
- (28) Lin, Q.; Tepfer, S.; Heideman, C.; Mortensen, C.; Nguyen, N.; Zschack, P.; Beekman, M.; Johnson, D. C. Influence of Selenium Vapor Postannealing on the Electrical Transport Properties of PbSe-WSe_2 Nanolaminates. *J. Mater. Res.* **2011**, 26 (15), 1866–1871.
- (29) Merrill, D. R.; Sutherland, D. R.; Ditto, J.; Bauers, S. R.; Falmbigl, M.; Medlin, D. L.; Johnson, D. C. Kinetically Controlled Site-Specific Substitutions in Higher-Order Heterostructures. *Chem. Mater.* **2015**, 27 (11), 4066–4072.
- (30) Rasch, J. C. E.; Stemmler, T.; Müller, B.; Dudy, L.; Manzke, R. 1T- TiSe_2 : Semimetal or Semiconductor? *Phys. Rev. Lett.* **2008**, 101 (23), 237602.
- (31) Pei, Y.; LaLonde, A. D.; Wang, H.; Snyder, G. J. Low Effective Mass Leading to High Thermoelectric Performance. *Energy Environ. Sci.* **2012**, 5 (7), 7963.
- (32) Merrill, D. R.; Moore, D. B.; Ditto, J.; Sutherland, D. R.; Falmbigl, M.; Winkler, M.; Pernau, H.-F.; Johnson, D. C. The Synthesis, Structure, and Electrical Characterization of $(\text{SnSe})_{1.2}\text{TiSe}_2$. *Eur. J. Inorg. Chem.* **2015**, 2015 (1), 83–91.
- (33) Zhou, W. Y.; Meetsma, A.; de Boer, J. L.; Wiegers, G. A. Characterization and Electrical Transport Properties of the Misfit Layer Compounds $(\text{BiSe})_{1.10}\text{NbSe}_2$ and $(\text{BiSe})_{1.09}\text{TaSe}_2$. *Mater. Res. Bull.* **1992**, 27 (5), 563–572.
- (34) Zhou, W. Y.; Meetsma, A.; de Boer, J. L.; Wiegers, G. A. Characterization, Electrical Transport and Magnetic Properties of the Rare Earth Misfit Layer Compounds $(\text{TbS})_{1.21}\text{NbS}_2$, $(\text{TbS})_{1.20}\text{TaS}_2$, $(\text{DyS})_{1.22}\text{NbS}_2$ and $(\text{DyS})_{1.21}\text{TaS}_2$. *J. Alloys Compd.* **1996**, 233 (1-2), 80–88.

CHAPTER VIII

- (1) Rowe, D. M. *CRC Handbook of Thermoelectrics*; CRC Press, 1995.
- (2) DiSalvo, F. J. Thermoelectric Cooling and Power Generation. *Science*. **1999**, 285 (5428), 703–706.
- (3) Snyder, G. J.; Toberer, E. S. Complex Thermoelectric Materials. *Nat. Mater.* **2008**, 7 (2), 105–114.

- (4) Sootsman, J. R.; Chung, D. Y.; Kanatzidis, M. G. New and Old Concepts in Thermoelectric Materials. *Angew. Chem. Int. Ed. Engl.* **2009**, 48 (46), 8616–8639.
- (5) Mahan, G. D.; Sofo, J. O. The Best Thermoelectric. *Proc. Natl. Acad. Sci.* **1996**, 93 (15), 7436–7439.
- (6) Mahan, G. D. Rare Earth Thermoelectrics. In *XVI ICT “97. Proceedings ICT”97. 16th International Conference on Thermoelectrics (Cat. No.97TH8291)*; IEEE, 1997; pp 21–27.
- (7) Rowe, D. M.; Kuznetsov, V. L.; Kuznetsova, L. A.; Min, G. Electrical and Thermal Transport Properties of Intermediate-Valence YbAl₃. *J. Phys. D. Appl. Phys.* **2002**, 35 (17), 2183–2186.
- (8) Sun, P.; Oeschler, N.; Johnsen, S.; Iversen, B. B.; Steglich, F. Narrow Band Gap and Enhanced Thermoelectricity in FeSb₂. *Dalton Trans.* **2010**, 39 (4), 1012–1019.
- (9) Hicks, L. D.; Dresselhaus, M. S. Effect of Quantum-Well Structures on the Thermoelectric Figure of Merit. *Phys. Rev. B* **1993**, 47 (19), 12727–12731.
- (10) Wang, Y.; Rogado, N. S.; Cava, R. J.; Ong, N. P. Spin Entropy as the Likely Source of Enhanced Thermopower in Na_xCo₂O₄. *Nature* **2003**, 423 (6938), 425–428.
- (11) Winkler, M.; Liu, X.; Schürmann, U.; König, J. D.; Kienle, L.; Bensch, W.; Böttner, H. Current Status in Fabrication, Structural and Transport Property Characterization, and Theoretical Understanding of Bi₂Te₃ / Sb₂Te₃ Superlattice Systems. *Zeitschrift für Anorg. und Allg. Chemie* **2012**, 638 (15), 2441–2454.
- (12) Bauers, S. R.; Merrill, D. R.; Moore, D. B.; Johnson, D. C. Carrier Dilution in TiSe₂ Based Intergrowth Compounds for Enhanced Thermoelectric Performance. *J. Mater. Chem. C* **2015**, 3 (40), 10451–10458.
- (13) Stein, A.; Keller, S. W.; Mallouk, T. E. Turning down the Heat: Design and Mechanism in Solid-State Synthesis. *Science*. **1993**, 259, 1558–1564.

- (14) DiSalvo, F. J. Solid-State Chemistry: A Rediscovered Chemical Frontier. *Science*. **1990**, *247*, 649–655.
- (15) Merrill, D. R.; Sutherland, D. R.; Ditto, J. J.; Moore, D. B.; Falmbigl, M.; Medlin, D. L.; Johnson, D. C. The Synthesis of $\{[(\text{PbSe})_{1+\delta}]_m (\text{TiSe}_2)_n [(\text{SnSe}_2)_{1+\gamma}]_m (\text{TiSe}_2)_n\}$ Heterostructures with Designed Nanoarchitectures by Self Assembly of Amorphous Precursors. *Nanoscale* **2016**, *8* (28), 13646–13651.
- (16) Merrill, D. R.; Moore, D. B.; Ditto, J.; Sutherland, D. R.; Falmbigl, M.; Winkler, M.; Pernau, H.-F.; Johnson, D. C. The Synthesis, Structure, and Electrical Characterization of $(\text{SnSe})_{1.2} \text{TiSe}_2$. *Eur. J. Inorg. Chem.* **2014**.
- (17) Wood, S. R.; Merrill, D. R.; Falmbigl, M.; Moore, D. B.; Ditto, J.; Esters, M.; Johnson, D. C. Tuning Electrical Properties through Control of TiSe_2 Thickness in $(\text{BiSe})_{1+\delta} (\text{TiSe}_2)_n$ Compounds. *Chem. Mater.* **2015**, *27* (17), 6067–6076.
- (18) Bauers, S.; Ditto, J.; Moore, D. B.; Johnson, D. C. Structure-Property Relationships in Non-Epitaxial Chalcogenide Heterostructures: The Role of Interface Density on Charge Exchange. *Nanoscale* **2016**.
- (19) Esters, M.; Alemayehu, M. B.; Jones, Z.; Nguyen, N. T.; Anderson, M. D.; Grosse, C.; Fischer, S. F.; Johnson, D. C. Synthesis of Inorganic Structural Isomers By Diffusion-Constrained Self-Assembly of Designed Precursors: A Novel Type of Isomerism. *Angew. Chemie* **2015**, *127* (4), 1146–1150.
- (20) Merrill, D. R.; Sutherland, D. R.; Ditto, J.; Bauers, S. R.; Falmbigl, M.; Medlin, D. L.; Johnson, D. C. Kinetically Controlled Site-Specific Substitutions in Higher-Order Heterostructures. *Chem. Mater.* **2015**, *27* (11), 4066–4072.
- (21) Westover, R. D.; Ditto, J.; Falmbigl, M.; Hay, Z. L.; Johnson, D. C. Synthesis and Characterization of Quaternary Monolayer Thick $\text{MoSe}_2/\text{SnSe}/\text{NbSe}_2/\text{SnSe}$ Heterojunction Superlattices. *Chem. Mater.* **2015**, *27* (18), 6411–6417.
- (22) Chiritescu, C.; Cahill, D. G.; Heideman, C.; Lin, Q.; Mortensen, C.; Nguyen, N. T.; Johnson, D.; Rostek, R.; Böttner, H. Low Thermal Conductivity in Nanoscale Layered Materials Synthesized by the Method of Modulated Elemental Reactants. *J. Appl. Phys.* **2008**, *104* (3), 033533.

- (23) Gunning, N. S.; Feser, J.; Beekman, M.; Cahill, D. G.; Johnson, D. C. Synthesis and Thermal Properties of Solid-State Structural Isomers: Ordered Intergrowths of SnSe and MoSe₂. *J. Am. Chem. Soc.* **2015**, *137* (27), 8803–8809.
- (24) Beekman, M.; Heideman, C. L.; Johnson, D. C. Ferecrystals: Non-Epitaxial Layered Intergrowths. *Semicond. Sci. Technol.* **2014**, *29* (6), 064012.
- (25) Merrill, D. R.; Moore, D. B.; Coffey, M. N.; Jansons, A. W.; Falmbigl, M.; Johnson, D. C. Synthesis and Characterization of Turbostratically Disordered (BiSe) 1.15 TiSe 2. *Semicond. Sci. Technol.* **2014**, *29* (6), 064004.
- (26) Moore, D.; Stolt, M.; Atkins, R.; Sitts, L.; Jones, Z.; Disch, S.; Beekman, M.; Johnson, D. Structural and Electrical Properties of (PbSe) 1.16 TiSe₂. *Emerg. Mater. Res.* **2012**, *1* (6), 292–298.
- (27) Lin, Q.; Smeller, M.; Heideman, C. L.; Zschack, P.; Koyano, M.; Anderson, M. D.; Kykyneshi, R.; Keszler, D. A.; Anderson, I. M.; Johnson, D. C. Rational Synthesis and Characterization of a New Family of Low Thermal Conductivity Misfit Layer Compounds [(PbSe) 0.99] M (WSe₂) N+. *Chem. Mater.* **2009**, *22* (3), 1002–1009.
- (28) Atkins, R.; Wilson, J.; Zschack, P.; Grosse, C.; Neumann, W.; Johnson, D. C. Synthesis of [(SnSe) 1.15] M (TaSe 2) N Ferecrystals: Structurally Tunable Metallic Compounds. *Chem. Mater.* **2012**, *24* (23), 4594–4599.
- (29) Phung, T. M.; Jensen, J. M.; Johnson, D. C.; Donovan, J. J.; McBurnett, B. G. Determination of the Composition of Ultra-Thin Ni-Si Films on Si: Constrained Modeling of Electron Probe Microanalysis and X-Ray Reflectivity Data. *X-Ray Spectrom.* **2008**, *37*, 608–614.
- (30) Di Salvo, F. J.; Waszczak, J. V. Transport Properties and the Phase Transition in Ti[1-x] M[x] Se[2] (M=Ta or V). *Phys. Rev. B* **1978**, *17* (10), 3801–3807.
- (31) Beekman, M.; Disch, S.; Rouvimov, S.; Kasinathan, D.; Koepernik, K.; Rosner, H.; Zschack, P.; Neumann, W. S.; Johnson, D. C. Controlling Size-Induced Phase Transformations Using Chemically Designed Nanolaminates. *Angew. Chemie Int. Ed.* **2013**, *52* (50), 13211–13214.

CHAPTER IX

- (1) Triscone, J.-M.; Karkut, M. G.; Antognazza, L.; Brunner, O.; Fischer, Ø. Y-Ba-Cu-O/Dy-Ba-Cu-O Superlattices: A First Step towards the Artificial Construction of High- T_c Superconductors. *Phys. Rev. Lett.* **1989**, 63 (9), 1016–1019.
- (2) John, S. Strong Localization of Photons in Certain Disordered Dielectric Superlattices. *Phys. Rev. Lett.* **1987**, 58 (23), 2486–2489.
- (3) Baibich, M. N.; Broto, J. M.; Fert, A.; Van Dau, F. N.; Petroff, F.; Etienne, P.; Creuzet, G.; Friederich, A.; Chazelas, J. Giant Magnetoresistance of (001)Fe/(001)Cr Magnetic Superlattices. *Phys. Rev. Lett.* **1988**, 61 (21), 2472–2475.
- (4) Venables, J. A.; Spiller, G. D. T.; Hanbucken, M.; F, A. F.; Akhter P, D. J. J. A. P. and V. J. A.; R, A.; M, A. R. and H.; Anton R, H. M. and M. T.; Anton R, H. M. P. M. and S. H.; E, A. C. and R. G.; et al. Nucleation and Growth of Thin Films. *Reports Prog. Phys.* **1984**, 47 (4), 399–459.
- (5) Daudin, B.; Widmann, F.; Feuillet, G.; Samson, Y.; Arlery, M.; Rouvière, J. L. Stranski-Krastanov Growth Mode during the Molecular Beam Epitaxy of Highly Strained GaN. *Phys. Rev. B* **1997**, 56 (12), R7069–R7072.
- (6) Hull, R.; Bean, J. C.; Cerdeira, F.; Fiory, A. T.; Gibson, J. M. Stability of Semiconductor Strained-Layer Superlattices. *Appl. Phys. Lett.* **1986**, 48 (1), 56.
- (7) Geim, A. K.; Grigorieva, I. V. Van Der Waals Heterostructures. *Nature* **2013**, 499 (7459), 419–425.
- (8) Li, M.-Y.; Chen, C.-H.; Shi, Y.; Li, L.-J. Heterostructures Based on Two-Dimensional Layered Materials and Their Potential Applications. *Mater. Today* **2015**.
- (9) Haigh, S. J.; Gholinia, A.; Jalil, R.; Romani, S.; Britnell, L.; Elias, D. C.; Novoselov, K. S.; Ponomarenko, L. A.; Geim, A. K.; Gorbachev, R. Cross-Sectional Imaging of Individual Layers and Buried Interfaces of Graphene-Based Heterostructures and Superlattices. *Nat. Mater.* **2012**, 11 (9), 764–767.
- (10) Beekman, M.; Heideman, C. L.; Johnson, D. C. Ferecrystals: Non-Epitaxial Layered Intergrowths. *Semicond. Sci. Technol.* **2014**, 29 (6), 064012.

- (11) Lin, Q.; Smeller, M.; Heideman, C. L.; Zschack, P.; Koyano, M.; Anderson, M. D.; Kykyneshi, R.; Keszler, D. A.; Anderson, I. M.; Johnson, D. C. Rational Synthesis and Characterization of a New Family of Low Thermal Conductivity Misfit Layer Compounds $[(\text{PbSe})_{0.99}]_M (\text{WSe}_2)_N$. *Chem. Mater.* **2009**, 22 (3), 1002–1009.
- (12) Westover, R. D.; Ditto, J.; Falmbigl, M.; Hay, Z. L.; Johnson, D. C. Synthesis and Characterization of Quaternary Monolayer Thick $\text{MoSe}_2/\text{SnSe}/\text{NbSe}_2/\text{SnSe}$ Heterojunction Superlattices. *Chem. Mater.* **2015**, 27 (18), 6411–6417.
- (13) Beekman, M.; Disch, S.; Rouvimov, S.; Kasinathan, D.; Koepernik, K.; Rosner, H.; Zschack, P.; Neumann, W. S.; Johnson, D. C. Controlling Size-Induced Phase Transformations Using Chemically Designed Nanolaminates. *Angew. Chemie Int. Ed.* **2013**, 52 (50), 13211–13214.
- (14) Alemayehu, M. B.; Ta, K.; Falmbigl, M.; Johnson, D. C. Structure, Stability, and Properties of the Intergrowth Compounds $[(\text{SnSe})_{1+\delta}]_m (\text{NbSe}_2)_n$, Where $M = N = 1$ –20. *J. Am. Chem. Soc.* **2015**, 137 (14), 4831–4839.
- (15) Atkins, R.; Wilson, J.; Zschack, P.; Grosse, C.; Neumann, W.; Johnson, D. C. Synthesis of $[(\text{SnSe})_{1.15}]_M (\text{TaSe}_2)_N$ Ferecrystals: Structurally Tunable Metallic Compounds. *Chem. Mater.* **2012**, 24 (23), 4594–4599.
- (16) Falmbigl, M.; Alemayehu, M. B.; Merrill, D. R.; Beekman, M.; Johnson, D. C. In-Plane Structure of Ferecrystalline Compounds. *Cryst. Res. Technol.* **2015**, 50 (6), 464–472.
- (17) Merrill, D. R.; Sutherland, D. R.; Ditto, J.; Bauers, S. R.; Falmbigl, M.; Medlin, D. L.; Johnson, D. C. Kinetically Controlled Site-Specific Substitutions in Higher-Order Heterostructures. *Chem. Mater.* **2015**, 27 (11), 4066–4072.
- (18) Merrill, D. R.; Moore, D. B.; Ditto, J.; Sutherland, D. R.; Falmbigl, M.; Winkler, M.; Pernau, H.-F.; Johnson, D. C. The Synthesis, Structure, and Electrical Characterization of $(\text{SnSe})_{1.2} \text{TiSe}_2$. *Eur. J. Inorg. Chem.* **2014**.
- (19) Bauers, S.; Ditto, J.; Moore, D. B.; Johnson, D. C. Structure-Property Relationships in Non-Epitaxial Chalcogenide Heterostructures: The Role of Interface Density on Charge Exchange. *Nanoscale* **2016**.

- (20) Chattopadhyay, T.; Pannetier, J.; Von Schnering, H. G. Neutron Diffraction Study of the Structural Phase Transition in SnS and SnSe. *J. Phys. Chem. Solids* **1986**, 47 (9), 879–885.
- (21) Bauers, S. R.; Merrill, D. R.; Moore, D. B.; Johnson, D. C. Carrier Dilution in TiSe₂ Based Intergrowth Compounds for Enhanced Thermoelectric Performance. *J. Mater. Chem. C* **2015**, 3 (40), 10451–10458.